THESIS

Mechanistic Visco-Elastic Modeling of Shear Deformation and Failure in Internally-Reinforced Geosynthetic Clay Liners

Submitted by

Aaron Baukus

Department of Civil & Environmental Engineering

In partial fulfillment of the requirements

For the Degree of Master of Science

Colorado State University

Fort Collins, Colorado

Summer 2022

Master's Committee:

Advisor: Christopher A. Bareither

Joseph Scalia
Mostafa Yourdkhani

ABSTRACT

MECHANISTIC VISCO-ELASTIC MODELING OF SHEAR DEFORMATION AND FAILURE IN INTERNALLY-REINFORCED GEOSYNTHETIC CLAY LINERS

Analysis and prediction of the shear behavior of a non-heat-treated needle punched geosynthetic clay liner (NHT NP GCL) have been conducted using a mechanistic model. A three-element Kelvin-chain model was employed to simulate the incremental loading of a rapid loading shear test. A performance analysis initially was conducted to evaluate variation in model parameters with respect to differences in physical properties of GCLs (i.e., peel strength) and experimental conditions (i.e., normal stress, temperature, creep shear stress). The optimized model parameters demonstrated sensitivity to the variation in internal and external factors and yielded empirical relationships that were carried forward to test model applicability for predicting time-to-failure for an internally-reinforced GCL. These data trends in combination with creep-test data were used to calibrate the creep deformation model. Time-to-failure predictions performed with the calibrated creep deformation model resulted in a percent error < 9%. A modified model-calibration procedure was developed to extend model applicability to stress conditions common in practice. The modified calibration procedure was used to predict NHT NP GCL creep deformation in a hypothetical landfill cover system. The time required for the projected deformation to surpass 3 mm exceeded one million years for all stress conditions evaluated, which suggested that the NHT NP GCL will not experience creep failure in the low-stress cover scenarios evaluated.

ACKNOWLEDGEMENTS

I would like to thank my advisor, Dr. Christopher Bareither, for his guidance and patience throughout each step of the research and writing process. Your helpful feedback challenged my thinking and pushed me to perform at higher levels.

I would also like to thank Dr. Joseph Scalia and Dr. Mostafa Yourdkhani for serving on my committee.

I would like to thank my parents for their encouragement and good advice. You always know what to say.

TABLE OF CONTENTS

LIST OF TABLES

LIST OF FIGURES

LIST OF SYMBOLS

A – Shear surface area

CS – constant stress creep test

CSR – Creep stress ratio

CSR_N – Normalized creep stress ratio

E – Elastic Modulus

ES – Entanglement strength

G_D – Shear deformation modulus

G_C – Creep deformation modulus

k – Number of required model elements

l – Specimen length

R – Retardation time

RD – Resistance to disentanglement

RLS – Rapid loading stress test

R_x, R_y – Reaction forces between fiber bundles and carrier geotextile

S – Slope of τ-δ_{EOL} curve during Stage II

SWS – Stepwise shear test

t – Time

T – Temperature

TTF – Time to failure

δ_{EID} – End of immediate deformation

δ_{EOL} – Horizontal deformation at the end of loading during an RLS test

δ_h– Horizontal deformation

δ_{hi} – Immediate horizontal deformation

δ_{h1} – Delayed I horizontal deformation

δ_{h2} – Delayed II horizontal deformation

δ_{max} – Maximum deformation represented by long-term or lifetime model

δ_T – Maximum tolerable deformation before entering failure

ε – Strain

η – Viscosity

Λ – Normalized deformation in the direction of shear

σ_{nt} – Total normal stress

σ_{nf} – Total normal stress at failure

τ_c – Shear stress applied during creep

τ_p – Short-term peak shear strength

1 INTRODUCTION

1.1 PROBLEM STATEMENT

Geosynthetic clay liners (GCLs) are an essential component of modern barrier systems for waste containment. A GCL acts as a hydraulic barrier to prevent leachate from entering the environment and must be capable of withstanding the normal and shear stresses that develop along the slopes of barrier systems. Reinforcement can be added to a GCL in the form of needle-punching to enhance the internal shear strength.

Shear stress applied to the surface of a needle-punched GCL (NP GCL) will produce internal tensile forces. The tensile forces acting on the reinforcements result in shear deformation that can be segregated into short-term and long-term deformation. Short-term deformation occurs rapidly after stress is applied and tends to be elastic at low stresses. Long-term deformation results from extended exposure to shear stresses and is known as creep in viscoelastic materials.

The Kelvin-chain model is a mechanistic model that has been widely used to represent creep deformation of viscoelastic materials (Roscoe 1950; Bazant 1996; Koerner 2001). The Kelvin-chain model describes material behavior in terms of elastic moduli and viscosity. These physical parameters of the Kelvin-chain model can be related to physical characteristics of the deforming material and help gain an understanding of the applicability of the model to predict creep deformation and failure.

Creep experiments conducted on GCLs have shown that deformation rate and magnitude is dependent on stress conditions and can lead to internal shear failure (Koerner 2001; Zanzinger and Saathoff 2010; Ghazizadeh and Bareither 2018b). Neglecting GCL creep deformation in engineering design can lead to unforeseen consequences and potentially failure of the waste-containment barrier system. Performing laboratory creep tests tends to be costly and time-consuming (Koerner 2001); therefore, a methodology is needed that minimizes the use of laboratory data to predict the stress-dependent creep deformation of NP GCLs and estimate time-to-failure.

1.2 OBJECTIVES

The objectives of this study were to (1) evaluate the ability of the Kelvin-chain model to capture short-term shear deformation behavior of a NP GCL and (2) develop a methodology for predicting long-term shear behavior of a NP GCL. A short-term analysis was conducted via the simulation of laboratory data to assess variation in model parameters with variation in GCL peel strength and experimental conditions (i.e., normal stress, temperature, and creep shear stress). Model parameterization was performed during the short-term analysis via lab data. The calibrated parameters were used to develop a methodology for predicting creep in NP GCLs.

2 BACKGROUND

2.1 GCL SHEAR BEHAVIOR

A GCL is a manufactured hydraulic barrier consisting of a layer of clay bonded to a geomembrane or encapsulated between geotextiles (ASTM D4439). The most common GCL incorporates a thin layer of bentonite (e.g., 5-10 mm) between polypropylene cover and carrier geotextiles. The cover geotextile is non-woven, whereas the carrier geotextile can be woven or nonwoven. Saturated sodium bentonite can attain hydraulic conductivity < 10^{-9} m/s (Kong et al. 2017) (Shackelford et al. 2000), which enables a thin GCL to function as a hydraulic barrier and obstruct the seepage of leachate from solid wastes into the environment.

A schematic of a needle-punched reinforced GCL (NP GCL) is shown in Fig. 1. Reinforcement can be added to GCLs in the form of needle punching to supplement the low shear strength of hydrated sodium bentonite. In a NP GCL, fiber bundles from the non-woven cover geotextile are punched through the bentonite layer and are left entangled in the carrier geotextile.

Needle-punched GCLs can be manufactured with heat treatment to create a heat treated (HT) NP GCL or non-heat treated (NHT) NP GCL. In a HT NP GCL, the application of heat fuses the fiber bundles to the carrier geotextile, forming a fixed connection between the fibers and carrier geotextile. In a

NHT NP GCL, the fiber bundles are left entangled within the carrier geotextile, which forms a frictional connection between the fiber bundles and geotextile.

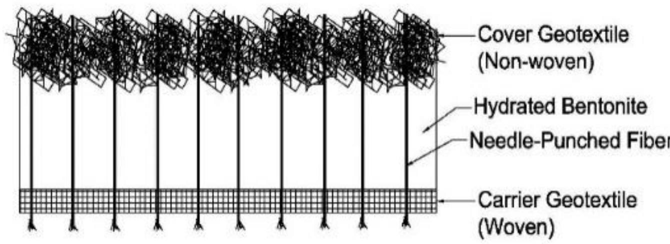

Figure 1. Cross-section schematic of a needle-punched geosynthetic clay liner from Ghazizadeh & Bareither (2018a).

2.2 MECHANICAL BEHAVIOR

Schematics of (i) a NP GCL subjected to shear stress and (ii) stresses developed within a given fiber bundle are shown in Fig. 2. Shear stress can develop within a GCL along slopes of barrier systems. The development of shear stress will cause the reinforcing fibers to align themselves in the direction of shear. The low shear strength of hydrated sodium-bentonite provides limited resistance to shear deformation (Müller et al. 2008). Therefore, shear stress is transferred across the bentonite layer via the reinforcing fibers. The free-body diagram of a fiber-bundle within a GCL in Fig. 2b includes the following forces: TF – tensile force induced by shear stress; BN and BT – normal and shear forces exerted from the bentonite on the fibers; and R – reaction force at the location of fiber entanglement. The forces BN and BT can be considered negligible based on an assumption of the lateral earth pressure of hydrated bentonite approximately equal to one (Ghazizadeh & Bareither 2018a). In a NHT NP GCL, Rx and Ry represent the frictional connection between the reinforcing fiber and carrier geotextile. In a HT NP GCL, Rx and Ry represent the fixed connection between the fiber bundles and carrier geotextile.

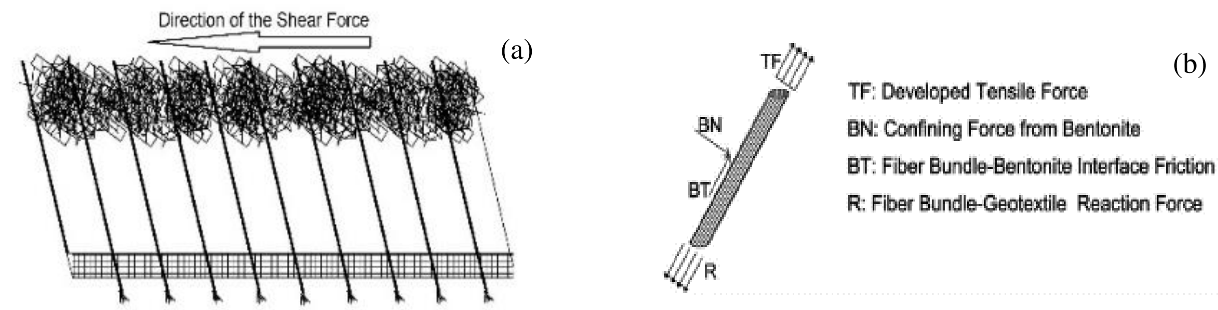

Figure 2: External (a) and internal (b) forces acting on a non-heat-treated needle-punched geosynthetic clay liner (NHT NP GCL) during shear.

There are two mechanisms that facilitate deformation within a NHT NP GCL: (i) tensile elongation of individual fiber bundles and (ii) disentanglement of fiber bundles from the carrier geotextile. Ghazizadeh and Bareither (2020) identified three stages of shear deformation in a NHT NP GCL that are shown in Fig. 3. In Stage I, the applied shear stress on the GCL generates tensile forces within the fiber bundles that are less than the reaction forces, and therefore, deformation is attributed to tensile elongation. Subsequent loading increases the tensile force in the fiber bundles and Stage II corresponds to disentanglement of the reinforcement fibers from the carrier geotextile. Disentanglement of fiber bundles is the dominant mechanism for shear deformation in a NHT NP GCL under low applied normal stress (e.g., less than 500 kPa as discussed in Bareither et al. 2018). Finally, Stage III is characterized by failure of individual fiber bundles, which develops as complete disentanglement of the fiber bundles from the carrier geotextile under low normal stress and transitions to tensile rupture of fiber bundles under higher normal stress.

Ghazizadeh and Bareither (2020) defined the entanglement strength (ES) as the average force increment in the direction of shear required to disentangle fiber bundles from the carrier geotextile. This entanglement strength can be computed as:

$$ES = \frac{S \cdot A}{n_1}(10^6) \tag{1}$$

where *S* is the slope of the shear stress vs. deformation at end-of-loading ($\tau - \delta_{h-EOL}$) curve in Stage II, A is the shear surface area, and n_1 is the average number of fiber bundles in the shear surface area.

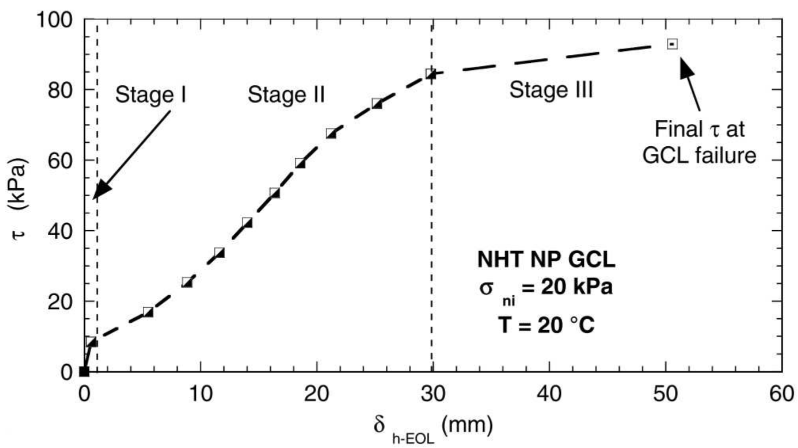

Figure 3: Relationships between shear stress (τ) and horizontal displacement at end of each loading ($\delta_{h\text{-}EOL}$) for a non-heat-treated needle-punched geosynthetic clay liner (NHT NP GCL) tested with an initial normal stress (σ_{ni}) of 20 kPa and at a temperature (T) of 20 (Ghazizadeh & Bareither 2020).

2.3 Factors affecting shear behavior

Properties of the frictional connections between the reinforcing fiber bundles and carrier geotextile are influenced by variations in the internal structure of the GCL and environmental factors of where the GCL is deployed in the field. In addition, changes in normal stress and temperature affect the forces acting on the fiber bundles and change properties of the polymeric materials used in the geotextiles of the GCL.

2.3.1 Peel strength

Geosynthetic clay liner peel strength is defined as the average load per unit width required to progressively separate the carrier and cover geotextiles of a GCL (ASTM D6496). Peel strength is used in quality control to assess the strength of a GCL (Fox and Stark 2015). A higher GCL peel strength is associated with an increase in the average number of fiber bundles per unit length (Ghazizadeh and Bareither 2018b; Ghazizadeh and Bareither 2021). An increase in peel strength has been correlated to an increase in internal shear strength of a GCL (Athanassopoulos and Yuan 2011; Bareither et al. 2018; Ghazizadeh and Bareither 2021).

Ghazizadeh and Bareither (2018b) performed rapid-loading shear tests on three GCLs with different peel strengths. The initial load resulted in deformation that was nearly identical for all three GCLs. This deformation was attributed to tensile elongation of the reinforcing fibers. Subsequent loading produced deformation due to reinforcement fiber disentanglement. The GCLs with higher peel strengths exhibited reduced shear deformation. The greater number of fiber bundles crossing the bentonite layer of a GCL with higher peel strength reduced the reaction forces acting on individual fiber bundles. The reduction in force per fiber bundle produced less disentanglement, leading to a reduction in shear deformation.

2.3.2 Normal Stress

The connections between the fiber bundles and carrier geotextile are frictional and, therefore, the strength of the connections is dependent on normal force. Fox et al. (1998) reported a positive correlation between normal stress and peak shear strength. This was attributed to the increased contribution of reinforcement to peak shear strength at higher normal stresses.

Ghazizadeh and Bareither (2018b) performed rapid-loading shear tests on NHT NP GCLs at initial normal stress (σ_{ni}) of 20, 40, and 60 kPa. Increasing σ_{ni} resulted in internal failure at higher shear stress. The higher shear stress at failure was attributed to higher entanglement strength as well as higher tensile modulus resulting from more confinement pressure. However, the ratio of shear stress to total normal stress (τ/σ_{nt}) decreased with increasing σ_{nt}, indicating curvature in the strength envelope.

Feng et al. (2020) evaluated the shear behavior of NHT NP GCLs with normal stress ranging from 250 kPa to 1000 kPa. Increasing normal stress created a stronger connection between fiber bundles and carrier geotextile. At higher normal stresses, the strength of the frictional connections exceeds the tensile strength of the individual fiber bundles, causing the fiber bundles to rupture rather than disentangle.

2.3.3 *Temperature*

The mechanical properties of polymers used in GCLs are dependent on temperature. Changes in temperature will affect the tensile properties of reinforcing fiber bundles within NHT NP GCLs and the strength of the fiber bundle-geotextile connections.

Karademir and Frost (2014) performed 105 micro-mechanical thermo-tensile tests on single polypropylene filaments at temperatures ranging from 21 to 50 ºC. The filaments exhibited a nonlinear elastic, perfectly-plastic stress-strain relationship. The tensile response of the filaments was dependent on strain rate and specimen dimensions. Increasing temperature was accompanied by a reduction in modulus of elasticity, ultimate tensile strength, and stiffness.

Ghazizadeh and Bareither (2018b) performed RLS tests at temperatures of 20, 40, 60, and 80 ºC. Increased temperatures resulted in increased shear deformation and decreased internal shear strength. This was attributed to a reduction in entanglement strength and tensile modulus of the fiber bundles. The increased temperature caused the polymers to be more flexible, which contributed to the reduction in entanglement strength and tensile modulus.

Ghazizadeh and Bareither (2020) found that an increase in temperature lead to reduction in entanglement strength that resulted in reduction in internal strength. The three stages of deformation (tensile elongation, fiber bundle disentanglement, and failure) were experienced by all GCLs regardless of temperature and normal stress. Failure occurred via bundle disentanglement for the temperatures and normal stresses evaluated.

2.4 LONG-TERM SHEAR BEHAVIOR

The displacement-controlled shear behavior of a GCL measured in a conventional direct shear test may not be indicative of the long-term shear behavior (i.e., creep). Non-heat-treated NP GCLs are viscoelastic materials that experience creep deformation under a state of constant normal and shear stress. Extended exposure to shear and normal stresses causes continuous fiber bundle disentanglement and/or tensile elongation, and under certain conditions can lead to failure.

The stages of creep deformation experienced by a NHT NP GCL are displayed in Figure 4. Immediate deformation occurs rapidly after a stress is applied and is elastoplastic in nature (Ghazizadeh & Bareither 2016). The end of immediate deformation (δ_{EID}) occurs at the inflection point of the displacement curve. Creep corresponds to progressive deformation under a constant shear stress. Failure is characterized by a rapid increase in deformation and deformation rate, which occurs concurrently with complete fiber bundle disentanglement and/or tensile rupture of the reinforcement fibers.

Stress-controlled shear testing of GCLs conducted to evaluate creep can be classified as stepwise shear (SWS) or rapid loading stress (RLS) tests. In a stepwise shear test, shear and normal stresses are applied to a GCL, and the specimen is allowed to deform for a set amount of time. If no failure occurs, the shear stress is increased, and deformation is continued under the new load. This incremental shearing process is repeated until failure is reached, or the test is terminated.

Generalized temporal deformation in a RLS test is shown in Figure 5. In this test, shear stress is incrementally increased until a desired stress is obtained, or failure occurs. If creep behavior is analyzed, shear loading is stopped at a target stress state and the GCL is allowed to creep. Zone I depicts deformation behavior during incremental loading, which is predominantly characterized as immediate deformation. Zone II represents creep behavior of the GCL, and failure is captured in Zone III.

The end of immediate deformation can be approximated using the τ-δ_{EOL} relationship (Figure 3). During loading in Stage I (Figure 5), the specimen undergoes immediate deformation and begins to transfer into creep before the next load is applied. Interpolating from δ_{EOL} provides an estimation for δ_{EID} occurring at the onset of creep. More rigorous methods for determining δ_{EID} can be found in Bareither et. al. (2013) and Handy et. al. (2002).

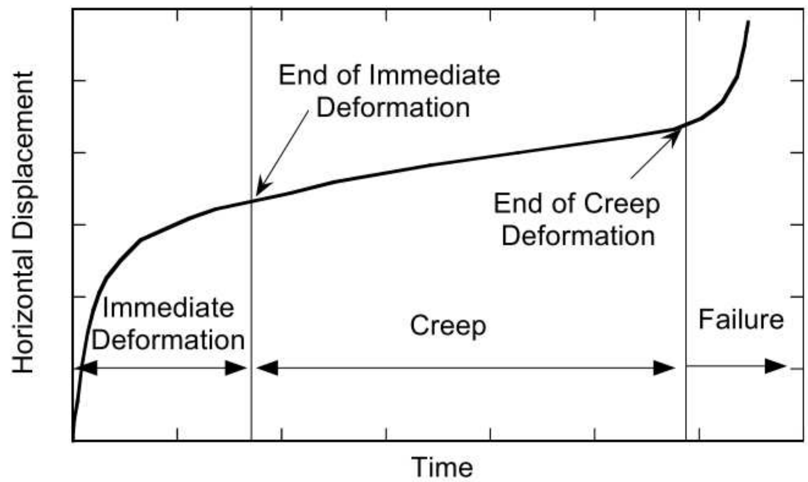

Figure 4: Stages of creep deformation experienced by a non-heat-treated needle-punched geosynthetic clay liner (NHT NP GCL).

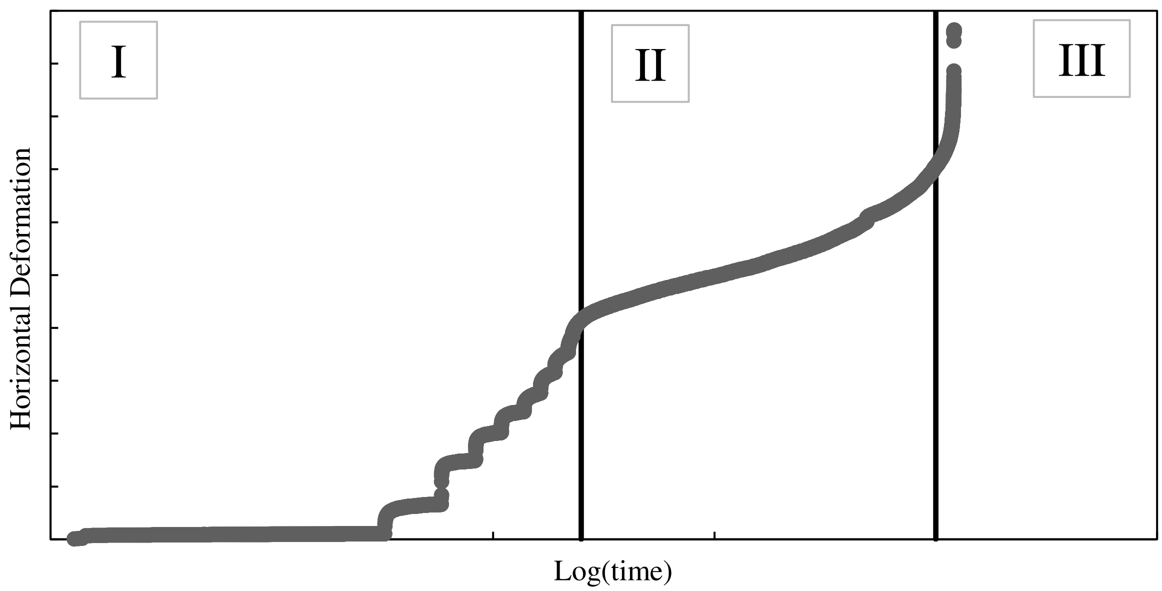

Figure 5: Generalized temporal deformation in a geosynthetic clay liner (GCL) during a rapid-loading-stress (RLS) test. Zone I: Loading, Zone II: Creep, Zone III: Failure.

2.4.1 GCL Creep Tests

Creep tests conducted on NHT NP GCLs provide insight into the deformation characteristics of the material. These tests lay the groundwork for developing predictions of creep deformation. A summary of creep tests that have been conducted on NHT NP GCLs is in Table 1. The summary includes reference, test specimen size, test temperature, creep stress ratio, test type, duration, and observation of failure. The creep stress ratio is defined as:

$$CSR = \frac{\tau_c}{\tau_p} \tag{2}$$

where τ_c is the shear stress applied during creep and τ_p is peak shear strength, which is commonly measured in a displacement-controlled direct shear test.

Koerner et al. (2001) observed different deformation characteristics while performing SWS creep tests on three GCLs. Each load was allowed to creep for 1000 h. Deformation exhibited elastic behavior for CSR < 0.3. As CSR increased and exceeded 0.4, deformation became more pronounced. Koerner et al. (2001) did not observe any secondary or tertiary creep, and post-testing inspection of the GCLs showed that the fiber bundles maintained their integrity during the creep experiments.

Relationships between shear stress and time to failure (TTF) have been observed by both Zanzinger (2016) and Ghazizadeh and Bareither (2018b). Ghazizadeh and Bareither (2018b) performed RLS tests on NP GCLs with a creep-stress ratio ranging from 0.73-0.95 so that the specimens would experience different creep durations. Tests were conducted under an initial normal stress of 20 kPa at a temperature of 20 °C. The constant-stress shear device developed by Ghazizadeh and Bareither (2018b) included a reaction frame to reduce specimen rotation during shear. Rotation developed in NP GCLs from an internal moment produced by the tensile forces in the reinforcing fibers. The moment increased with shear stress and contributed to an increase in normal stress during a given experiment. A linear relationship was observed between shear stress at failure and the logarithm of TTF. Failure was observed for shear stresses greater than 67.6 kPa and fiber disentanglement was reported as the failure mechanism.

Zanzinger (2016) performed RLS tests on NP GCLs with a max creep-stress ratio of 0.6. Tests were conducted under a normal stress of 50 kPa at a temperature of 80 °C. Tests were conducted at elevated temperatures to ensure the specimens would fail within a reasonable time. Time to failure was dependent on the applied shear stress, and failure was attributed to a combination of fiber disentanglement and fiber rupture.

The dependence of failure mechanisms on external factors was observed by Muller et al. (2008). Müller et al. (2008) performed creep tests on HT and NHT NP GCLs at temperatures ranging from room temperature to 80 °C to assess the effects of aging. The long-term shear behavior was dependent on the testing medium, whereby no failure was observed in specimens tested in tap water, but failure was observed in specimens tested in de-ionized water. The absence of failure in tap water was attributed to an increase in bentonite shear strength resulting from cation exchange. Failure observed for specimens hydrated in DI water, was dependent on fiber-resin, product design, and temperature. The NHT NP GCLs exhibited ductile failure due to fiber disentanglement. Muller et al. (2008) reported no correlation between short term peel strength and long-term time-to-failure of a GCL.

Table 1: Summary of creep tests conducted to evaluate the internal shear beahvior of non-heat treated needle-punched geosynthetic clay liners (NHT-NP-GCLs).

Reference	Specimen Size (mm)	Temperature (ºC)	Creep Stress Ratio	Test Type	Duration	Failure
Koerner et al. (2001)	300 x 300	20	0.2-0.6	SWS	Up to 5000 h	No
Muller et al. (2008)	230 x 120	Up to 80	0.39	CS	Up to 1351 d	Yes
Zanzinger et al. (2016)	200 x 200	80	0.4-0.6	RLS	Up to 7519 h	Yes
Ghazizadeh et al. (2018)	150 x 150	20	0.73-0.95	RLS	Up to 780 d	Yes

*CS = Constant Stress

2.5 VISCOELASTIC MODELS

Viscoelastic materials demonstrate both viscous and elastic characteristics during deformation. Elastic deformation in polymers is attributed to polymer bond-stretching, whereas viscous behavior is a function of local molecular mobility (Roylance 2001). The elastic and viscous mechanisms acting in tandem produce a time-dependent strain response.

Mechanistic models allow the time-dependent response seen in viscoelastic materials to be represented with material parameters. The basic elements of mechanistic viscoelastic models are the elastic spring and Newtonian dashpot. Force applied to a spring will induce immediate strain, whereas force applied to a dashpot yields a time-dependent deformation response. In viscoelastic models, a Hookean spring is used to describe elastic behavior and a Newtonian dashpot is used to describe viscous behavior. The constitutive equations for these two elements are presented in Equations 3 and 4:

$$\epsilon = \frac{\sigma}{E} \tag{3}$$

$$\epsilon = \frac{\sigma_o}{\eta} t \tag{4}$$

where σ is applied normal stress, *E* is elastic modulus, η is viscosity, and *t* is time.

Constitutive equations of mechanistic models often are written in terms of a compliance function, which is achieved by factoring out the applied stress. Rearranging the constitutive equations for a spring in compliance form yields Equations 5 and 6.

$$\epsilon(t) = \sigma J(t) \tag{5}$$

$$J(t) = \frac{1}{E} \tag{6}$$

A Kelvin element is formed by arranging a spring and dashpot in parallel. When a stress is applied, the instantaneous elastic response of the spring will be held back by the time-dependent viscous response of the dashpot. The Kelvin model is not capable of representing the immediate response displayed by many viscoelastic materials. Additionally, the strain predicted by this model reaches an upper boundary. As a result, this model is incapable of representing the increasing strain rate observed in GCL failure.

More realistic material responses are obtained by combining multiple Kelvin elements in series. A generalized Kelvin-chain model is shown in Figure 6, which consists of *N* number of Kelvin elements placed in series. A spring can be added to the series of Kelvin elements to account for the initial elastic deformation commonly observed in solid materials. The constitutive equations for the Kelvin-chain model are presented in Equations 7-9:

$$\epsilon(t) = \sigma J(t) \tag{7}$$

$$J(t) = \frac{1}{E_0} + \sum_{i=1}^{n} \frac{1}{E_i}\left(1 - \exp\left(-\frac{t}{R_i}\right)\right) \tag{8}$$

$$R = \frac{\eta}{E} \tag{9}$$

where *R* is retardation time and *J* is the creep compliance function. The retardation factor represents the time required for the strain predicted by a Kelvin element to accumulate.

The maximum strain that can be represented by a Kelvin-chain model is governed by the elastic modulus. The maximum strain is defined by Equation 10.

$$\epsilon_{maximum} = \sigma \sum \frac{1}{E_i} \tag{10}$$

According to Bažant and Prasannan (1989), determining *R* from test data can be difficult; therefore, *R* can be chosen via satisfying Equation 11, which will yield sufficiently smooth simulated creep curves.
If the first retardation time is selected as 10^{-2}, then subsequent retardation times should be selected as 10^{-1}, 10^{0}, 10^{1}, and so forth.

$$R_i = R_1 10^{i-1}, i = 1,2, \ldots i \tag{11}$$

When an external stress is applied to the Kelvin-chain model, the first spring will deform. Then, subsequent Kelvin elements with higher spring moduli and lower viscosities will deform. The initial Kelvin element will have limited retardation owing to a lower viscosity. Ensuing deformations will take longer to accumulate due to larger dashpot viscosities. The result is a model that captures the time dependent response of viscoelastic materials. Roscoe (1950) has shown that the Kelvin-chain model can be used to represent any linear viscoelastic material.

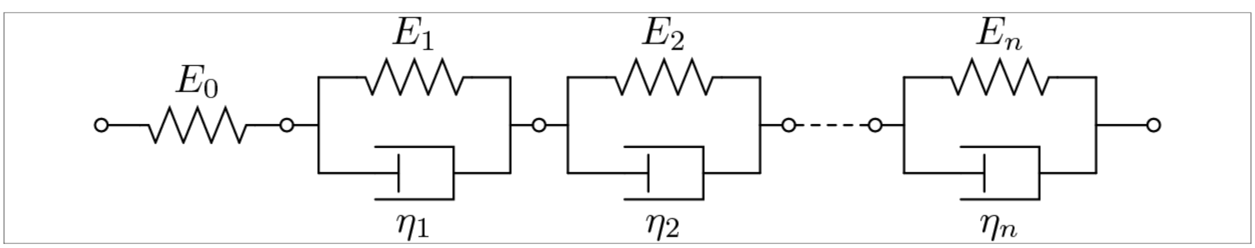

Figure 6: Kelvin-chain model schematic consisting of springs with elastic moduli (E) and dashpots with viscosity (η).

2.6 MODEL PARAMETERS

The resistance of a NHT NP GCL to deformation develops from tensile strength of reinforcing fiber bundles and entanglement strength between the fiber bundles and carrier geotextile. A shear deformation modulus (G_D) was defined herein to capture shear resistance of a GCL as a mechanistic parameter:

$$G_D = \frac{\tau}{\Lambda} \tag{12}$$

$$\Lambda = \frac{\delta_h}{l} \tag{13}$$

where τ is shear stress, δ_h is horizontal deformation, *l* is initial specimen length, and Λ is normalized horizontal deformation in the direction of shear. In a NHT NP GCL, G_D is a measure of the collective shear resistance of the fiber bundles to disentanglement and tensile elongation.

Converting the shear deformation modulus to units of N/m is useful to compare to entanglement strength. The resistance to disentanglement (RD) is presented in Equation 14:

$$RD = \frac{G_D \cdot A}{n_1 \cdot l}(10^3) \tag{14}$$

whereby the 10^3 is included for units of GD in kPa, A in m^2, and l in m. In a NHT NP GCL, *RD* is the resistance provided by the fiber bundle-geotextile connection opposing internal tensile forces.

2.7 MODELING EFFORTS

The use of mechanistic models to predict creep deformation of NHT NP GCLs has been limited. Koerner et al. (2001) used a Kelvin-chain model to extrapolate 1000-hr creep tests to 114 years. The model had retardation times ranging from 10^{-4} h to 10^6 h, which indicates the use of 10 Kelvin elements. The large number of Kelvin elements was necessary to extrapolate the temporal prediction more than two orders of magnitude.

In this study, a performance assessment was performed with a Kelvin-chain model to evaluate the incremental loading of a NHT NP GCL during an RLS test. The performance assessment evaluated the ability of the model to capture changes in shear behavior caused by variations in the GCL material structure and environmental factors. Observations from the performance assessment were used to inform predictions of creep deformation and approximations of time-to-failure (TTF).

2.7.1 Performance Assessment

Model simulations of creep deformation of a NHT NP GCL using different order Kelvin models are shown in Figure 7. These simulations exemplify the sensitivity tests performed to determine the minimum number of Kelvin elements needed to represent deformation occurring during a load increment. The number of elements in each Kelvin-chain model was increased until an improved fit was obtained to the shear deformation response from a single load increment of a RLS test. Visual observation of the model simulations in Figure 7 suggests that a three-element Kelvin-chain model was sufficient to capture shear behavior. The model simulations in Figure 7 for the four and five element models produced identical deformation curves for the time range included. In all sensitivity tests, preference was given to fewer elements in a Kelvin-chain model to reduce the number of model parameters.

The three-element Kelvin-chain model used for the model simulations was:

$$\epsilon(t) = \tau\left[\frac{1}{G_{Di}} + \frac{1}{G_{D1}}\left(1 - \exp\left(-\frac{t}{R_1}\right)\right) + \frac{1}{G_{D2}}\left(1 - \exp\left(-\frac{t}{R_2}\right)\right)\right] \tag{15}$$

where $\epsilon(t)$ is predicted normalized shear deformation, G_{Di} is the initial shear deformation modulus, G_{D1} is the delayed I shear deformation modulus, G_{D2} is the delayed II shear deformation modulus, and R_1 and R_2 are the retardation factors associated with G_{D1} and G_{D2}, respectively.

The load-increment performance assessment captured the behavior of the fiber bundle-geotextile connections during the duration of a RLS creep test. Two assumptions were made during the performance assessment: (1) deformation occurring during the first load increment is solely attributed to the tensile elongation of reinforcing fiber-bundles (i.e., no disentanglement of the fiber bundles occurs during the initial stress application). (2) When the deformation mechanism fully shifts to disentanglement, tensile elongation is negligible and does not contribute to the strain accumulation for all subsequent load increments.

The three Kelvin-element model allows for a load increment to be separated into three short-term deformation states as shown in Figure 8. During immediate deformation, the deformation is instantaneous and represented by a Hookean spring. The resistance to shear deformation is described by the immediate shear deformation moduli G_{Di}. Delayed deformation I marks the beginning of time-dependent deformation that occurs as material behavior transitions into creep. During delayed deformation I, both the first and second Kelvin-elements begin to strain; however, the strain contribution of the second Kelvin-element is negligible owing to a larger retardation time. In delayed deformation I, the resistance to shear deformation is described by the delayed shear deformation moduli G_{D1}. In delayed deformation II, the strain contribution of the first Kelvin element becomes asymptotic to the upper boundary of possible shear deformation, and therefore, all deformation is associated with the second Kelvin element. In delayed deformation II, the resistance to shear deformation is described by the delayed shear deformation moduli G_{D2}.

The magnitude of horizontal deformation associated with the immediate and delayed deformation states is determined with Equations 16 through 18.

$$\delta_{hi} = \frac{\tau}{G_{Di}} l \tag{16}$$

$$\delta_{h1} = \frac{\tau}{G_{D1}} l \tag{17}$$

$$\delta_{h2} = \frac{\tau}{G_{D2}} l \tag{18}$$

Mechanistic changes in NP GCL shear deformation can be identified by comparing the resistance to disentanglement (RD) to the entanglement strength (ES). When RD exceeds ES for a given short-term shear deformation state (Figure 8), NP GCL shear resistance exceeds the average force required to produce disentanglement. This renders that deformation state “inactive” as the magnitude of deformation for the deformation state is greatly reduced. Deformation is then attributed to the remaining active short-term shear deformation states for subsequent load increments.

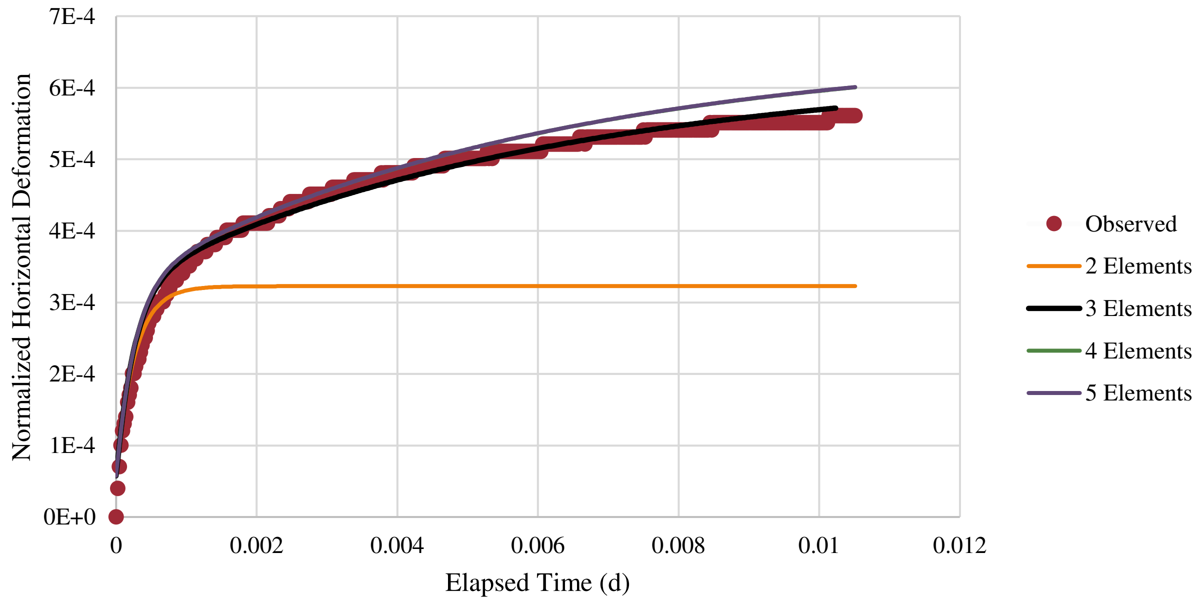

Figure 7: Model simulations of shear deformation using kelvin-chain models with elements ranging from one to five.

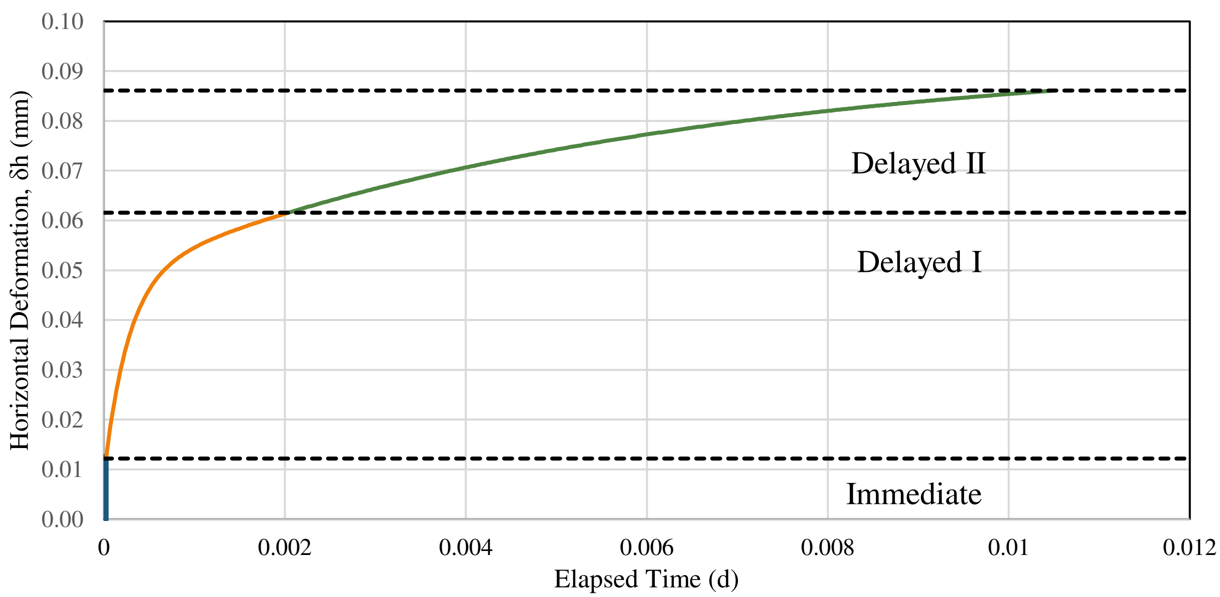

Figure 8: Shear deformation states during an individual load increment of a rapid loading shear (RLS) test. Immediate deformation: described by the immediate shear deformation moduli, G_{Di}. Delayed deformation I: time-dependent shear deformation captured by the delayed shear deformation moduli G_{D1}. Delayed deformation II: time-dependent shear deformation captured by the delayed shear deformation moduli G_{D2}.

2.7.2 *Time-to-Failure Predictions*

Performing time-to-failure predictions with a Kelvin-chain model requires ensuring the predicted deformation exceeds the tolerable deformation of a material at which failure will occur. The maximum tolerable deformation, δ_T, is the amount of deformation a NHT NP GCL can withstand before initiating internal shear failure. In the case of creep deformation, δ_T corresponds to the magnitude of deformation occurring at the end of Zone II in Figure 5. Immediately before the end of Zone II, the internal shear resistance of the material reaches a maximum. Internal shear resistance is lost as deformation continues into Zone III due to complete fiber-bundle disentanglement or rupture. The initiation of failure causes the internal shear stress to be redistributed to the remaining fiber-bundles. However, the internal reinforcement is inadequate to resist this shear stress, and the NHT NP GCL enters an accelerated rate of deformation that is indicative of internal failure. The transition from Zone II to III in Figure 5 is marked by the inflection point of the shear displacement curve (Ghazizadeh & Bareither 2018a).

Equation 10 can be modified to determine the total deformation predicted by a Kelvin-chain model:

$$\delta_{max} = \delta_{EID} + \left(\tau \sum \frac{1}{G_{Dn}}\right) l \tag{19}$$

where δ_{EID} is deformation at the end of immediate deformation. A Kelvin-chain model can accommodate δ_T if $\delta_{max} > \delta_T$.

The three Kelvin-element model used in the performance assessment is not capable of predicting time-to-failure during creep owing to limited strain capacity. Additional Kelvin-elements with a calibrated creep-modulus must be introduced to compensate for the discrepancy in deformation between load increments and creep curves. The creep modulus is defined as the shear deformation moduli capturing resistance to shear deformation during creep. According to Koerner et al. (2001), an ideal Kelvin element will have a shear deformation modulus that is inversely proportional to the accompanying retardation time. To achieve the proper parameter ratio, the appropriate creep modulus is selected with the aid of observed behavior during the model calibration.

The creep deformation model is presented in Equation 20:

$$\epsilon(t) = \tau\left[\frac{1}{G_{Di}} + \frac{1}{G_{D1}}\left(1 - exp\left(-\frac{t}{R_1}\right)\right) + \frac{1}{G_{D2}}\left(1 - exp\left(-\frac{t}{R_2}\right)\right) + \sum_{n=1}^{k}\frac{1}{G_{Cn}}\left(1 - exp\left(-\frac{t}{R_n}\right)\right)\right] \quad (20)$$

where ε(t) is predicted normalized shear deformation, τ is shear stress (kPa), *R* is the retardation factor, *k* is the number of Kelvin creep-elements necessary to accommodate δ_T, and G_C is the creep modulus. The number of required creep-elements can be determined by comparing δ_{Max} to δ_T. If δ_{Max} is less than δ_T, then *k* is increased until δ_{Max} exceeds δ_T.

3 MATERIALS AND METHODS

The data evaluated in this study were obtained from Ghazizadeh and Bareither (2018b). The RLS device used allowed for testing 150 mm x 150 mm square GCL specimens. Shear load was applied to each specimen via dead weight incremented at a rate of 20 kg every 15 minutes until reaching the target creep shear stress or until the GCL failed internally.

Ghazizadeh and Bareither (2018b) performed numerous RLS tests to evaluate the effects of internal factors (peel strength), external environmental factors (initial normal stress, temperature), and creep on NP GCl shear behavior. In this study, a performance assessment was applied to the RLS test data from Ghazizadeh and Bareither (2018b) to evaluate the effects of internal and external environmental factors on the Kelvin-Chain's model parameters. The knowledge gained from the performance assessment informed the development of the creep deformation model.

Test Series 1 through 4 obtained from Ghazizadeh and Bareither (2018b) are summarized in Table 2. Each RLS test in Table 2 is identified by the test series followed by the test number. The summary includes initial applied normal stress, maximum applied shear stress, test temperature, and GCL peel strength. Test Series 1 was conducted to evaluate the effects of GCL peel strength on shear behavior. Test Series 2 was conducted to evaluate the effects of normal stress on shear behavior. Test Series 3 was conducted to evaluate the effects of temperature on shear behavior. Test Series 4 was conducted to evaluate creep behavior. The maximum applied shear stress, τ_{max}, in Test Series 4 is the stress at which the specimens were allowed to creep. The experiment conducted with τ_{max} = 67.6 kPa (i.e., T4-5) did not reach internal failure and was terminated after 1000 h.

A flowchart that outlines the model performance assessment using the short-term model and long-term (creep deformation) model development procedures used in this study is shown in Figure 9. Shear deformation measured during incremental specimen loading during an RLS test (i.e., Zone I in Figure 5) was separated from the composite shear deformation data set of a given test. A performance assessment was conducted on each incremental load data set from Test Series 1, 2, 3, and 4 using the three-element Kelvin-chain model (Equation 15). Shear deformation moduli from the performance assessment served to (1) verify model applicability and (2) provide insight into model parameters that capture GCL internal shear behavior.

Development of the long-term model to predict time-to-failure incorporated model simulations of the creep deformation curves (i.e., Zone II in Figure 5) from each data set in Test Series 4. Creep data from each test were isolated and preprocessed (described subsequently). The three-element Kelvin-chain model was applied to each data set from Test Series 4 to obtain unique shear deformation moduli (G_D) corresponding to different magnitudes of creep shear stress. Subsequently, retardation times and creep moduli were calibrated to the creep deformation curve. The creep deformation model was constructed via combining the calibrated three-element model, retardation times, and creep moduli into a cohesive Kelvin-chain model. Time-to-failure predictions were performed by returning the time required for the creep deformation model to reach δ_T. Time-to-failure predictions could then be made.

Table 2: Summary of Test Series 1-4, which evaluated the effect of peel strength, normal stress, temperature, and creep on the internal shear beahvior of non-heat treated needle-punched GCLs.

Test No	GCL	Initial Applied Normal Stress, σ_{ni} (kPa)	Maximum Applied Shear Stress, τ_{max} (kPa)	Temperature (°C)	Peel Strength (N/m)	Time to Failure, TTF (h)
T1-1	GCL3	20	92.9	20	720	
T1-2	GCL2	20	92.9	20	1490	
T1-3	GCL1	20	92.9	20	2170	
T2-1	GCL3	20	92.9	20	720	
T2-2	GCL3	40	99.3	20	720	
T2-3	GCL3	60	111.5	20	720	
T3-1	GCL3	20	67.6	40	720	
T3-2	GCL3	20	59.1	60	720	
T3-3	GCL3	20	33.8	80	720	
T4-1	GCL3	20	92.9	20	720	0.08
T4-2	GCL3	20	88.7	20	720	0.7
T4-3	GCL3	20	84.5	20	720	1.4
T4-4	GCL3	20	80.3	20	720	117.7
T4-5	GCL3	20	67.6	20	720	NA

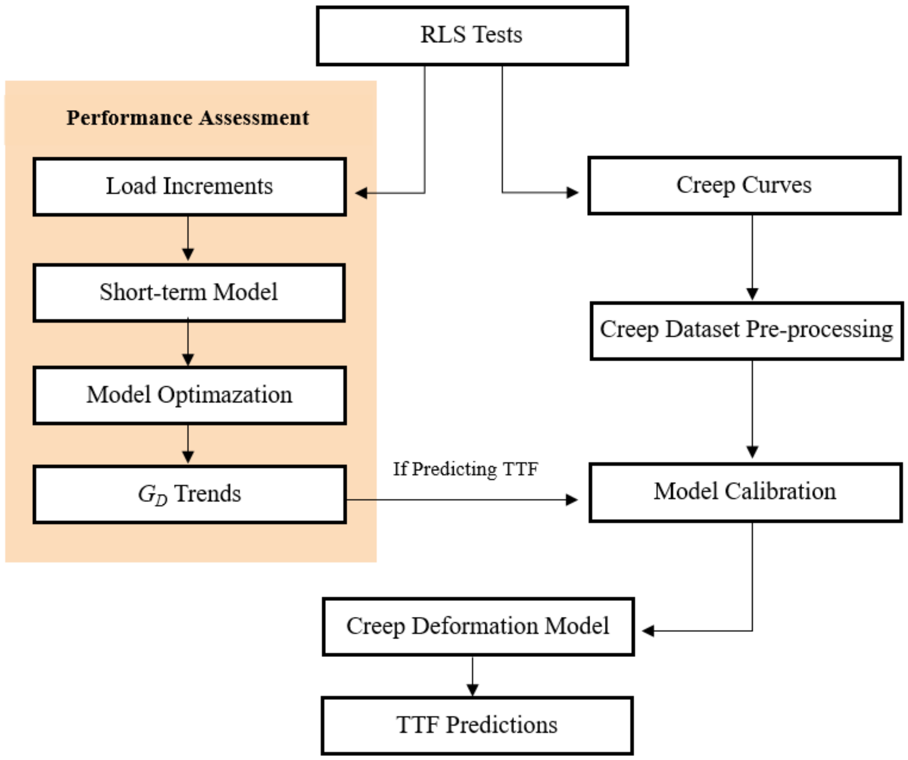

Figure 9: Flowchart of this study: (1) Shear deformation measured in a rapid loading stress (RLS) test is separated into load increments and creep deformation curves. (2) A performance assessment is performed by optimizing the three-element model to individual load increments. The performance assessment returns trends of shear deformation moduli (G_D) variation with shear stress. (3) The isolated creep deformation curves are subjected to a pre-processing procedure. Retardation times and creep elements are calibrated to the creep deformation curves to form the creep deformation model. (4) Time-to-failure predictions are performed with the creep deformation model.

3.1 MODEL OPTIMIZATION

The short-term model was fit to the individual load increments of data from Test Series 1 through 4. Model fitting involved a two-step process: (1) preprocessing the test data and (2) determining optimum model parameters for each dataset.

Data preprocessing began with isolating and transposing individual load increments so that each increment began at δ = 0 and t = 0. Horizontal displacement of the GCL was normalized with respect to specimen length in the direction of shear, and units of time were converted to days. The normalized load increment was converted to creep compliance to simplify the optimization process and facilitate comparisons between tests. Normalized deformation, time, and creep compliance are shown in Equations 21 - 23:

$$\Lambda = \frac{\delta_h}{l} \tag{21}$$

$$T = \frac{t}{24} \tag{22}$$

$$J(t) = \frac{\Lambda(t)}{\tau_i} \tag{23}$$

where Λ is normalized horizontal deformation, l is specimen length, t is elapsed time (h) and τ_i is applied shear stress during a given RLS load increment (kPa). A normalized creep stress ratio was computed to account for variation of the total normal stress during shear:

$$CSR_N = \frac{\frac{\tau}{\sigma_{nt}}}{\frac{\tau_f}{\sigma_{nf}}} \tag{24}$$

where τ and σ_{nt} are the shear and average total normal stress for a given load increment, and τ_f and σ_{nf} are the shear and total normal stress at failure. A value of $CSR_N > 1$ indicates curvature in the failure envelope, which has been observed by Ghazizadeh & Bareither (2018b), Athanassopolous and Yuan (2011), and Fox and Stark (2015) . The CSR_N is undefined for specimens that do not reach failure.

The optimization process involved (1) selecting initial values for G_D and R, and (2) performing least-squares regression to determine optimum values for G_D and R. Based on experience, selecting initial values that satisfied Equations 25 and 26 aided in achieving a convergent solution. Initial values of G_{Di} were selected such that the total deformation predicted by these parameters was approximately equivalent to the observed normalized horizontal deformation. Initial values of G_{Di} ranged from 10^2 to 10^5 and were chosen so that subsequent values decreased. Initial values of R_i were selected such that the sum of their values was approximately equivalent to the time transpiring during a load increment. Initial values were selected in accordance with the recommendations of Bažant et al. (1989).

$$\Lambda \cong \tau \sum \frac{1}{G_{Dn}}, \qquad \mathrm{G_{Di}} > \mathrm{G_{D1}} > \mathrm{G_{D2}} \ldots \tag{25}$$

$$T \cong \sum R_n, \qquad R_1 < R_2 < R_3 \ldots \tag{26}$$

3.1.1 Example Model Optimization Process

An example data set from the RLS creep test on T4-3 is shown in Figure 10. The sections identified as 1 through 9 depict incremental loading of the GCL to the target shear stress of 84 kPa. Section 10 identifies the creep stage of the experiment whereby the GCL was allowed to creep under a shear stress of 85 kPa until failure.

Stages of the model optimization process are presented in Figure 11. The second load increment (τ = 16.9 kPa) was isolated from the remainder of the test data and reproduced in Figure 11(A). Individual load increments for each RLS test in Test Series 1 through 4 were isolated by visual inspection to fit the short-term model. The duration of each load increment data set was approximately 0.25 h. Post-processed data from the load increment in Fig. 11(A) is shown in Fig. 11(B). Data in Fig. 11(B) have been transposed, normalized, and converted to creep compliance. The result of the optimization process applied to the second load increment is shown in Figure 11(C). The coefficient of determination (R^2) between the observed data and the fitted short-term model is 0.99.

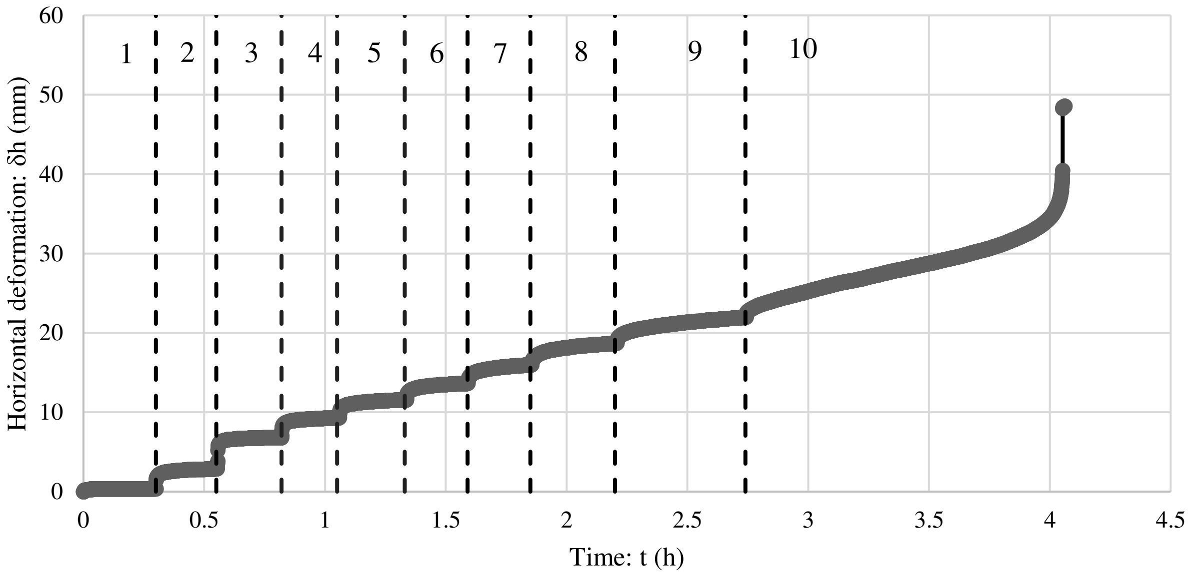

Figure 10: Rapid-loading-stress (RLS) creep test conducted on a non-heat-treated needle-punched geosynthetic clay liner (NHT NP GCL) tested with an initial normal stress (σ_{ni}) of 20 kPa and at a temperature of 20^oC.

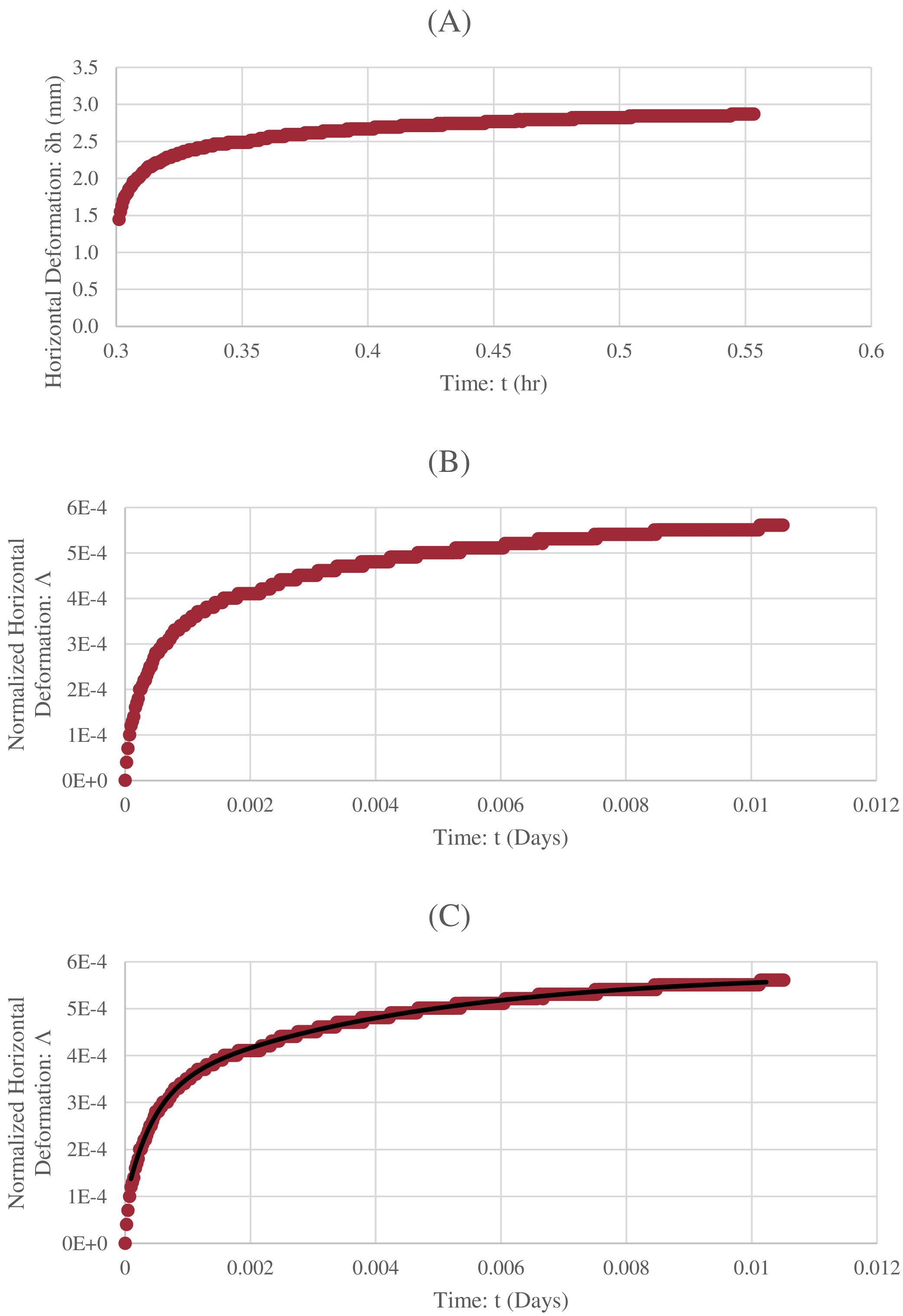

Figure 11:Temporal trends of shear deformation from Test T4-3 that depict the stages of model optimization used in this study: (A) isolated load increment; (B) transposed and normalized load increment data in the form of creep compliance; and (C) measured data fit with an optimized short-term model.

3.1.2 Optimized Model Parameters

Optimized model parameters plotted against shear stress for RLS Test T4-3 are shown in Figures 12 and 13. Values for G_D, δ_h, and R provide insight into how resistance to shear deformation develops during a given RLS test. The optimized shear deformation moduli, G_D, describes the resistance to immediate and delayed deformation during individual load increments of an RLS test. The immediate shear deformation moduli (G_{Di}) experiences a dip for $9\ kPa \leq \tau \leq 25\ kPa$ as the deformation mechanism shifts from tensile elongation to fiber-bundle disentanglement (Stage I to Stage II in Figure 3). The immediate shear deformation moduli is consistent for $25\ kPa \leq \tau \leq 51\ kPa$, and then increased steadily for the subsequent load increments. At $\tau = 51\ kPa$, the initial resistance to disentanglement (RD_i) exceeds the entanglement strength, which marks a mechanistic change in the deformation behavior caused by resistance of the connections being strengthened by the increased σ_{nt}. The connection strength during instantaneous deformation exceeds the force required to generate disentanglement producing the increase seen in G_{Di}.

Model parameters G_{D1} and G_{D2} both exhibit an initial decrease followed by an increasing trend for $9\ kPa \leq \tau \leq 51\ kPa$. Subsequent load increments produce an increase in G_{D1} and a reduction in G_{D2}. The reduction in G_{D2} for $\tau \geq 51\ kpa$ indicates that the resistance to delayed deformation II (Figure 8) reduces as the resistance to immediate and delayed deformation I (Figure 8) increases.

The magnitude of deformation occurring during each shear deformation state was determined with Equations 16-18. Deformation is accumulated in all three of the previously defined shear deformation states (Figure 8) and contribute to the total deformation for $9\ kPa \leq \tau \leq 42\ kPa$. As the material is loaded past $\tau = 42\ kPa$, the magnitude of immediate and delayed deformation I is reduced whereas the magnitude of delayed deformation II increases. The divergence seen at $\tau = 42\ kPa$ is indicative of mechanistic changes that occur as the resistance to instantaneous and delayed deformation I increases. This is reflected in the increasing trend seen in the immediate shear deformation moduli (G_{Di}) and delayed shear deformation moduli I (G_{D1}) after $\tau = 42\ kPa$.

The optimized retardation times associated with the load increments describe how the time required for delayed deformation to accumulate changes during the duration of an RLS test. The parameter R_1 exhibits a decrease occurring at $\tau = 25\ kPa$, whereas R_2 remained constant. Both parameters R_1 and R_2 follow a linear trend that increased with shear stress from $25\ kPa \leq \tau \leq 68\ kPa$. The reduction in R for $\tau \geq 68\ kPa$ occurs as the specimen transitions into failure.

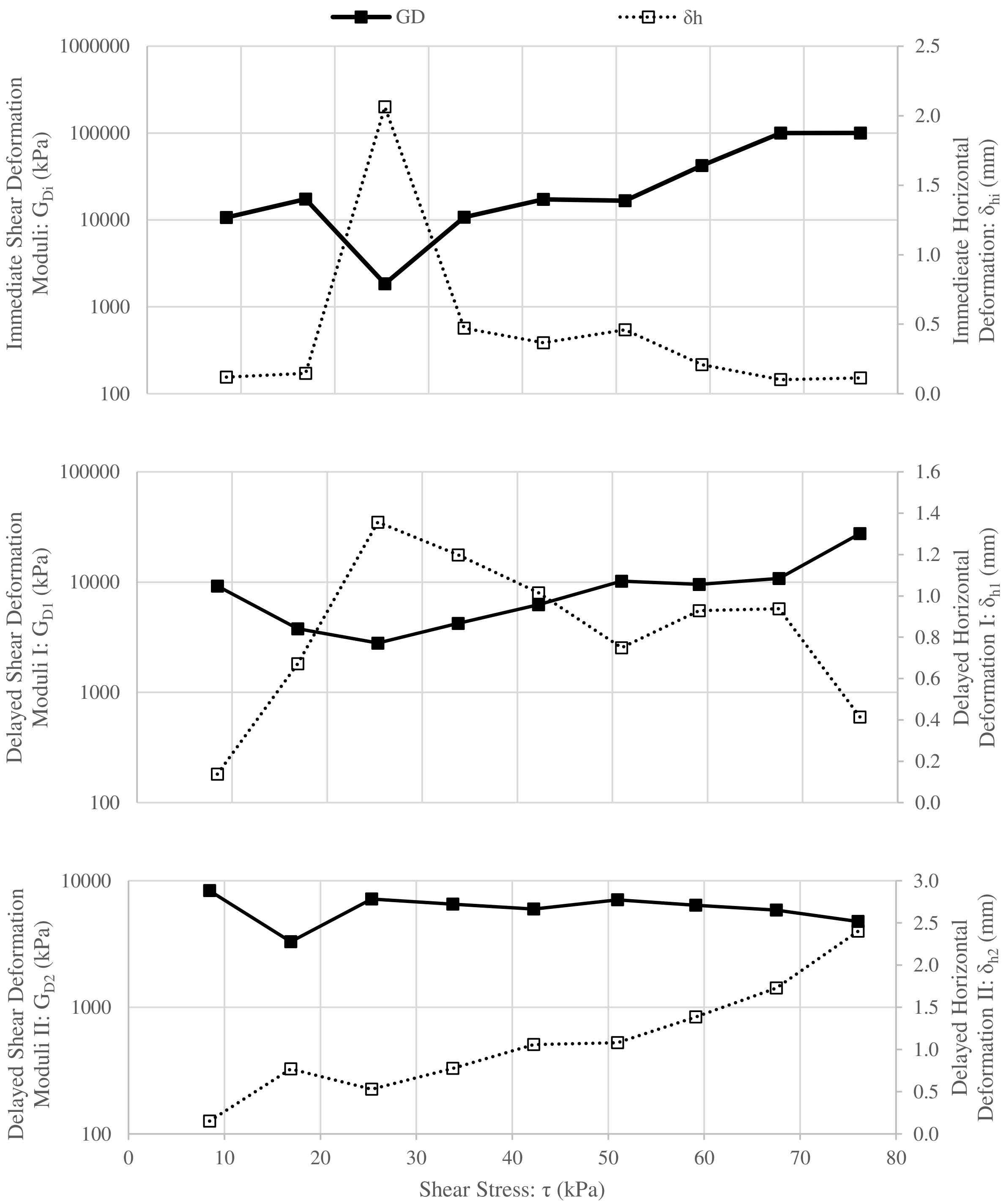

Figure 12: Relationship between optimized shear deformation moduli (G_D), horizontal deformation (δ_h) and shear stress (τ) during a rapid-loading stress test (RLS) for a non-heat-treated needle- punched geosynthetic clay liner (NHT NP GCL) tested with an initial normal stress (σ_{ni}) of 20 kPa and at a temperature (T) of 20^oC.

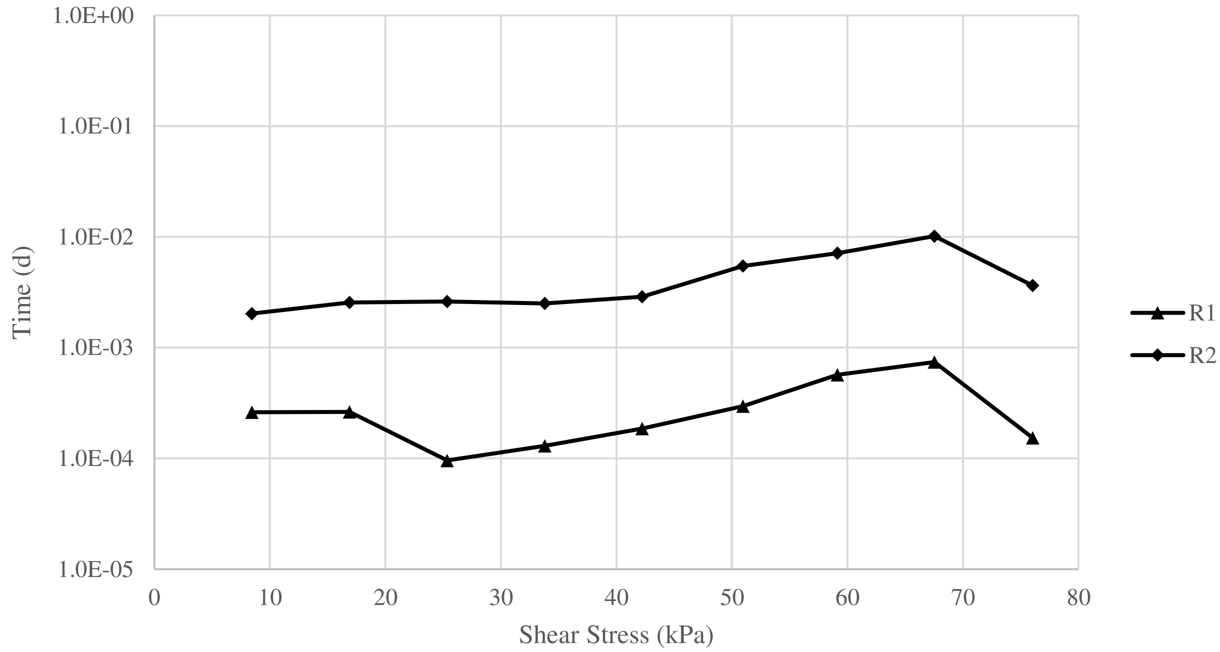

Figure 13: Optimized retardation time (R) associated with delayed response I and II for a non-heat-treated needle punched geosynthetic clay liner (NHT NP GCL) tested with an initial normal stress (σ_{ni}) of 20 kPa and at a temperature (T) of $20^{o}C$.

3.2 Creep Dataset Pre-processing

Test Series 4 was subjected to a pre-processing procedure to ensure compatibility between the dataset and model parameters. The model is designed to predict creep deformation and cannot accommodate large amounts of immediate deformation or failure. The pre-processing procedure applied to Test Series 4 consisted of (1) determining the bounds of creep deformation and (2) transposing the data.

The bounds of creep deformation are defined by the end-of-immediate deformation (δ_{EID}) and tolerable deformation (δ_T). At lower shear stresses, immediate deformation continues after the final stress application before transitioning to creep. To reduce the amount of immediate deformation, δ_{EID} was approximated by extrapolating from the τ-δ_{EOL} relationship and removed from each dataset.

The tolerable deformation was determined by locating the inflection point that occurs as deformation transitions from steady-state creep to failure (Zone II to Zone III in Figure 5). An n^{th}-order polynomial was fit to the deformation data to obtain a smooth function and the second derivative was approximated with Equation (27):

$$f''(x) = \frac{f(x+h) - 2f(x) + f(x-h)}{h^2} \tag{27}$$

where, $f''(x)$ is the second derivative, $f(x)$ is the original function, and h is step size. The point of inflection was identified as the location where the second derivative changed sign from positive to negative. With the bounds of creep deformation established, the data set was isolated, normalized with Equations 21-23, and transposed.

3.2.1 Example Creep Pre-Processing

The τ-δ_{EOL} relationship for the example RLS creep test (Figure 9) is presented in Figure 14. Here, the horizontal deformation is taken as the deformation at the end of each load increment. Extrapolating from the τ-δ_{EOL} relationship gives δ_{EID} = 24 mm.

The isolated creep dataset is presented in Figure 15. Here, the immediate deformation has been removed, and the dataset has been normalized and transposed. A cubic polynomial has been fit to the creep dataset and the point of inflection has been determined.

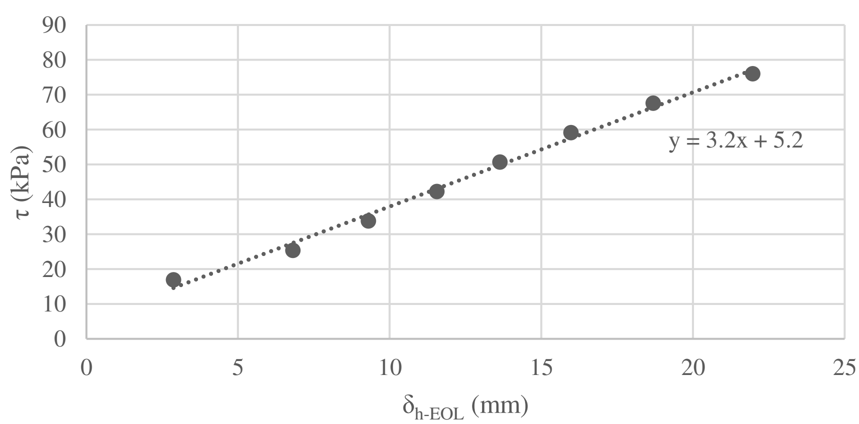

Figure 14: Relationship between shear stress (τ) and horizontal displacement at the end of each loading stage (dh-EOL) for a non-heat-treated needle-punched geosynthetic clay liner (NHT NP GCL) tested with an initial normal stress (σ_{ni}) of 20 kPa at a temperature (T) of $20^{o}C$.

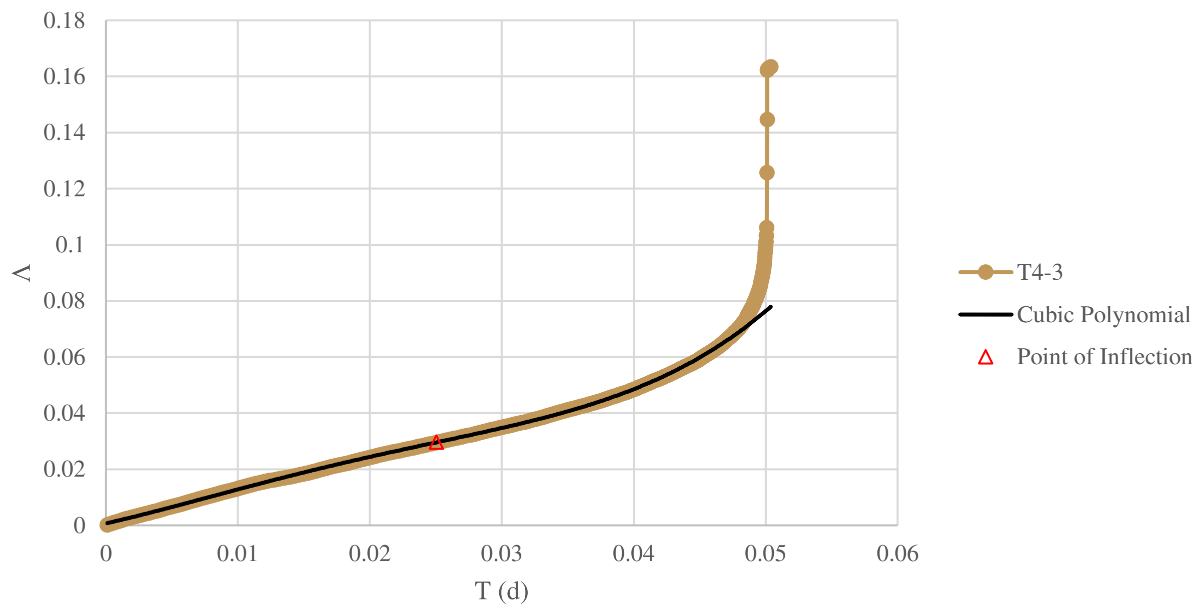

Figure 15: Point of inflection for a non-heat-treated needle-punched geosynthetic clay liner (NHT NP GCL) evaluated in a rapid loading stress (RLS) creep test at a shear stress (τ) of 85 kPa. The Specimen was tested with an initial normal stress (σ_{ni}) of 20 kPa at a temperature (T) of $20^{o}C$.

3.3 Model Calibration

The long-term creep deformation model (Equation 20) is an extension of the three-element model in Equation 15. The first three-elements of the creep deformation model capture the gradual transition from short-term shear behavior to creep and the additional creep-element(s) capture steady-state creep deformation. With these elements, the creep deformation model is used to predict NHT NP GCL creep at a target shear stress. To properly implement the creep deformation model, the shear deformation moduli of the first three model elements are calibrated to a target shear stress. Next, the calibrated shear deformation moduli are used in combination with test data to ascertain the appropriate retardation times. Finally, the calibrated creep moduli and retardation times are used to determine the correct creep modulus.

3.3.1 Shear Deformation Moduli Calibration

The shear deformation moduli obtained from the performance assessment imply that shear resistance will continue to develop along the same trends (Figure 12) as shear stress increases. Predicting creep deformation at a target shear stress with the creep deformation model (Equation 20) requires that the appropriate shear deformation moduli (G_{Di}, G_{D1}, G_{D2}) be selected for that shear stress. An empirical model was developed to aid in estimates of shear deformation moduli at higher shear stresses ($\tau \geq 76\ kPa$). The empirical model consisted of a power-law function fit to the shear deformation moduli trends. To estimate parameters, the power-law function was used to extrapolate forward to a target shear stress.

3.3.2 Retardation Time Calibration

The time required for creep strain to accumulate within a NHT NP GCL is controlled by applied shear stress and shear resistance of the material. Calibrating retardation times involved (1) approximating the first and second retardation times from test data and (2) determining subsequent retardation times. First, the maximum deformation predicted by the immediate response (δ_{hi}) was determined with Equation 16. Next, the maximum deformation predicted by the immediate and delayed response (δ_{hi}, δ_{h1}) was determined by summing the results of Equations 16 and 17. The time required for δ_{hi} and $\delta_{hi} + \delta_{h1}$ to accumulate was determined by matching the predicted deformation with the observed deformation and obtaining their timestamps. These two times were subtracted to obtain R_1.

To determine the second retardation time (R_2): first, the maximum deformation predicted by the delayed II response (δ_{h2}) was determined with Equation 18. Next, the maximum deformation predicted by the immediate, delayed I, and delayed II response was determined by summing the results of Equations 16, 17, and 18. The time required for δ_{h2} and $\delta_{hi} + \delta_{h1} + \delta_{h2}$ was then determined by matching the predicted deformation with the observed deformation and obtaining their timestamps. These two times were subtracted to obtain R_2. The retardation times for the subsequent elements in the model were selected using Equation 11.

3.3.3 Creep Modulus Calibration

The creep modulus calibration is informed by the shear deformation moduli and retardation times of the first two kelvin elements in Equation 20. This is necessary to ensure that the inversely proportional relationship between shear deformation moduli and retardation time established by these elements is maintained in the subsequent creep element. To capture the relationship between the first two elements, the retardation times and shear deformation moduli $((R_1, G_{D1}), (R_2, G_{D2}))$ were plotted, and a power-function was fit to the data trend. The retardation time to be used in the creep element (R_3) was then approximated with Equation 11. The appropriate creep modulus was selected by extrapolating to R_3 from the aforementioned power-function.

4 RESULTS AND DISCUSSION

The performance assessment was applied to Test Series 1 through 3 to evaluate the ability of the model to capture changes in peel strength, normal stress, and temperature. The performance assessment was then applied to Test Series 4 to identify characteristics of shear loading and develop the creep deformation model. All model parameters and model fits are included the Appendix.

4.1 PERFORMANCE ASSESSMENT

4.1.1 Peel Strength

Results of the model optimization procedure applied to evaluate peel strength are summarized in Figure 16. An increase in peel strength corresponded with an increase in the immediate shear deformation modulus (G_{Di}) and a reduction in the magnitude of immediate deformation (δ_{hi}). During the first three load increments (τ ≤ 25 kPa), G_{Di} was consistent for T1-1, T1-2, and T1-3. The consistency in G_{Di} for all specimens is reflected in the near identical magnitude of immediate deformation (δ_{hi}). The magnitude of immediate deformation during these load increments peaked, reaching values ranging from 0.5-0.6 mm. This peak in deformation occurs as the deformation mechanism shifts from tensile elongation to fiber-bundle disentanglement (stage I to stage II in Figure 3). As the applied shear stress increased above 25 kPa, values of G_{Di} diverge and there was a greater increase in G_{Di} (and decrease in δ_{hi}) for NHT NP GCLs with higher peel strength. As observed by Ghazizadeh and Bareither (2021), specimens with higher peel strengths demonstrate a greater resistance to shear deformation owing to the larger number of reinforcing fiber bundles present in their internal structure. The greater number of reinforcing fiber bundles reduces the tensile force per fiber bundle. This reduces the reaction forces at the fiber bundle geotextile interface (R_x and R_y in Figure 2a) and yields less tensile elongation and disentanglement.

An increase in peel strength corresponded with an increase in the delayed shear deformation moduli I (G_{D1}). A dip occurs in G_{D1} that is more pronounced for specimens with lower peel strengths. This decrease in shear resistance implies that specimens with greater peel strength undergo less tensile elongation and disentanglement during delayed deformation I (δ_{h1}). The greater tensile force per fiber bundle present in specimen with lower peel strength induces more tensile elongation during stage I (Figure 3). As loading continues and the deformation mechanism fully shifts from tensile elongation to disentanglement, the magnitude of δ_{h1} converges on a value 0.5 mm.

The shear deformation moduli defined for the delayed response II (G_{D2}) exhibited increasing trends with increasing applied shear stress to approximately 60 to 70 kPa. The trend in G_{D2} was similar for all three NHT NP GCLS with varying peel strength. However, values of the shear deformation moduli determined for T1-3, which was the GCL with the highest peel strength, increased for shear stress > 70 kPa, whereas the other two GCLs did not exhibit consistently increasing trends. The magnitude of G_{D2} for T1-3 peaked at the highest applied shear stress, which implies that there was less accumulation of shear deformation at higher shear stresses. In contrast, the reduction observed in G_{D2} for T1-1 and T1-2 as shear stress reached a maximum are representative of the GCL approaching failure. As observed by Ghazizadeh and Bareither (2018b), specimens with higher peel strengths have a greater ability to transfer shear stress through their internal reinforcement owing to the larger number of fiber-bundles present. This produced a larger internal moment and increased the total normal stress (σ_{nt}). The greater σ_{nt} present in T1-3 increased the internal shear resistance, producing the increase observed in G_{D2}.

The resistance to disentanglement (RD) associated with the immediate shear deformation moduli (G_{Di}) was calculated with Equation 14. The immediate resistance to disentanglement (RD_i) was found to exceed the entanglement strength (ES) of the material at the load increment corresponding to $\tau = 50\ kPa$ for T1-1. Subsequent load increments produced consistent amounts of immediate deformation as the internal resistance of the material is enhanced by the higher σ_{nt} caused by the internal moment present at higher shear stresses. The entanglement strength could not be determined for T1-2 and T1-3 as the average number of fiber bundles within these specimens was unknown. However, the immediate resistance to disentanglement (RD_i) for T1-2 and T1-3 was hypothesized to exceed the entanglement strength within a shear stress range of $34\ kPa \leq \tau \leq 52\ kPa$. This is supported by the reduction in δ_{hi}

in T1-2 and T1-3 that occurs in this range. The NHT NP GCLs evaluated in Test Series 1 have a higher entanglement strength owing to their greater number of reinforcing fiber bundles. Additionally, the internal resistance of the NHT NP GCLs evaluated in T1-2 and T1-3 were enhanced by the larger internal moment in these specimens, which increased the resistance to fiber bundle disentanglement.

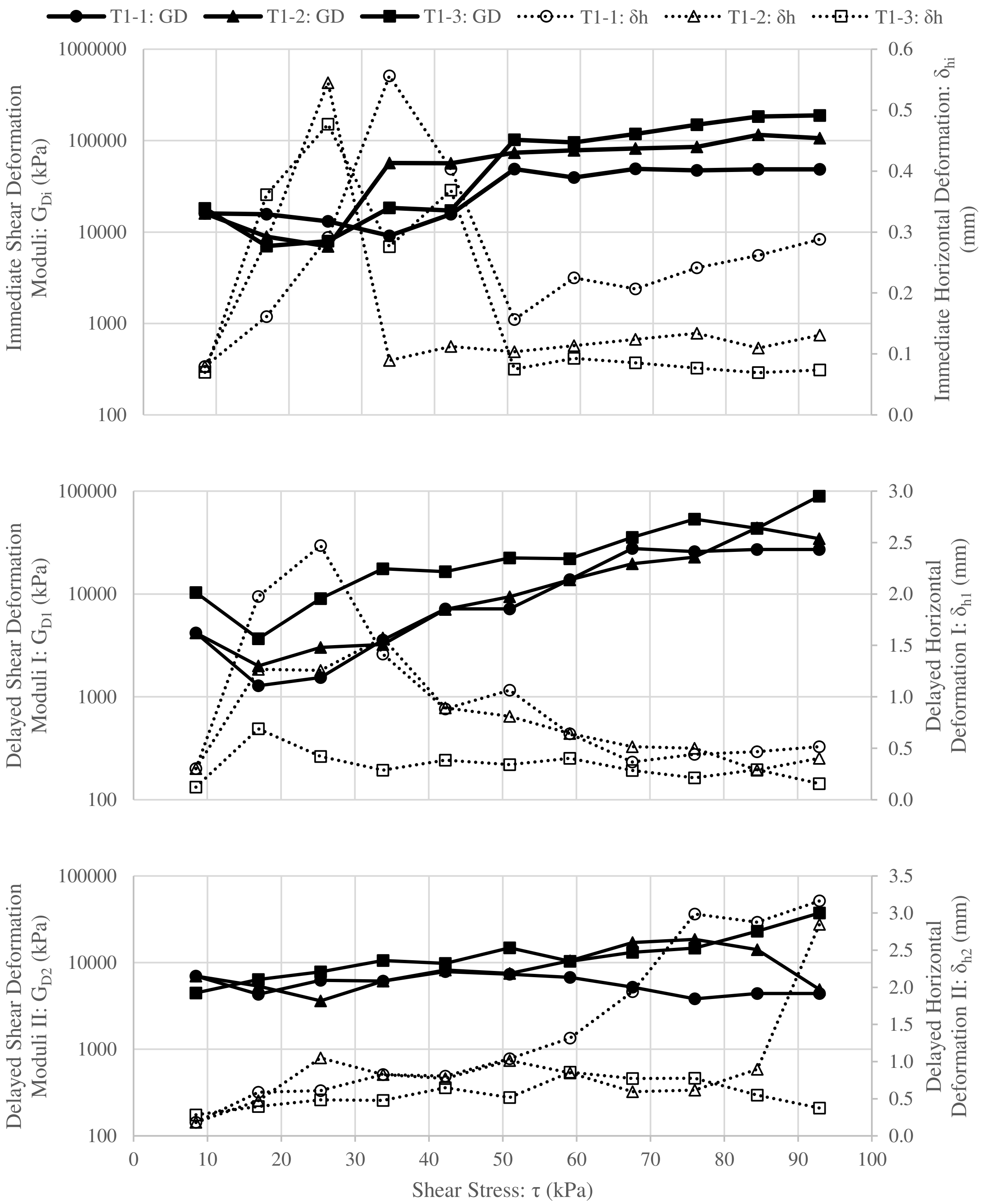

Figure 16: Relationship between shear deformation moduli (G_D), horizontal deformation (δ_h) and shear stress (τ) for non-heat-treated needle punched geosynthetic clay liners (NHT NP GCLs) of different peel strengths. T1-1: 720 N/m, T1-2: 1490 N/m, T1-3: 2170 N/m. Specimen was tested with an initial normal stress (σ_{ni}) of 20 kPa at a temperature (T) of $20^{o}C$.

4.1.2 Normal Stress

The results of the model optimization procedure applied to evaluate the effects of normal stress is summarized in Figure 17. Increasing normal stress resulted in an increase in the immediate shear deformation moduli (G_{Di}) and a reduction in the magnitude of immediate horizontal deformation (δ_{hi}). The specimen evaluated at an initial normal stress (σ_{ni}) of 40 kPa (T3-1) exhibits a drop in G_{Di} at a shear stress of 17 kPa. The reduction in shear resistance is likely due to the effects of specimen variability observed by Ghazizadeh & Bareither (2021). As shear stress increased, specimens subjected to higher normal stresses exhibit greater resistance to immediate deformation. The higher normal stress enhances the strength of the fiber bundle geotextile connection and provides greater confinement pressure on the individual fiber bundles. These forces act to hold the fiber bundles in place longer, which reduces immediate deformation.

The delayed shear deformation modulus I (G_{D1}) drops in value for shear stresses ranging from 17 kPa to 32 kPa. In this range, the drop is more pronounced for tests conducted at higher initial normal stress (T2-2 and T2-3). There is a spike in delayed deformation I (δ_{h1}) corresponding to the observed reduction in shear resistance. The increased normal stress was hypothesized to cause the shift from tensile elongation to disentanglement in these specimens to occur during delayed deformation I rather than during immediate deformation. The stronger fiber-bundle connections present at higher normal stresses that held the fiber-bundles in place during immediate deformation begin to slip during delayed deformation I, thus producing the spike observed in shear deformation. The shift in observed behavior exemplifies the time-dependent nature of geotextile-fiber bundle connections. Interestingly, increasing the normal stress appears to result in a more abrupt spike in deformation in this stress range. This is likely due to the greater shear stress required to produce disentanglement at higher normal stresses.

There is little variation seen in the delayed shear deformation modulus II (G_{D2}) for shear stresses raining from 25 kPa to 42 kPa. As shear stress increased above 42 kPa, the specimen evaluated at an initial normal stress of 60 kPa (T2-3) demonstrated greater shear resistance that was reflected in the reduced magnitude of delayed deformation II (δ_{h2}). The magnitude of δ_{h2} for the specimen tested at lower normal stress showed greater increase as these specimens tended toward failure.

The resistance to disentanglement (RD) associated with the immediate and delayed shear deformation moduli (G_{Di}, G_{D1}) were calculated with Equation 14 and are summarized in Table 3. The summary includes test number, initial normal stress, shear stress at which the resistance to disentanglement exceeds the entanglement strength, and that stress application associated with CSR_N. Increasing the initial normal stress resulted in both the immediate and delayed resistance to disentanglement (RD_i, RD_1) exceeding the entanglement strength at lower values of CSR_N. This is indicative of the higher confinement pressure present at higher σ_{ni}. This acts to stiffen the material, producing larger values of resistance to disentanglement. Additionally, Ghazizadeh & Bareither (2018b) observed a decrease in τ/σ_{nt} with increasing σ_{nt}, which could contribute to lower CSR_N values at comparable shear stresses.

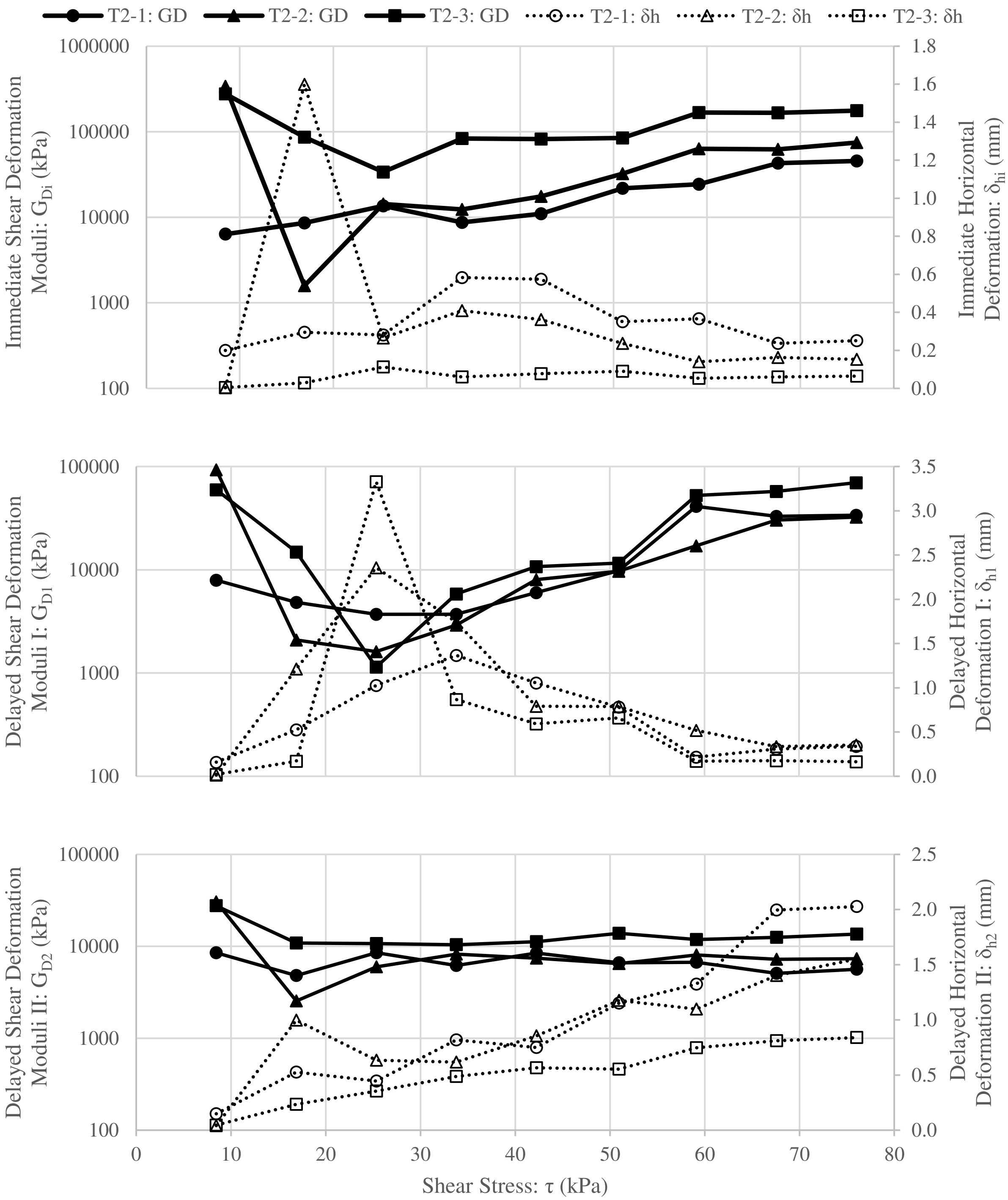

Figure 17: Relationship between shear deformation moduli (G_D), horizontal deformation (δ_h) and shear stress (τ) for non-heat-treated needle punched geosynthetic clay liners (NHT NP GCLs) evaluated at different initial normal stresses (σ_{ni}). T2-1: 20 kPa, T2-2: 40 kPa, T2-3: 60 kPa. Specimen was tested at a temperature (T) of 20^oC.

Table 3: Resistance to deformation for the immediate and delayed response I (R_{Di}, R_{D1}) for T2: evaluation of normal stress.

Test	σ_{ni} (kPa)	τ: RD_i>ES (kPa)	CSR_N	τ: RD_1>ES (kPa)	CSR_N
T2-1	20	59	0.89	67	0.94
T2-2	40	51	0.74	67	0.80
T2-3	60	59	0.72	59	0.72

* σ_{ni}: Initial Normal Stress
* τ: Shear Stress
* CSR_N: Normalized creep stress ratio
* RD: Resistance to disentanglement
* ES: Entanglement Strength

4.1.3 Temperature

The results of the model optimization procedure applied to evaluate the effects of temperature are summarized in Figure 18. An increase in temperature produced a reduction in the immediate shear deformation moduli (G_{Di}) that corresponded with an increase in the magnitude of immediate deformation (δ_{hi}). All three specimens experienced a dip in G_{Di} as disentanglement began. Subsequent loading produces less immediate deformation in specimens evaluated at 40^oC and 60^oC. The immediate deformation for the specimen evaluated at 80^oC (T3-3) continues to increase with stress as the GCL approached failure. As observed by Ghazizadeh & Bareither (2020), increased temperatures act to reduce the tensile modulus and entanglement strength of NHT NP GCLs, which reduced internal shear resistance and resulted in increased deformation.

Increased temperatures produced limited variation in the delayed shear deformation moduli I and II. Interestingly, the greatest magnitude of delayed deformation I was observed in the specimen evaluated at 40^oC (T3-1). This indicates that increased temperatures reduced the amount of time-dependent deformation that occurred at a given shear stress. The specimens tested at 60^oC an 80^oC have lower internal shear resistance, limiting their ability to resist the initial stress application occurring during the immediate deformation state. Thus, the majority of deformation for these specimens occurred during the immediate deformation stage. The delayed shear deformation modulus II followed a linear trend that decreased with shear stress, which was observed in all specimens as they approached failure.

The resistance to disentanglement (RD) associated with the immediate and delayed shear deformation moduli (G_{Di}, G_{D1}) were calculated with Equation 14. The immediate resistance to disentanglement (RD_i) exceeded the entanglement strength for T3-1 at a shear stress of 33 kPa. The higher temperatures present in T3-2 and T3-3 reduced the internal shear resistance such that the resistance to disentanglement never exceeded the entanglement strength.

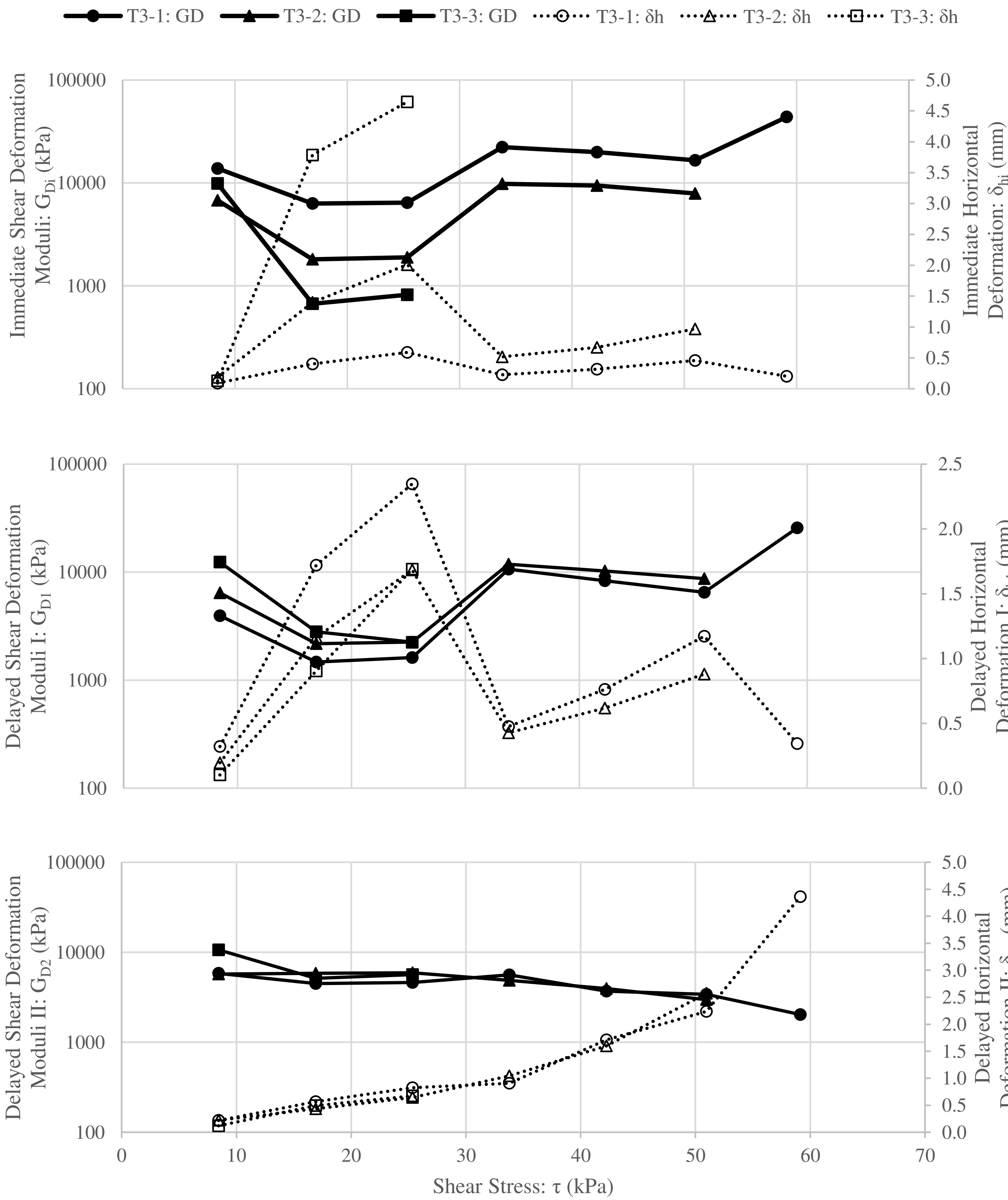

Figure 18: Relationship between shear deformation moduli (G_D), horizontal deformation (δ_h) and shear stress (τ) for non-heat-treated needle punched geosynthetic clay liners (NHT NP GCLs) evaluated at different temperatures (T). T3-1: 40^oC, T3-2: 60^oC, T3-3: 80^oC. Specimen was tested at an initial normal stress (σ_{ni}) of 20 kPa.

4.2 PREDICTIONS OF CREEP DEFORMATION AND TIME-TO-FAILURE

4.2.1 Performance Assessment

Results of the short-term model performance assessment applied to Test Series 4 are shown in Figure 19. Model parameters determined for shear stresses less than 76 kPa were similar for all tests with values of shear deformation moduli (G_{Di}, G_{D1}, G_{D2}) following a linear trend that increases with shear stress. Outliers occur in G_{D2} for T4-1 and T4-2 as those specimens approached failure.

The retardation times (R_1 and R_2) demonstrate a linear trend with no notable stress sensitivity for $\tau \leq 76$ kPa. During RLS loading (Zone I, figure 5), the incremental application of shear stress constrains the time allowed for strain accumulation to 15 min. This produces the consistency seen in the retardation times. Generalized retardation times, RG_1 and RG_2, were computed by averaging values of R_1 and R_2 for $\tau \leq 76\ kPa$. The values for RG_1 and RG_2 were determined to be 2.63×10^{-4} and 5.96×10^{-3}, respectively.

The model optimization step of the performance assessment was repeated with the generalized retardation times. During this re-computation, R_1 and R_2 in Equation 15 were substituted with the generalized retardation times, and the regression analysis was repeated to determine the shear deformation moduli. The generalized retardation times were held constant during the regression analysis.

The results of the second iteration of the model optimization are shown in Figure 20. This iteration of model optimization resulted in the values being more tightly grouped. The immediate and delayed I shear deformation moduli (G_{Di}, G_{D1}) displayed a trend that increased with applied shear stress. The drop occurring in the immediate shear deformation modulus for shear stresses ranging from 17 kPa to 25 kPa was hypothesized to result from shear deformation shifting from Stage I to Stage II (Figure 3). The immediate shear deformation moduli converge at $\tau = 25$ kPa, which marked the beginning of Stage II. The application of $\tau = 25$ kPa was the first load increment that produced fiber-bundle disentanglement in all five tests. It is assumed that tensile elongation is negligible in the $\tau = 25\ kPa$ load increment and all subsequent load increments. All deformation is attributed to fiber-bundle disentanglement for load increments $\tau > 25$ kPa. The amount of deformation ensuing $\tau = 25\ kPa$ decreased as shear stress increased. This was attributed to the increased total normal stress that increased concurrently with increasing shear stress. The spike in delayed deformation I (δ_{h1}) seen in T4-1 and T4-3 was attributed to specimen variability. The delayed shear deformation modulus II (G_{D2}) exhibits a linear trend with minimal reduction as shear stress is increased. The magnitude of delayed deformation II (δ_{h2}) increased as the specimens trend toward failure.

An analysis of the deformation behavior was conducted by comparing the resistance to disentanglement (RD) to the entanglement strength (ES). Values of RD were determined for $\tau < 76$ kPa for T4-1 through T4-4. The creep test evaluated at $\tau = 67$ kPa (T4-5) was excluded because the test was terminated prior to failure, which resulted in an undefined CSR_N. For shear stresses ranging from 8 kPa to 42 kPa, RD for all load-increment deformation states remained beneath the entanglement strength, indicating that all deformation states were active during these load increments. As shear stress increased beyond this stress range ($\tau \geq 51\ kPa$), the total normal stress increased due to the presence of the internal moment within the NP GCL. The increased normal stress increased shear resistance of a given NP GCL, which caused the immediate resistance to disentanglement (RD_i) to exceed the entanglement strength. As can be seen in Figure 20, the magnitude of immediate deformation beyond this point reduced to less than 0.5 mm. The delayed resistance to disentanglement I (RD_1) exceeded the entanglement strength at a shear stress of 68 kPa. Subsequent increments in shear stress reduced the magnitude of delayed deformation I to less than 0.5 mm.

Four deformation phases can be identified for a non-heat-treated NP GCL subjected to incremental shear loading and are summarized in Table 4. Included in Table 4 are descriptions of the deformation phase, the associated CSR_N, deformation type, model behavior, mechanistic behavior, and hypothesized shear deformation mechanisms. The CSR_N listed in Table 4 were taken as the average CSR_N per load increment for T4-1 through T4-4. The shift from elastic to viscoelastic behavior began $CSR_N \approx$ 0.41, which aligns with observations from Koerner (2001).

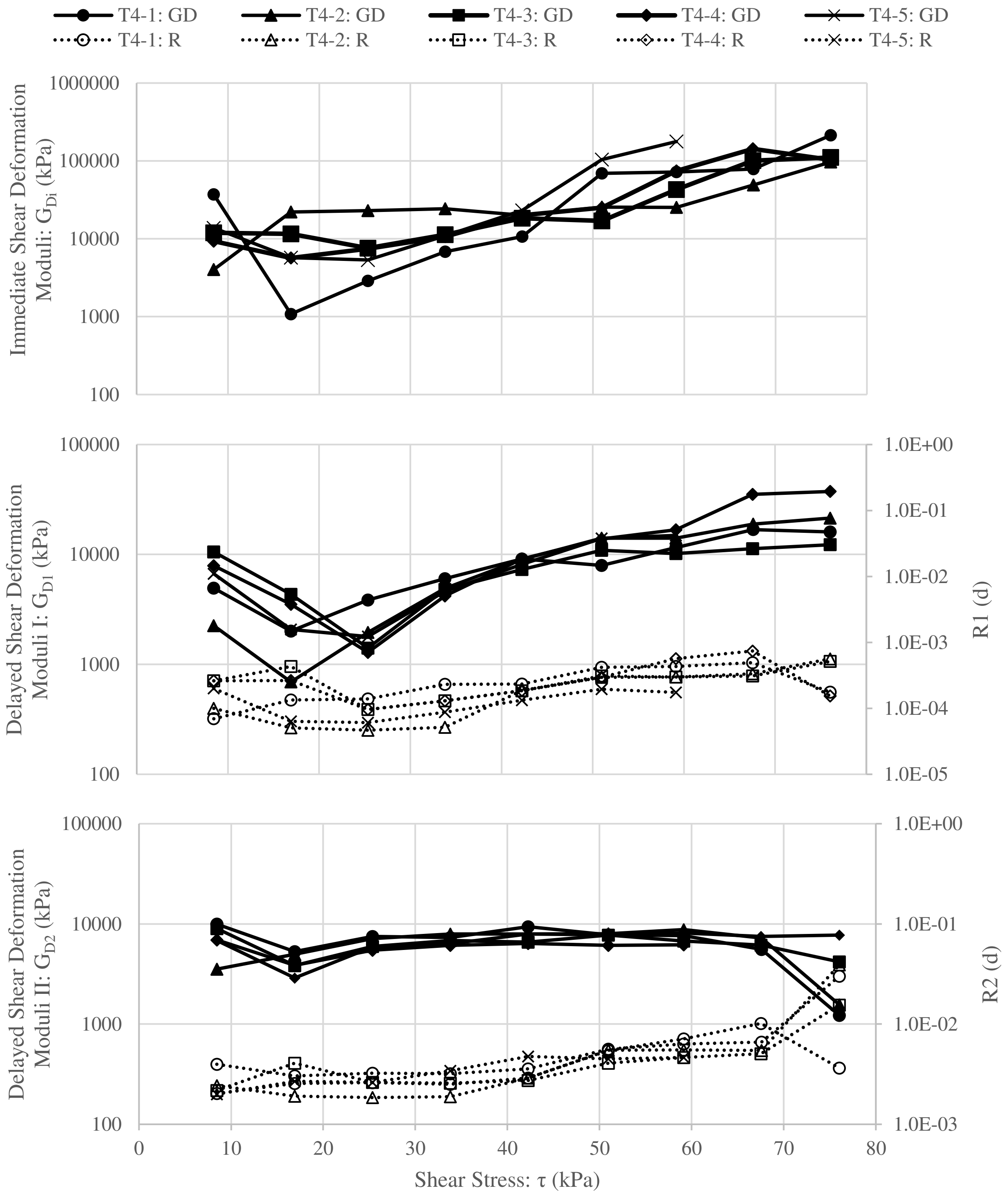

Figure 19: Relationship between optimized shear deformation moduli (G_D) and retardation time (R_1, R_2) with shear stress (τ) for a non-heat-treated needle punched geosynthetic clay liner (NHT NP GCL) during shear loading. The specimen was evaluated with an initial normal stress (σ_{ni}) of 20 kPa at a temperature of 20^oC.

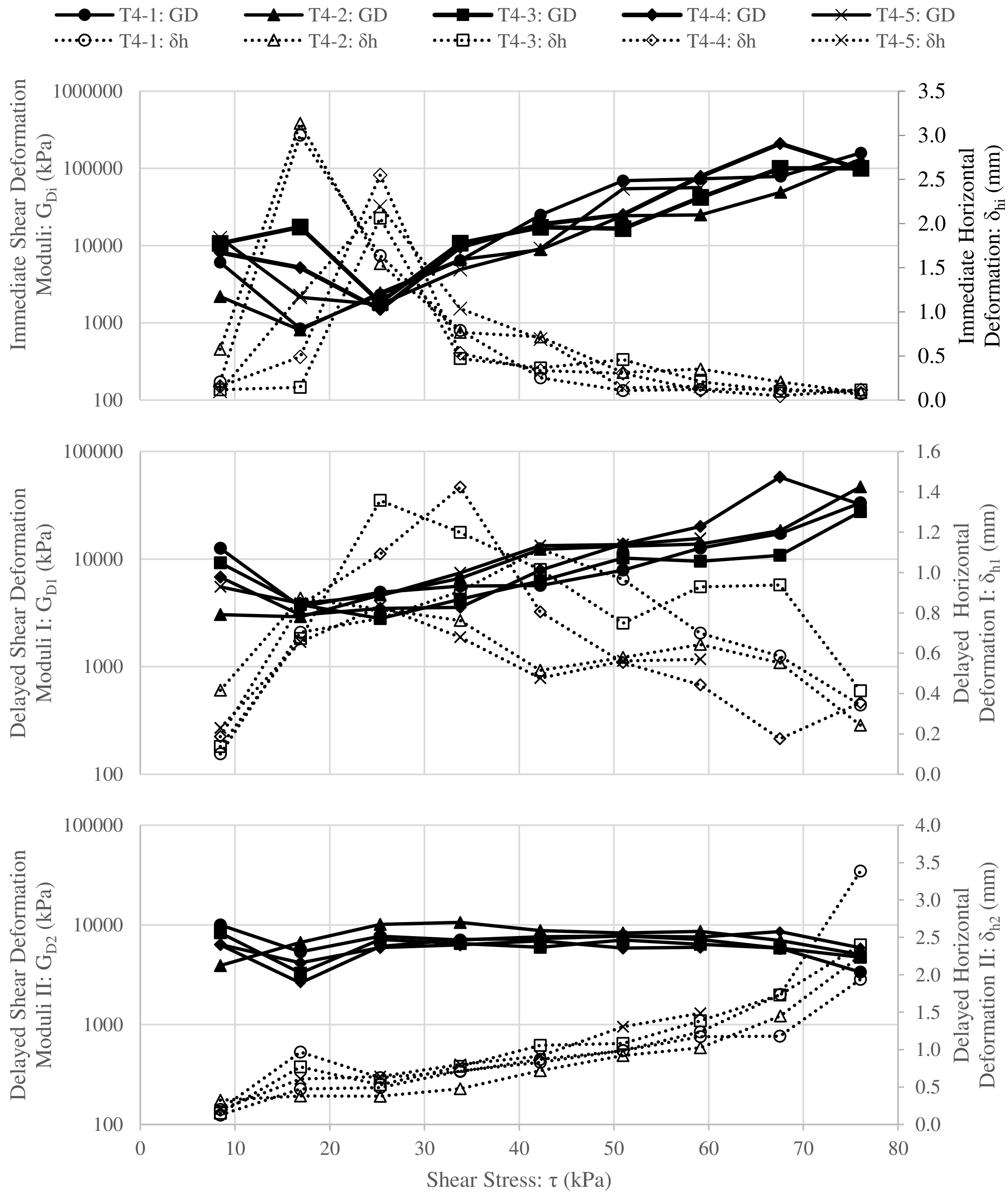

Figure 20: Relationship between immediate and delayed shear deformation moduli (G_D) and deformation (δ_h) with shear stress (τ) for a for a non-heat-treated needle punched geosynthetic clay liner (NHT NP GCL) during shear loading. The specimen was evaluated with an initial normal stress (σ_{ni}) of 20 kPa at a temperature of 20^oC.

Table 4*:* Hypothesized phases of deformation for a non-heat-treated needle punched geosynthetic clay liner (NHT NP GCL) during a rapid loading stress test.

Deformation Phase	CSR_N	Deformation Type	Model Behavior	Mechanistic Behavior	Hypothesized Mechanisms
I	0.21	Elastic	Spring, K1, and K2 Contribute to Deformation	T<ES	Applied shear stress produces tensile elongation of fiber bundles
II	0.41-0.86	Elastic → Viscoelastic	Spring, K1, and K2 Contribute to Deformation	RD < ES	The immediate response begins to reduce as the frictional connections are strengthened by increasing normal stress. Tensile elongation of fiber-bundles is considered negligible past this point.
III	0.86-0.98	Viscoelastic	K1 and K2 Contribute to Deformation	RD_i > ES	Deformation is attributed to time-dependent delayed response; immediate deformation is insignificant.
IV	0.98-End	Viscoelastic → Failure	K2 contributes to Deformation	RD_i, RD_1 > ES	Frictional connections are strengthened by increasing normal stress. The delayed response II is the primary deformation mechanism.

* K1 and K2 refer to the first and second kelvin elements of the three-element model.
* T: Tensile force acting on fiber bundles
* ES: Entanglement Strength
* RD: Resistance to disentanglement

4.2.2 Model Calibration: Proof of Concept

The long-term creep model calibration process was based on the hypothesis that internal shear resistance of a NP GCL continues to develop along the observed trends (Figure 20) as deformation progresses from Phase II to Phase IV (Table 4). To validate this hypothesis, the model calibration process was used to predict the strain of an 85 kPa load increment from T4-1. The load increment has a $CSR_N = 1.0$, indicating curvature in the failure envelope and deformation aligned with Phase IV.

The shear deformation moduli (G_D) for T4-1 through T4-4 are shown as a function of applied shear stress in Figure 21. These shear deformation moduli were used in the model calibration process and a power function was fit to each data set to aid initial estimates of model parameters. Performing a log-log transformation of the data-trends reveals a linear relationship between shear deformation moduli and shear stress – which is typically indicative of a power function relationship. Therefore, a power function was selected for the empirical model. All four tests were included in the trend to account for the effects of specimen variability. The power functions were used to extrapolate the immediate, delayed I, and delayed II shear deformation moduli to the target shear stress of 85 kPa.

Results of the model calibration process are shown in Figure 22. A description of each plot in Figure 22 is included in Table 5. In Figure 22(A), the three-element model (Equation 15) was used to produce the predicted deformation curve along with the extrapolated moduli and generalized retardation times (RG_1, RG_2) as model parameters. The discrepancy between observed and predicted data arises from the use of the generalized retardation times. As deformation transitions from Phase III to IV, the delayed response II becomes the primary mode of deformation. This shift in behavior correlates to a reduction in R_1 and an increase in R_2. As a result, using the average retardation time from Phase II and III to predict deformation in Phase IV will give inaccurate results. To remedy this issue, the retardation times must be calibrated to the test data.

The initial retardation time calibration is presented in Figure 22 (B). Here, R_1 was calibrated to the test data and R_2 was determined with Equation 11. The resulting deformation curve overpredicts the deformation rate and reaches the upper strain-boundary too rapidly. This is due to the large magnitude of immediate and delayed deformation I present in the load increment. Calibrating R_1 involves determining the time required for δ_{h1} (Equation 17) to accumulate from test data. When excessive amounts of immediate deformation are present, δ_{h1} is reached very rapidly and therefore, the retardation time calibration returns a small R_1. When R_2 is determined based off R_1, the rapid deformation rate is carried over to the second kelvin-element. This culminates in a model that accumulates deformation more rapidly than the observed data. To obtain more accurate predictions, either (1) the amount of immediate deformation can be incrementally reduced until a good alignment between observed and predicted deformation is reached or (2) R_2 can be calibrated to test data. Here, the second option was chosen as the underlying methodology is less ambiguous.

The results of the retardation time calibration are presented in Figure 22 (C). Here, R_1 and R_2 are calibrated to test data. The resulting deformation predictions align much closer with the observed data; however, the predicted deformation begins to diverge nearing the end of the load increment. This divergence is due to the three-element model approaching the upper strain-boundary and can be resolved with the addition of creep elements.

The relationship between retardation time and shear deformation moduli used to for the creep modulus calibration is presented in Figure 23. Plotting the shear deformation moduli and retardation times of the two kelvin elements in Equation 16 on log axis reveals a linear relationship between the data points. Therefore, a power law relationship was selected for the creep modulus extrapolation. The third retardation time (R_3) was estimated by increasing R_2 by an order of magnitude (e.g., see Equation 11). The creep modulus was determined by extrapolating to R_3 from the power-function. The arrow in Figure 23 indicates the direction of extrapolation.

The creep deformation model calibrated to the 85 kPa load increment is presented in Figure 22 (D). The model parameters for the model are summarized in Table 6. The summary includes shear deformation moduli (G_{Di}, G_{D1}, G_{D2}), the creep modulus (G_C) and the retardation factors (R_1, R_2, R_3).

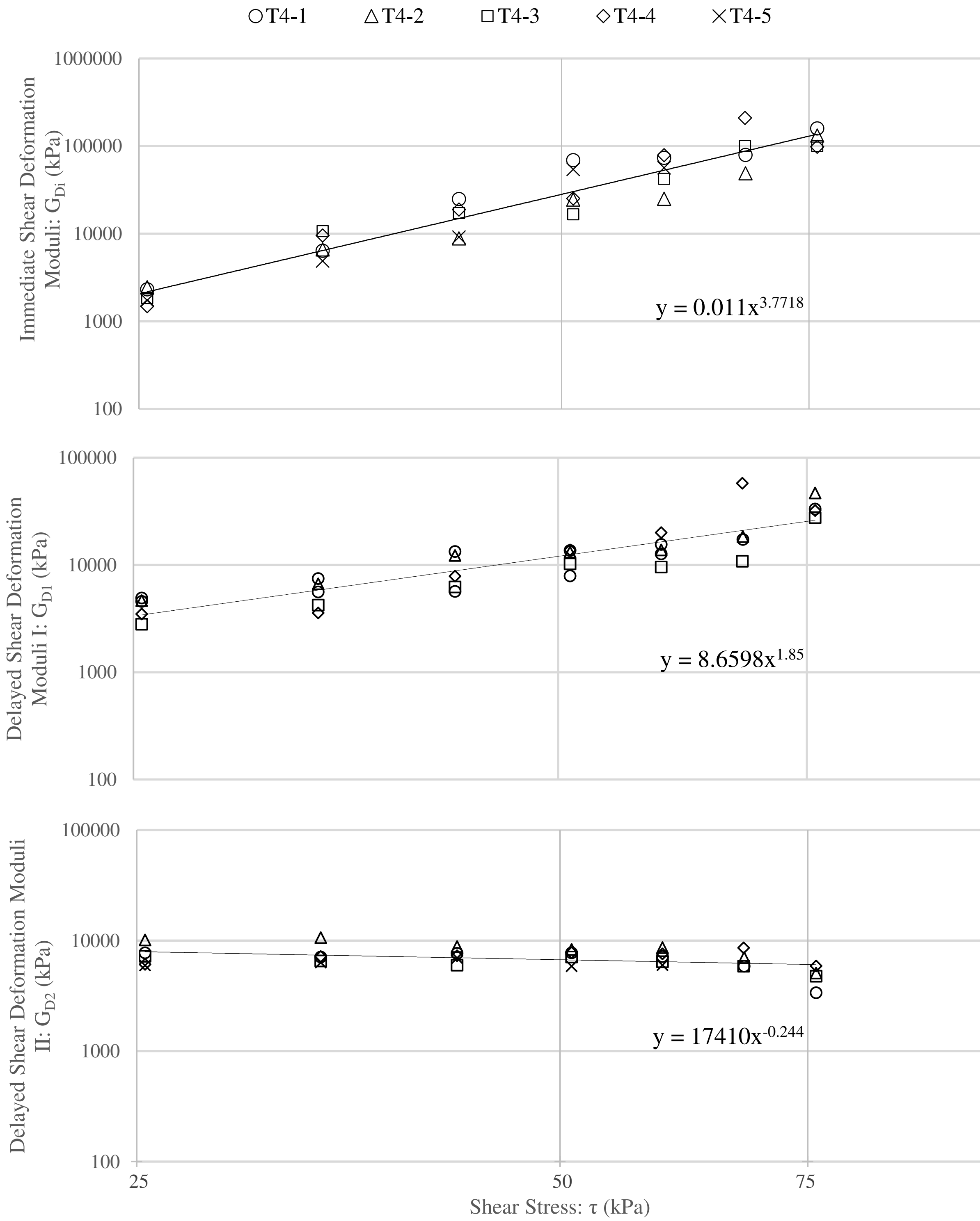

Figure 21: Shear deformation moduli trends for T4-1 – T4-4. Specimen was a non-heat-treated needle-punched geosynthetic clay liner (NHT NP GCL) tested with an initial normal stress (σ_{ni}) of 20 kPa at a temperature (T) of $20^{o}C$. The specimens were allowed to creep at shear stresses (τ_c) of: T4-2: 89 kPa, T4-3: 85 kPa, T4-4: 80 kPa.

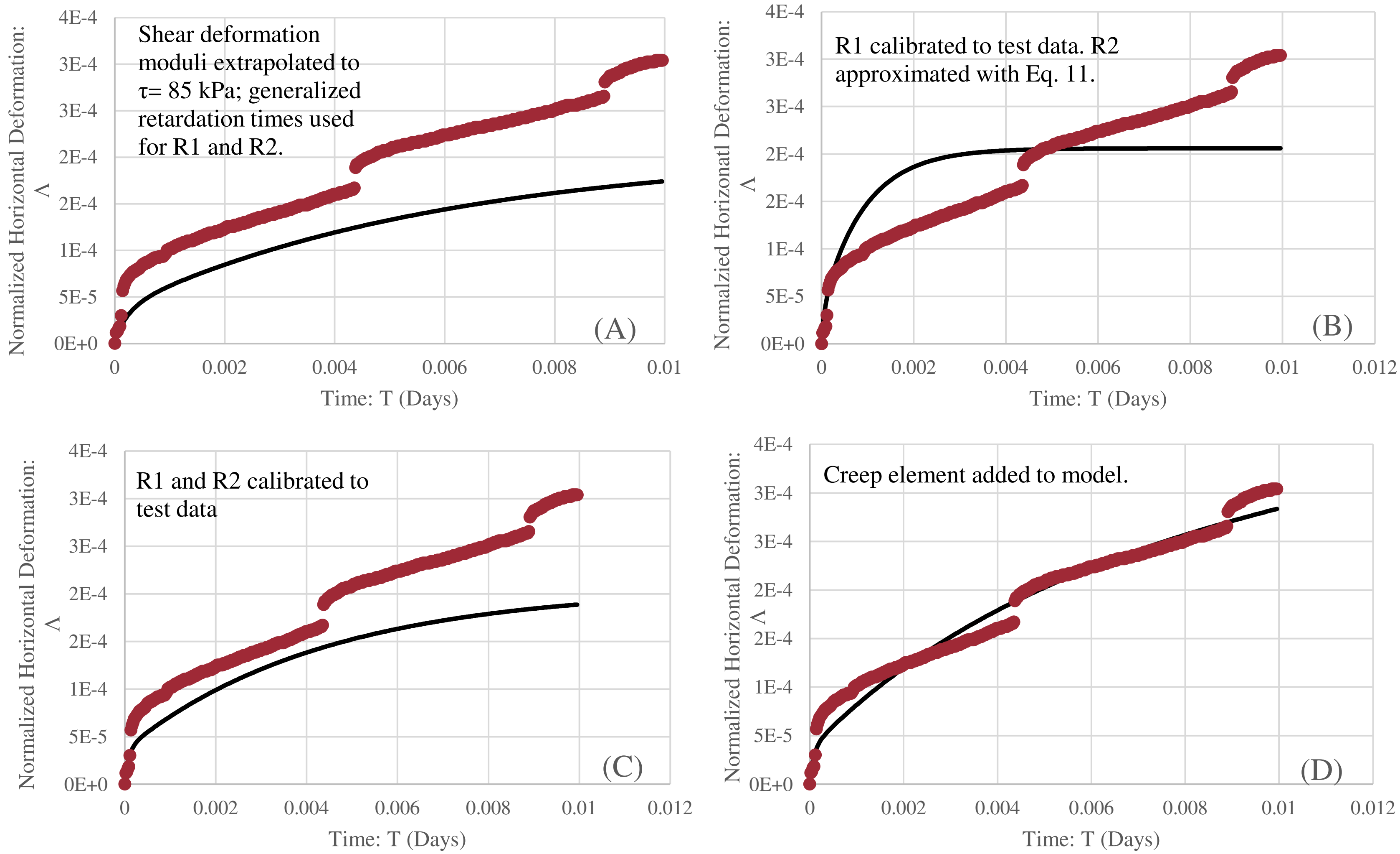

Figure 22: Predicted shear deformation curves generated with shear deformation moduli calibrated to a shear stress (τ) of 85 kPa. Observed data was taken from non-heat-treated needle punched geosynthetic clay liner (NHT NP GCL) tested with an initial normal stress (σ_{ni}) of 20 kPa and at a temperature (T) of $20^{o}C$.

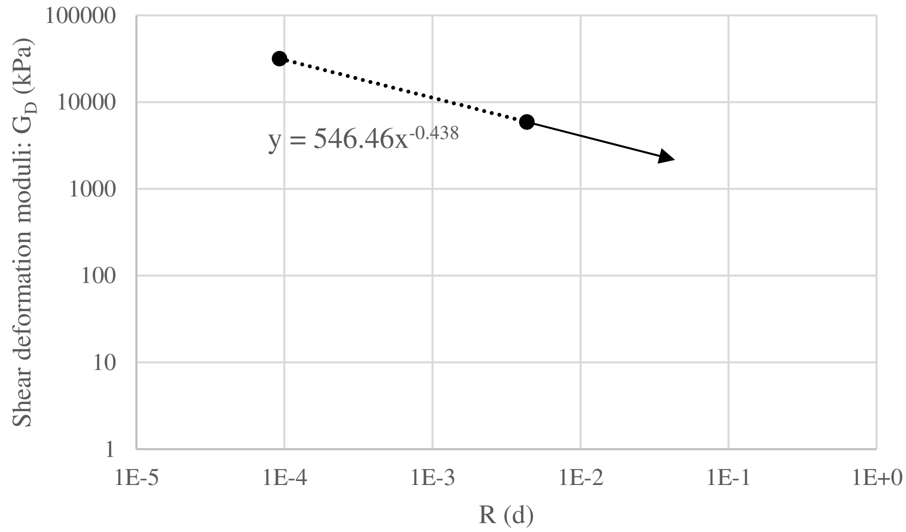

Figure 23: Creep modulus approximated at a shear stress of 85 kPa for a non-heat-treated needle punched geosynthetic clay liner (NHT NP GCL) tested with an initial normal stress (σ_{ni}) of 20 kPa and at a temperature (T) of $20^{o}C$. The 85 kPa load increment was taken from T4-1. The arrow indicates the direction of the approximation.

Table 5: Summary of model calibration steps detailed in Figure 22.

Figure 22 Subplot	Number of Model Elements	Shear Deformation Moduli (Gdi, GD1, GD2)	First Retardation Factor (R1)	Second Retardation Factor (R2)	Third Retardation Factor (R3)	Creep Moduli (GC)
A	3 elements (Equation 15)	Extrapolated to τ=85 kPa with empirical models in Figure 21.	Generalized retardation factor (RG1): the average R1 per load increment in deformation zones I-III.	Generalized retardation factor (RG2): the average R2 per load increment in deformation zones I-III.	N/A	N/A
B	3 elements (Equation 15)	Extrapolated to τ=85 kPa with empirical models in Figure 21.	R1 calibrated to test data.	R2 approximated with Equation 11.	N/A	N/A
C	3 elements (Equation 15)	Extrapolated to τ=85 kPa with empirical models in Figure 21.	R1 calibrated to test data.	R2 calibrated to test data.	N/A	N/A
D	4 elements (Equation 20)	Extrapolated to τ=85 kPa with empirical models in Figure 21.	R1 calibrated to test data.	R2 calibrated to test data.	R3 approximated with Equation 11.	Creep modulus extrapolated with empirical model in Figure 23.

Table 6*:* Creep deformation model parameters calibrated to a 85 kPa load increment for a non-heat -treated needle punched geosynthetic clay liner (NHT NP GCL) tested with an initial normal stress (σ_{ni}) of 20 kPa and at a temperature (T) of $20^{o}C$. The 85 kPa load increment was taken from T4-1.

G_{Di} (kPa)	G_{D1} (kPa)	R_1 (d)	G_{D2} (kPa)	R_2 (d)	G_C (kPa)	R_3 (d)
203756	31783	9.26E-05	5897	4.35E-03	2157	0.04

4.2.3 *Model Calibration: Summary*

The steps required to calibrate the creep deformation model in Equation 20 to a target shear stress are as follows:

1. Obtain shear deformation moduli trends for the immediate, delayed I, and delayed II response (G_{Di}, G_{D1}, G_{D2}) and fit a power-function to each data set (Figure 21).
2. Calibrate the shear deformation moduli (G_{Di}, G_{D1}, G_{D2}) to the target shear stress by extrapolating the power-function relationships. For example, if time-to-failure predictions are desired at a shear stress of 85 kPa, then the power-functions are used to extrapolate $G_{Di}, G_{D1}, and\ G_{D2}$ to that shear stress.
3. Calibrate the retardation times to the test data:
    a. The initial retardation time (R_1) is determined by (1) calculating the deformation predicted by G_{Di} and $G_{Di} + G_{D1}$, (2) locating the timestamps for this deformation to occur from test data, and (3) subtracting the two timestamps to obtain R_1.
    b. Similarly, R_2 is determined by (1) calculating the deformation predicted by $G_{Di} + G_{D1} + G_{D2}$ and G_{D2}, (2) locating the timestamps for this deformation to occur from test data, and (3) subtracting the two timestamps to obtain R_2.
    c. Subsequent retardation times are determined with Equation 11.
4. Calibrate the creep modulus. The creep modulus is selected by (1) plotting the calibrated retardation times and shear deformation moduli of the first two kelvin-elements $((R_1, G_{D1}), (R_2, G_{D2}))$, (2) fitting a power-function to the data-trend, (3) estimating R_3 with Equation 11, and (4) extrapolating from the power-function to R_3 to get the creep modulus.

4.2.4 Creep Deformation Model Calibration

Creep deformation models were calibrated for experiments T4-2 through T4-5 and are summarized in Table 7. This summary includes test number, shear deformation moduli, creep moduli, retardation time, end-of-immediate deformation (δ_{EID}), maximum deformation predicted by the model (δ_{Max}), and the tolerable deformation (δ_T). The tolerable deformation for T4-2 – T4-4 was identified as the point of inflection in the deformation curve as the material approaches failure. The tolerable deformation for T4-5 was taken as the average δ_T for T4-2 – T4-4. In experiments T4-2 through T4-5, the maximum predicted deformation exceeded the tolerable deformation because all experiments were loaded to failure.

The relationships between shear deformation moduli and retardation time for T4-2 – T4-5 are shown in Figure 24. Power functions were fit to each log-log relationship. Retardation times increased as shear stress decreased owing to lower rates of deformation at lower applied shear stress. The reduced deformation rate in T4-5 is reflected in the R-G_D trendline, whereby the reduced slope of the trendline indicates a more gradual reduction in shear resistance as the behavior transitions between delayed deformation I and II. The R-G_D trends for T4-2 and T4-3 are nearly identical due to the timescale of these two tests being within the same order of magnitude. The calibrated creep deformation moduli were extrapolated from these trends. The creep test evaluated at 65 kPa (T4-5) required two creep moduli to satisfy the condition that $\delta_{Max} > \delta_T$.

The calibrated creep deformation models for T4-2 through T4-4 are presented in Figure 25. Each subplot is delineated into "Calibration" and "Prediction" sections. The "Calibration" portion of the graphs include the observed data used during the model calibration and the "Prediction" portions highlight the model validation. The creep predictions align with the observations for $\delta \leq \delta_T$. As deformation exceeds δ_T, the predictions diverge from the observed data due to the increase in deformation rate as specimens approached failure.

The calibrated creep deformation model for T4-5 is presented in Figure 26. The plot is delineated into "Calibration" and "Prediction" sections. The "Calibration" portion of the graphs include the observed data used during the model calibration and the "Prediction" portion highlights the model validation. The predicted deformation aligns closely with the observed data for $t \leq 5\ days$. Past this point, the creep deformation model slightly overpredicts the observed deformation.

Table 7: Summary of calibrated creep deformation models developed to predict the creep deformation of non-heat-treated needle punched geosynthetic clay liners (NHT NP GCls). The specimens were allowed to creep at maximum shear stresses (τ_{Max}) of: T4-2: 89 kPa, T4-3: 85 kPa, T4-4: 80 kPa and T4-5, 68 kPa.

	Test No.			
	T4-2	T4-3	T4-4	T4-5
G_{Di} (kPa)	244665	203756	167718	87720
G_{D1} (kPa)	34767	31783	28889	21020
R_1 (d)	6.25E-04	9.03E-04	1.51E-02	0.1
G_{D2} (kPa)	5828	5897	5972	6228
R_2 (d)	6.09E-03	9.75E-03	0.147	1.85
G_{C1} (kPa)	957	1155	1215	2417
R_3 (d)	6.09E-02	9.75E-02	1.47	18.52
G_{C2} (kPa)	N/A	N/A	N/A	938
R_4 (d)	N/A	N/A	N/A	185.21
δ_{EID} (mm)	24	23	22	18
δ_{Max} (mm)	41	38	34	35
δ_{T} (mm)	28	29	32	30

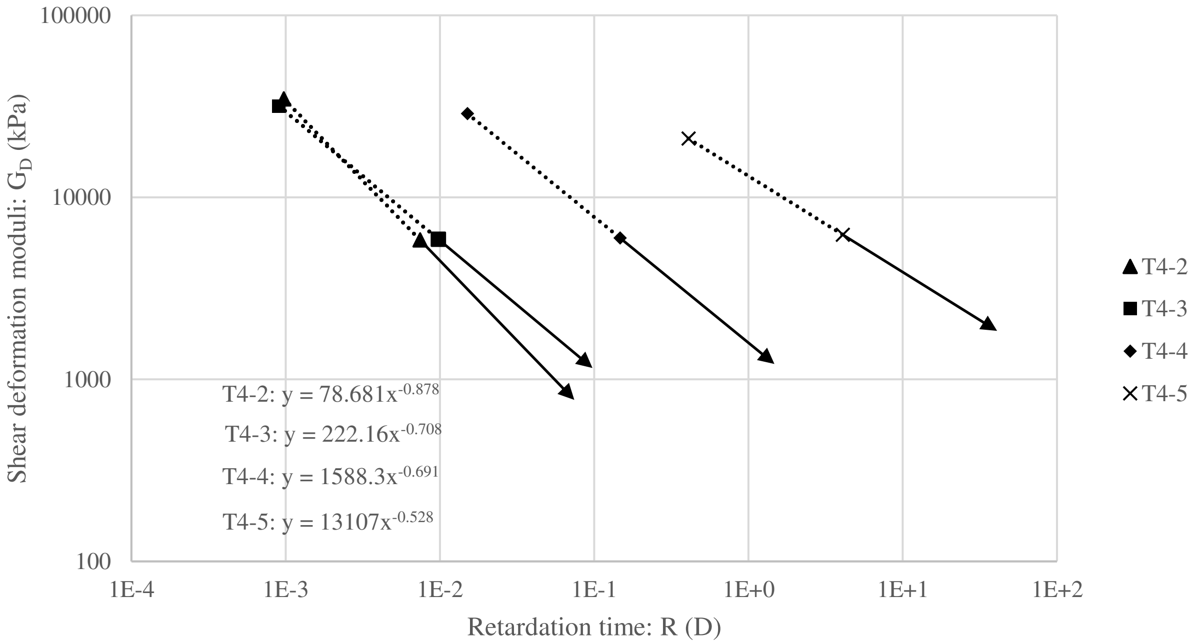

Figure 24: Relationship between retardation times (R_1, R_2) and shear deformation moduli (G_{D_1}, G_{D2}) used in creep modulus calibrations. Creep moduli were determined by extrapolating from the power-function relationships to subsequent retardation time determined with Equation 11. The arrows indicate the direction of extrapolation. The retardation times (R_1, R_2) and shear deformation moduli (G_{D1}, G_{D2}) were determined from rapid loading stress (RLS) creep tests of non-heat-treated needle punched geosynthetic clay liners (NHT NP GCLs). The NHT NP GCLs were tested with an initial normal stress (σ_{ni}) of 20 kPa and at a temperature (T) of 20^oC. The specimens were allowed to creep at shear stresses (τ_c) of T4-2: 89 kPa, T4-3: 85 kPa, T4-4, 80 kPa, and T4-5: 68 kPa.

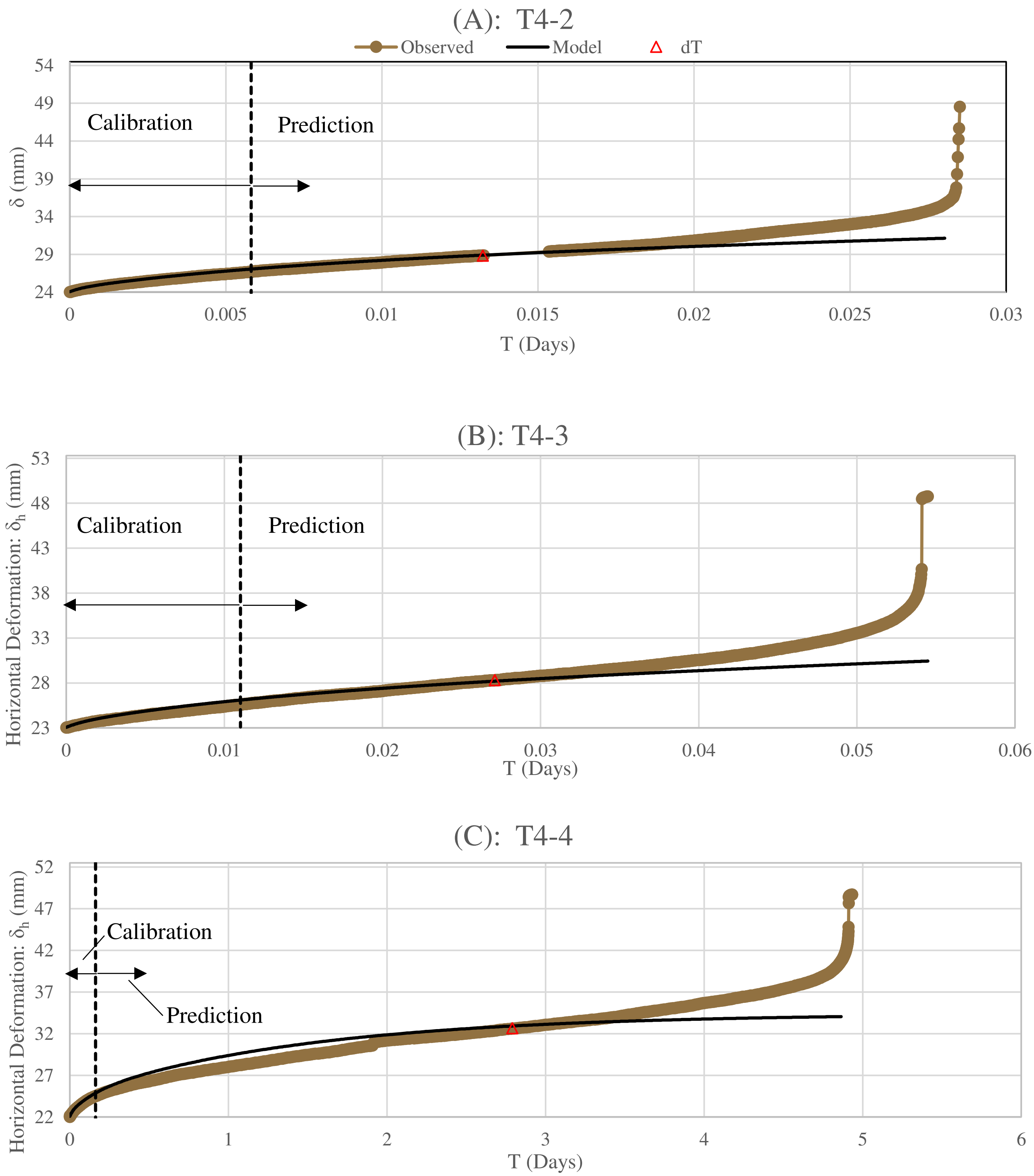

Figure 25: Calibrated creep deformation models for a non-heat-treated needle punched geosynthetic clay liner evaluated in a rapid loading stress (RLS) creep test with an initial normal stress (σ_{ni}) of 20 kPa and at a temperature (T) of $20^{o}C$.The specimens were allowed to creep at shear stresses (τ_c) of: T4-2: 89 kPa, T4-3: 85 kPa, and T4-4: 80 kPa. The test data to the left of the dashed line was used for model calibration.

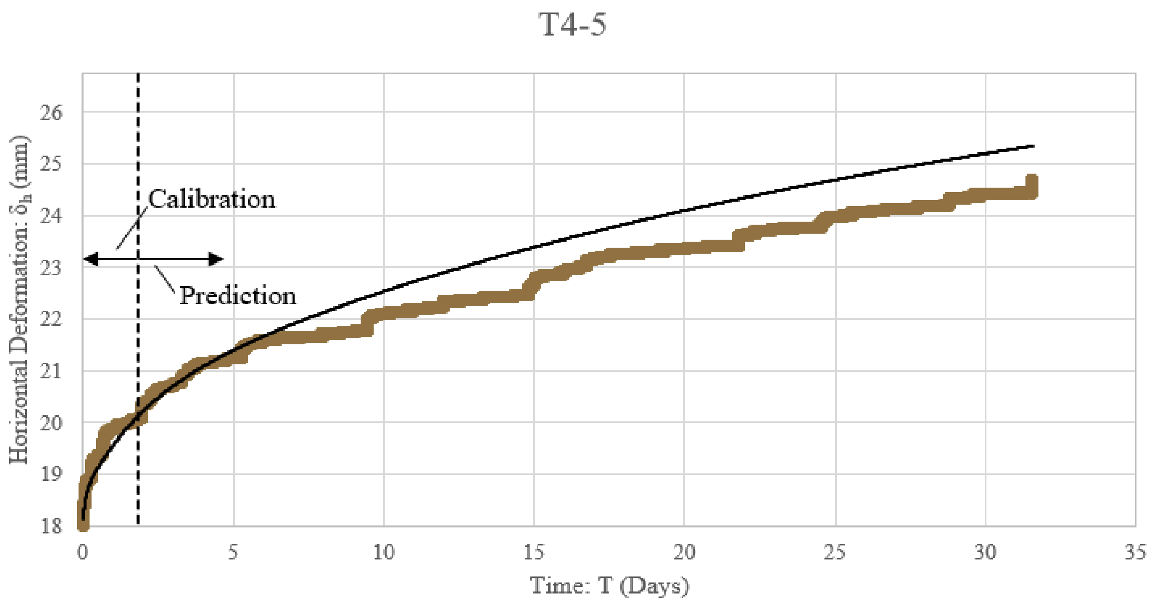

Figure 26: Calibrated creep deformation model for a non-heat-treated needle punched geosynthetic clay liner evaluated in a rapid loading stress (RLS) creep test with an initial normal stress (σ_{ni}) of 20 kPa and at a temperature (T) of $20^{o}C$.The specimens were allowed to creep at shear stresses (τ_c) of: T4-5: 68 kPa and did not reach failure. The test data left of the dashed line was used for model calibration.

4.2.5 Time-to-Failure Predictions

A summary of the time-to-failure predictions performed with the creep deformation model is presented in Table 7. The summary includes test number, observed time-to-failure, time-to-failure predicted with the calibrated creep deformation models, and the percent error between the observations and predictions. The time-to-failure is defined as the time required for the specimen to deform from the end-of-immediate deformation (δ_{EID}) to the tolerable deformation (δ_T). The percent error was calculated with Equation 28.

$$\% \, Err = \left| \frac{Predicted\ TTF - Observed\ TTF}{Observed\ TTF} \right| \times 100 \tag{28}$$

The percent error between the observations and predictions for T4-2 through T4-4 was less than 9%. The low error of the time-to-failure predictions verifies the legitimacy of the model calibration process in the stress range evaluated. Inspection of the calibrated creep deformation models in Figure 25 reveals that the predicted deformation for T4-2 and T4-3 reaches the tolerable deformation slightly after the observed data - producing liberal time-to-failure estimates. Conversely, the calibrated creep deformation model for T4-4 reaches the tolerable deformation prior to the observed data providing conservative estimates of time-to-failure. The prediction for experiment T4-5 is that horizontal deformation of 30 mm will be achieved after 94 ds. This implies that the RLS test would have to be carried out for an additional 62 d for failure to begin to initiate in the specimen.

A comparison of time-to-failure predictions performed with the creep deformation model and time-to-failure observed in Ghazizadeh and Bareither (2018b) is presented in Figure 27. The discrepancy between the predicted time-to-failures and time-to-failures reported in Ghazizadeh and Bareither (2018b) arises from how time-to-failure was defined. In Ghazizadeh and Bareither (2018b), time-to-failure was defined as the time required for the NHT NP GCL to reach a deformation of 50 mm, which was the maximum deformation permitted by the RLS device. Internal shear failure initiated prior to δ=50 mm; however, once failure was initiated, the time required for deformation to reach 50 mm was minimal. In this study, the time-to-failure was adopted as the time required for failure to initiate in the NHT NP GCLs. The specimens entered failure at the point of inflection on the displacement curves and corresponded to a deformation of 30 mm on average. The time associated with the excess 20 mm of deformation within the failure envelope produced the discrepancy seen in Figure 27.

Table 8: Summary of time-to-failure (TTF) predictions performed for a non-heat-treated needle punched geosynthetic clay liners (NHT NP GCL) during creep deformation. The specimens were allowed to creep at shear stresses (τ_c) of: T4-2: 89 kPa, T4-3: 85 kPa, T4-4: 80 kPa, and T4-5: 68 kPa.

Test No.	Observed TTF (d)	Predicted TTF (d)	% Err
T4-2	0.0132	0.0130	2.07%
T4-3	0.0271	0.0281	3.80%
T4-4	2.79	2.53	9.35%
T4-5	N/A	94	N/A

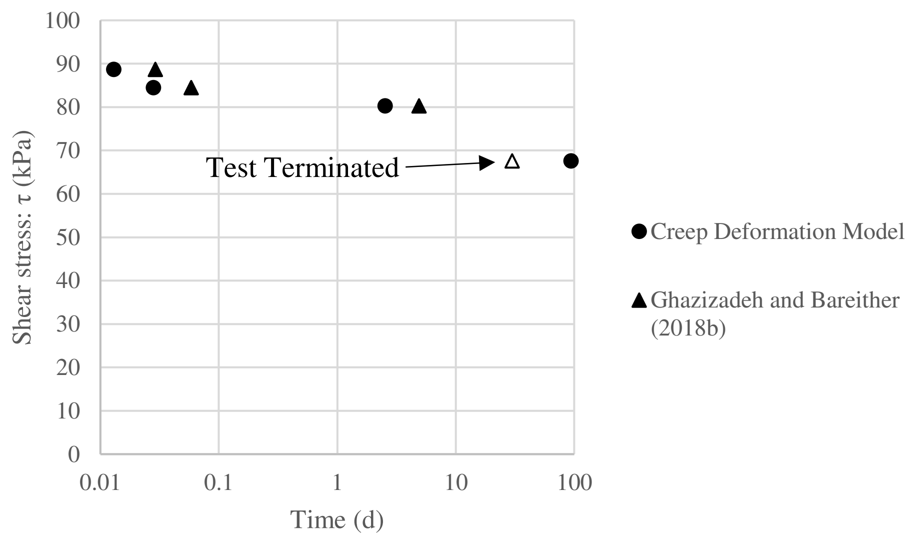

Figure 27: Comparison of predicted time-to-failure and time-to-failure observed in Ghazizadeh and Bareither (2018b). The creep test performed at τ=68 kPa was terminated after a period of 30 days.

4.3 HYPOTHETICAL IN-SITU DEFORMATION PREDICTIONS

A hypothetical slope consisting of a layer of base soil, a NHT NP GCL, and a 1.2 m layer of cover soil is shown in Figure 28. The slope conditions were selected so that (i) stresses acting on the GCL were comparable to the laboratory RLS conditions and (ii) representative of cover systems used in practice. Projected deformation predictions were performed on 2:1, 3:1, and 4:1 variations of the slope so that the NHT NP GCL would experience different shear stresses. In these scenarios, no slippage was assumed at all interfaces such that all shear stress transferred through the internal region of the GCL. The normal and shear forces acting on the NP GCL were calculated with Equations 29 and 30:

$$\sigma = \gamma \cdot z \cdot cos^2 \beta \tag{29}$$

$$\tau = \gamma \cdot z \cdot cos\beta \cdot sin\,\beta \tag{30}$$

where γ is the unit weight of the cover soil in kN/m^3, z is the depth of the cover soil layer in m, and β is the slope angle in degrees.

The three slope variations used for projected deformation predictions are summarized in Table 9. The summary includes the ratio of horizontal to vertical, the corresponding slope angle β, the depth of the soil layer, and the normal and shar stresses acting on the GCL.

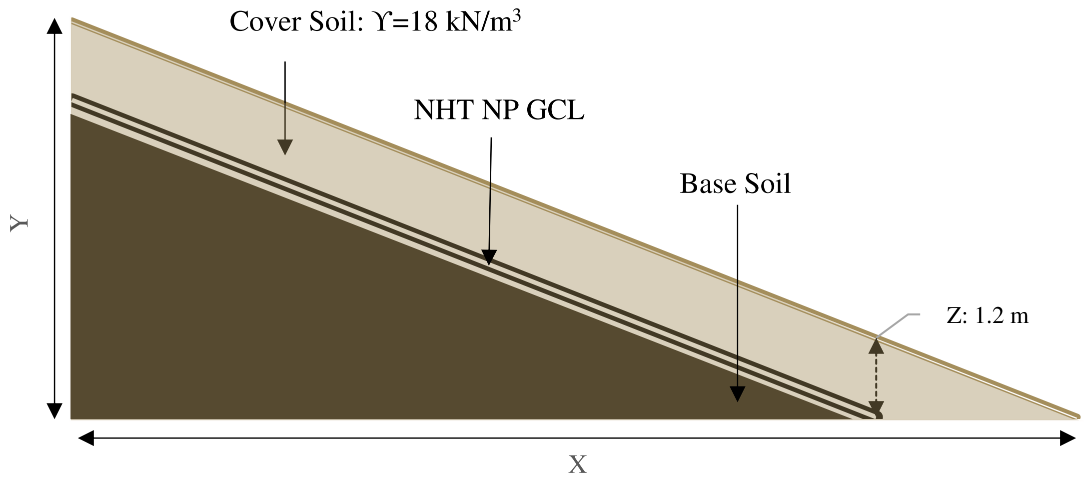

Figure 28: Hypothetical in-field deployment of a non-heat-treated needle-punched geosynthetic clay liner (NHT NP GCL). The slope consists of a layer of base soil, a NHT NP GCL, and a layer of cover soil of depth z. It is assumed that no slippage occurs along the soil-GCL interface and that all stress transfers through the material.

Table 9: Summary of hypothetical slope variations used in projected deformation predictions for a non-heat-treated needle-punched geosynthetic clay liner (NHT NP GCL).

Horizontal	Vertical	Slope angle, β (deg)	Cover soil thickness, z (m)	Normal stress on GCL, σ (kPa)	Shear stress within GCL, τ (kPa)
2	1	26.6	1.2	17	8.64
3	1	18.4	1.2	19	6.48
4	1	14.0	1.2	20	5.08

4.3.1 In-Situ Model Calibration Methodology

The shear stresses experienced by the GCL in Figure 28 lie at the lower range of shear stresses evaluated in the performance assessment. This adds a layer of uncertainty to the model calibration process as the low shear stresses place the deformation within Phase I (Table 4). Here, the tensile force is not sufficient to produce disentanglement, therefore; all deformation is attributed to tensile elongation.

Backwards extrapolation is not appropriate from the shear deformation moduli trends to obtain parameters in Phase I owing to this shift in deformation mechanism. Instead, the average optimized shear deformation moduli (G_{Di}, G_{D1}, G_{D2}) from the first load increment ($\tau = 8.5\ kPa$) were used as an approximation for calibrated shear deformation moduli in this situation. This approximation provides a conservative prediction of deformation as the fiber bundles will have greater resistance to tensile elongation at lower shear stresses ($\tau \leq 8.5\ kPa$).

There are no long-term laboratory or in-situ creep tests available to provide insight into the retardation time at the shear stresses computed for the hypothetical cover designs. Therefore, the average deformation occurring during the first load increment was used for the retardation time calibration.

4.3.2 In-Situ Model Calibration: Summary

The model calibration procedure summarized in Section 4.2.3 was modified to incorporate the aforementioned changes. The steps required to calibrate the creep deformation model in Equation 20 for low shear stresses ($\tau \leq 8\ .5kPa$) are as follows:

1. Obtain the immediate, delayed I, and delayed II optimized shear deformation moduli (G_{Di}, G_{D1}, G_{D2}) for the first load increment ($\tau = 8.5\ kPa$). Average the shear deformation moduli associated with their short-term deformation stage. The resulting average immediate, delayed I, and delayed II shear deformation moduli ($\overline{G_{D\iota}}, \overline{G_{D1}}, \overline{G_{D2}}$) were then used as the first three shear deformation moduli in Equation 15.
2. Calibrate the retardation time(s) to the test data:
    a. The initial retardation time (R_1) is determined by (1) calculating the deformation predicted by $\overline{G_{D\iota}}$ and $\overline{G_{D\iota}} + \overline{G_{D1}}$, (2) locating the timestamps for this deformation to occur from test data, and (3) subtracting the two timestamps to obtain R_1.

b. Similarly, R_2 is determined by (1) calculating the deformation predicted by $\overline{G_{D\iota}} + \overline{G_{D1}} + \overline{G_{D2}}$ and $\overline{G_{D2}}$, (2) locating the timestamps for this deformation to occur from test data, and (3) subtracting the two timestamps to obtain R_2.

c. Subsequent retardation times used in the creep elements $(R_3, R_4, R_5 \ldots)$ are determined with Equation 11.

3. Calibrate the creep modulus. The creep modulus is selected by (1) plotting the calibrated retardation times and shear deformation moduli of the first two Kelvin-elements $((R_1, \overline{G_{D1}}), (R_2, \overline{G_{D2}}))$, (2) fitting a power-function to the data-trend, (3) estimating R_3 with Equation 11, and (4) extrapolating from the power-function to R_3 to get the creep modulus.

4.3.3 In-situ model calibration

The creep deformation model was calibrated to the average deformation for the $\tau = 8.45\ kPa$ load increment and is summarized in Table 10. This summary includes the model element, shear deformation moduli, creep moduli, and retardation times. The first three shear deformation moduli $(\overline{G_{D\iota}}, \overline{G_{D1}}, \overline{G_{D2}})$ represent the average optimized shear deformation moduli for the first load increment $(\tau = 8.5\ kPa)$. T4-2 was excluded from the average as the load increment for this test exhibited an uncharacteristically large amount of deformation. This spike in deformation was attributed specimen variability.

The first two in-situ retardation times (R_1, R_2) in Table 10 were calibrated to the test data and are associated with the average optimized shear deformation moduli. These two in-situ retardation times fall within the same order of magnitude as the generalized retardation times measured during the performance assessment (Section 4.2.1). However, the in-situ retardation times are slightly larger than the generalized retardation times. This is explained by the different deformation mechanisms; i.e., tensile elongation versus fiber disentanglement. During the performance assessment, the generalized retardation times captured the average time transpiring as the fiber-bundles disentangle from the carrier geotextile whereas the in-situ retardation times represent the time required for the fiber-bundles to deform via tensile elongation. The larger in-situ retardation times indicate that deformation accumulates more slowly during tensile elongation.

The relationship between shear deformation moduli and retardation time used in the creep modulus calibration is shown in Figure 29. The slope of the power-function trendline is nearly horizontal indicating a minimal reduction in shear resistance as deformation transitions into creep. The creep moduli were extrapolated from the $R - G_D$ relationship in Figure 29, and a total of 18 creep elements were necessary to capture any notable deformation.

The calibrated creep deformation model is presented in Figure 30. The observed deformation data in Figure 30 are the average deformation from the 8.5 kPa shear stress applied to experiments T4-1, T4-3, T4-4, and T4-5. The creep deformation model is shown to provide an accurate representation of the observed data.

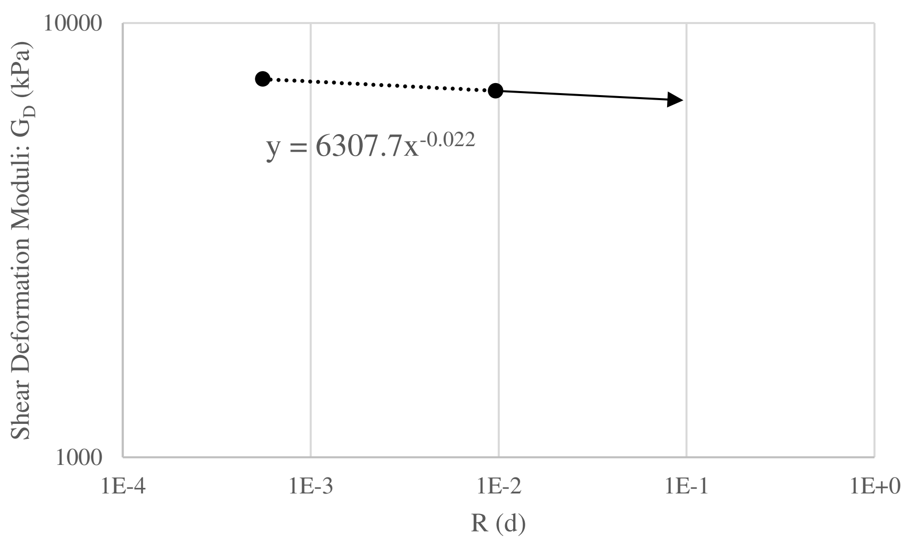

Figure 29: Relationship between retardation times (R_1, R_2) and shear deformation moduli ($G_{D1}.G_{D2}$) used in creep modulus calibration Creep moduli were determined by extrapolating from the power-function relationship to subsequent retardation times determined with Equation 11. The arrow indicates the direction of extrapolation.

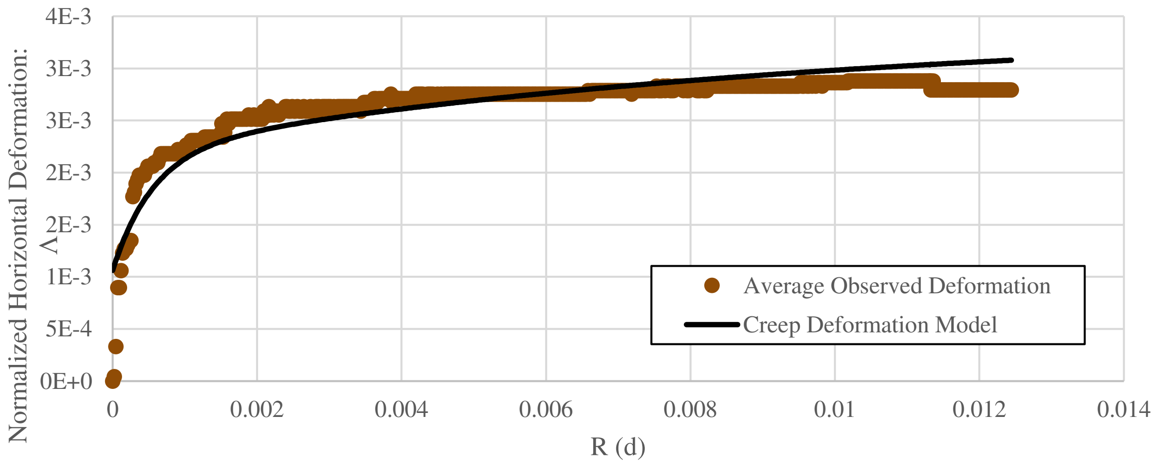

Figure 30: Creep deformation model calibrated to a shear stress of 8.5 kPa used for projected creep deformation predictions at low shear stresses. The observed deformation was taken as the average of T4-1, T4-3, T4-4, and T4-5 $\tau = 8.5\ kPa$ load increment deformation.

Table 10: Summary of the creep deformation model calibrated to a shear stress of 8.5 kPa. The first and second retardation times (R_1, R_2) were determined from test data and all subsequent retardation times were approximated with Equation 11.

Model Element	$\overline{G_D}$(kPa)	R (d)	G_C (kPa)	R (d)
i	7954	N/A	N/A	N/A
1	7429	5.56E-04	N/A	N/A
2	6980	9.62E-03	N/A	N/A
3	N/A	N/A	6638	9.62E-02
4	N/A	N/A	6313	9.62E-01
5	N/A	N/A	6004	9.62E+00
6	N/A	N/A	5709	9.62E+01
7	N/A	N/A	5430	9.62E+02
8	N/A	N/A	5164	9.62E+03
9	N/A	N/A	4911	9.62E+04
10	N/A	N/A	4670	9.62E+05
11	N/A	N/A	4441	9.62E+06
12	N/A	N/A	4223	9.62E+07
13	N/A	N/A	4016	9.62E+08
14	N/A	N/A	3820	9.62E+09
15	N/A	N/A	3632	9.62E+10
16	N/A	N/A	3454	9.62E+11
17	N/A	N/A	3285	9.62E+12
18	N/A	N/A	3124	9.62E+13

*$\overline{G_D}$: Average optimized shear deformation moduli from $\tau = 8.5\ kPa$ load increment
* R: Retardation time
* G_C: Creep Modulus

4.3.4 *In-Situ Projected Deformation predictions*

A summary of the projected deformation predictions performed with the creep deformation model is in Table 11. The summary includes the slope proportions, shear stress, target deformation, and predicted time for the NHT NP GCL to reach the target deformation. The time required for the NHT NP GCL to reach a deformation of 1, 3, and 5 mm was determined with the creep deformation model. The in-situ deformation predictions indicate that a decrease in shear stress corresponds with an increase in the time required to reach the target deformation. The time required for the projected deformation to surpass 3 mm for all slopes exceeds one million years. Therefore, the creep deformation model predicts that the NHT NP GCL in Figure 28 will not experience shear failure under these conditions.

Table 11: Summary of in-situ projected deformation for a non-heat-treated needle-punched geosynthetic clay liner (NHT NP GCL) subjected to low shear stresses ($\tau \leq 8.5\ kPa$).

Slope	τ (kPa)	δ (mm)	Time to δ (yr)
2:1	8.64	1	0.1
		3	1,580,000
		5	372,000,000,000
3:1	6.48	1	1
		3	95,300,000
		5	21,500,000,000,000
4:1	5.08	1	17
		3	24,574,792,097
		5	16,269,981,253,361,200

*τ: Shear Stress
*δ: Horizontal deformation

4.4 DISCUSSION

Developing a creep deformation model for a non-heat-treated needle-punched geosynthetic clay liners consists of three steps: (1) data pre-processing, (2) conducting a performance assessment, and (3) calibrating the creep deformation model. The creep deformation model can then be used to predict the time-to-failure.

4.4.1 Data Pre-processing

Data pre-processing is conducted on both RLS load increments and creep deformation curves to ensure compatibility between the datasets. During this step, individual load increments and creep deformation curves are normalized and transposed. The normalized creep stress ratio (CSR_N) is determined for each load increment. This parameter allows for load increments to be compared to one another while accounting for variation in total normal stress (σ_{nt}).

The bounds of creep deformation are defined by the end-of-immediate deformation and the tolerable deformation. The end-of-immediate deformation was approximated by extrapolating from the $\tau - \delta_{EOL}$ relationship. The tolerable deformation was defined as the point of inflection on the creep deformation curve as the creep deformation transitioned into failure. These boundaries were used to isolate the creep deformation curves. For the shear stresses evaluated in this study, the creep dataset pre-processing produced creep curves that were compatible with the creep deformation model calibration procedure.

4.4.2 Performance Assessment

The performance assessment provides insight into how internal shear resistance of a given NP GCL develops during the incremental loading of an RLS test. Constraining the model optimization procedure is important so that the parameters have physical significance. This was accomplished by ensuring the total deformation predicted by the immediate and delayed shear deformation moduli (G_{Di}, G_{D1}, G_{D2}) are approximately equivalent to the total load increment deformation. Additionally, the retardation times (R_1, R_2) should have the property that $\Delta \log(R) = 1$ to ensure smooth deformation curves.

The performance assessment conducted to evaluate the effects of peel strength, normal stress, and temperature captured variation in shear deformation moduli with these internal and external factors. An increase in peel strength corresponded to an increase in the immediate and delayed I shear deformation moduli (G_{Di}, G_{D1}). Increased peel strength had no notable effect on delayed shear deformation moduli II

(G_{D2}). Increasing normal stress resulted in an increase in the immediate shear deformation moduli (G_{Di}). The delayed shear deformation moduli I (G_{D1}) exhibited a drop at 25 kPa that was more pronounced for specimen tested at higher normal stress. The delayed shear deformation moduli II (G_{D2}) demonstrated no sensitivity to normal stress. Increasing temperature corresponded to a reduction in the immediate shear deformation moduli (G_{Di}). Elevated temperatures produced minor variation in the delayed I and II shear deformation moduli (G_{D1}, G_{D2}).

The performance assessment highlights the shear deformation moduli sensitivity to peel strength, normal stress, and temperature. This implies that shear deformation moduli trends for NHT NP GCLs can be used in the model calibration process to determine time-to-failure under different conditions.

The resistance to disentanglement (RD) was calculated during the performance assessment for the immediate, delayed I, and delayed II short-term shear deformation states. When RD exceeded entanglement strength for a given short-term deformation state, the internal shear resistance exceeded the average force required to produce disentanglement. When this mechanistic transition occurs, that deformation state is rendered "inactive", and all deformation is attributed to the remaining active short-term shear deformation states. The load increment corresponding to $RD > ES$ demonstrated sensitivity to changes in peel strength, normal stress, and temperature.

Four phases of deformation were identified from the $RD - ES$ analysis. Phase I captures elastic deformation, Phase II & III captures the transition from elastic to viscoelastic deformation, and Phase IV captures the transition to failure. Tensile elongation of the reinforcing fiber-bundles was assumed to be negligible during deformation Phases II-IV.

4.4.3 Model Calibration

Model calibration involved (1) shear deformation moduli calibration, (2) retardation time calibration, and (3) creep modulus calibration. The shear deformation moduli calibration methodology selected was dependent on the deformation phase of the target shear stress. For shear stresses within deformation phases II, III, and IV, an empirical model was used to aid in parameter selection. The empirical model consisted of a power-function fit to the shear deformation moduli trends from deformation Phases II and III. A power-function was deemed suitable for the empirical model because the shear deformation moduli trends follow a linear trend when plotted on log-log axis. Shear deformation moduli were selected by extrapolating from the empirical model to a target shear stress.

For shear stresses within deformation phase I, average-optimized shear deformation moduli were used as approximations for extrapolated model parameters. The average-optimized shear deformation moduli are calculated by taking the average immediate, delayed I, and delayed II shear deformation moduli for the $\tau = 8.5\ kPa$ load increment from the performance assessment. While this approximation does introduce uncertainty in the projected deformation, these shear deformation moduli provided a conservative prediction for projected deformation.

The retardation times were calibrated by identifying the time required for the strain predicted by the first two kelvin-elements to accumulate from the test data. As of now, this step of the model calibration process requires test data to be complete, which limits a priori model predictions without test data that can be used for model calibration. Additional research is needed to develop a continuous retardation time spectrum for a NHT NP GCL over a range of shear stresses.

The creep modulus calibration consisted of (1) plotting R and G_D of the Kelvin-elements in the three-element model and fitting a power-law trend to the data, (2) approximating the retardation time for the subsequent kelvin element with Equation 11, and (3) extrapolating with the aforementioned relationship to obtain the appropriate creep modulus. Extrapolating from two data points is indeed not best practice; however, the resulting creep deformation models aligned closely with the observed data, which provide some justification for the extrapolated modulus. The power law relationship between the model parameters indicated that the change in shear deformation moduli between kelvin-elements is inversely proportional to the change in retardation time. This finding aligns with the recommendations of Koerner et al. (2001). Additional research is needed to verify the relationship between retardation time and shear deformation modulus.

The error between the observed and predicted time-to-failure reached a maximum of 9% in T4-4. The low error of the time-to-failure predictions verifies the legitimacy of the model calibration process in the stress range evaluated.

4.4.4 Time-to-failure Predictions

Time-to-failure predictions were performed by returning the time required for the model to reach the tolerable deformation. The tolerable deformation was defined as the maximum horizontal deformation the NHT NP GCl can sustain before entering failure and was located by finding the point of inflection on the displacement curves. The time-to-failure predictions had a maximum percent error of 9% when compared to the tolerable deformation. There is a discrepancy between the time-to-failure predictions performed in this study and the time-to-failure observed in Ghazizadeh and Bareither (2018b) arising from how time-to-failure was defined. In Ghazizadeh and Bareither (2018b), time-to-failure was defined as the time required for the NHT NP GCL to reach a horizontal deformation of 50 mm, which was the maximum deformation permitted by the RLS device. This definition of time-to-failure includes the failure envelope and resulted in larger values of time-to-failure.

The time required for in situ deformation to accumulate on hypothetical cover scenarios was estimated to be very large (e.g., surpassing millions of years). However, the projected deformations cannot be taken as accurate as there are several factors that affect NHT NP GCL shear behavior in the long-term. As demonstrated by the performance assessment, changes in normal stress and temperature affect internal shear resistance. Additionally, factors such as material degradation can act to reduce the internal shear resistance.

5 RECOMMENDATIONS

The performance assessment and model calibration procedure can be used to predict creep deformation of a non-heat treated, needle-punched geosynthetic clay liner (NHT HP GCL) at a range of shear stresses. Rapid loading shear tests (e.g., Ghazizadeh & Bareither 2018a) can be performed to develop a continuous trend of retardation times. This retardation time-trend can increase the ease of parameter selection. Each one of these scenarios requires proper testing, data collection, and data-processing.

A bullet-point list of some recommendations and guidance is offered based on the assessment documented herein. If NHT NP GCL creep deformation is being predicted at a range of shear stresses:

1. RLS creep tests conducted on the material should include:
    a. One test performed at a high shear stress so that time-to-failure is minimal and tolerable deformation can be determined.
    b. Additional tests performed at a range of target shear stresses such that steady-state creep is reached and retardation times can be calibrated.
2. The RLS loading increments are then isolated and subjected to the performance assessment to obtain the shear deformation moduli trends.
    a. A 4-element kelvin model is recommended for model optimization, which provides additional data-points to verify the $R - G_D$ trendlines used in the creep modulus calibration.
3. Deformation curves at the target shear stresses are subject to preprocessing to ensure compatibility with the shear deformation moduli trends.
4. The creep deformation model is calibrated to the target shear stresses with the shear deformation moduli trends and deformation curves.
5. Time-to-failure predictions are then performed.

The following recommendations are offered to develop a trend of retardation times:

1. RLS creep tests should be performed at target shear stresses ranging from deformation phase I to III (Table 4).
    a. During these tests, the specimen shall be allowed to deform until steady-state creep is reached.
2. Next, the retardation times at the target shear stresses are determined by:
    a. Calibrating shear deformation moduli to the target shear stress from the shear deformation moduli trends
    b. Determining the calibrated retardation times (R_1, R_2) from the test data.
3. Hypothetically, this trend of retardation times can be used to interpolate between shear stresses; thus, eliminating the need for test data at different (site-specific) shear stresses in future retardation time calibrations.

6 SUMMARY AND CONCLUSIONS

Analysis and predictions of the shear behavior of a non-heat-treated needle punched geosynthetic clay liner (NHT NP GCL) have been conducted using a mechanistic model. A three-element Kelvin-chain model was employed in a performance assessment of the incremental loading of a rapid loading stress (RLS) test. The results of the performance assessment were used to inform the creep deformation model used for time-to-failure predictions.

The performance assessment was conducted to evaluate the ability of the Kelvin-chain model to capture changes in deformation behavior of NHT NP GCLs with different internal structure (e.g., peel strength) and when subjected to different environmental factors (e.g., normal stress, temperature) in the lab. Model parameters demonstrated sensitivity to the variation in internal and external factors.

Load increments from RLS creep tests were subjected to the performance assessment to obtain data trends to inform the long-term creep deformation model. These data trends in combination with creep-test data were used to calibrate the creep deformation model. The percent error between the observed time-to-failure and predicted time-to-failure was less than 9%.

Projected field deformations were performed with the creep deformation model. The creep deformation model was calibrated with lab data. The time required for the projected deformation to accumulate indicated that the specimen would not reach failure within a relevant timeframe.

BIBLIOGRAPHY

Athanassopoulos, C., & Yuan, Z. (2011). Geo-Frontiers 2011 © ASCE 2011 1922. *Geo-Frontiers 2011*, 1922–1930.

Bažant, Z. P., & Prasannan, S. (1989). Solidification Theory for Concrete Creep. II: Verification and Application. *Journal of Engineering Mechanics*, *115*(8), 1704–1725. https://doi.org/10.1061/(asce)0733-9399(1989)115:8(1704)

Geosynthetic Research Institute. (2011). *GRI-GCL5* Standard Guide for "Design Considerations for Geosynthetic Clay Liners (GCLs) in Various Applications."* https://geosynthetic-institute.org/grispecs/gcl5.pdf#page=13&zoom=auto,-265,50

Feng, S. J., Chang, J. Y., Chen, H. X., Shen, Y., & Shi, J. L. (2020). Shear strength and failure mechanism of needle-punched geosynthetic clay liner. *Geotextiles and Geomembranes*, *48*(6), 962–972. https://doi.org/10.1016/j.geotexmem.2020.08.003

Fox, P. J., Rowland, M. G., Scheithe, J. R., & Members, J. A. (1998). Internal shear strength of three geosynthetic clay liners. In *Journal of Geotechnical and Geoenvironmental Engineering* (Vol. 124, Issue 10). https://doi.org/10.1061/(ASCE)1090-0241(1998)124:10(933)

Ghazizadeh, S., & Bareither, C. A. (2016). *Critical Evaluation of the Long-Term Shear Strength of Geosynthetic Clay Liners Shahin Ghazizadeh 1 and Christopher A. Bareither 2 1*. 11–23. https://doi.org/10.1061/9780784480144.002

Ghazizadeh, S., & Bareither, C. A. (2018a). Stress-controlled direct shear testing of geosynthetic clay liners I: Apparatus development. *Geotextiles and Geomembranes*, *46*(5), 656–666. https://doi.org/10.1016/j.geotexmem.2018.06.003

Ghazizadeh, S., & Bareither, C. A. (2018b). Stress-controlled direct shear testing of geosynthetic clay liners II: Assessment of shear behavior. *Geotextiles and Geomembranes*, *46*(5), 667–677. https://doi.org/10.1016/j.geotexmem.2018.06.004

Ghazizadeh, S., & Bareither, C. A. (2020). Temperature Effects on Internal Shear Behavior in Reinforced GCLs. *Journal of Geotechnical and Geoenvironmental Engineering*, *146*(1), 04019124.

https://doi.org/10.1061/(asce)gt.1943-5606.0002193

Ghazizadeh, S., & Bareither, C. A. (2021). Variability of Fiber Reinforcement, Peel Strength, and Internal Shear Strength in Needle-Punched GCLs. *Journal of Geotechnical and Geoenvironmental Engineering*, *147*(3), 04020181. https://doi.org/10.1061/(asce)gt.1943-5606.0002471

Koerner, R. M., Soong, T. Y., Koerner, G. R., & Gontar, A. (2001). Creep testing and data extrapolation of reinforced GCLs. *Geotextiles and Geomembranes*, *19*(7), 413–425. https://doi.org/10.1016/S0266-1144(01)00015-2

Kong, D. J., Wu, H. N., Chai, J. C., & Arulrajah, A. (2017). State-of-the-art review of geosynthetic clay liners. *Sustainability (Switzerland)*, *9*(11). https://doi.org/10.3390/su9112110

Müller, W., Jakob, I., Seeger, S., Tatzky-Gerth, R., Mueller, W., Jakob, I., Seeger, S., & Tatzky-Gerth, R. (2008). Long-term shear strength of geosynthetic clay liners. *Geotextiles and Geomembranes*, *26*(2), 130–144. https://doi.org/10.1016/j.geotexmem.2007.08.001

Roscoe, R. (1950). Mechanical models for the representation of visco-elastic properties. *British Journal of Applied Physics*, *1*(12), 332–333. https://doi.org/10.1088/0508-3443/1/12/106

Roylance, D. (2001). *Engineering Viscoelasticity (Mit)*. 1–38. http://web.mit.edu/course/3/3.11/www/modules/visco.pdf

Shackelford, C. D., Benson, C. H., Katsumi, T., Edil, T. B., & Lin, L. (2000). Evaluating the hydraulic conductivity of GCLs permeated with non-standard liquids. *Geotextiles and Geomembranes*, *18*(2–4), 133–161. https://doi.org/10.1016/S0266-1144(99)00024-2

Zanzinger, H. (2016). Contribution to the Long-Term Shear Strength of a Needle Punched GCL. *International Journal of Geosynthetics and Ground Engineering*, *2*(1), 8. https://doi.org/10.1007/s40891-016-0049-3

7 APPENDIX: PERFORMANCE ASSESSMENT

7.1 T1: EVALUATION OF PEEL STRENGTH

- RLS tests were conducted on NHT NP GCLs with peel strengths of T1-1: 720 N/m, T1-2: 1490 N/m, and T1-3: 2170 N/m.
- Graph titles consist of a test series identifier (e.g. T2-1) and load increment shear stress (e.g. τ=8.45 kPa).

7.1.1 T1-1

T1-1: Peel strength = 720 N/m						
τ (kPa)	CSR-N	G_{Di} (kPa)	G_{D1} (kPa)	G_{D2} (kPa)	R_1 (d)	R_2 (d)
8.45	0.22	15982	4197	7011	3.15E-04	2.29E-03
16.9	0.22	15718	1283	4322	9.19E-05	3.65E-03
25.34	0.59	13060	1538	6242	1.28E-04	3.16E-03
33.79	0.71	9109	3580	6132	2.03E-04	4.31E-03
42.24	0.80	15709	7171	7865	1.77E-04	3.12E-03
50.96	0.88	48886	7176	7362	3.21E-04	4.54E-03
59.13	0.94	39422	13811	6730	3.51E-04	3.74E-03
67.58	0.99	49073	27667	5222	2.62E-04	4.06E-03
76.03	1.00	47301	25901	3818	2.62E-04	3.69E-03
84.48	0.99	48413	27051	4405	2.62E-04	4.06E-03
92.92	1.00	48413	27051	4405	2.61E-04	3.86E-03

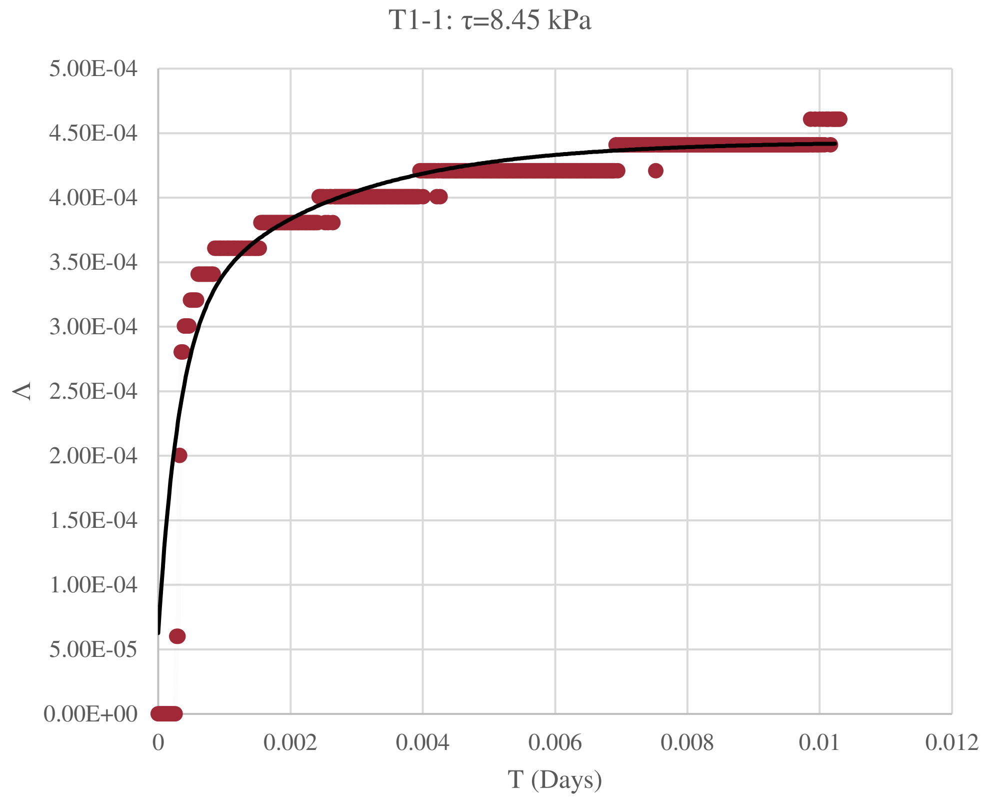
T1-1: τ=8.45 kPa
5.00E-04
4.50E-04
4.00E-04
3.50E-04
3.00E-04
2.50E-04
2.00E-04
1.50E-04
1.00E-04
5.00E-05
0.00E+00
Λ
0
0.002
0.004
0.006
0.008
0.01
0.012
T (Days)

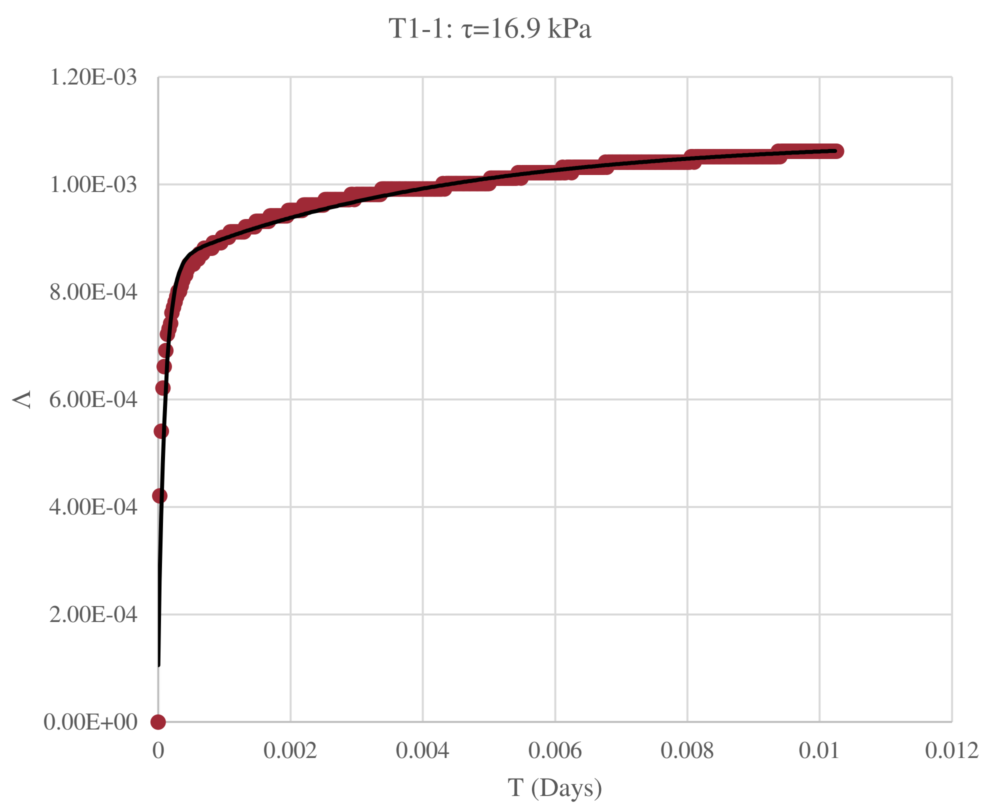
T1-1: τ=16.9 kPa
1.20E-03
1.00E-03
8.00E-04
6.00E-04
4.00E-04
2.00E-04
0.00E+00
Λ
0
0.002
0.004
0.006
0.008
0.01
0.012
T (Days)

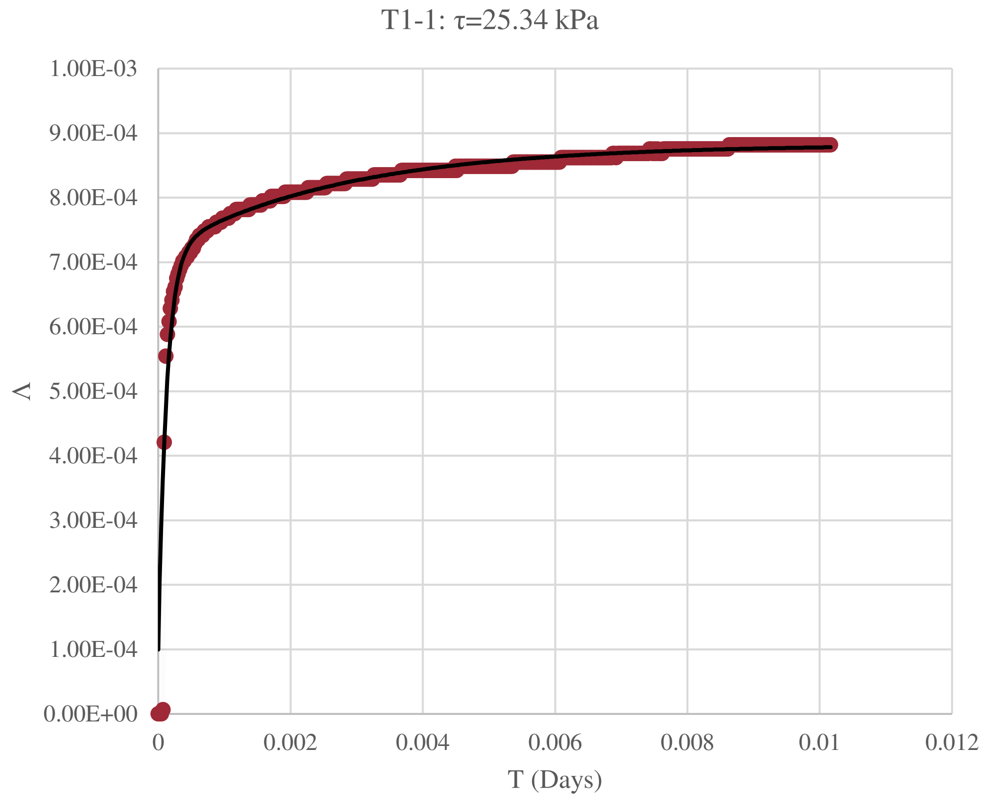
T1-1: τ=25.34 kPa
1.00E-03
9.00E-04
8.00E-04
7.00E-04
6.00E-04
5.00E-04
4.00E-04
3.00E-04
2.00E-04
1.00E-04
0.00E+00
Λ
0
0.002
0.004
0.006
0.008
0.01
0.012
T (Days)

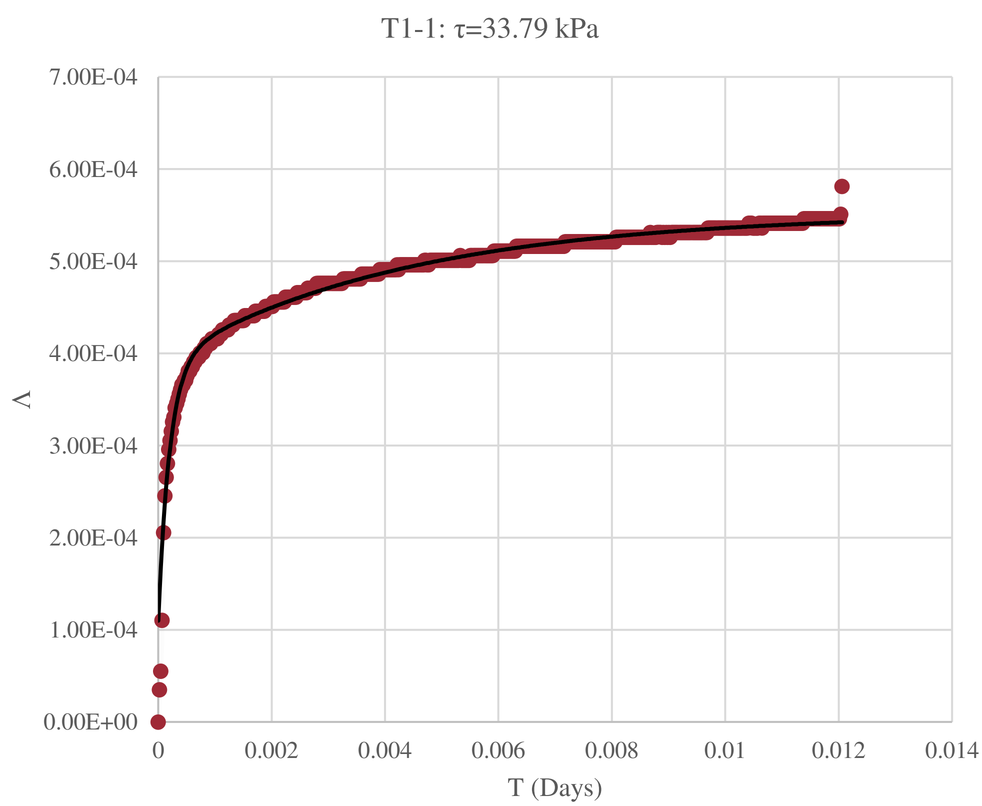
T1-1: τ=33.79 kPa
7.00E-04
6.00E-04
5.00E-04
4.00E-04
3.00E-04
2.00E-04
1.00E-04
0.00E+00
Λ
0
0.002
0.004
0.006
0.008
0.01
0.012
0.014
T (Days)

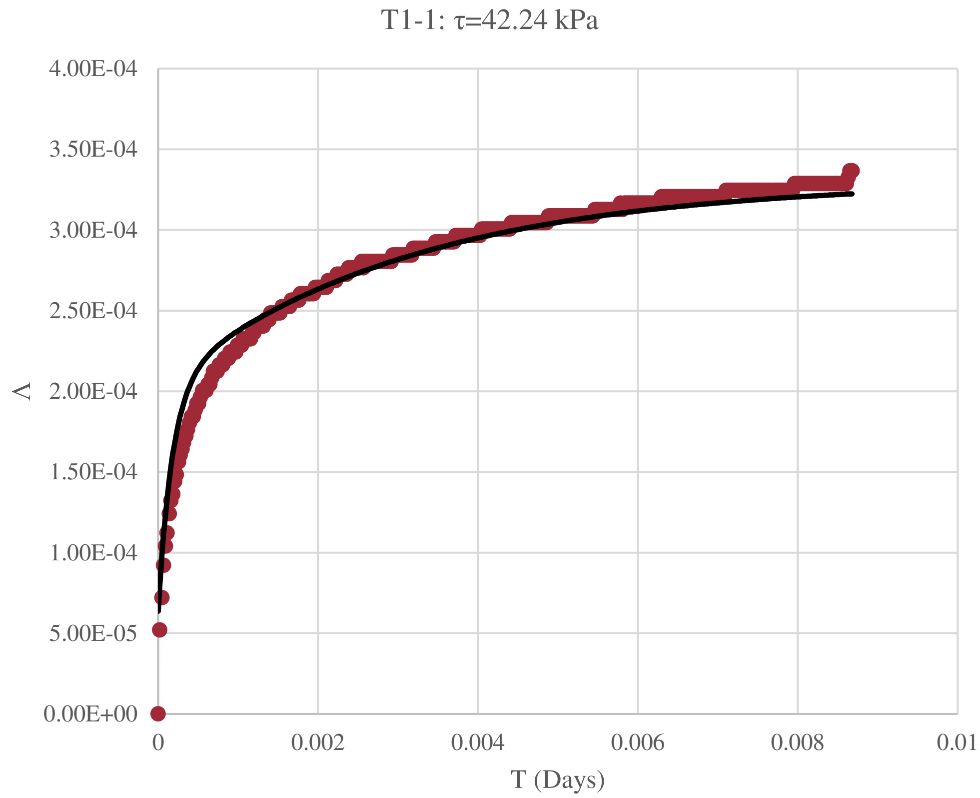
T1-1: τ=42.24 kPa
4.00E-04
3.50E-04
3.00E-04
2.50E-04
2.00E-04
1.50E-04
1.00E-04
5.00E-05
0.00E+00
Λ
0
0.002
0.004
0.006
0.008
0.01
T (Days)

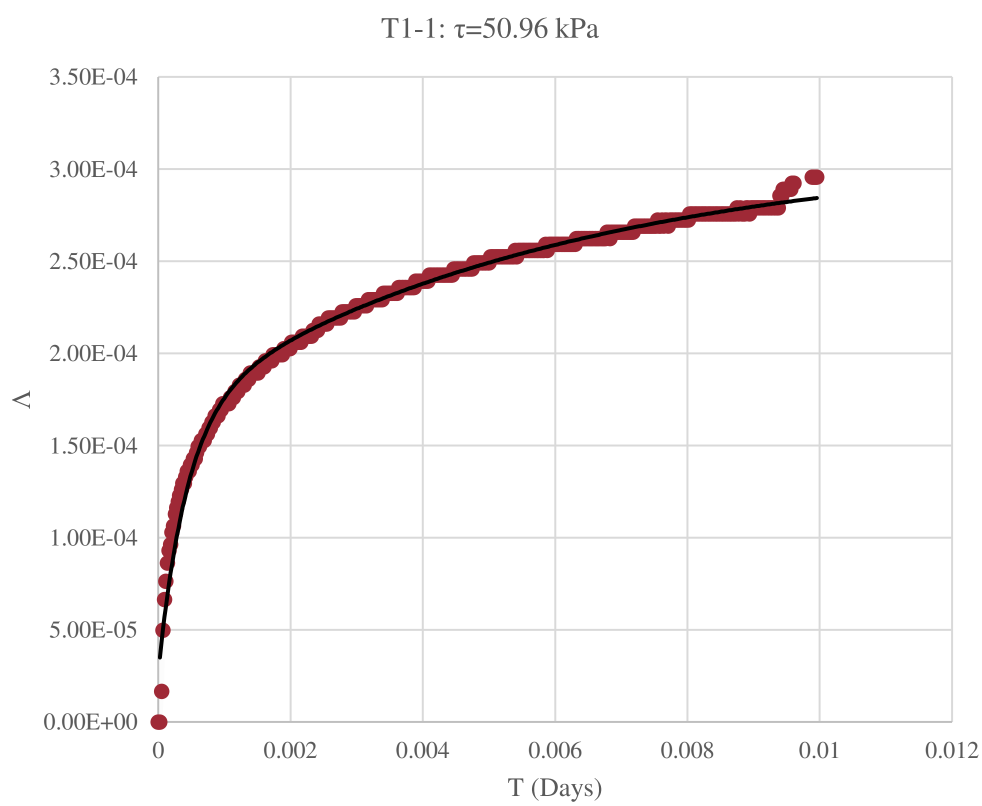
T1-1: τ=50.96 kPa
3.50E-04
3.00E-04
2.50E-04
2.00E-04
1.50E-04
1.00E-04
5.00E-05
0.00E+00
Λ
0
0.002
0.004
0.006
0.008
0.01
0.012
T (Days)

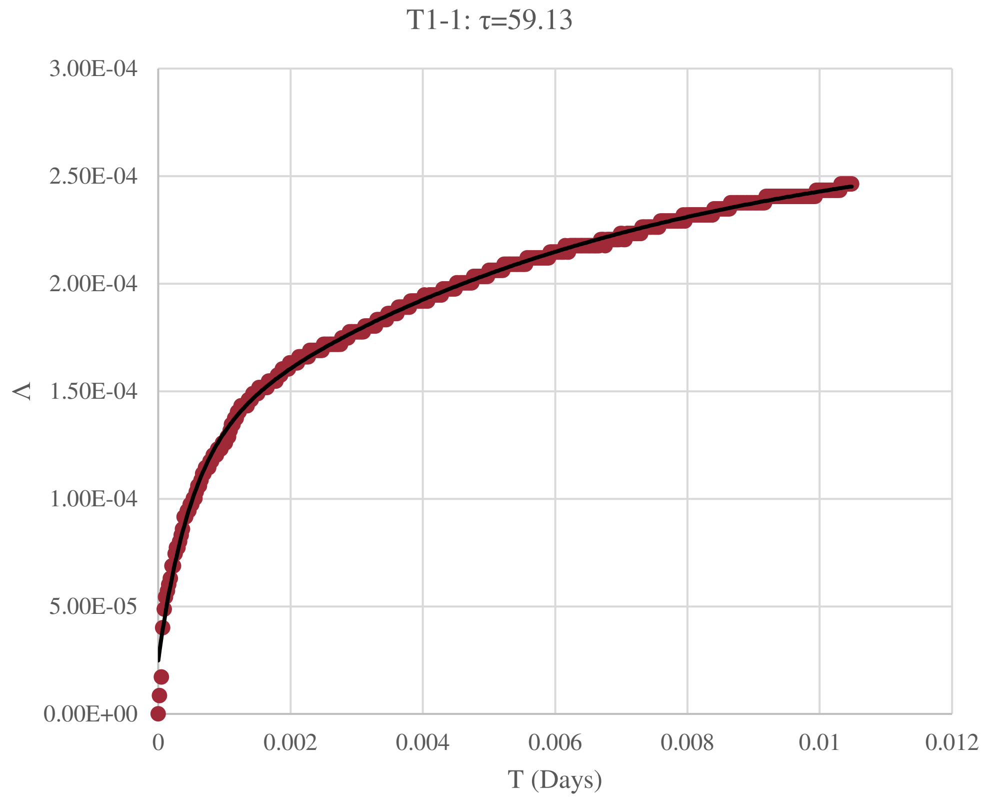
T1-1: τ=59.13
3.00E-04
2.50E-04
2.00E-04
1.50E-04
1.00E-04
5.00E-05
0.00E+00
Λ
0
0.002
0.004
0.006
0.008
0.01
0.012
T (Days)

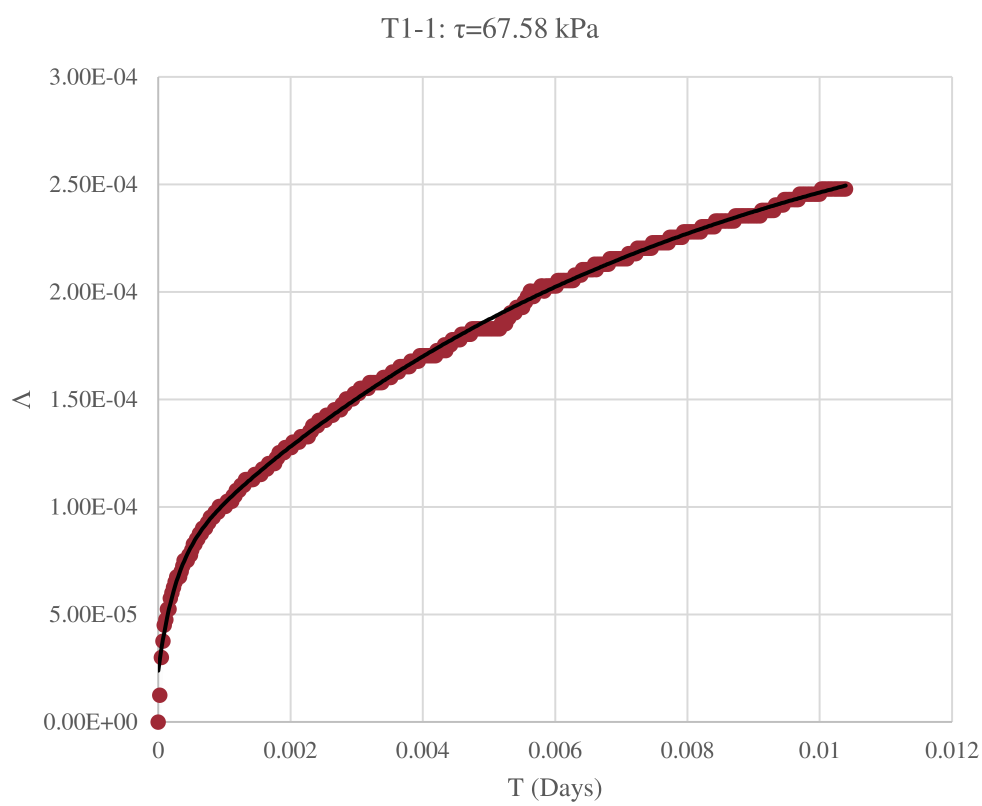
T1-1: τ=67.58 kPa
3.00E-04
2.50E-04
2.00E-04
1.50E-04
1.00E-04
5.00E-05
0.00E+00
Λ
0
0.002
0.004
0.006
0.008
0.01
0.012
T (Days)

T1-1: τ=76.03 kPa

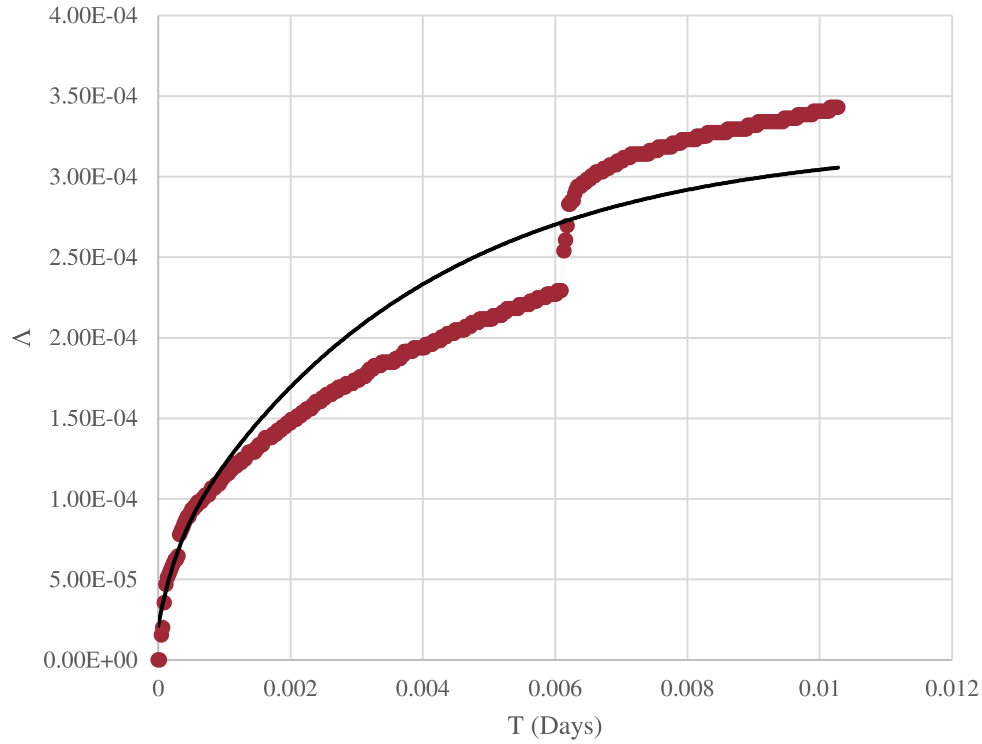

T1-1: τ=84.48 kPa

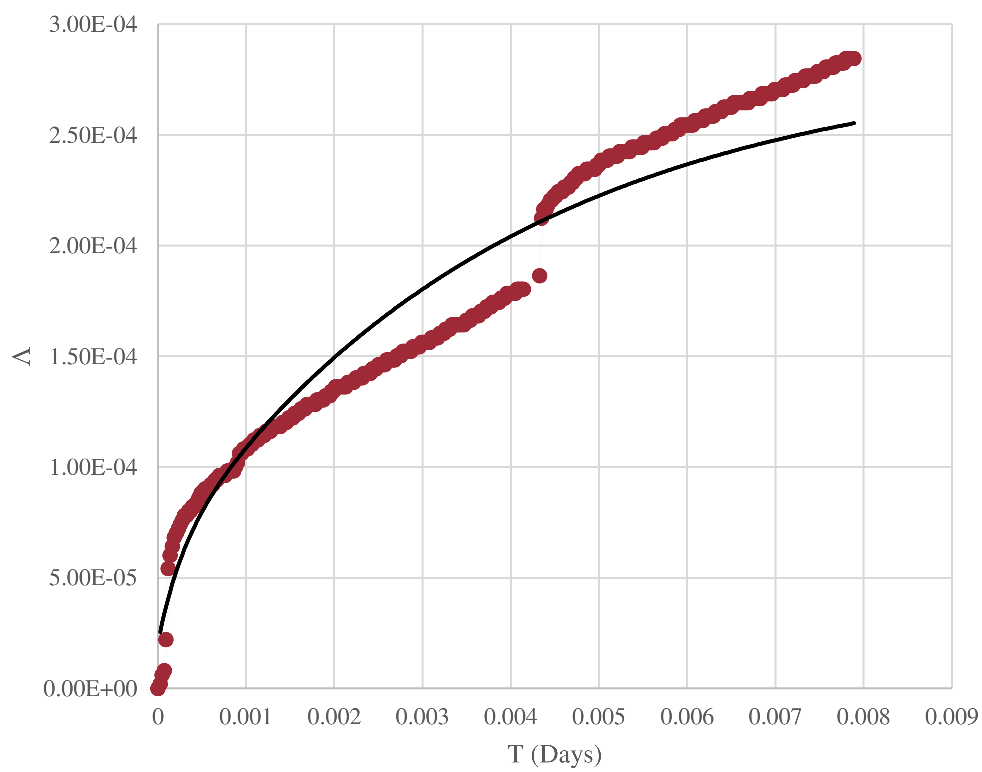

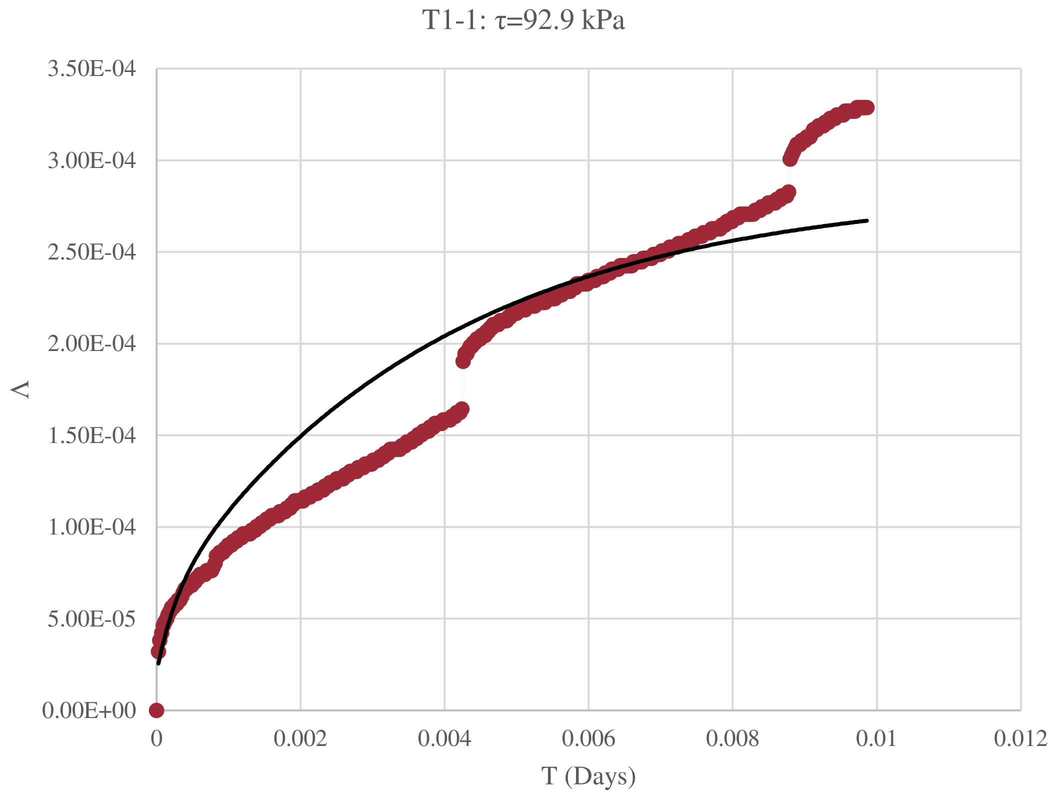

7.1.2 T1-2

T1-2: Peel strength = 1490 N/m						
τ (kPa)	CSR-N	G_{Di} (kPa)	G_{D1} (kPa)	G_{D2} (kPa)	R_1 (d)	R_2 (d)
8.45	N/A	15982	4197	7011	3.15E-04	2.29E-03
16.9	N/A	8968	2006	5405	7.21E-05	3.19E-03
25.34	N/A	10478	2258	4458	8.50E-05	4.06E-03
33.79	N/A	45666	3090	5429	1.28E-04	7.87E-03
42.24	N/A	27529	7020	3993	1.63E-04	1.78E-02
50.96	N/A	74958	10402	6286	1.40E-04	4.31E-03
59.13	N/A	110131	15907	8934	2.24E-04	3.86E-03
67.58	N/A	479175	18006	9706	7.39E-04	7.35E-03
76.03	N/A	486618	24500	8941	8.52E-04	7.72E-03
84.48	N/A	479175	18006	9706	7.39E-04	7.35E-03
92.92	N/A	477508	16389	4011	7.37E-04	6.51E-03

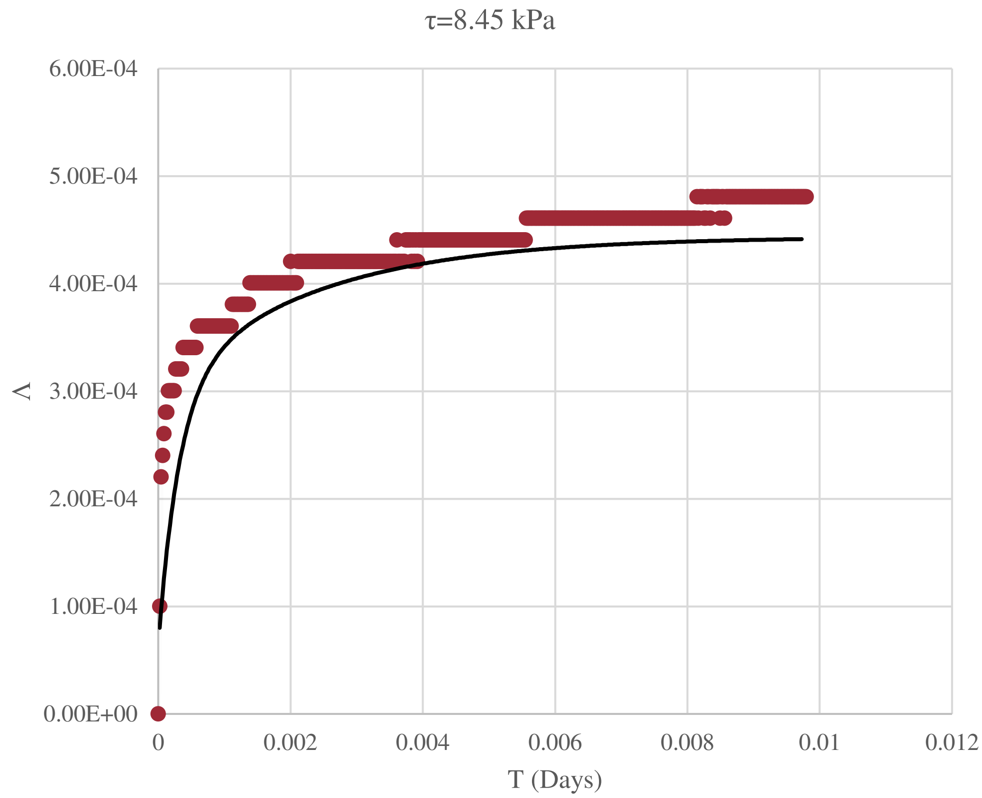
τ=8.45 kPa
6.00E-04
5.00E-04
4.00E-04
3.00E-04
2.00E-04
1.00E-04
0.00E+00
Λ
0
0.002
0.004
0.006
0.008
0.01
0.012
T (Days)

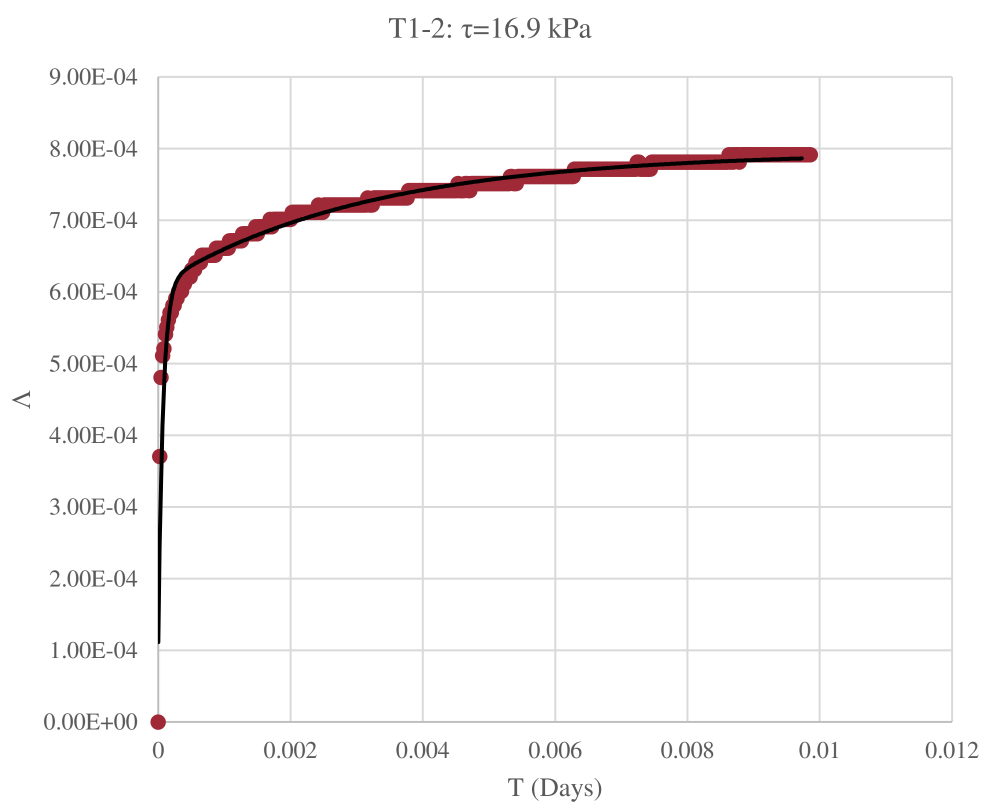
T1-2: τ=16.9 kPa
9.00E-04
8.00E-04
7.00E-04
6.00E-04
5.00E-04
4.00E-04
3.00E-04
2.00E-04
1.00E-04
0.00E+00
Λ
0
0.002
0.004
0.006
0.008
0.01
0.012
T (Days)

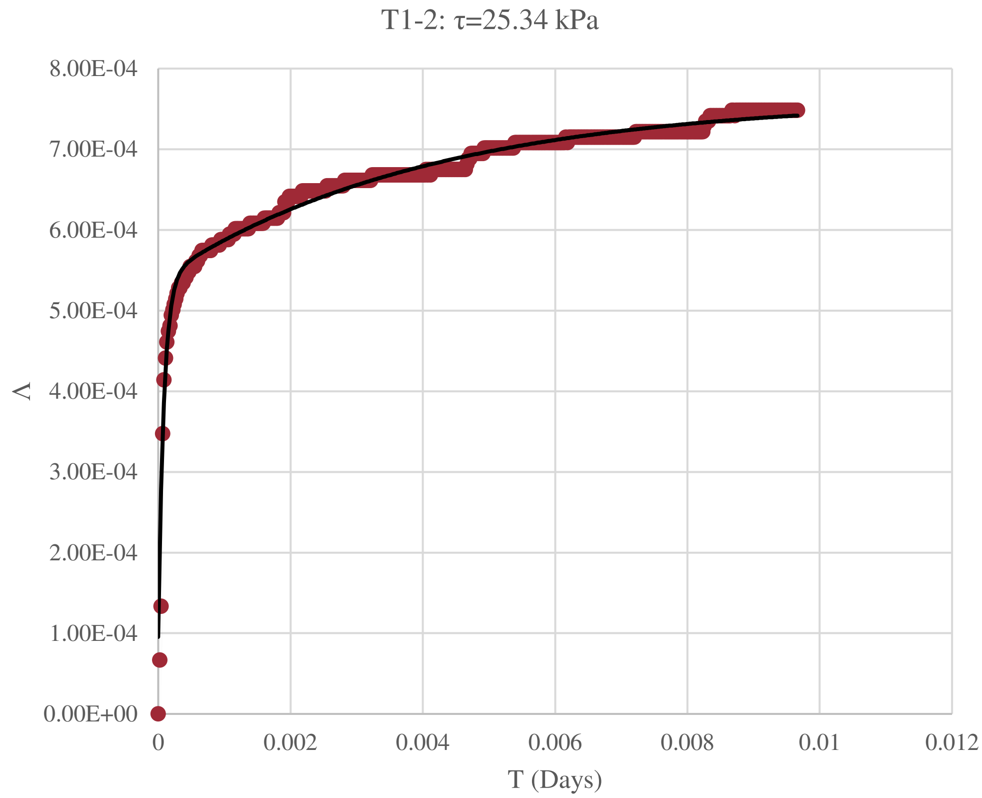
T1-2: τ=25.34 kPa
8.00E-04
7.00E-04
6.00E-04
5.00E-04
4.00E-04
3.00E-04
2.00E-04
1.00E-04
0.00E+00
Λ
0
0.002
0.004
0.006
0.008
0.01
0.012
T (Days)

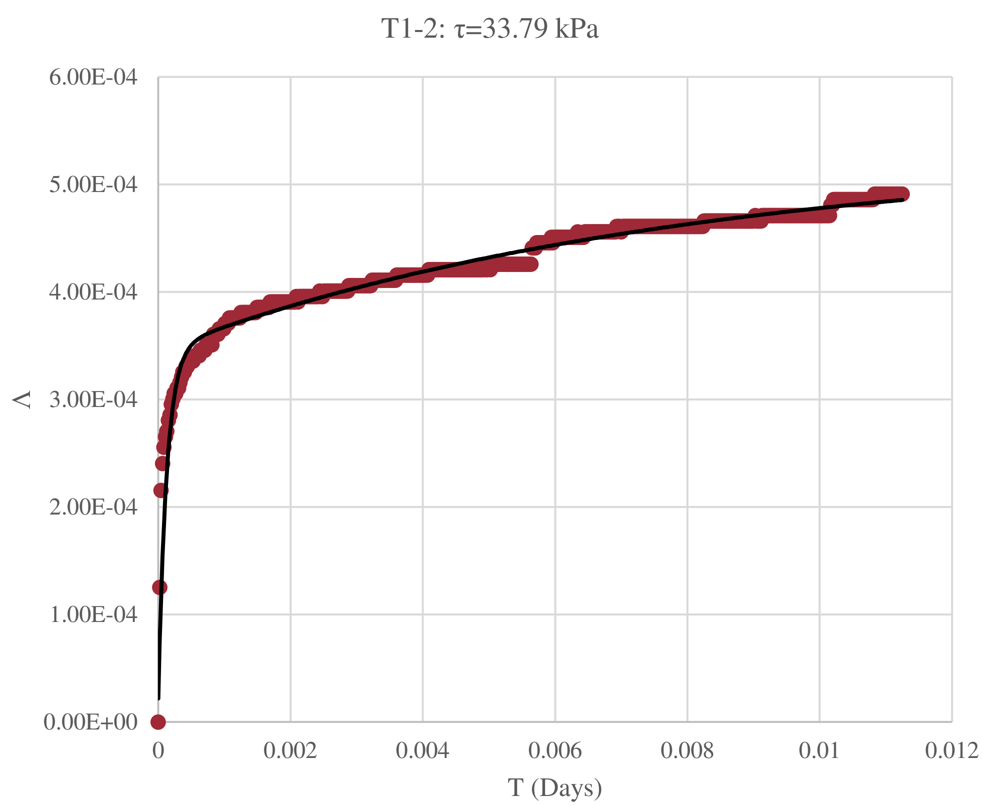
T1-2: τ=33.79 kPa
6.00E-04
5.00E-04
4.00E-04
3.00E-04
2.00E-04
1.00E-04
0.00E+00
Λ
0
0.002
0.004
0.006
0.008
0.01
0.012
T (Days)

T1-2: τ=42.24 kPa

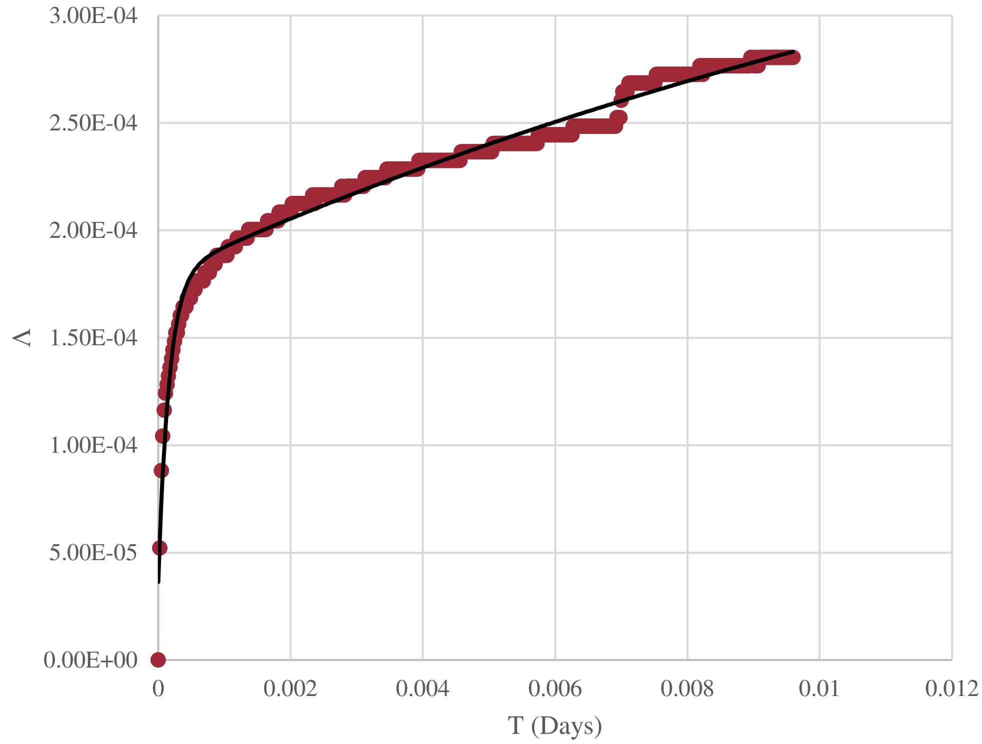

T1-2: τ=50.96 kPa

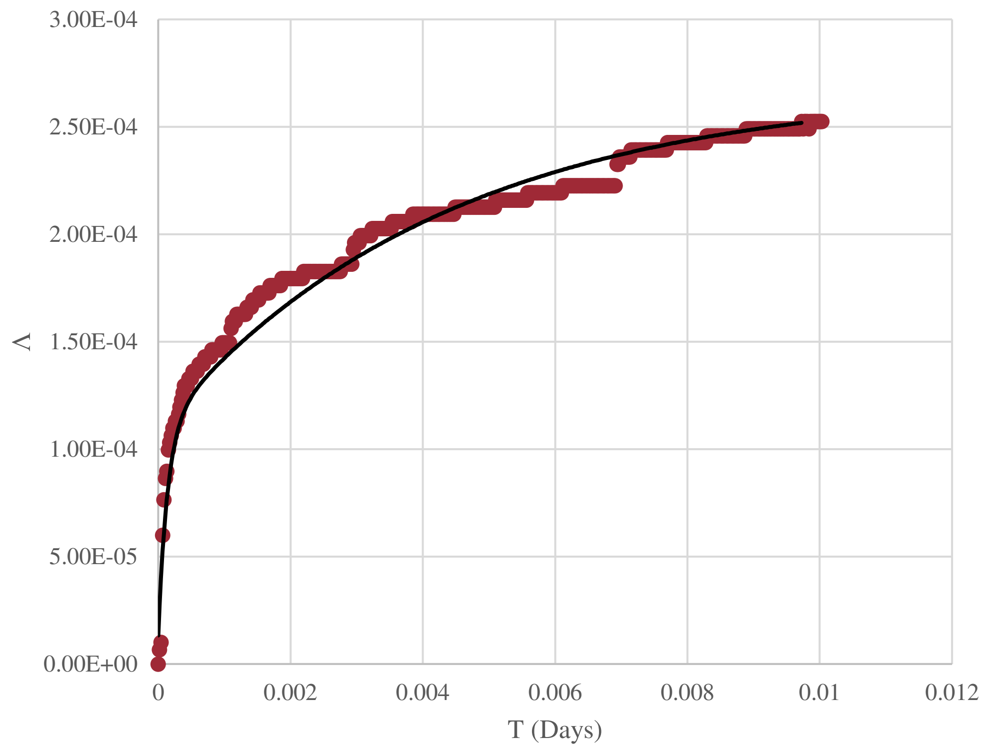

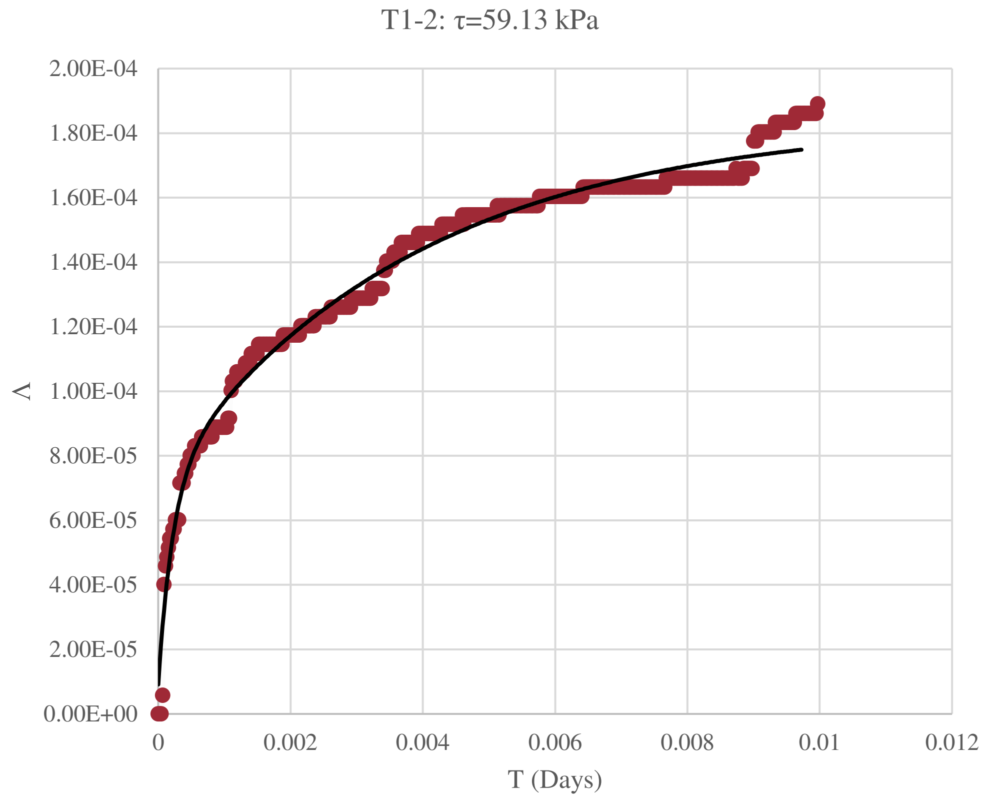
T1-2: τ=59.13 kPa
2.00E-04
1.80E-04
1.60E-04
1.40E-04
1.20E-04
1.00E-04
8.00E-05
6.00E-05
4.00E-05
2.00E-05
0.00E+00
Λ
0
0.002
0.004
0.006
0.008
0.01
0.012
T (Days)

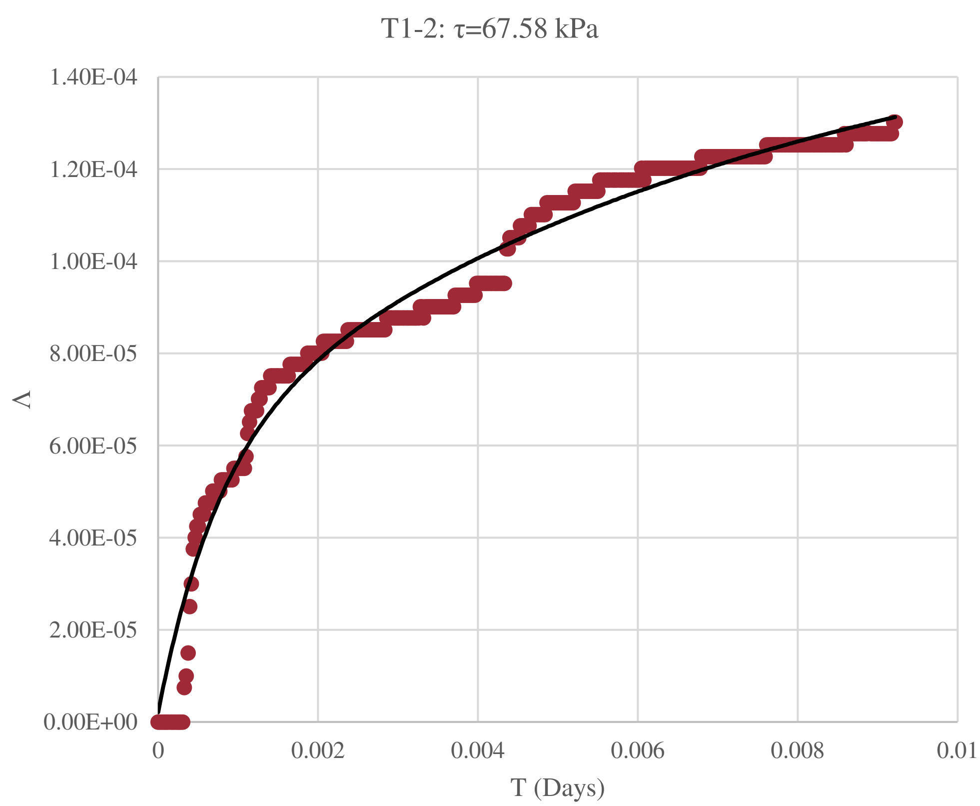
T1-2: τ=67.58 kPa
1.40E-04
1.20E-04
1.00E-04
8.00E-05
6.00E-05
4.00E-05
2.00E-05
0.00E+00
Λ
0
0.002
0.004
0.006
0.008
0.01
T (Days)

T1-2: τ=76.03 kPa

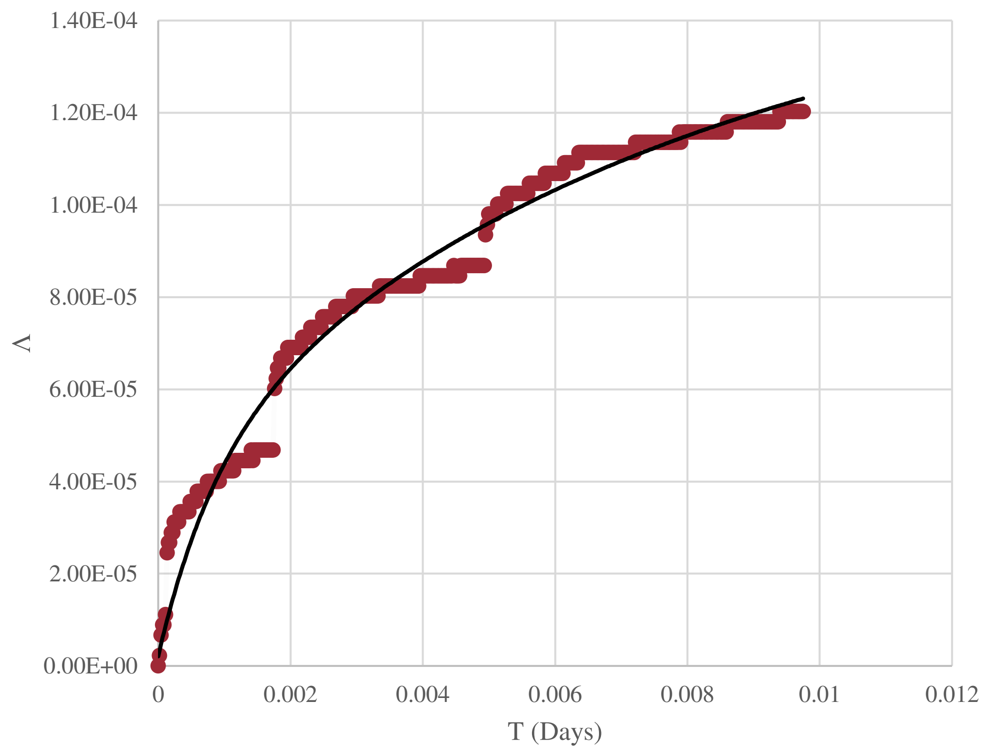

T1-2: τ=84.48 kPa

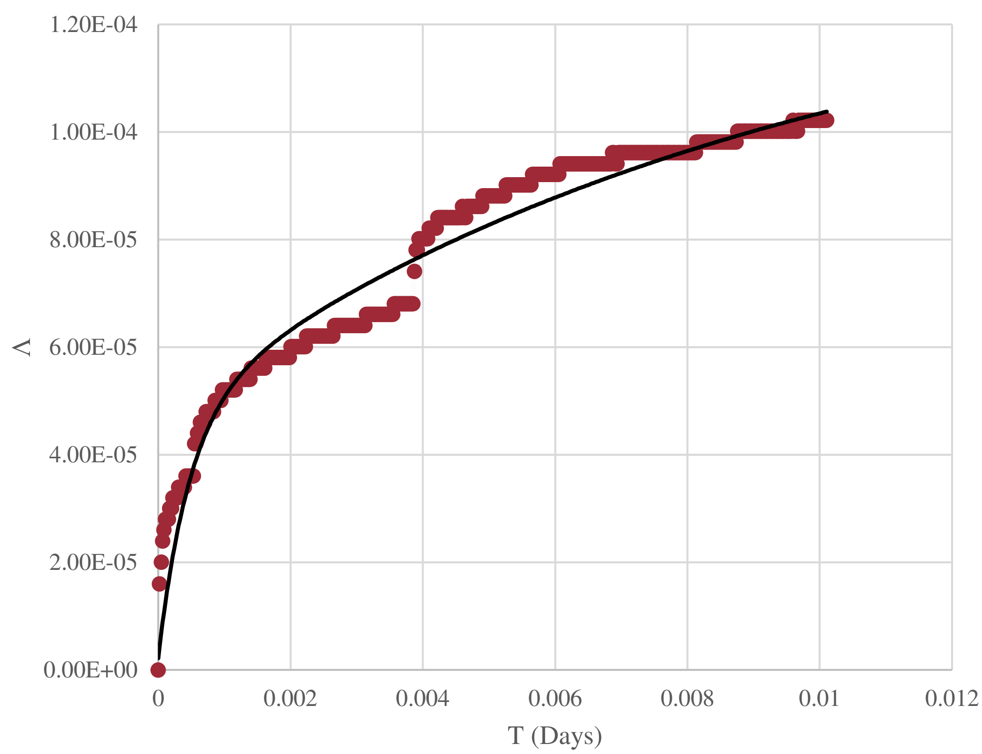

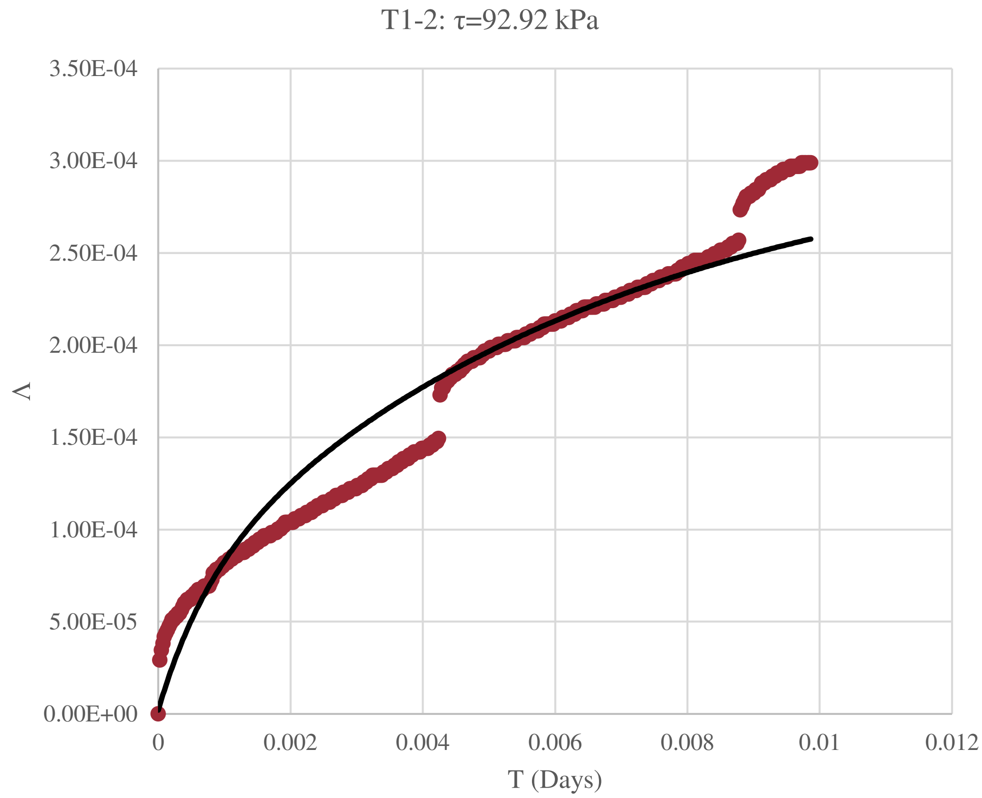

7.1.3 T1-3

Table 12: Optimized model parameters for T1-3

T1-3: Peel strength = 2170 N/m						
τ (kPa)	CSR-N	G_{Di} (kPa)	G_{D1} (kPa)	G_{D2} (kPa)	R_1 (d)	R_2 (d)
8.45	N/A	18130	10348	4470	2.48E-04	1.43E-02
16.9	N/A	7545	3003	5173	2.86E-04	1.12E-02
25.34	N/A	7586	7526	5356	2.86E-04	1.12E-02
33.79	N/A	1192544	8660	8430	1.07E-04	6.83E-03
42.24	N/A	1191784	7905	7996	1.07E-04	6.63E-03
50.96	N/A	1198403	15429	7510	4.17E-04	1.55E-02
59.13	N/A	1195893	12958	6806	4.14E-04	1.43E-02
67.58	N/A	1822129	19586	3186	7.68E-04	4.52E-02
76.03	N/A	3249739	24865	3152	3.10E-04	4.76E-02
84.48	N/A	1822129	19586	3186	7.68E-04	4.52E-02
92.92	N/A	271952	116467	15442	1.90E-03	1.19E-02

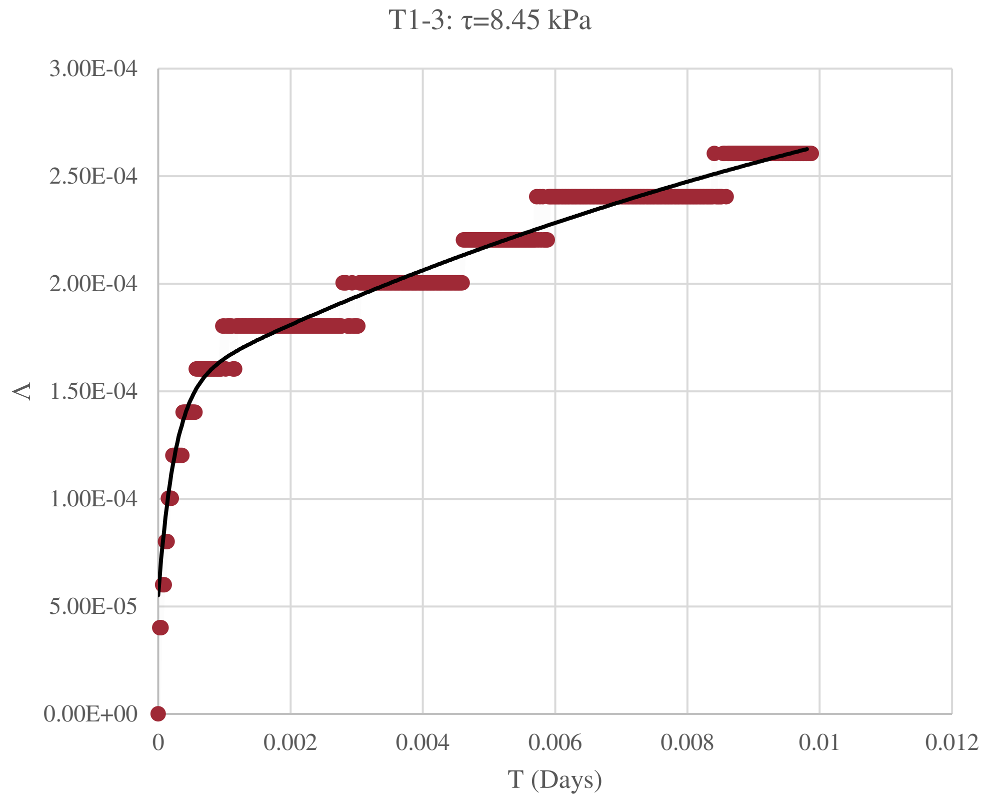
T1-3: τ=8.45 kPa
3.00E-04
2.50E-04
2.00E-04
1.50E-04
1.00E-04
5.00E-05
0.00E+00
Λ
0
0.002
0.004
0.006
0.008
0.01
0.012
T (Days)

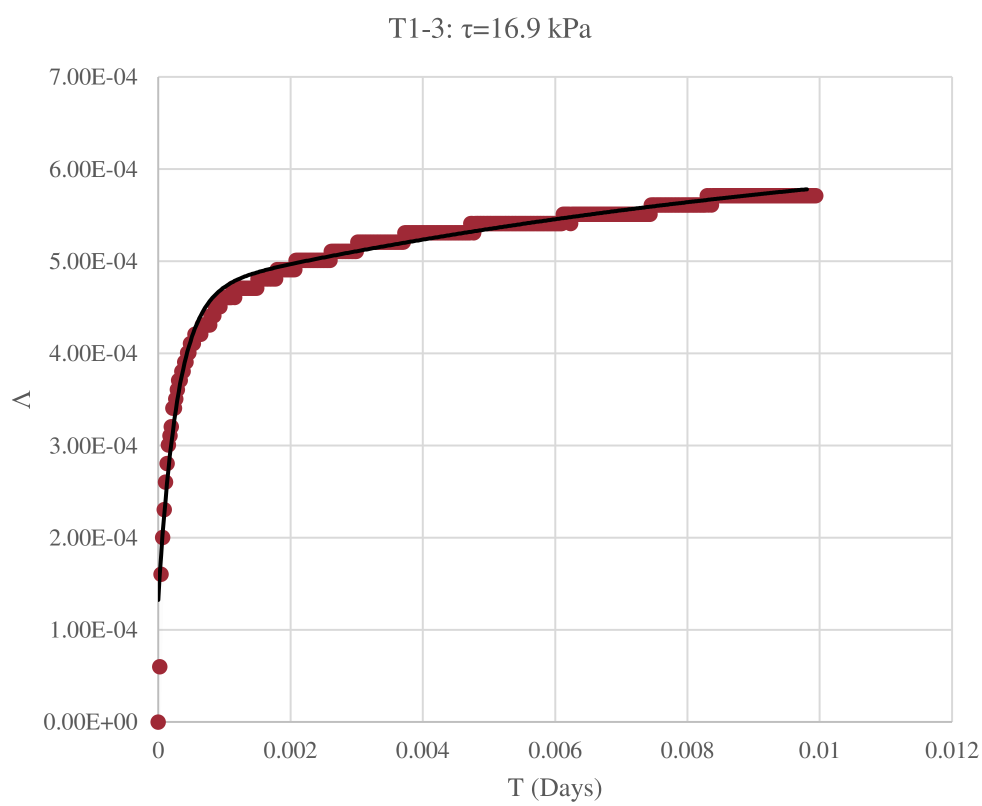
T1-3: τ=16.9 kPa
7.00E-04
6.00E-04
5.00E-04
4.00E-04
3.00E-04
2.00E-04
1.00E-04
0.00E+00
Λ
0
0.002
0.004
0.006
0.008
0.01
0.012
T (Days)

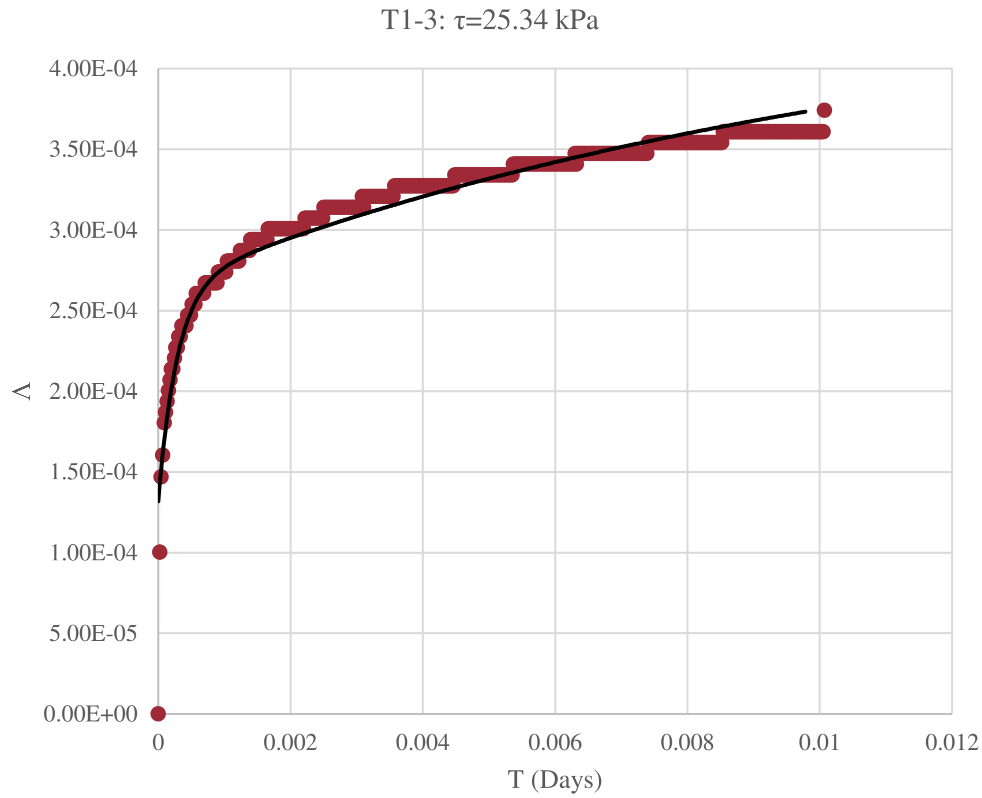

T1-3: τ=25.34 kPa
4.00E-04
3.50E-04
3.00E-04
2.50E-04
2.00E-04
1.50E-04
1.00E-04
5.00E-05
0.00E+00
Λ
0
0.002
0.004
0.006
0.008
0.01
0.012
T (Days)

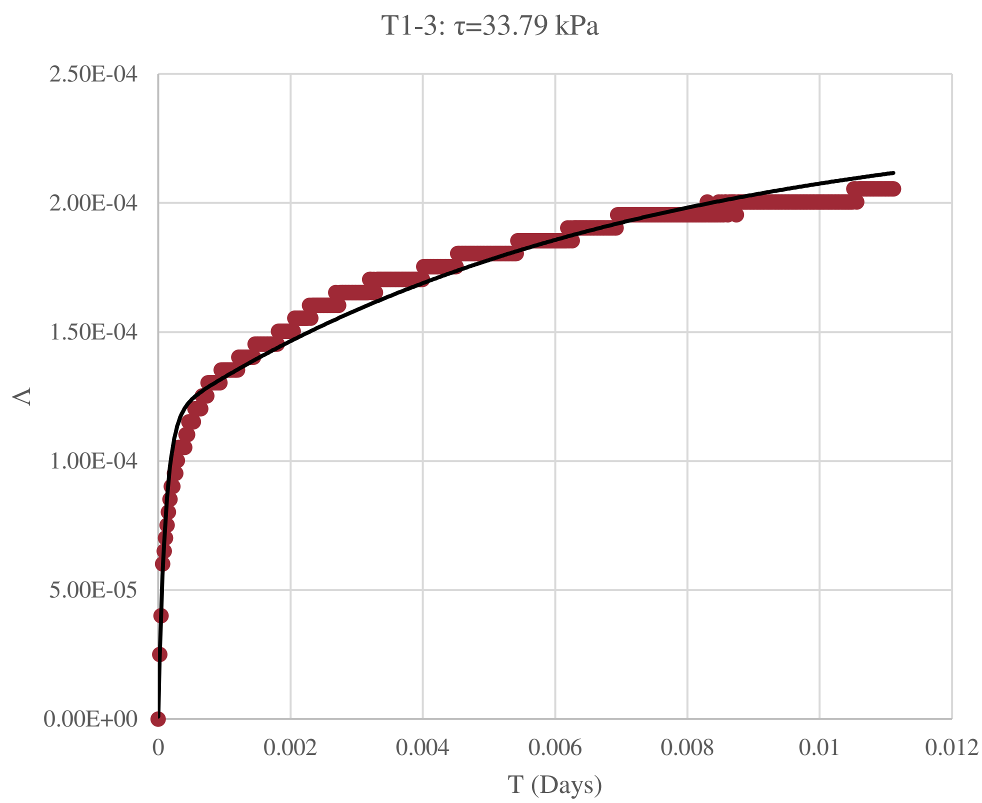

T1-3: τ=33.79 kPa
2.50E-04
2.00E-04
1.50E-04
1.00E-04
5.00E-05
0.00E+00
Λ
0
0.002
0.004
0.006
0.008
0.01
0.012
T (Days)

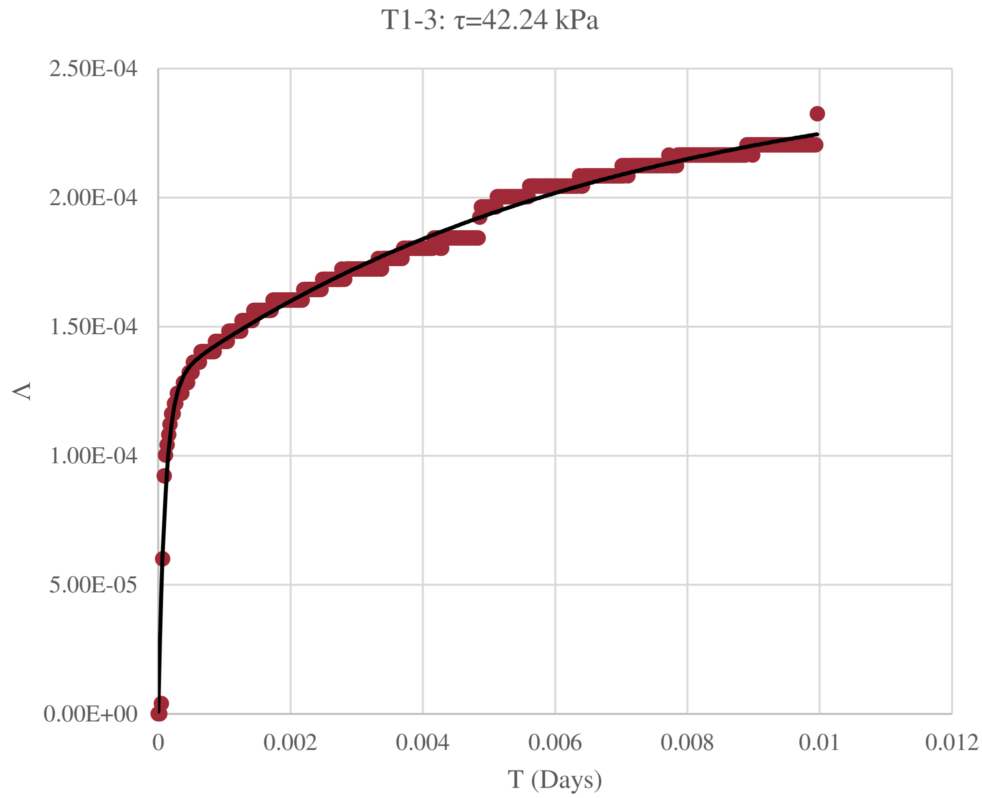
T1-3: τ=42.24 kPa
2.50E-04
2.00E-04
1.50E-04
1.00E-04
5.00E-05
0.00E+00
Λ
0
0.002
0.004
0.006
0.008
0.01
0.012
T (Days)

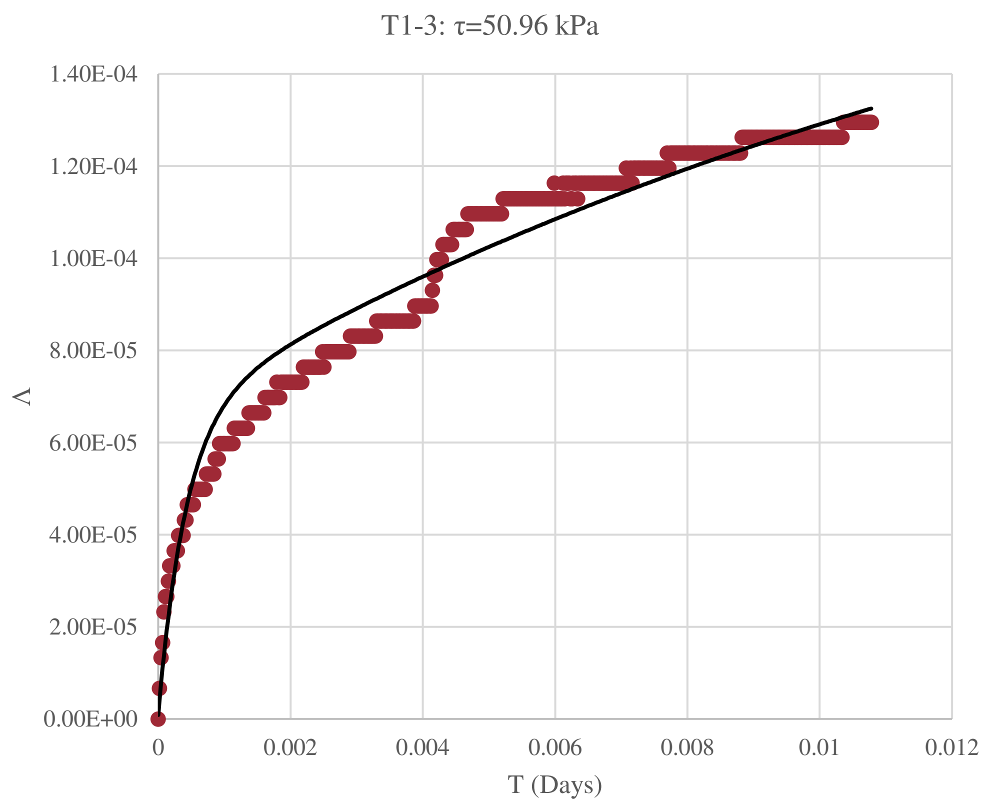
T1-3: τ=50.96 kPa
1.40E-04
1.20E-04
1.00E-04
8.00E-05
6.00E-05
4.00E-05
2.00E-05
0.00E+00
Λ
0
0.002
0.004
0.006
0.008
0.01
0.012
T (Days)

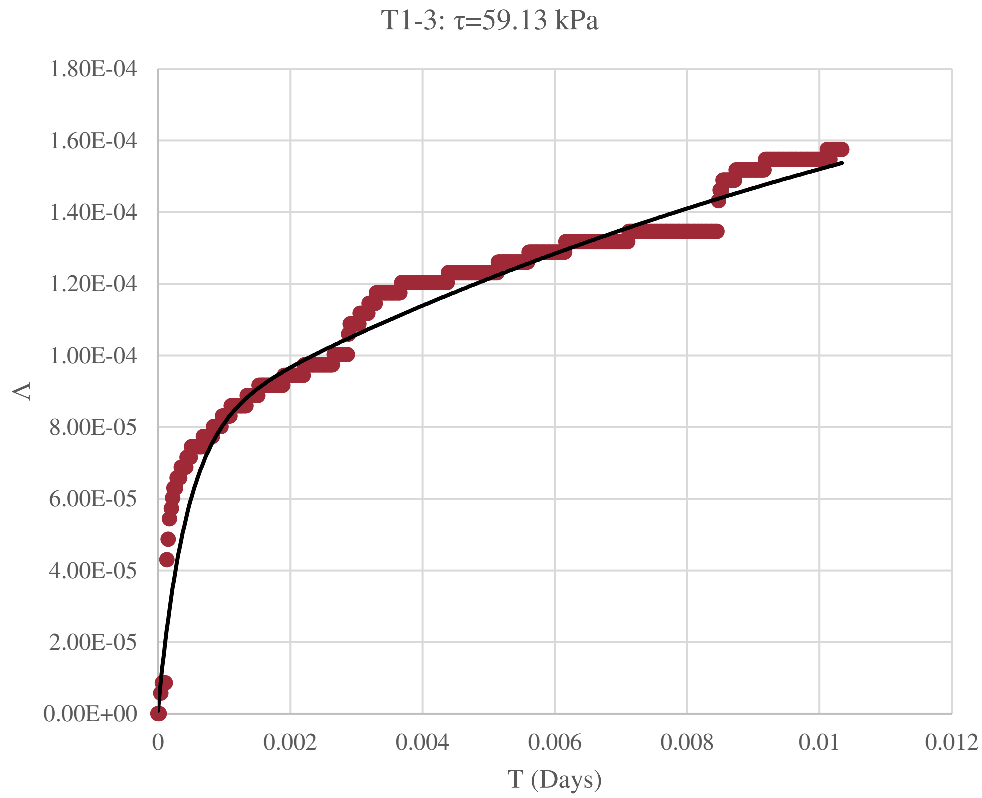
T1-3: τ=59.13 kPa
1.80E-04
1.60E-04
1.40E-04
1.20E-04
1.00E-04
8.00E-05
6.00E-05
4.00E-05
2.00E-05
0.00E+00
Λ
0
0.002
0.004
0.006
0.008
0.01
0.012
T (Days)

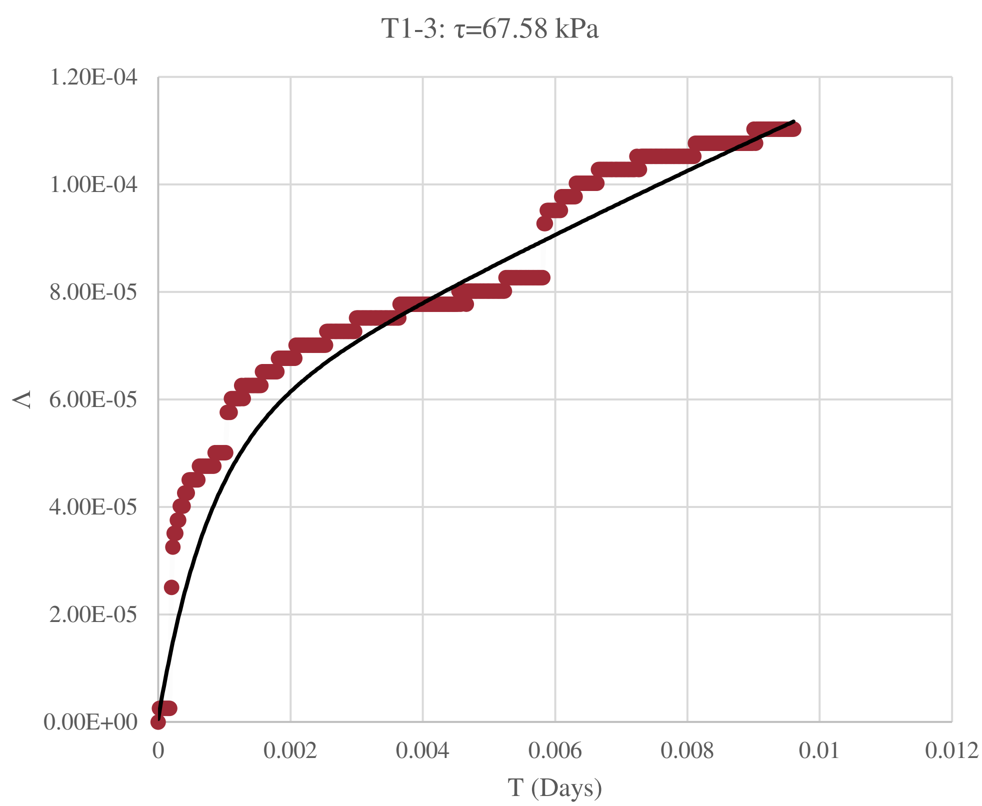
T1-3: τ=67.58 kPa
1.20E-04
1.00E-04
8.00E-05
6.00E-05
4.00E-05
2.00E-05
0.00E+00
Λ
0
0.002
0.004
0.006
0.008
0.01
0.012
T (Days)

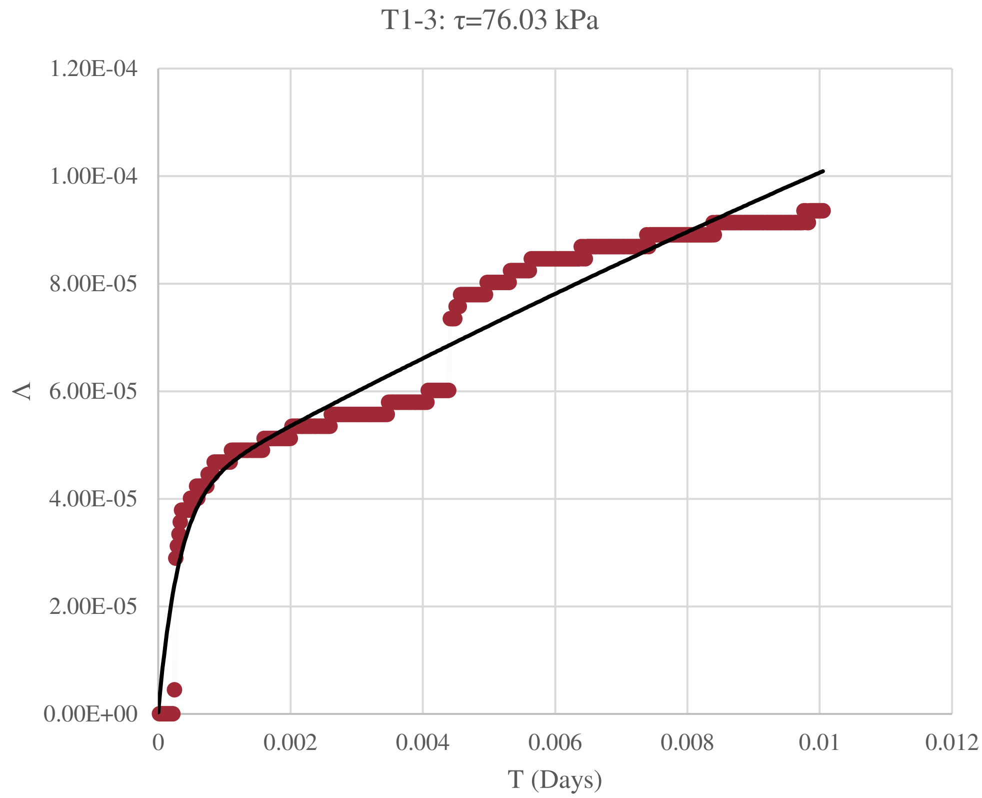

T1-3: τ=76.03 kPa
1.20E-04
1.00E-04
8.00E-05
6.00E-05
4.00E-05
2.00E-05
0.00E+00
Λ
0
0.002
0.004
0.006
0.008
0.01
0.012
T (Days)

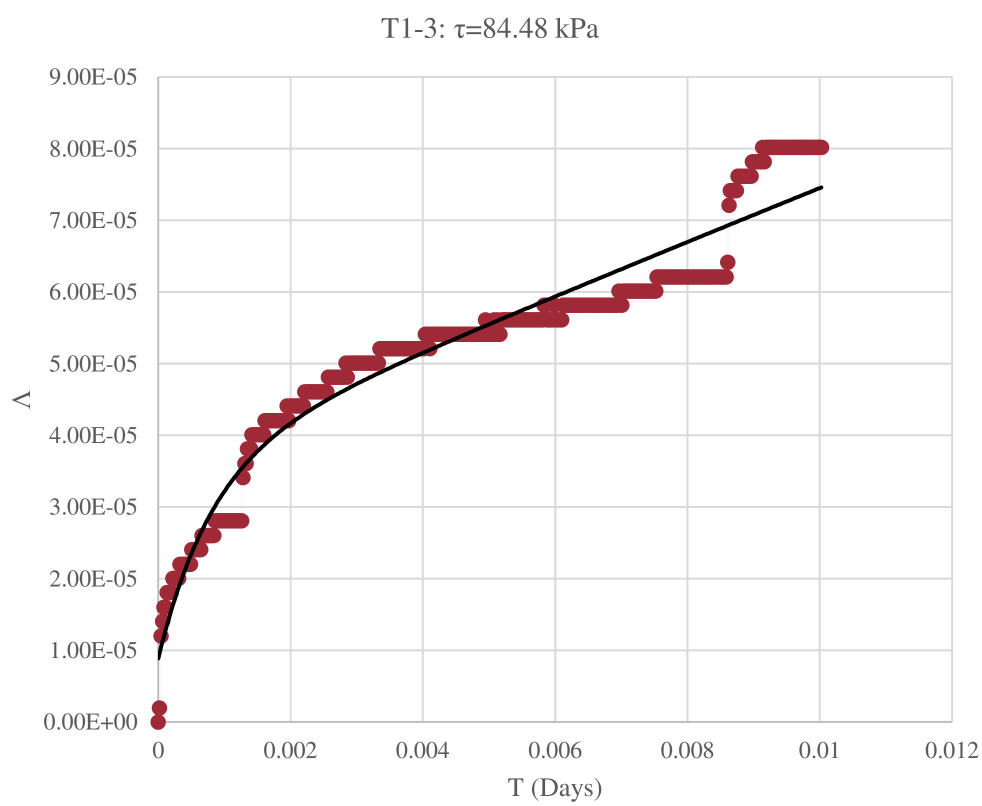

T1-3: τ=84.48 kPa
9.00E-05
8.00E-05
7.00E-05
6.00E-05
5.00E-05
4.00E-05
3.00E-05
2.00E-05
1.00E-05
0.00E+00
Λ
0
0.002
0.004
0.006
0.008
0.01
0.012
T (Days)

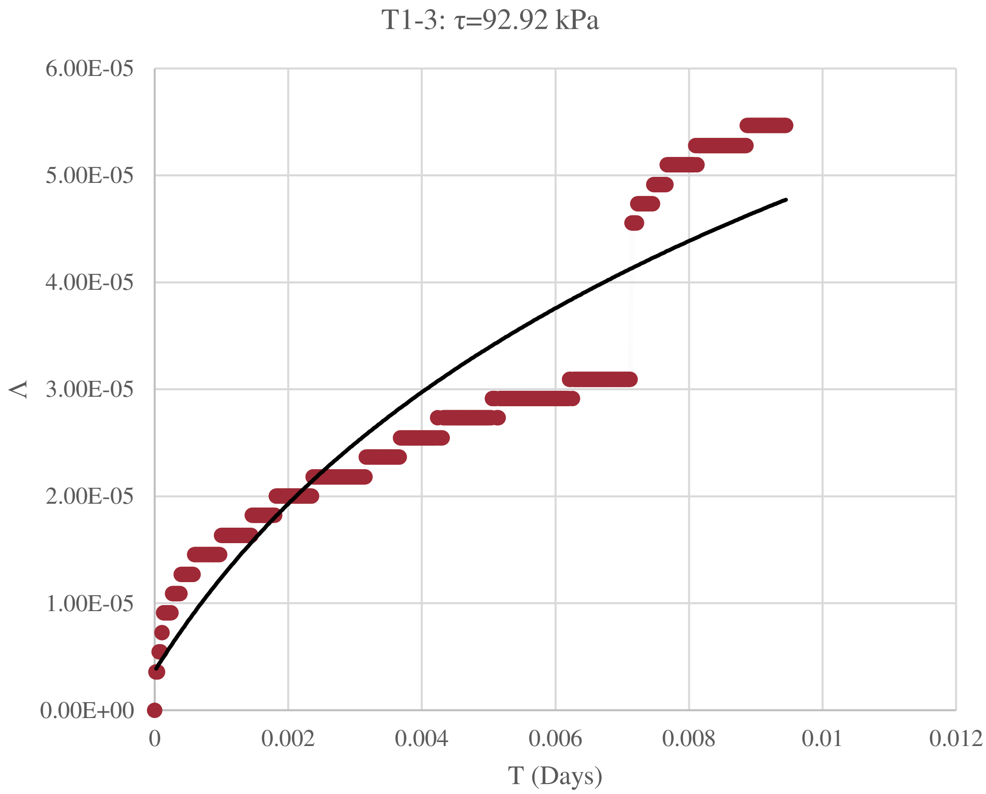

7.2 T2: Evaluation of Normal Stress

- RLS tests were conducted on a NHT NP GCl at a normal stress of 20, 40, and 60 kPa.
- Graph titles consist of a test series identifier (e.g. T2-1) and load increment shear stress (e.g. τ=8.45 kPa).

7.2.1 T2-1

T2-1: Normal Stress = 20 kPa						
τ (kPa)	CSR-N	G_{Di} (kPa)	G_{D1} (kPa)	G_{D2} (kPa)	R_1 (d)	R_2 (d)
8.45	0.2	8973	5940	8437	9.54E-05	4.17E-03
16.9	0.2	7096	4953	4816	3.52E-04	5.18E-03
25.34	0.54	9601	4060	7680	3.52E-04	5.18E-03
33.79	0.65	8030	3859	6308	2.30E-04	3.65E-03
42.24	0.74	10759	6200	7816	2.33E-04	4.05E-03
50.96	0.82	22058	8553	6431	4.18E-04	6.11E-03
59.13	0.89	43774	15395	6459	6.33E-04	7.52E-03
67.58	0.94	43774	18690	4179	2.75E-04	7.83E-03
76.03	0.97	46308	19871	3622	2.96E-04	7.05E-03

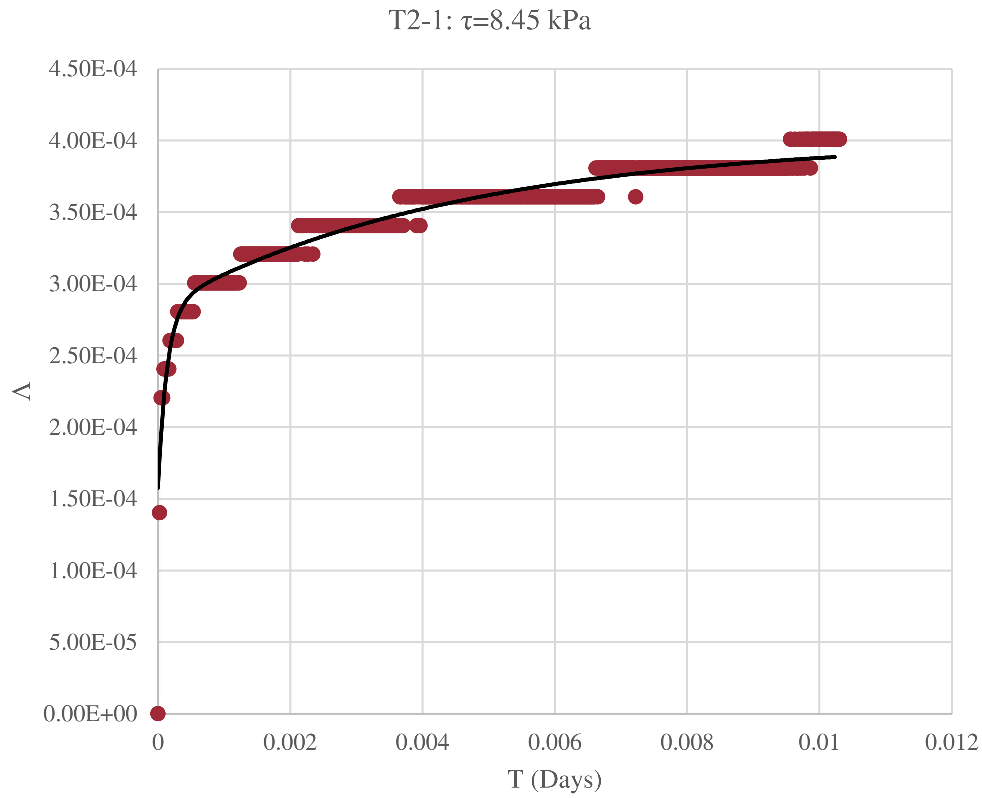
T2-1: τ=8.45 kPa
4.50E-04
4.00E-04
3.50E-04
3.00E-04
2.50E-04
2.00E-04
1.50E-04
1.00E-04
5.00E-05
0.00E+00
Λ
0
0.002
0.004
0.006
0.008
0.01
0.012
T (Days)

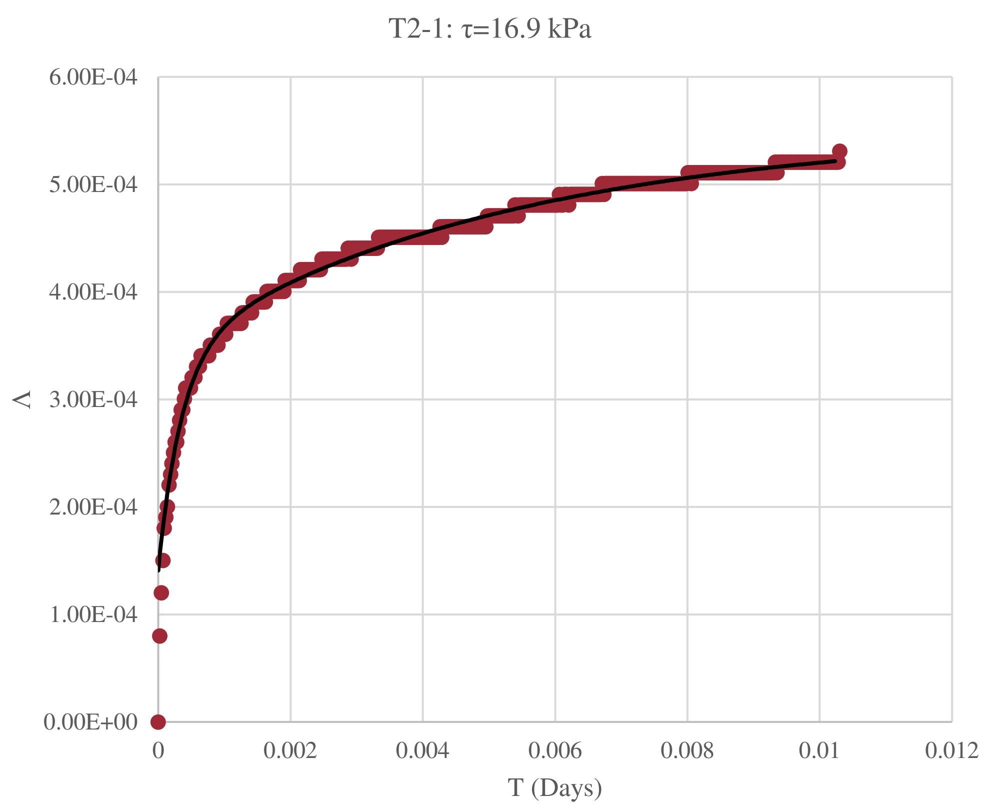
T2-1: τ=16.9 kPa
6.00E-04
5.00E-04
4.00E-04
3.00E-04
2.00E-04
1.00E-04
0.00E+00
Λ
0
0.002
0.004
0.006
0.008
0.01
0.012
T (Days)

T2-1: τ=25.34 kPa

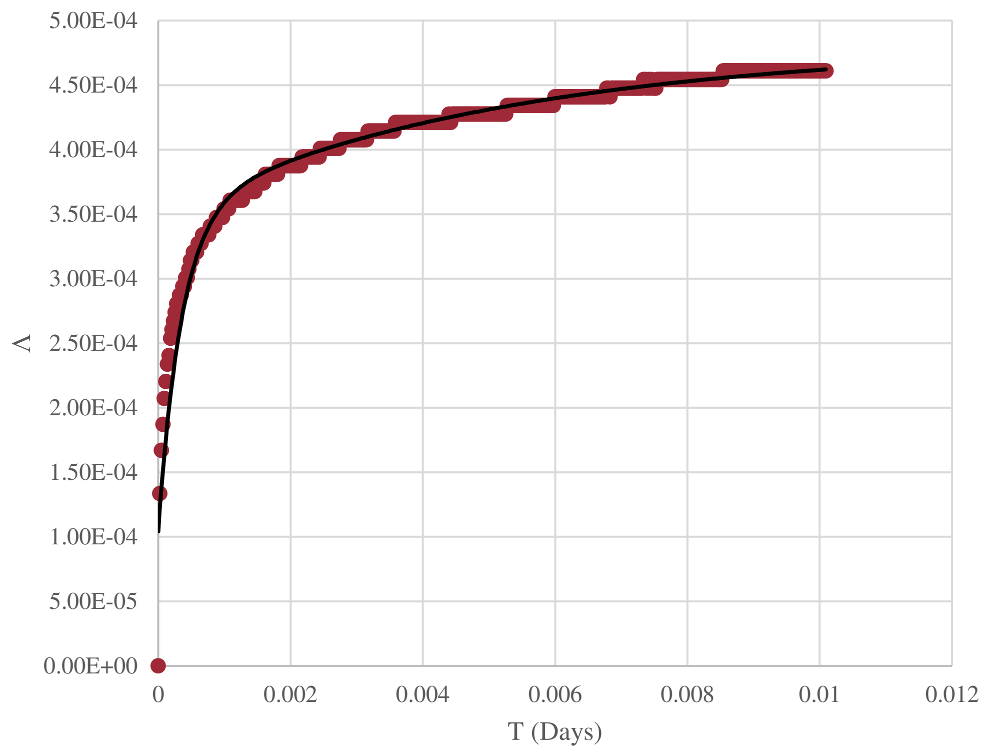

T2-1: τ=33.79 kPa

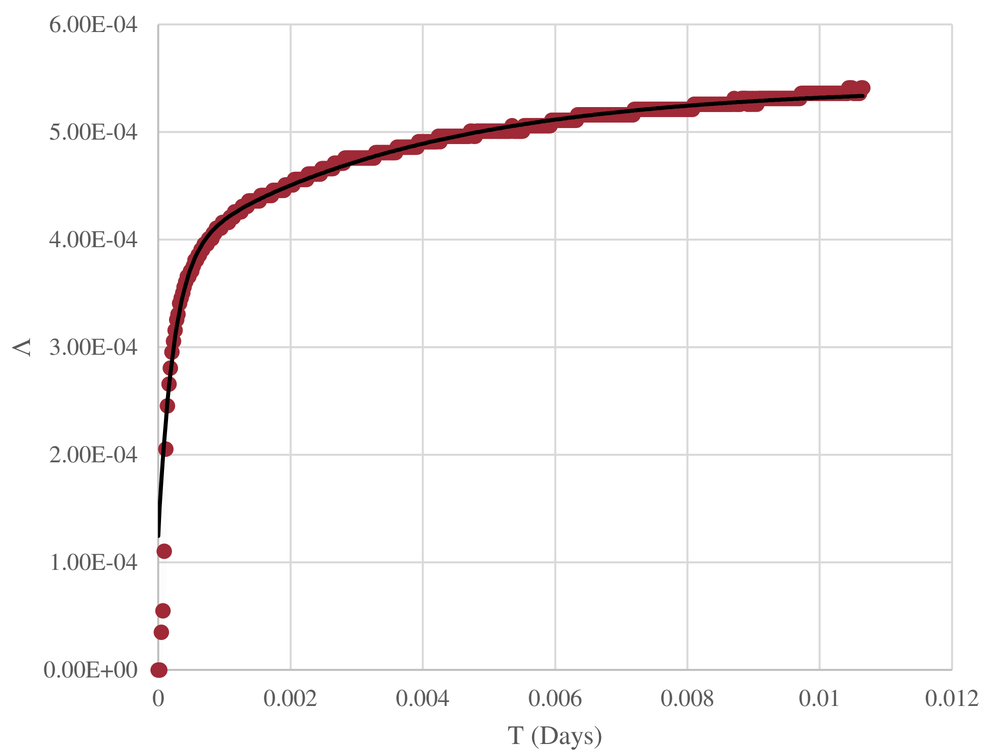

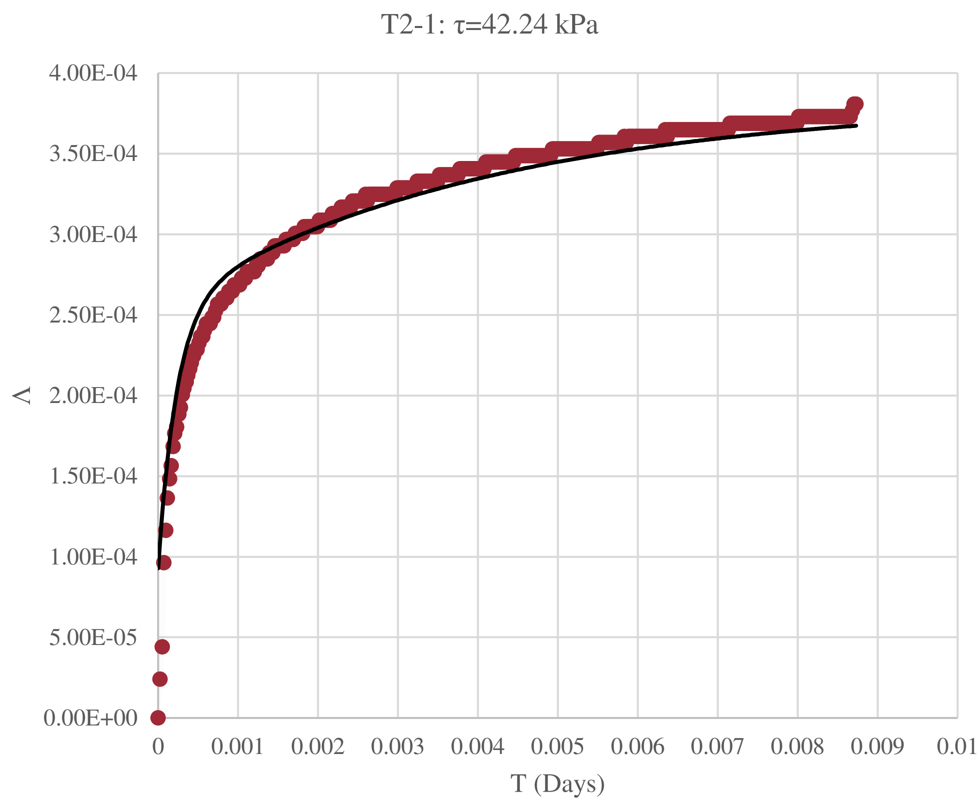
T2-1: τ=42.24 kPa
4.00E-04
3.50E-04
3.00E-04
2.50E-04
2.00E-04
1.50E-04
1.00E-04
5.00E-05
0.00E+00
Λ
0
0.001
0.002
0.003
0.004
0.005
0.006
0.007
0.008
0.009
0.01
T (Days)

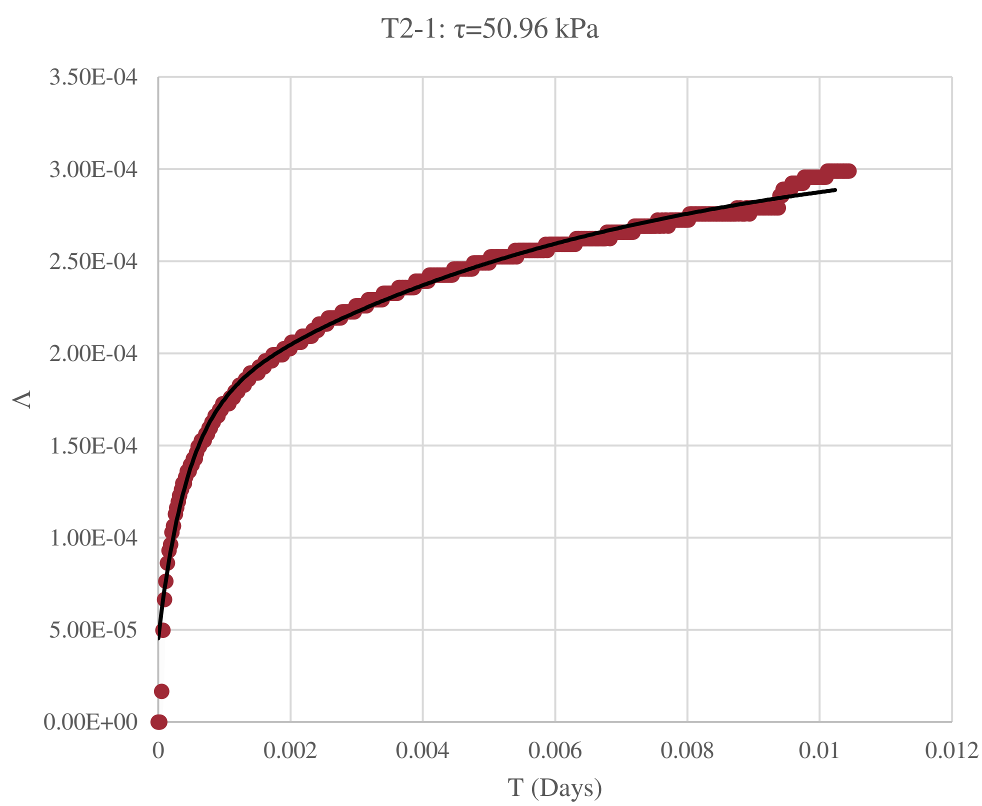
T2-1: τ=50.96 kPa
3.50E-04
3.00E-04
2.50E-04
2.00E-04
1.50E-04
1.00E-04
5.00E-05
0.00E+00
Λ
0
0.002
0.004
0.006
0.008
0.01
0.012
T (Days)

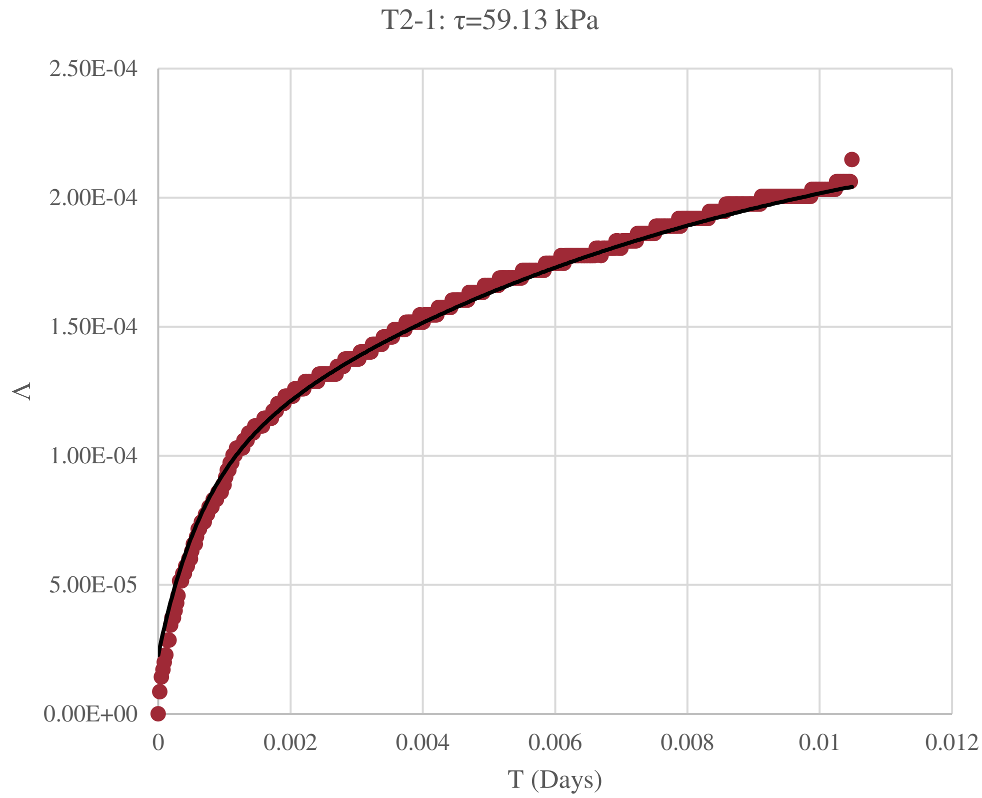
T2-1: τ=59.13 kPa
2.50E-04
2.00E-04
1.50E-04
1.00E-04
5.00E-05
0.00E+00
Λ
0
0.002
0.004
0.006
0.008
0.01
0.012
T (Days)

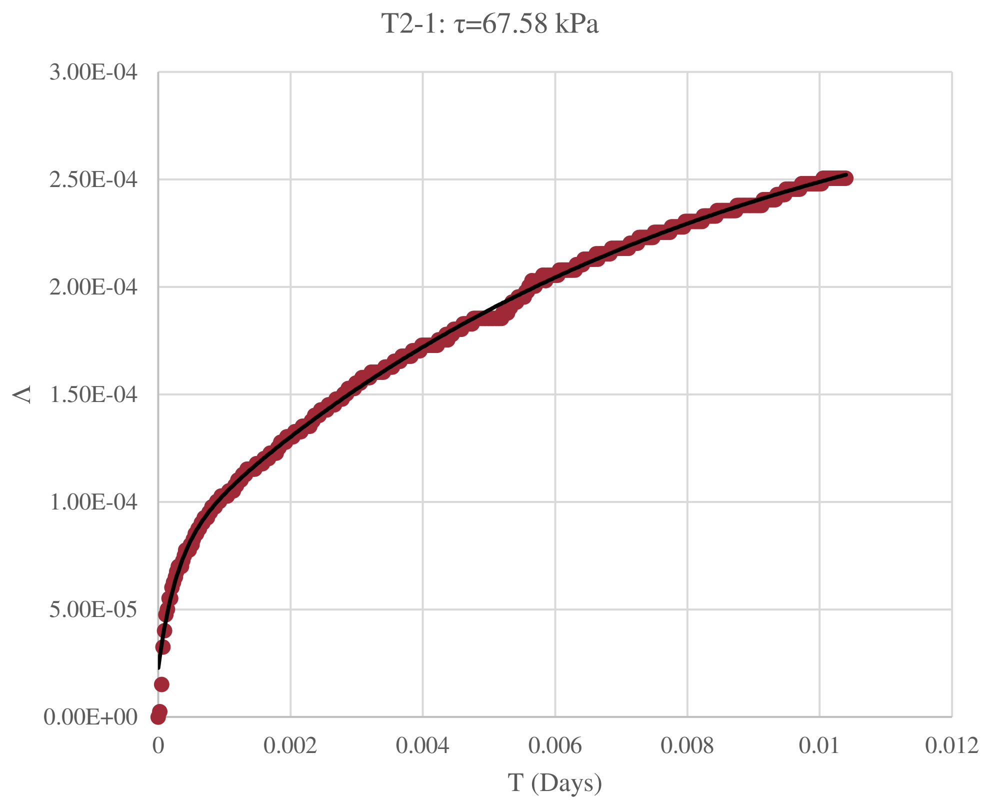
T2-1: τ=67.58 kPa
3.00E-04
2.50E-04
2.00E-04
1.50E-04
1.00E-04
5.00E-05
0.00E+00
Λ
0
0.002
0.004
0.006
0.008
0.01
0.012
T (Days)

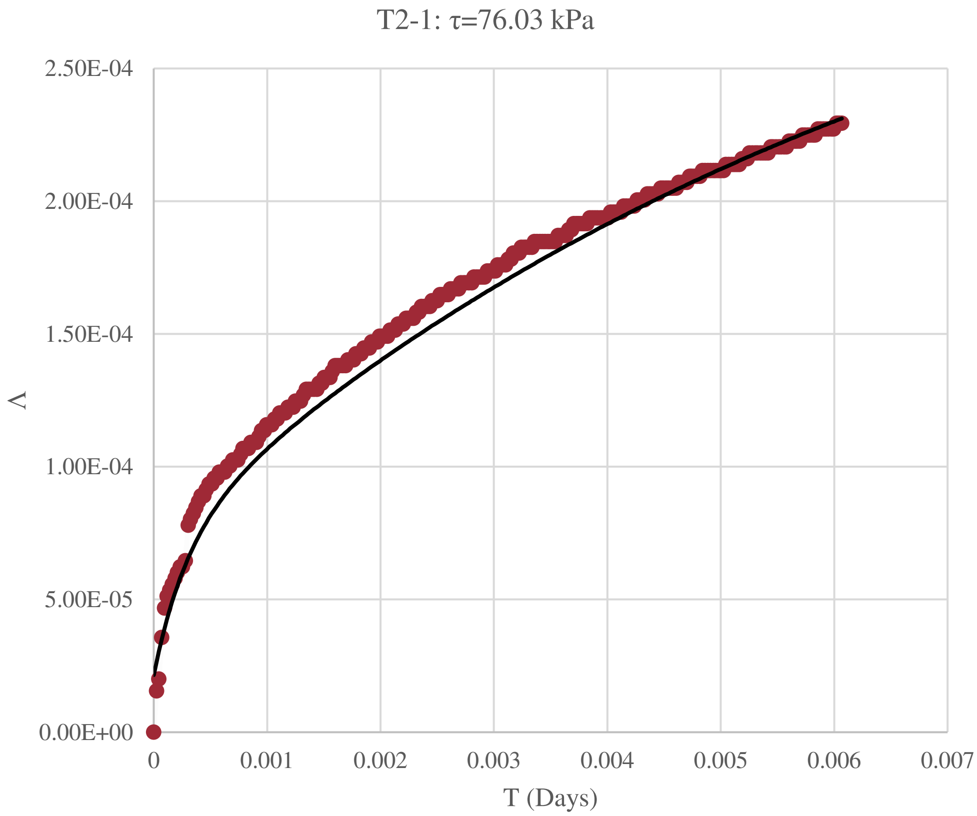

7.2.2 *T2-2*

T2-2: Normal Stress = 40 kPa						
τ (kPa)	CSR-N	G_{Di} (kPa)	G_{D1} (kPa)	G_{D2} (kPa)	R_1 (d)	R_2 (d)
8.45	0.14	74190	32715	64962	7.81E-03	1.16E-01
16.9	0.39	1264	2144	4080	4.00E-04	6.00E-03
25.34	0.42	3431	2062	8495	5.65E-04	9.40E-03
33.79	0.54	4539	4474	7089	2.37E-04	9.86E-03
42.24	0.64	11040	9108	5709	3.90E-04	5.90E-03
50.96	0.72	13974	12514	7257	3.94E-04	6.87E-03
59.13	0.79	39772	15546	6784	5.84E-04	7.25E-03
67.58	0.86	57701	15546	8079	5.84E-04	7.76E-03
76.03	0.92	79246	32366	6761	2.09E-04	4.36E-03

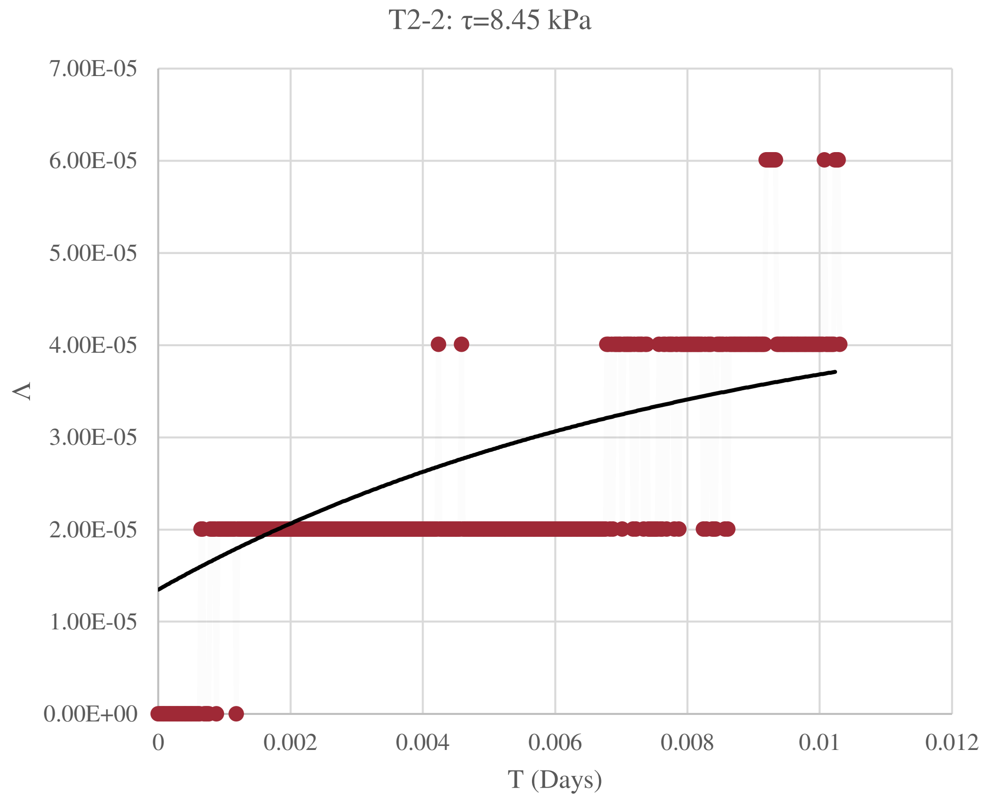
T2-2: τ=8.45 kPa
7.00E-05
6.00E-05
5.00E-05
4.00E-05
3.00E-05
2.00E-05
1.00E-05
0.00E+00
Λ
0
0.002
0.004
0.006
0.008
0.01
0.012
T (Days)

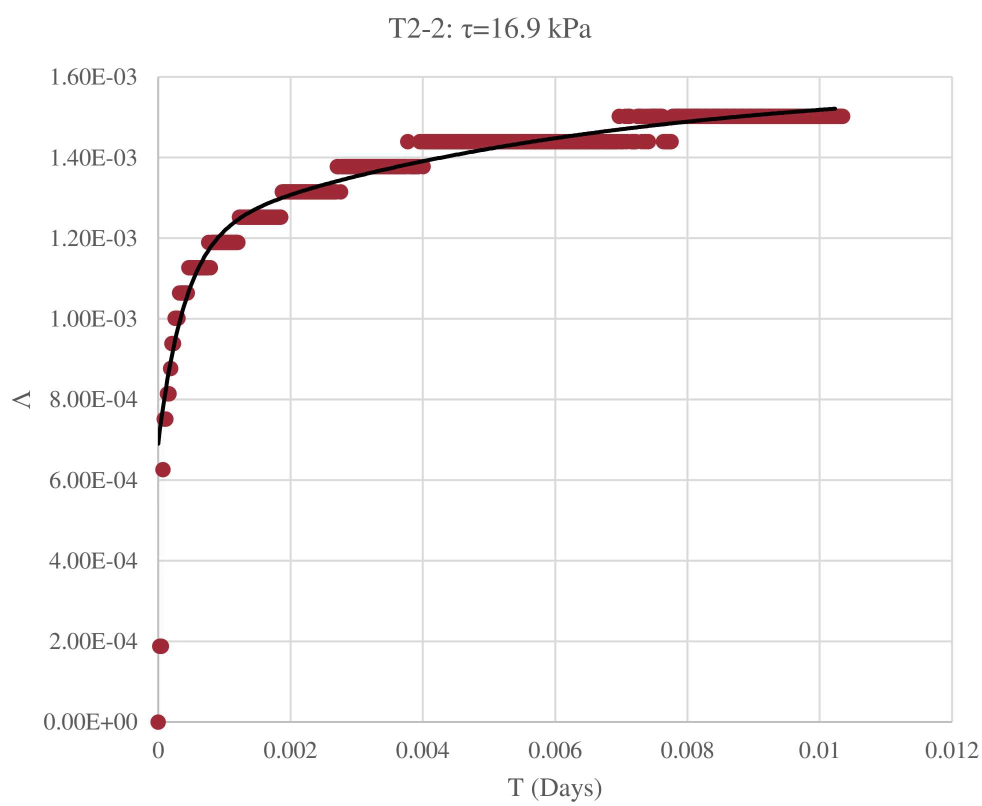
T2-2: τ=16.9 kPa
1.60E-03
1.40E-03
1.20E-03
1.00E-03
8.00E-04
6.00E-04
4.00E-04
2.00E-04
0.00E+00
Λ
0
0.002
0.004
0.006
0.008
0.01
0.012
T (Days)

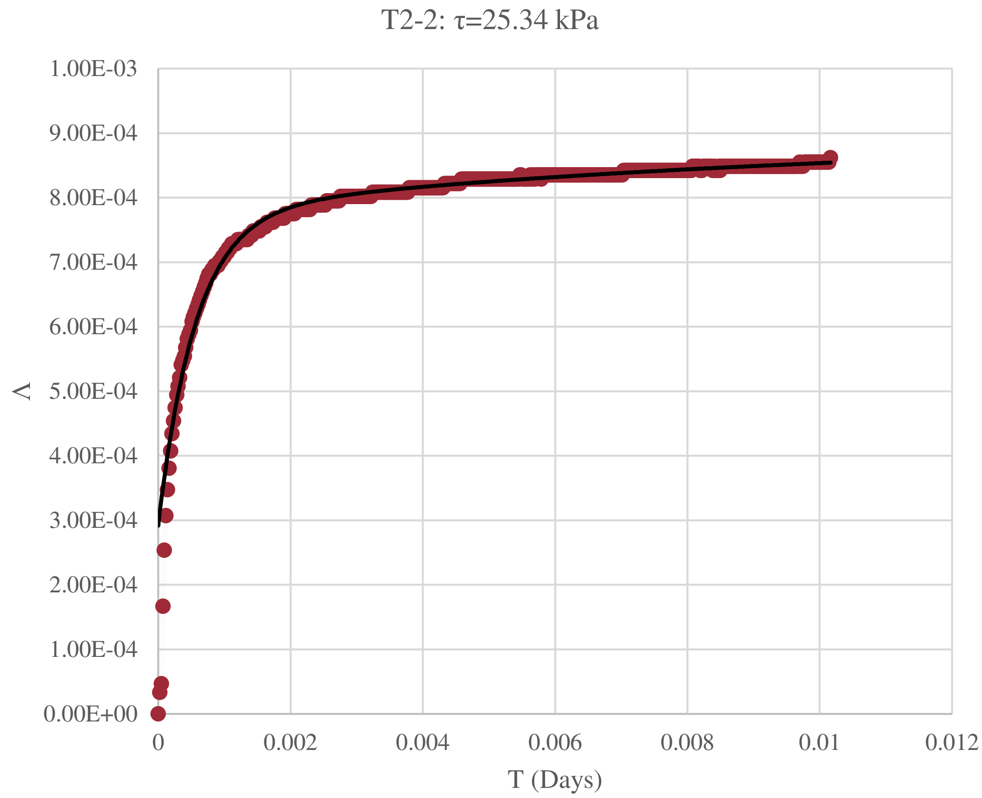
T2-2: τ=25.34 kPa
1.00E-03
9.00E-04
8.00E-04
7.00E-04
6.00E-04
5.00E-04
4.00E-04
3.00E-04
2.00E-04
1.00E-04
0.00E+00
Λ
0
0.002
0.004
0.006
0.008
0.01
0.012
T (Days)

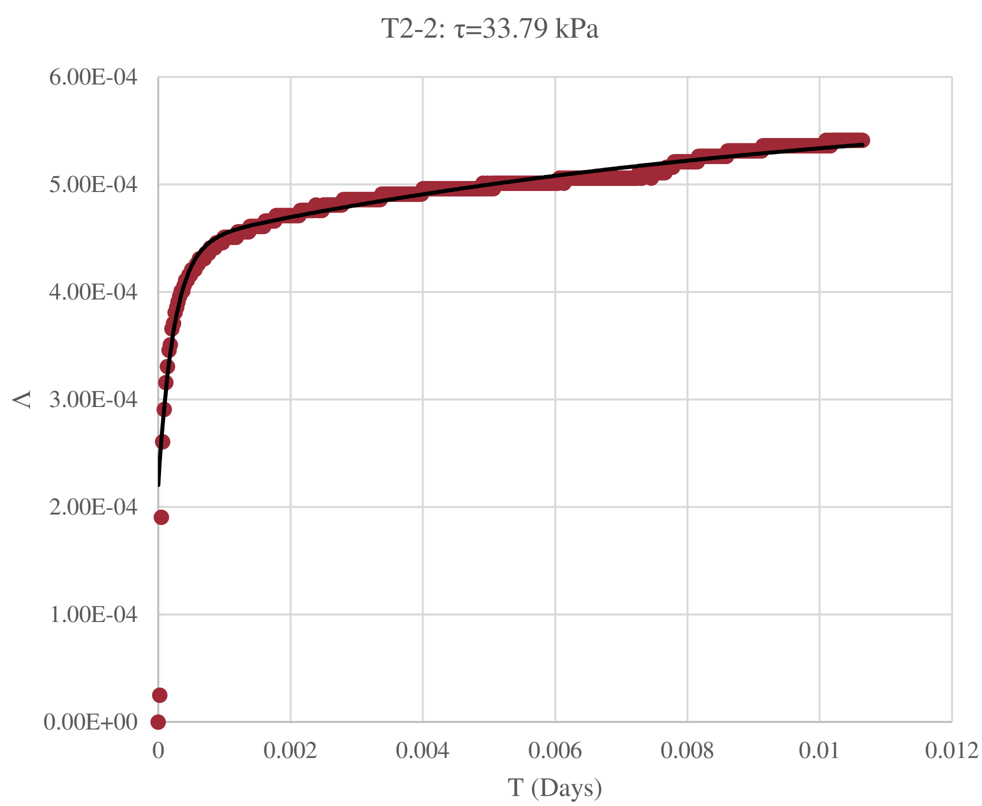
T2-2: τ=33.79 kPa
6.00E-04
5.00E-04
4.00E-04
3.00E-04
2.00E-04
1.00E-04
0.00E+00
Λ
0
0.002
0.004
0.006
0.008
0.01
0.012
T (Days)

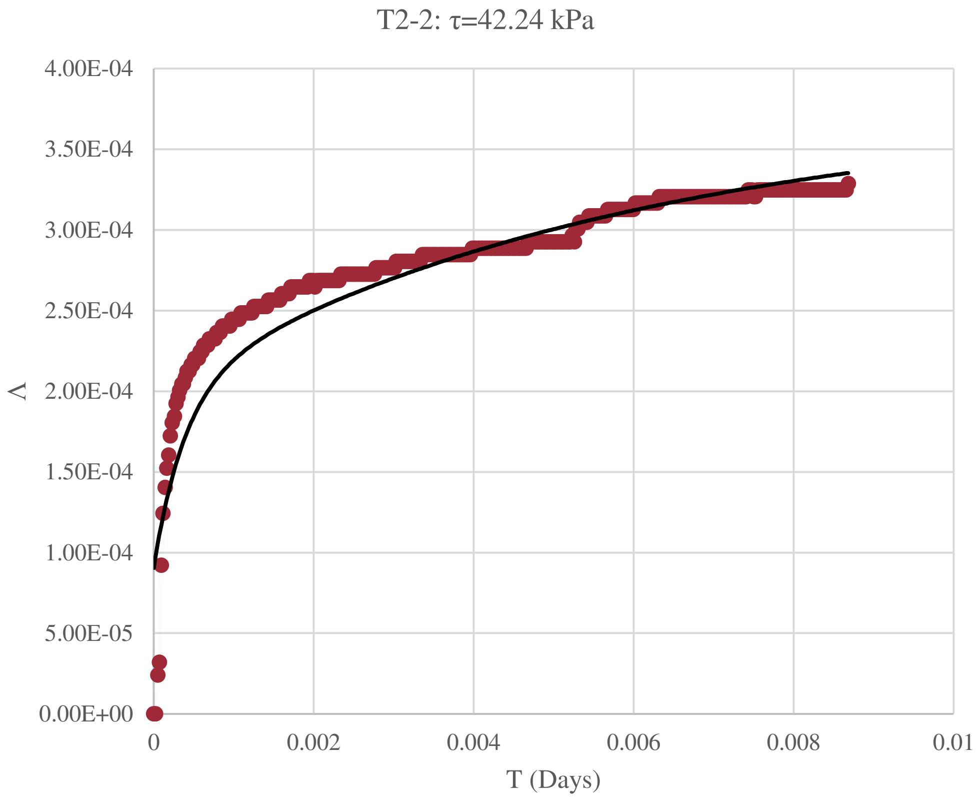
T2-2: τ=42.24 kPa
4.00E-04
3.50E-04
3.00E-04
2.50E-04
2.00E-04
1.50E-04
1.00E-04
5.00E-05
0.00E+00
Λ
0
0.002
0.004
0.006
0.008
0.01
T (Days)

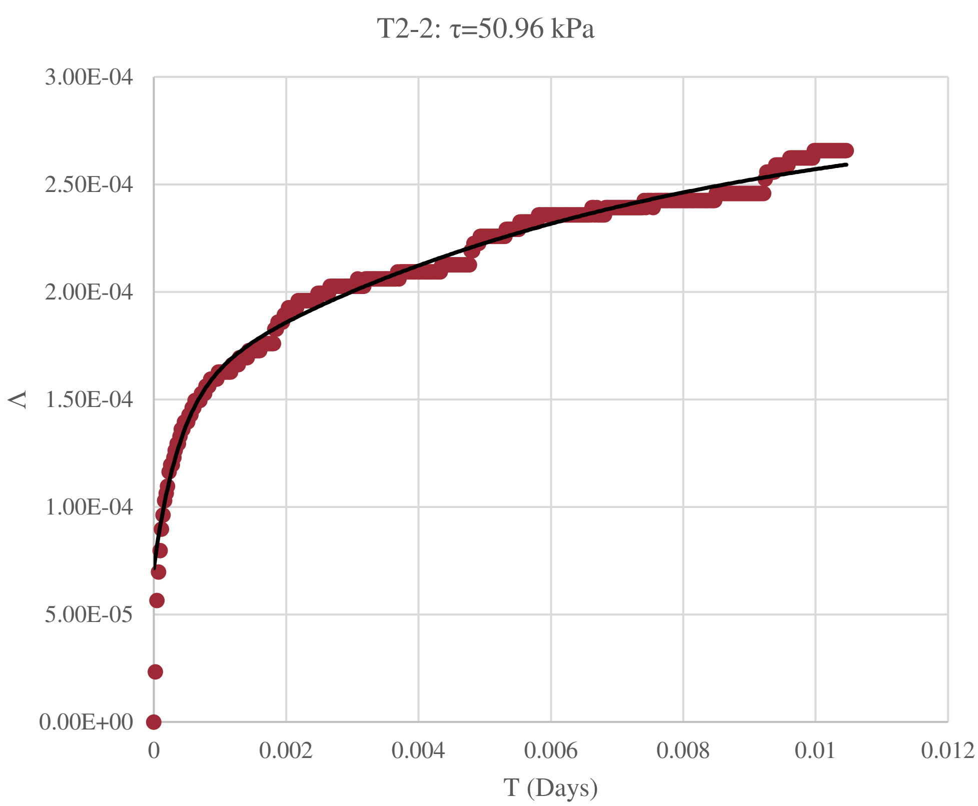
T2-2: τ=50.96 kPa
3.00E-04
2.50E-04
2.00E-04
1.50E-04
1.00E-04
5.00E-05
0.00E+00
Λ
0
0.002
0.004
0.006
0.008
0.01
0.012
T (Days)

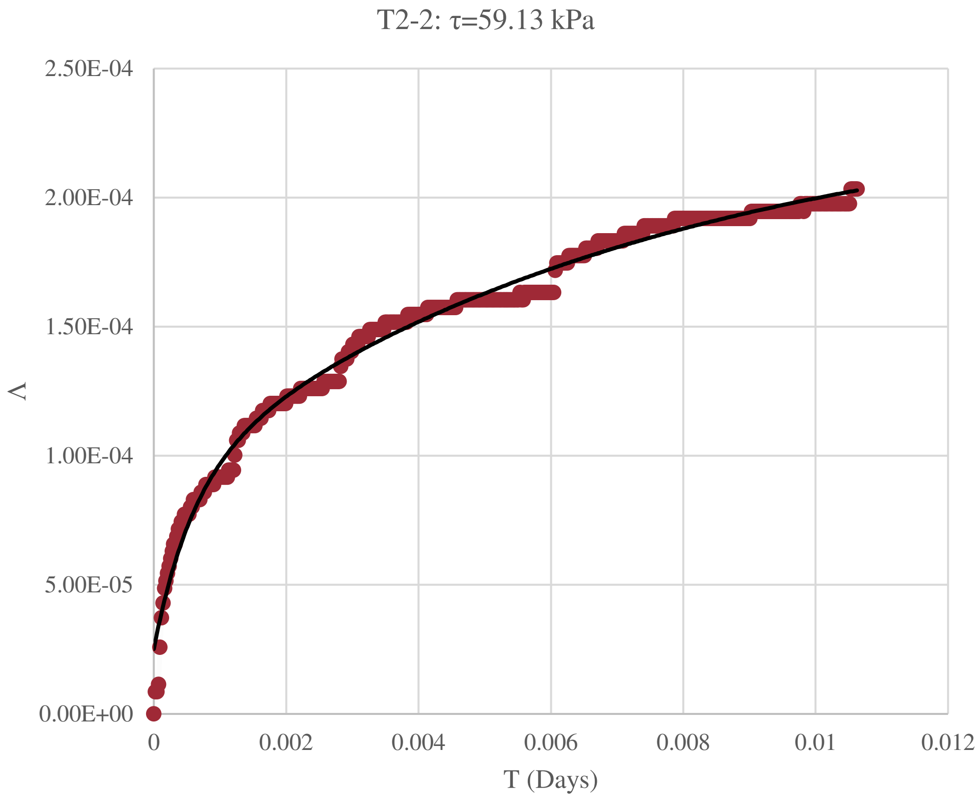
T2-2: τ=59.13 kPa
2.50E-04
2.00E-04
1.50E-04
1.00E-04
5.00E-05
0.00E+00
Λ
0
0.002
0.004
0.006
0.008
0.01
0.012
T (Days)

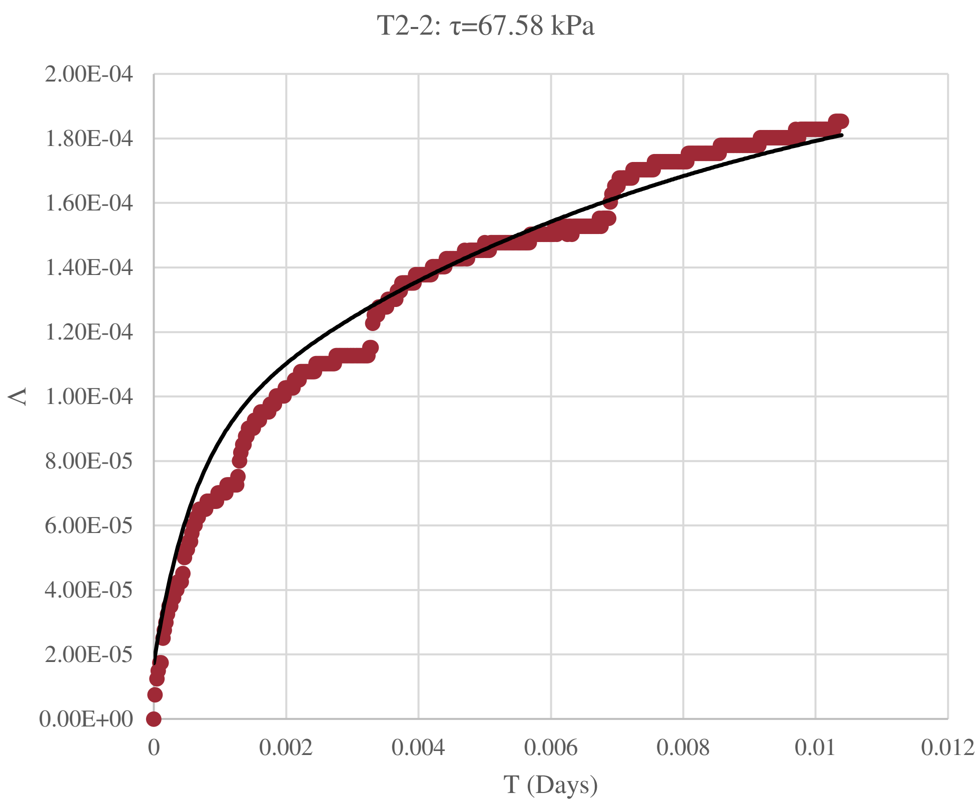
T2-2: τ=67.58 kPa
2.00E-04
1.80E-04
1.60E-04
1.40E-04
1.20E-04
1.00E-04
8.00E-05
6.00E-05
4.00E-05
2.00E-05
0.00E+00
Λ
0
0.002
0.004
0.006
0.008
0.01
0.012
T (Days)

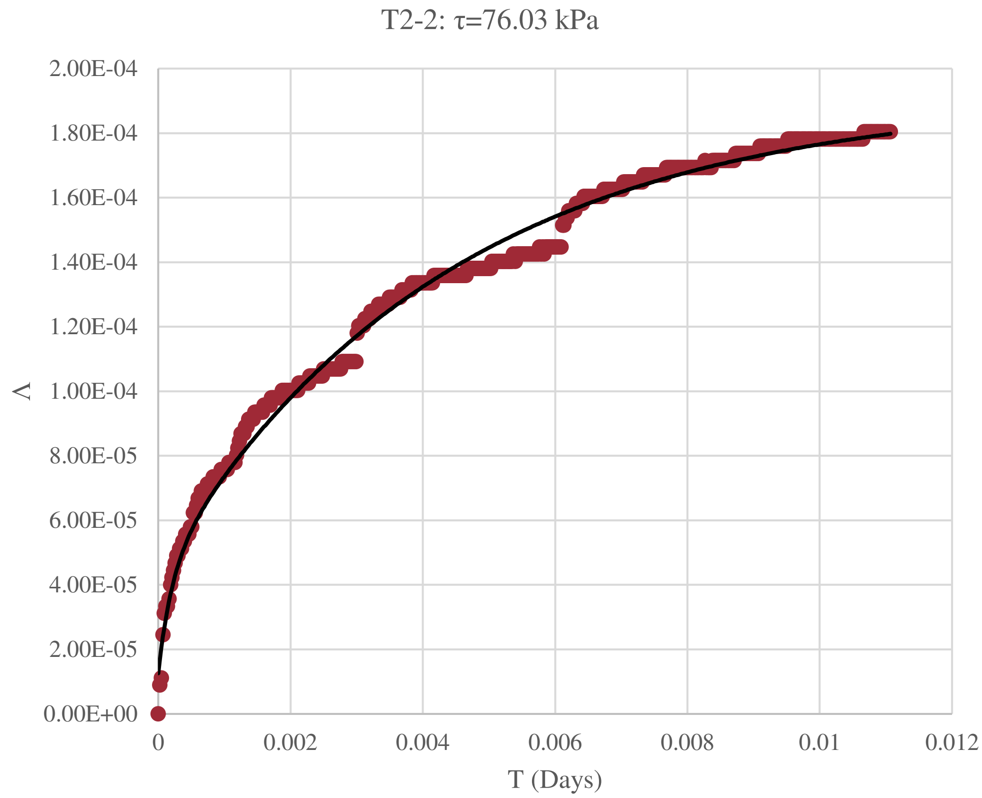

7.2.3 T2-3

T2-3: Normal Stress = 60 kPa						
τ (kPa)	CSR-N	G_{Di} (kPa)	G_{D1} (kPa)	G_{D2} (kPa)	R_1 (d)	R_2 (d)
8.45	0.1	277675	59506	27586	7.07E-04	1.11E-02
16.9	0.2	18914	18827	9124	9.66E-04	1.39E-02
25.34	0.31	12322	1214	6628	1.80E-04	1.34E-02
33.79	0.45	82311	5330	8370	2.04E-04	9.98E-03
42.24	0.52	82311	11340	9389	9.74E-05	4.34E-03
50.96	0.61	84390	13053	10467	9.75E-05	4.60E-03
59.13	0.7	167562	52490	11867	3.52E-04	1.12E-03
67.58	0.79	167103	57357	12521	3.65E-04	1.49E-03
76.03	0.87	176958	69789	13583	3.56E-04	3.38E-03

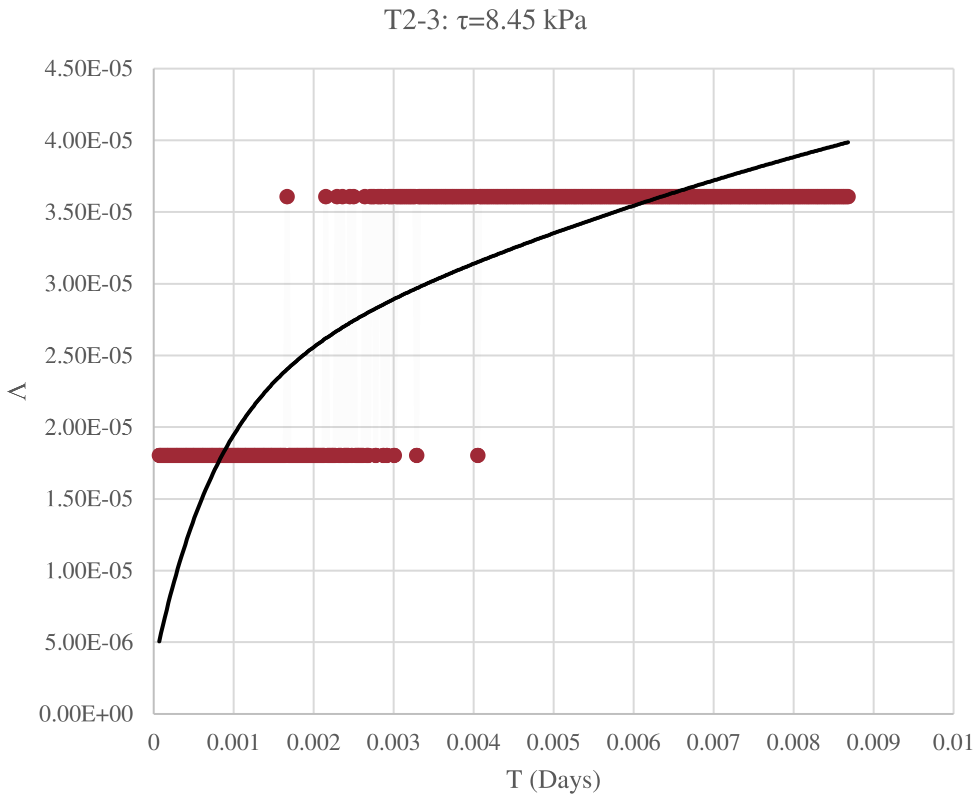
T2-3: τ=8.45 kPa
4.50E-05
4.00E-05
3.50E-05
3.00E-05
2.50E-05
2.00E-05
1.50E-05
1.00E-05
5.00E-06
0.00E+00
Λ
0
0.001
0.002
0.003
0.004
0.005
0.006
0.007
0.008
0.009
0.01
T (Days)

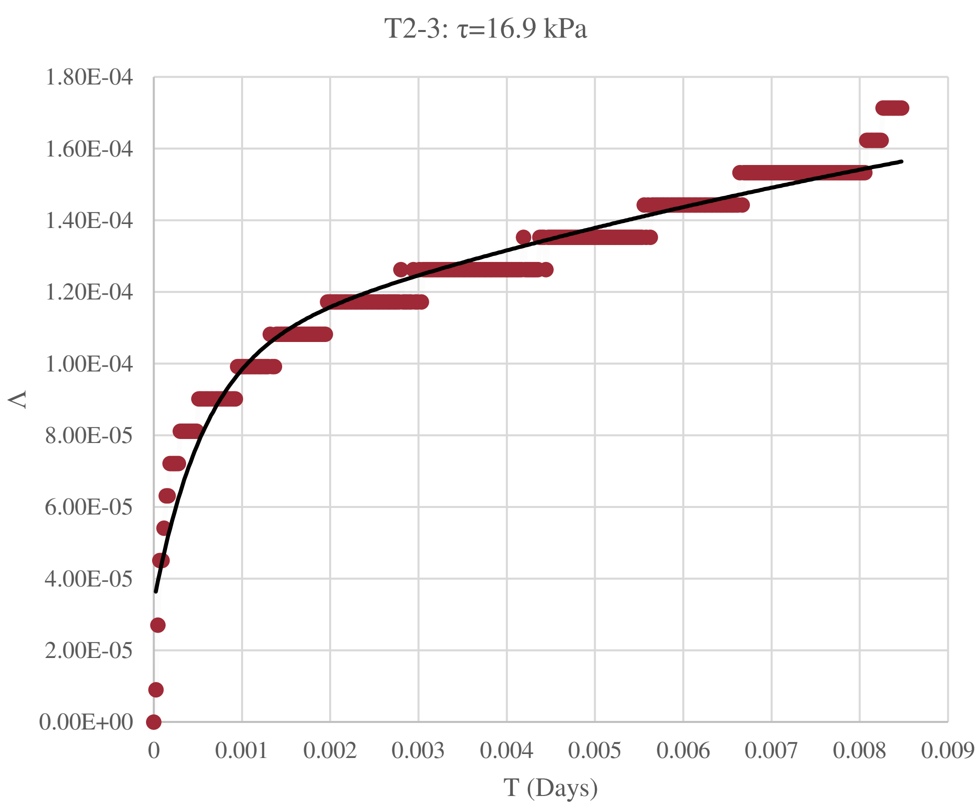
T2-3: τ=16.9 kPa
1.80E-04
1.60E-04
1.40E-04
1.20E-04
1.00E-04
8.00E-05
6.00E-05
4.00E-05
2.00E-05
0.00E+00
Λ
0
0.001
0.002
0.003
0.004
0.005
0.006
0.007
0.008
0.009
T (Days)

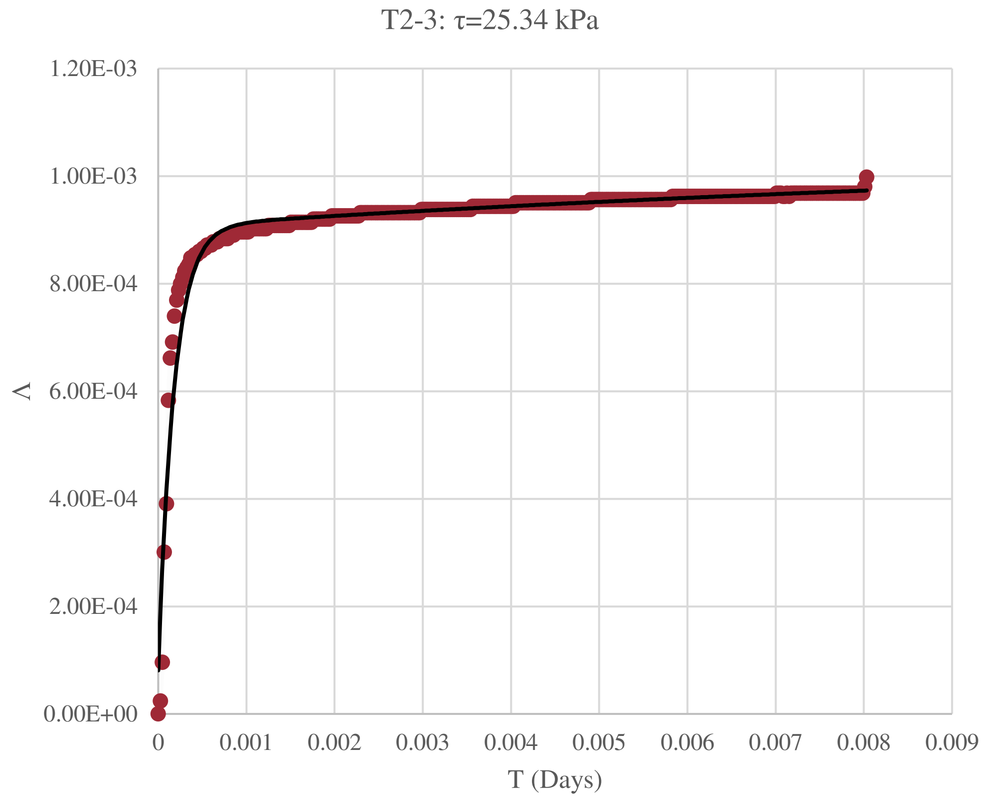
T2-3: τ=25.34 kPa
1.20E-03
1.00E-03
8.00E-04
6.00E-04
4.00E-04
2.00E-04
0.00E+00
Λ
0
0.001
0.002
0.003
0.004
0.005
0.006
0.007
0.008
0.009
T (Days)

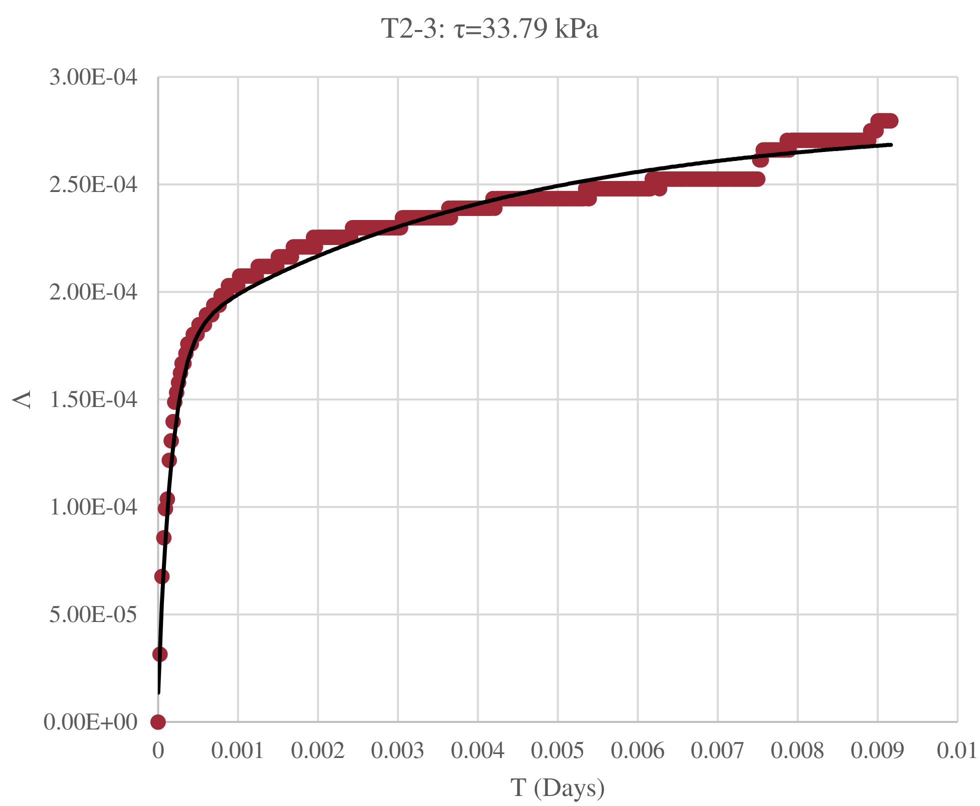
T2-3: τ=33.79 kPa
3.00E-04
2.50E-04
2.00E-04
1.50E-04
1.00E-04
5.00E-05
0.00E+00
Λ
0
0.001
0.002
0.003
0.004
0.005
0.006
0.007
0.008
0.009
0.01
T (Days)

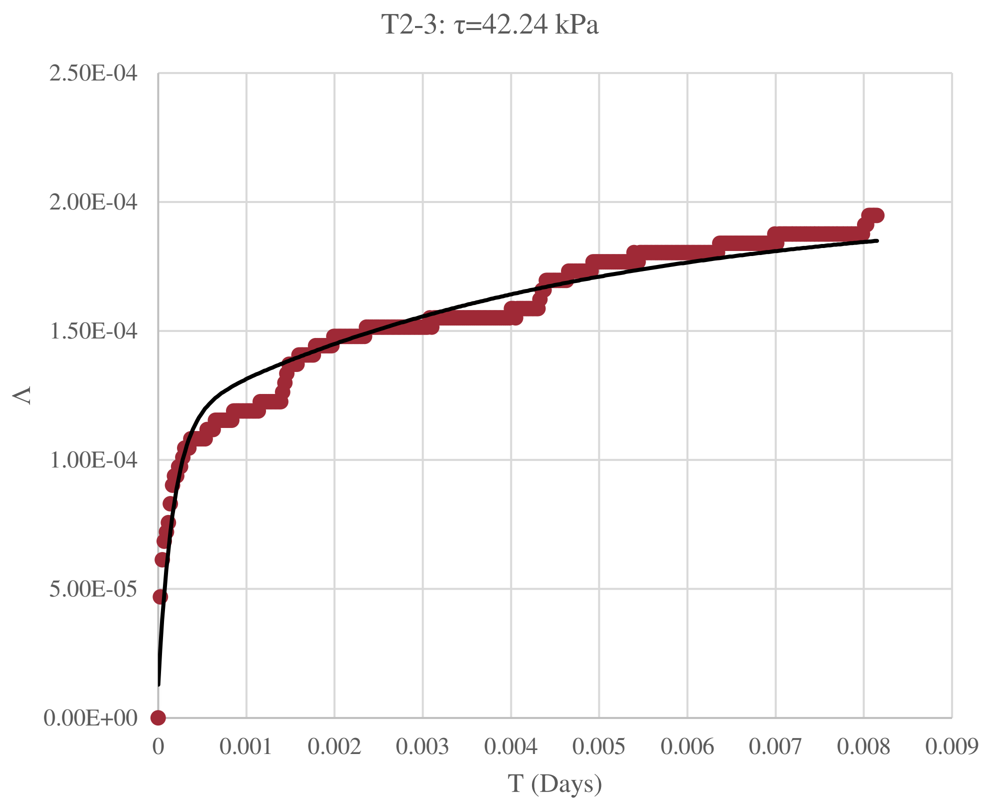
T2-3: τ=42.24 kPa
2.50E-04
2.00E-04
1.50E-04
1.00E-04
5.00E-05
0.00E+00
Λ
0
0.001
0.002
0.003
0.004
0.005
0.006
0.007
0.008
0.009
T (Days)

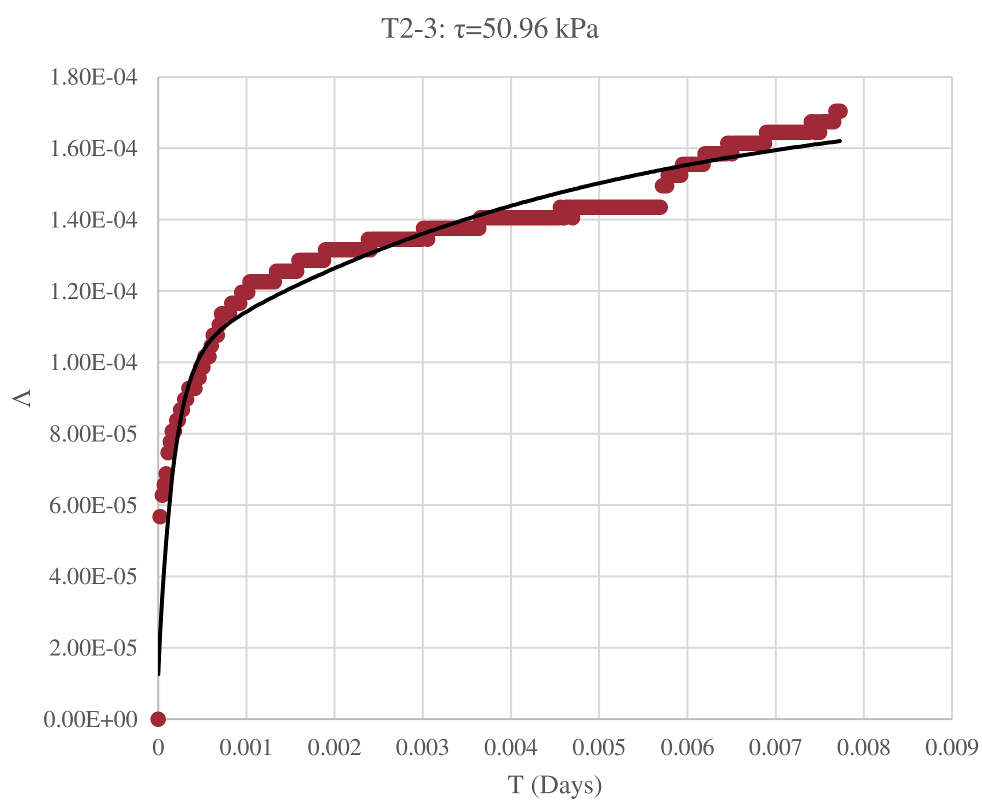
T2-3: τ=50.96 kPa
1.80E-04
1.60E-04
1.40E-04
1.20E-04
1.00E-04
8.00E-05
6.00E-05
4.00E-05
2.00E-05
0.00E+00
Λ
0
0.001
0.002
0.003
0.004
0.005
0.006
0.007
0.008
0.009
T (Days)

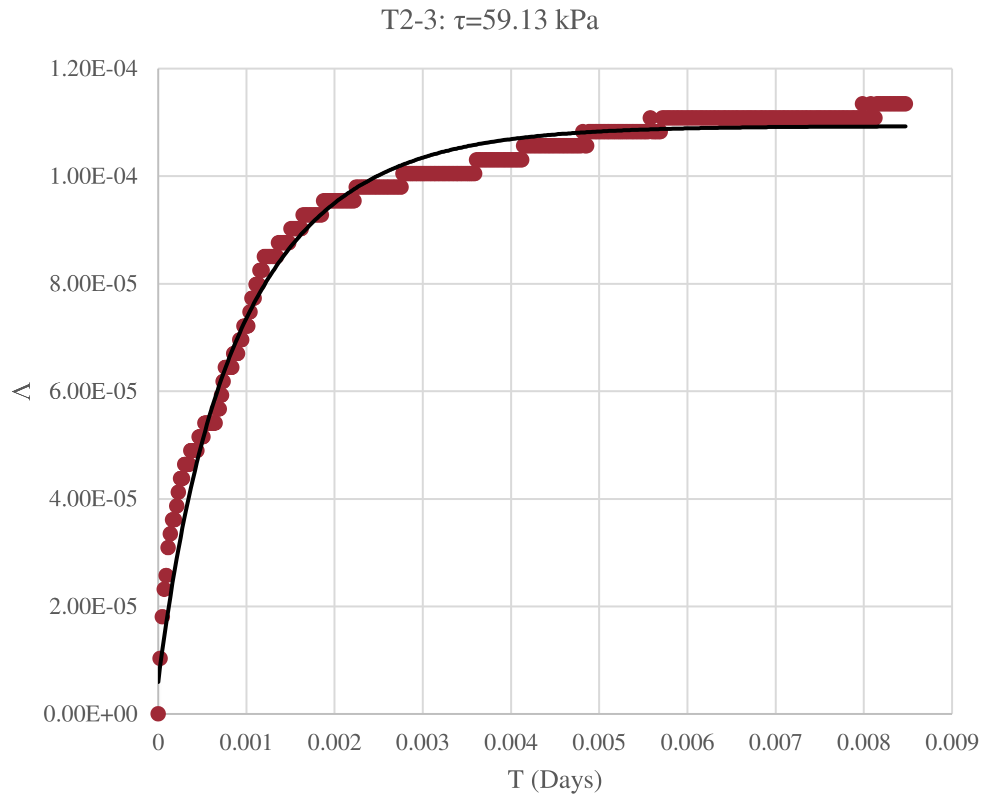

T2-3: τ=59.13 kPa
1.20E-04
1.00E-04
8.00E-05
6.00E-05
4.00E-05
2.00E-05
0.00E+00
Λ
0
0.001
0.002
0.003
0.004
0.005
0.006
0.007
0.008
0.009
T (Days)

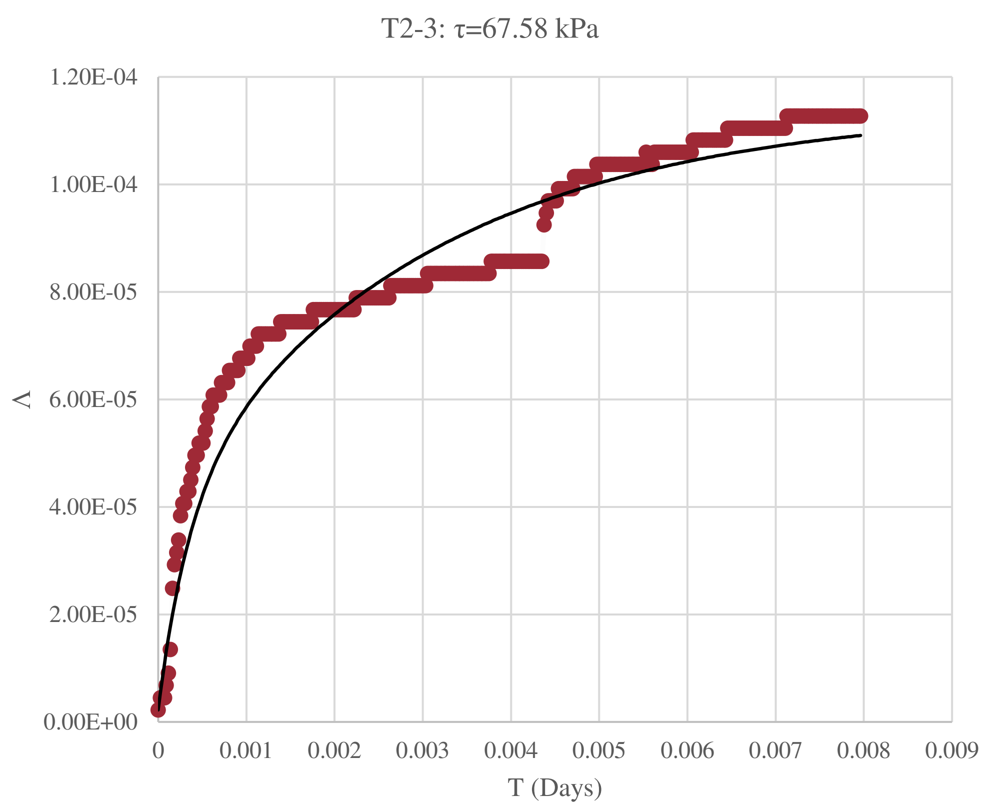

T2-3: τ=67.58 kPa
1.20E-04
1.00E-04
8.00E-05
6.00E-05
4.00E-05
2.00E-05
0.00E+00
Λ
0
0.001
0.002
0.003
0.004
0.005
0.006
0.007
0.008
0.009
T (Days)

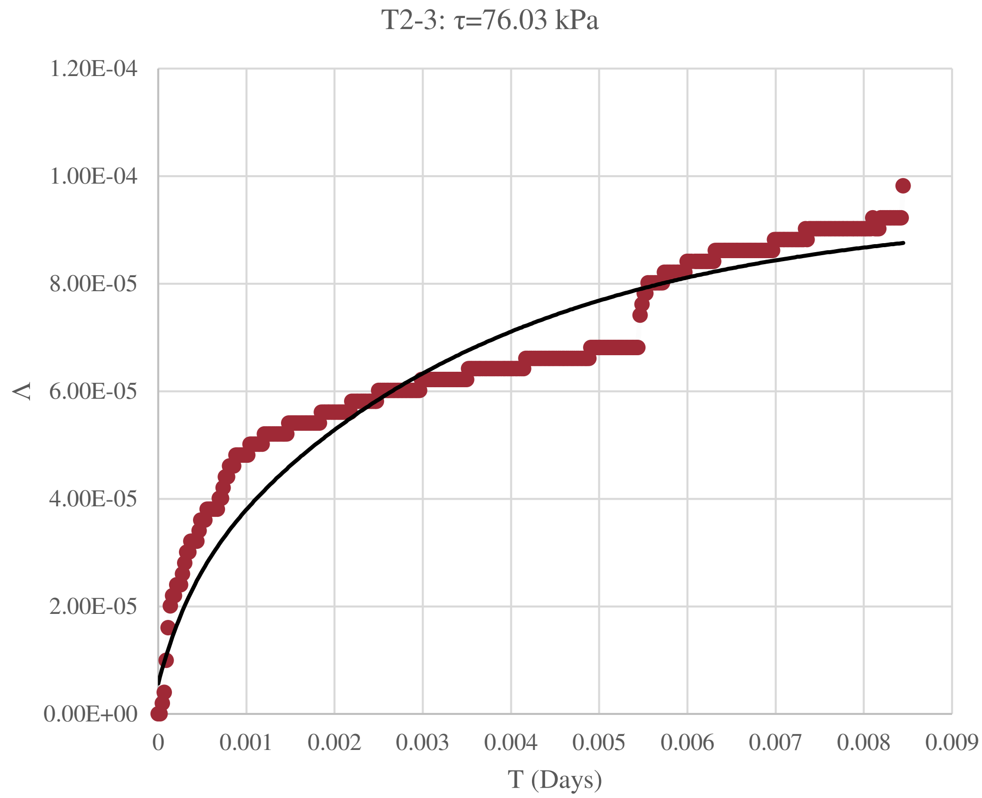

7.3 T3: Evaluation of Temperature

- RLS tests were conducted on a NHT NP GCL at temperatures of 40ºC, 60ºC, and 80ºC.
- Graph titles consist of a test series identifier (e.g. T3-1) and load increment shear stress (e.g. τ=8.45 kPa).

7.3.1 T3-1

T3-1: Temperature= 40 C						
τ (kPa)	CSR-N	G_{Di} (kPa)	G_{D1} (kPa)	G_{D2} (kPa)	R_1 (d)	R_2 (d)
8.45	0.21	13814	3942	5824	2.58E-04	3.92E-03
16.9	0.39	6308	1473	4485	1.24E-04	2.58E-03
25.34	0.54	6453	1619	4602	1.24E-04	2.60E-03
33.79	0.67	22300	10669	5602	2.72E-04	2.36E-03
42.24	0.77	19894	8313	3703	2.70E-04	2.15E-03
50.96	0.86	16641	6520	3418	2.48E-04	3.99E-03
59.13	0.92	43769	25713	2033	3.51E-04	3.20E-03

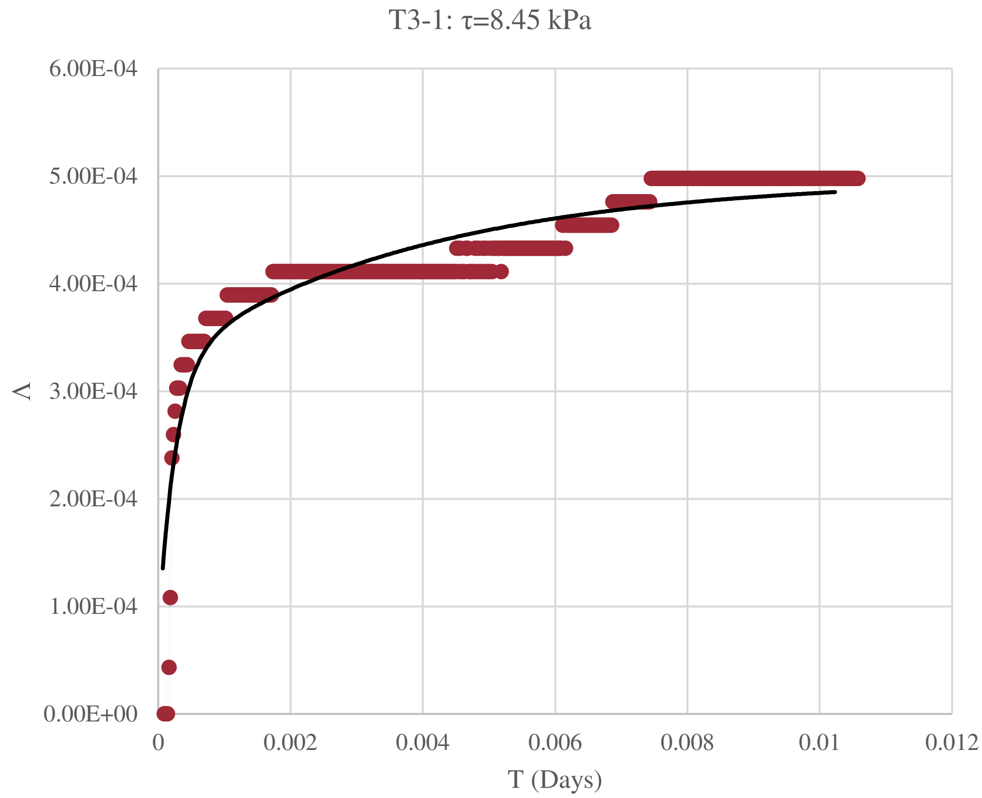
T3-1: τ=8.45 kPa
6.00E-04
5.00E-04
4.00E-04
3.00E-04
2.00E-04
1.00E-04
0.00E+00
Λ
0
0.002
0.004
0.006
0.008
0.01
0.012
T (Days)

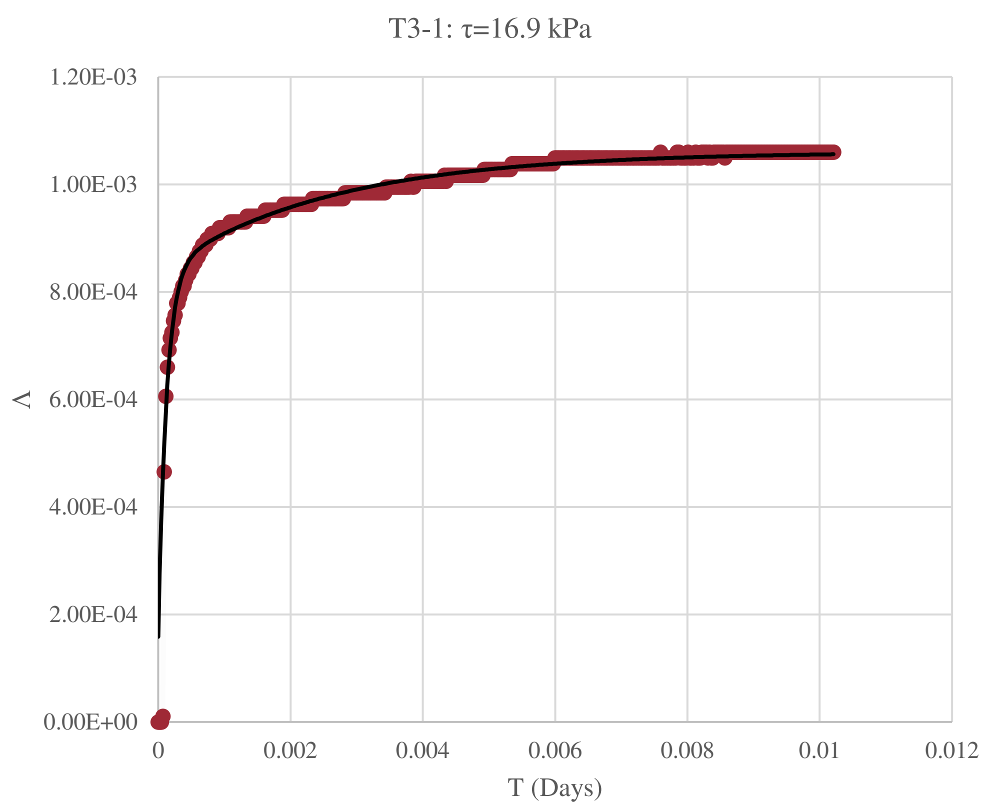
T3-1: τ=16.9 kPa
1.20E-03
1.00E-03
8.00E-04
6.00E-04
4.00E-04
2.00E-04
0.00E+00
Λ
0
0.002
0.004
0.006
0.008
0.01
0.012
T (Days)

T3-1: τ=25.34 kPa

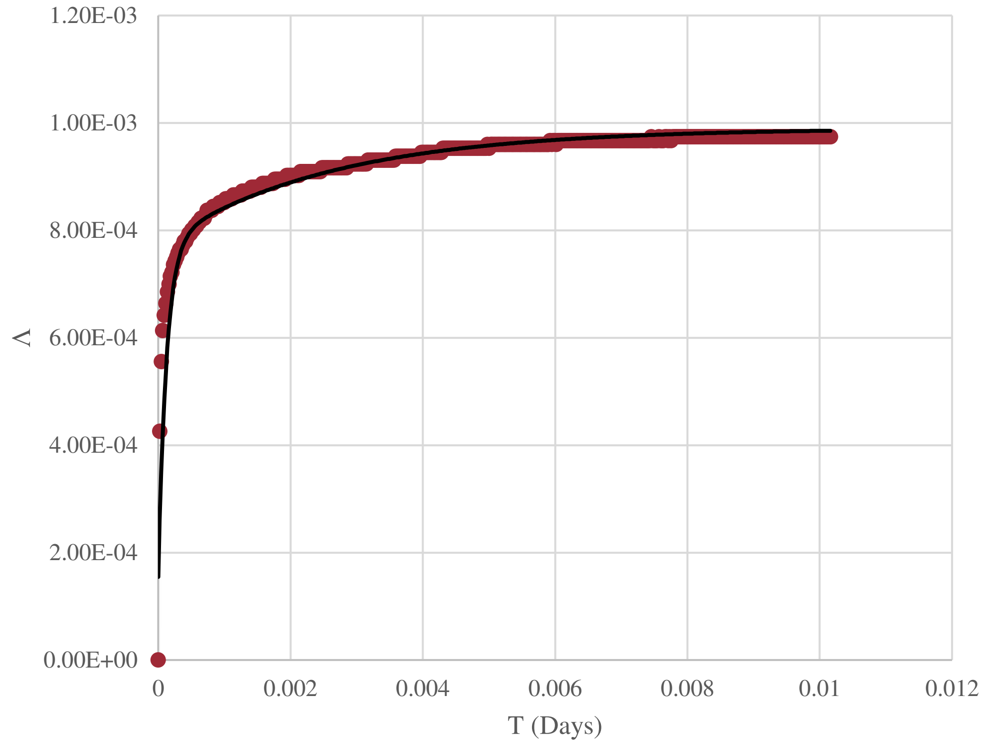

T3-1: τ=33.79 kPa

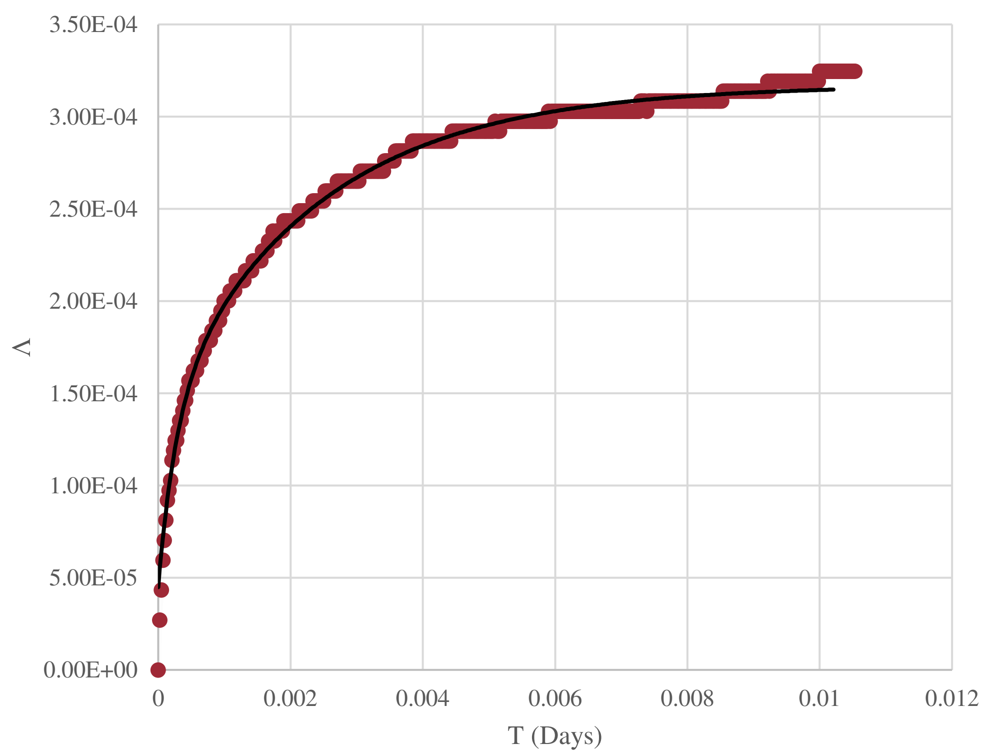

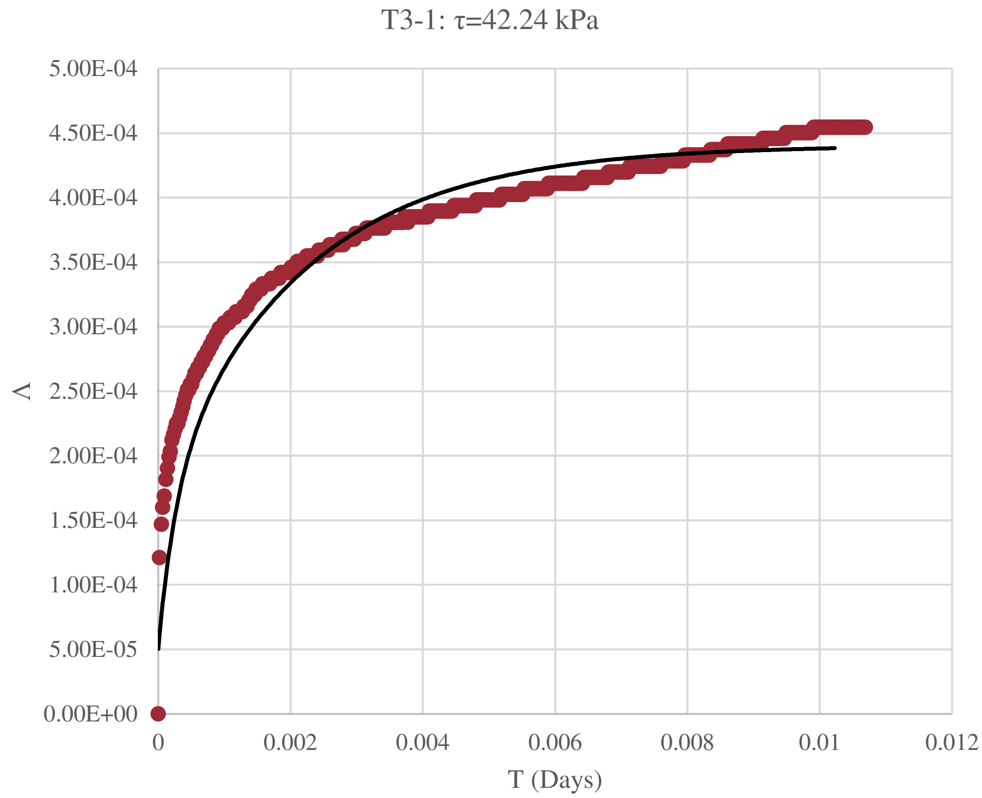
T3-1: τ=42.24 kPa
5.00E-04
4.50E-04
4.00E-04
3.50E-04
3.00E-04
2.50E-04
2.00E-04
1.50E-04
1.00E-04
5.00E-05
0.00E+00
Λ
0
0.002
0.004
0.006
0.008
0.01
0.012
T (Days)

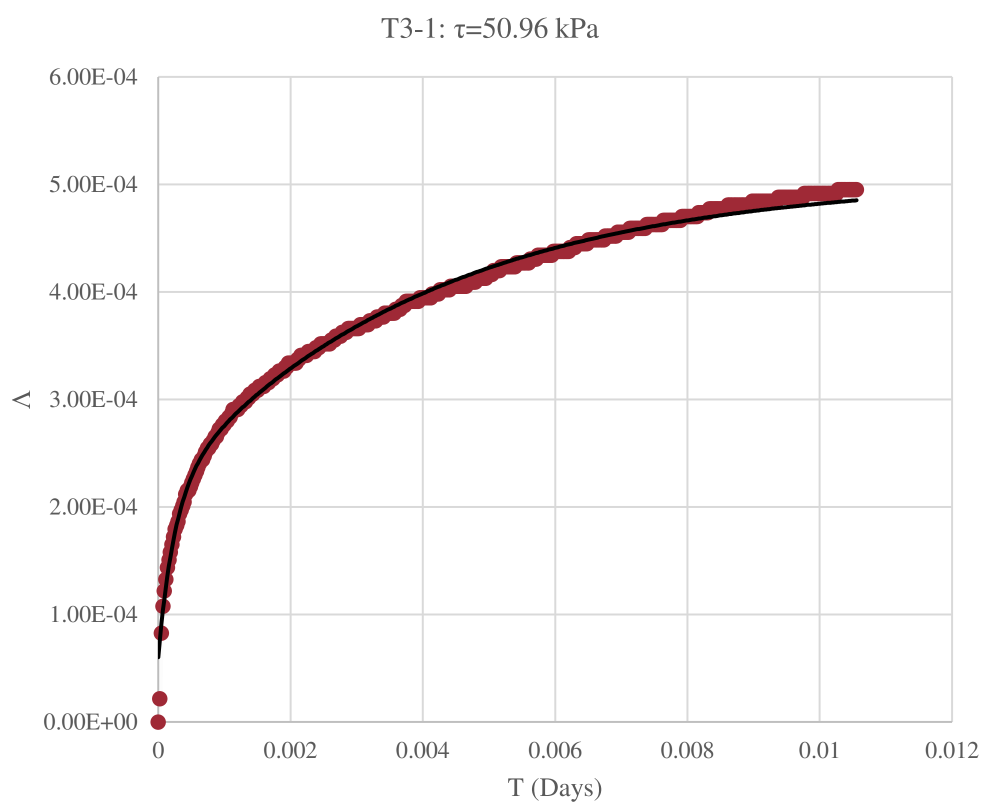
T3-1: τ=50.96 kPa
6.00E-04
5.00E-04
4.00E-04
3.00E-04
2.00E-04
1.00E-04
0.00E+00
Λ
0
0.002
0.004
0.006
0.008
0.01
0.012
T (Days)

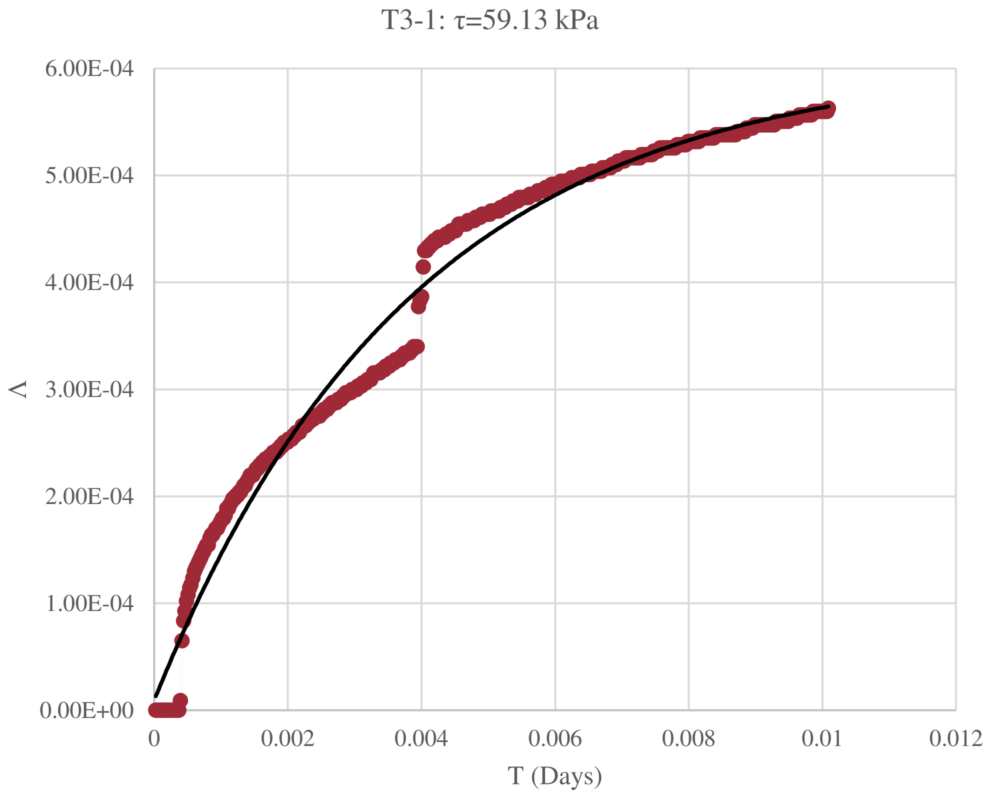

7.3.2 T3-2

T3-1: Temperature= 60 C						
τ (kPa)	CSR-N	G_{Di} (kPa)	G_{D1} (kPa)	G_{D2} (kPa)	R_1 (d)	R_2 (d)
8.45	0.24	6789	6447	5706	1.61E-04	3.88E-03
16.9	0.47	1810	2178	5855	1.47E-04	3.16E-03
25.34	0.65	1891	2258	5916	1.47E-04	3.17E-03
33.79	0.77	9944	10493	4694	4.67E-04	7.39E-03
42.24	0.85	9447	10233	3964	2.64E-04	5.48E-03
50.96	0.93	7899	8693	2970	2.64E-04	4.79E-03

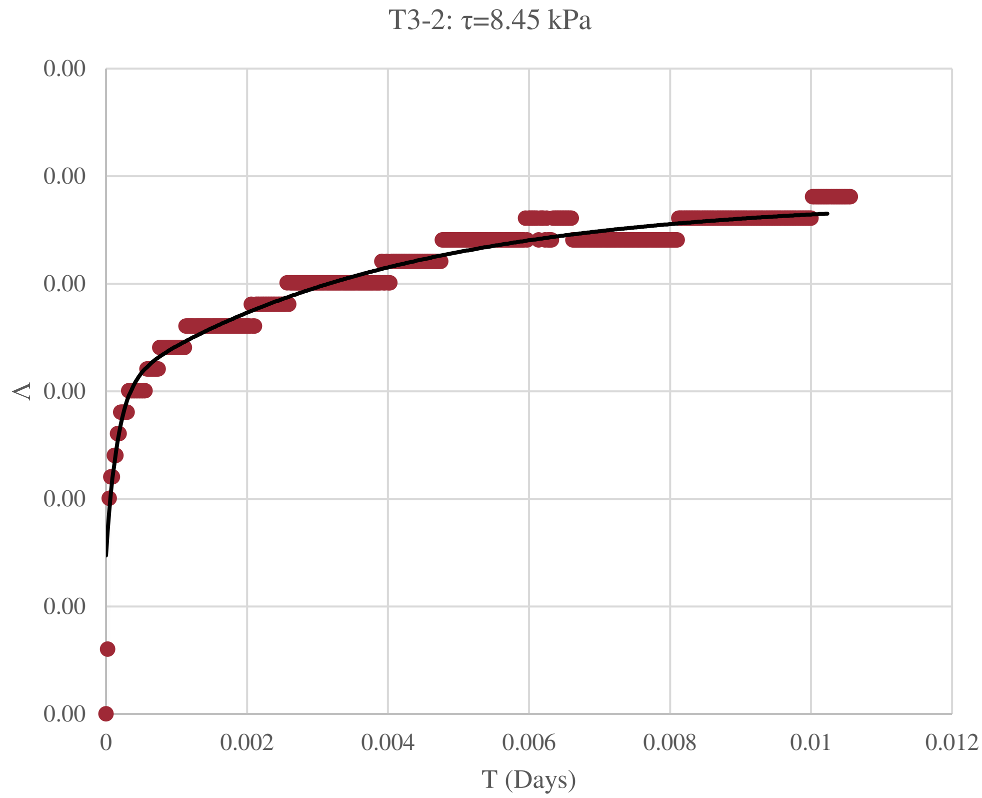
T3-2: τ=8.45 kPa
0.00
0.00
0.00
0.00
0.00
0.00
0.00
Λ
0
0.002
0.004
0.006
0.008
0.01
0.012
T (Days)

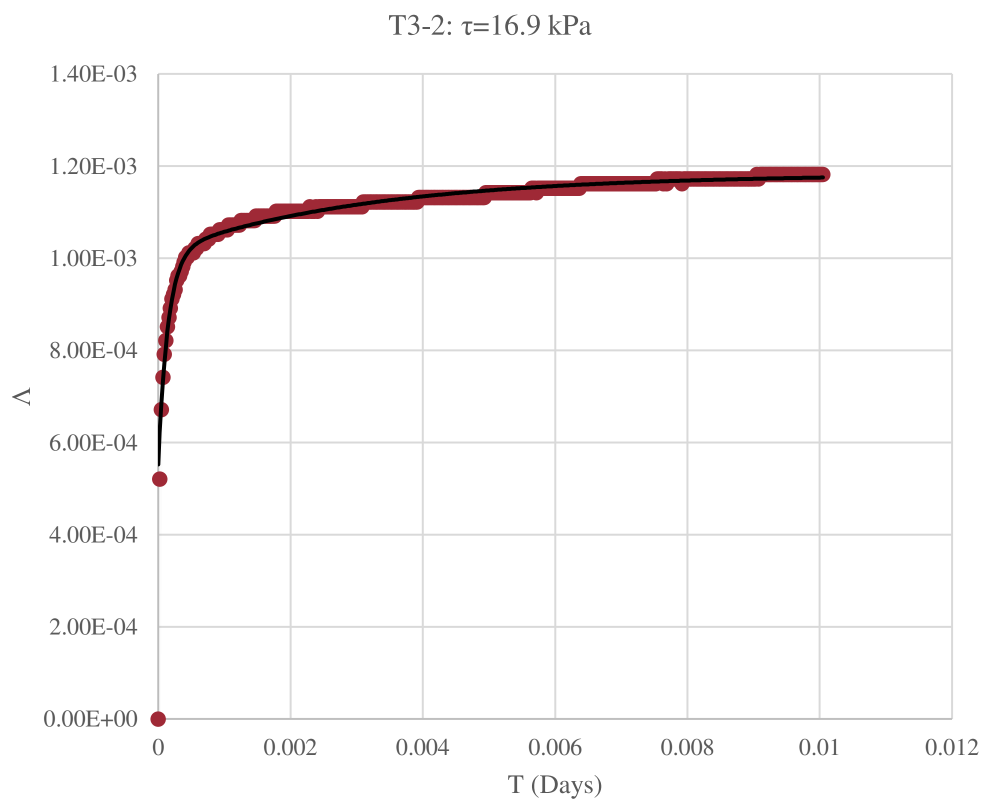
T3-2: τ=16.9 kPa
1.40E-03
1.20E-03
1.00E-03
8.00E-04
6.00E-04
4.00E-04
2.00E-04
0.00E+00
Λ
0
0.002
0.004
0.006
0.008
0.01
0.012
T (Days)

T3-2: τ=25.34 kPa

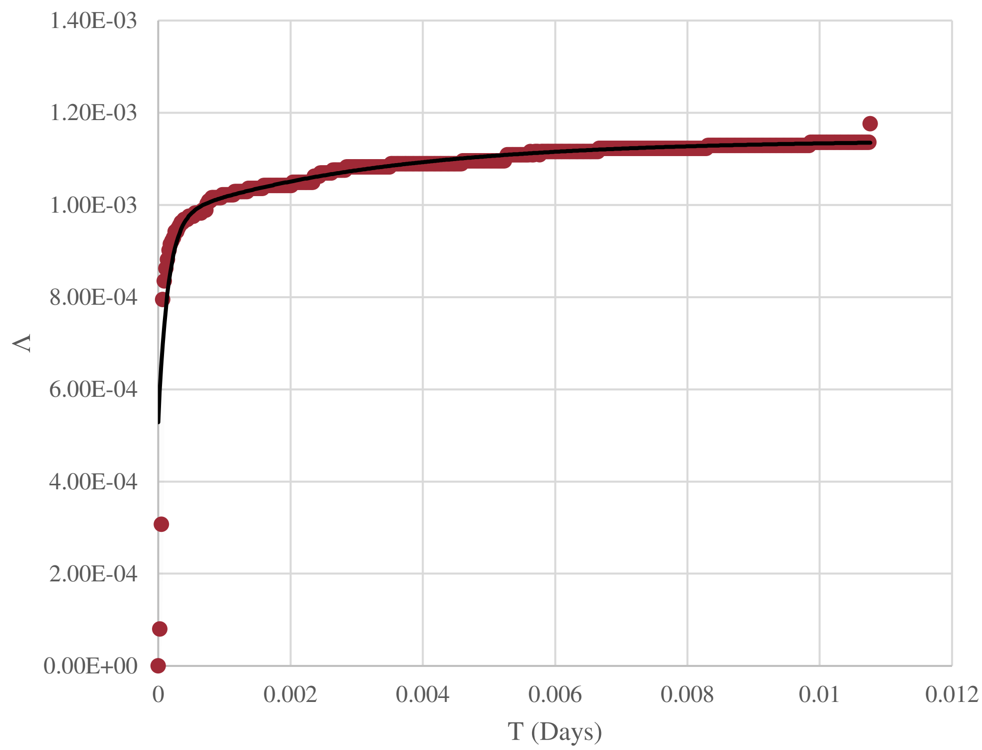

T3-2: τ=33.79 kPa

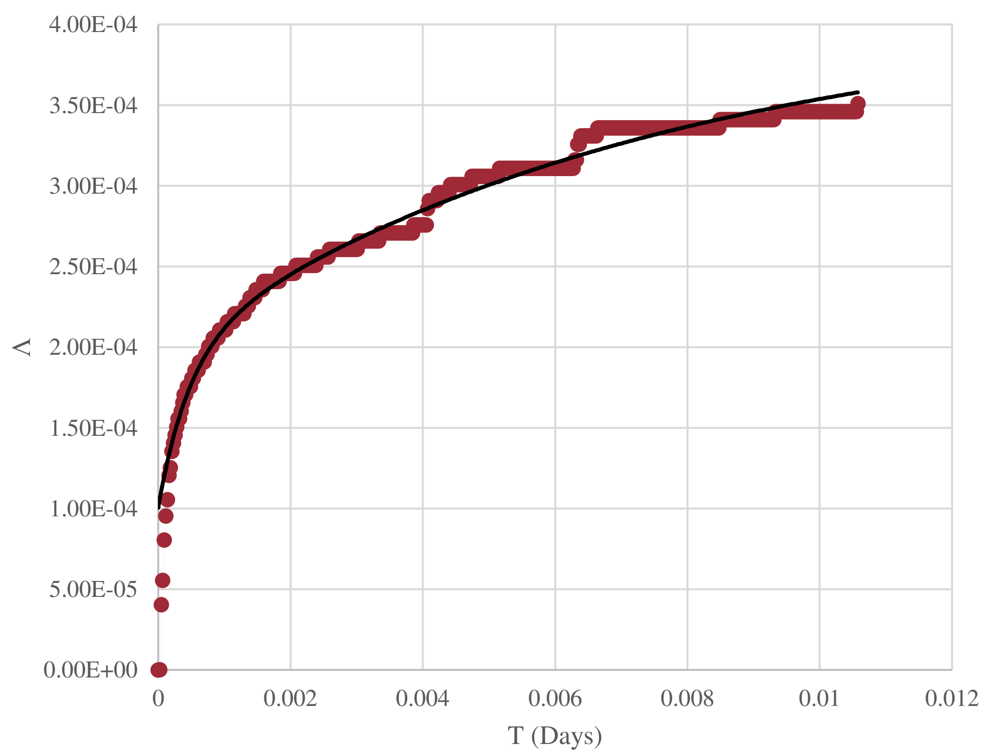

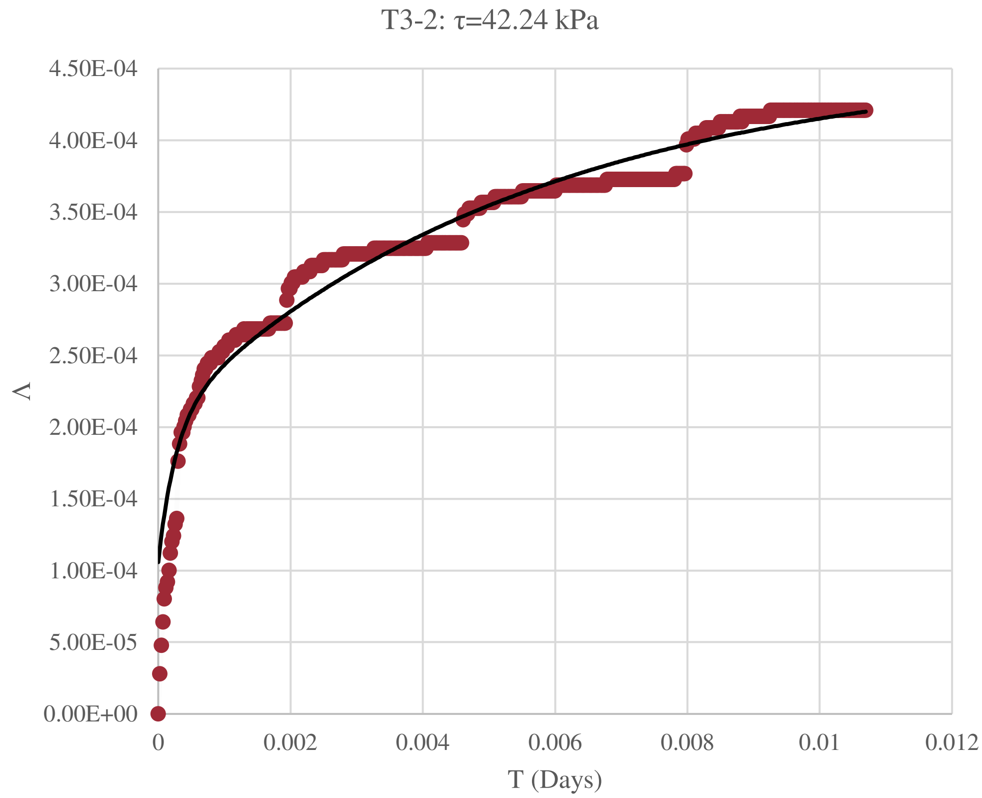
T3-2: τ=42.24 kPa
4.50E-04
4.00E-04
3.50E-04
3.00E-04
2.50E-04
2.00E-04
1.50E-04
1.00E-04
5.00E-05
0.00E+00
Λ
0
0.002
0.004
0.006
0.008
0.01
0.012
T (Days)

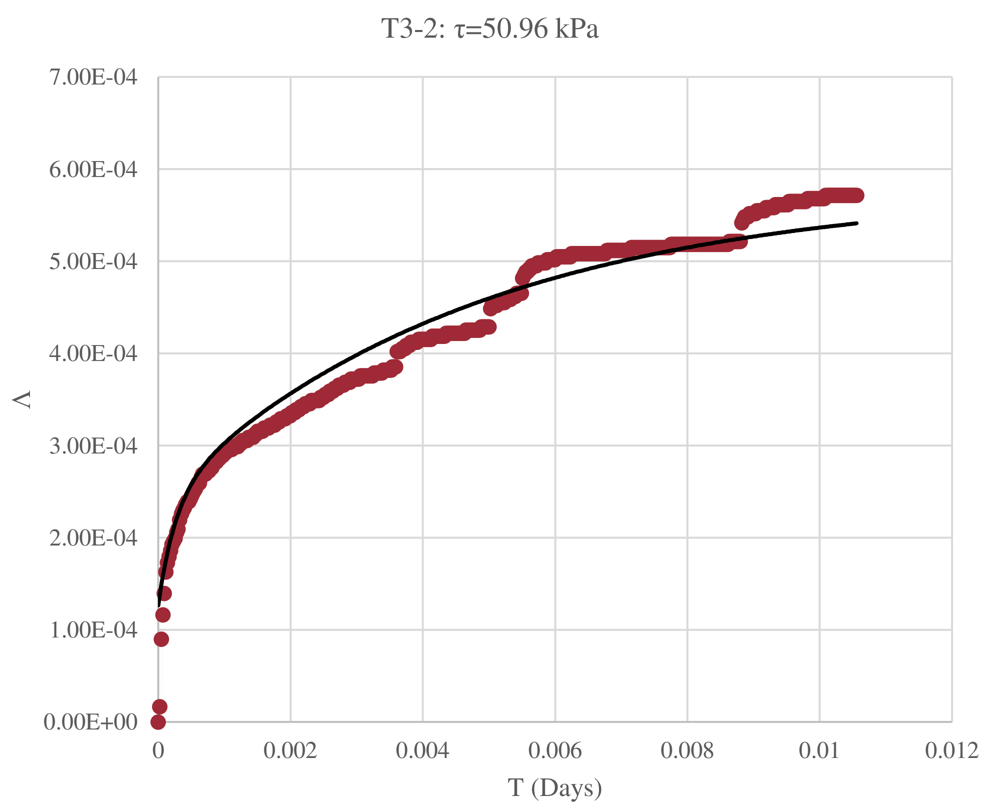
T3-2: τ=50.96 kPa
7.00E-04
6.00E-04
5.00E-04
4.00E-04
3.00E-04
2.00E-04
1.00E-04
0.00E+00
Λ
0
0.002
0.004
0.006
0.008
0.01
0.012
T (Days)

7.3.3 T3-3

T3-3: Temperature= 80 C						
τ (kPa)	CSR-N	G_{Di} (kPa)	G_{D1} (kPa)	G_{D2} (kPa)	R_1 (d)	R_2 (d)
8.45	0.29	10317	15721	8589	2.00E-04	4.25E-03
16.9	0.57	1202	976	5341	1.83E-04	2.43E-03
25.34	0.79	1650	948	5443	2.00E-04	4.25E-03

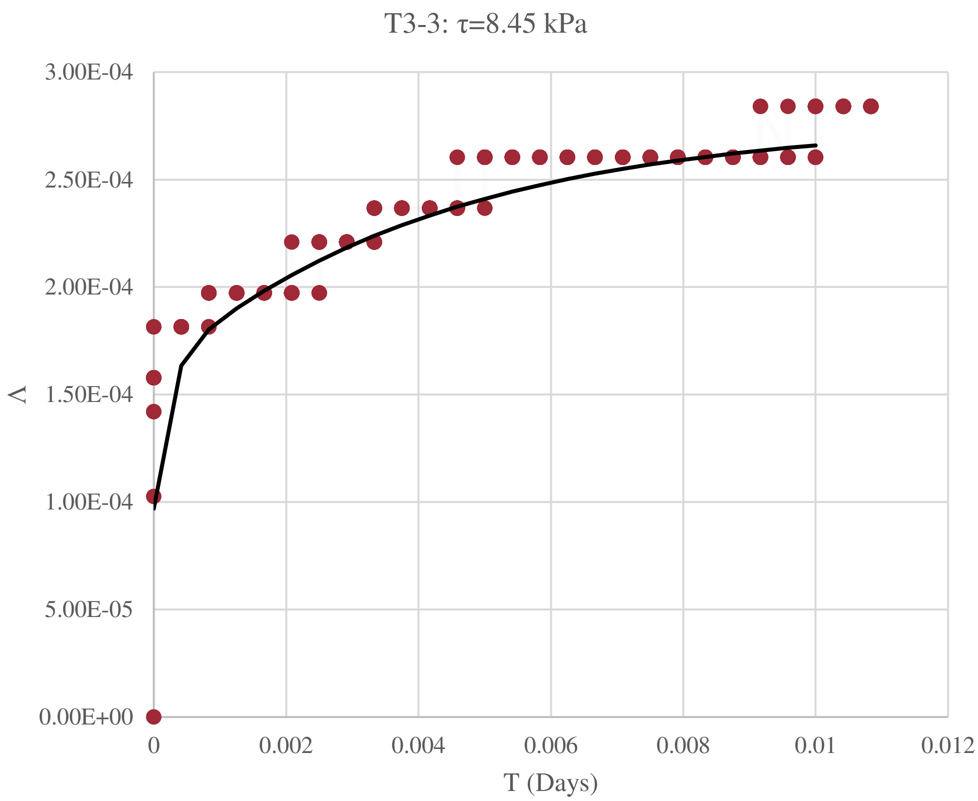

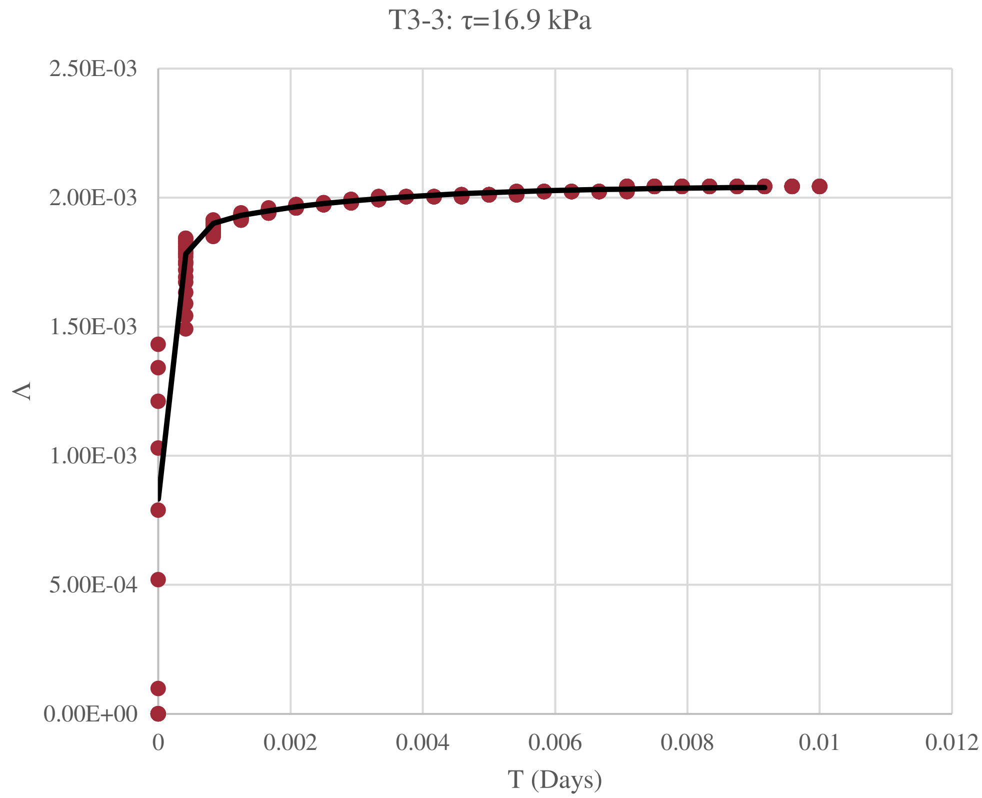
T3-3: τ=16.9 kPa
2.50E-03
2.00E-03
1.50E-03
1.00E-03
5.00E-04
0.00E+00
Λ
0
0.002
0.004
0.006
0.008
0.01
0.012
T (Days)

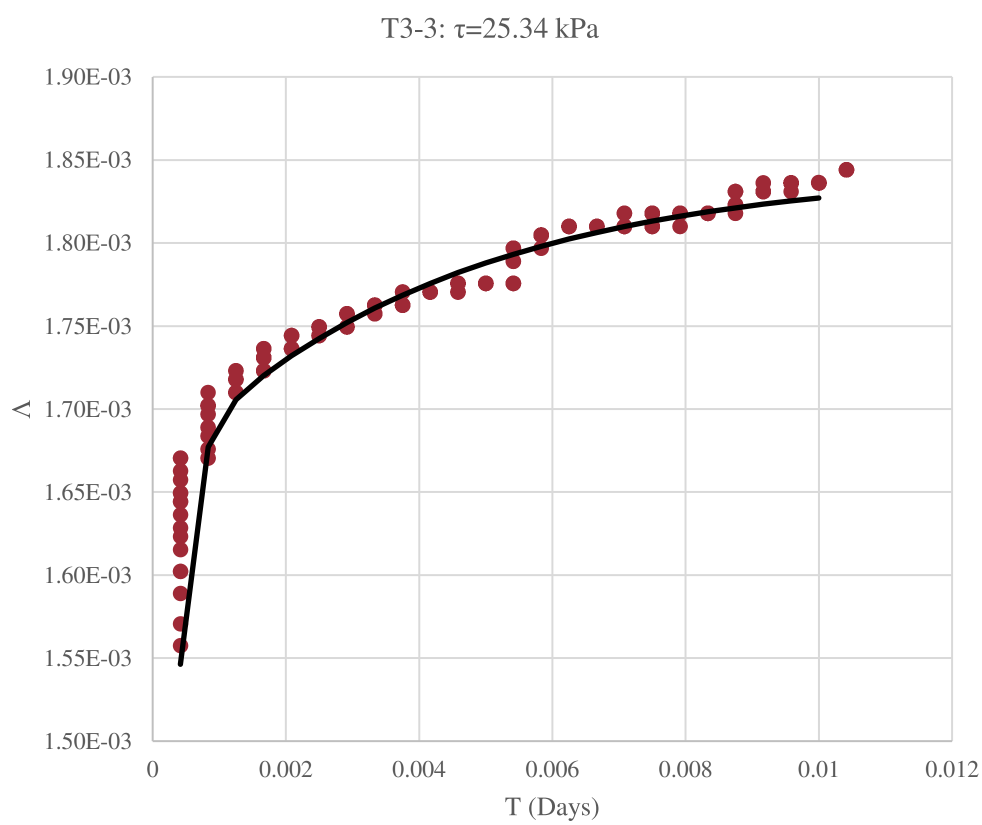
T3-3: τ=25.34 kPa
1.90E-03
1.85E-03
1.80E-03
1.75E-03
1.70E-03
1.65E-03
1.60E-03
1.55E-03
1.50E-03
Λ
0
0.002
0.004
0.006
0.008
0.01
0.012
T (Days)

7.4 T4: Evaluation of Creep

- RLS creep tests were conducted on a NHT NP GCL at T4-1: τ_{max}=92.9 kPa, T4-2: τ_{max}= kPa, T4-3: τ_{max}=84.5 kPa, T4-4: τ_{max}=80.25 kPa, and T4-5: τ_{max}=67.58 kPa.
- Graph titles consist of a test series identifier (e.g. T4-1) and load increment shear stress (e.g. τ=8.45 kPa) followed by the descriptor "Optimized Retardation Time" or "Generalized Retardation Time".
    - Optimized Retardation Times: Denotes the first iteration of the performance assessment applied to T4 (see section 4.2.1). Here, the retardation times (R_1 and R_2) and shear deformation moduli (GD_i, GD_1, GD_2) were optimized to individual load increments during the model optimization step of the performance assessment.
    - Generalized Retardation Times: Denotes the second iteration of the performance assessment applied to T4. The generalized retardation times RG_1 and RG_2 were determined by averaging R_1 and R_2 for $\tau \leq 76\ kPa$. The model optimization step of the performance assessment was repeated using the generalized retardation times in lieu of the optimized retardation times. Here, the shear deformation moduli were optimized to individual load increments while the generalized retardation times were held constant.

7.4.1 T4-1

T4-1: τmax = 93 kPa, Optimized Retardation Times

τ (kPa)	CSR-N	G_{Di} (kPa)	G_{D1} (kPa)	G_{D2} (kPa)	R_1 (d)	R_2 (d)
8.45	0.23	37077	4925	9948	6.95E-05	3.98E-03
16.9	0.45	1082	2007	5304	1.34E-04	3.04E-03
25.34	0.61	2883	3847	7519	1.39E-04	3.24E-03
33.79	0.73	6838	6016	7307	2.31E-04	3.19E-03
42.24	0.83	10676	9088	9397	2.34E-04	3.58E-03
50.96	0.91	69349	7956	7797	4.18E-04	5.63E-03
59.13	0.98	71936	11527	7624	4.33E-04	6.33E-03
67.58	1.03	78655	16821	5577	4.93E-04	6.60E-03
76.03	1.06	153139	21577	3789	1.77E-04	3.01E-02

T4-1: τmax = 93 kPa, Generalized Retardation Times						
τ (kPa)	CSR-N	G_{Di} (kPa)	G_{D1} (kPa)	G_{D2} (kPa)	RG_1 (d)	RG_2 (d)
8.45	0.23	6108	12572	9995	2.63E-04	5.96E-03
16.9	0.45	844	3606	5360	2.63E-04	5.96E-03
25.34	0.61	2320	4923	7721	2.63E-04	5.96E-03
33.79	0.73	6414	5596	7079	2.63E-04	5.96E-03
42.24	0.83	24971	5674	7621	2.63E-04	5.96E-03
50.96	0.91	69309	7907	7734	2.63E-04	5.96E-03
59.13	0.98	73549	12676	7170	2.63E-04	5.96E-03
67.58	1.03	79140	17304	5831	2.63E-04	5.96E-03
76.03	1.06	158704	33226	3369	2.63E-04	5.96E-03

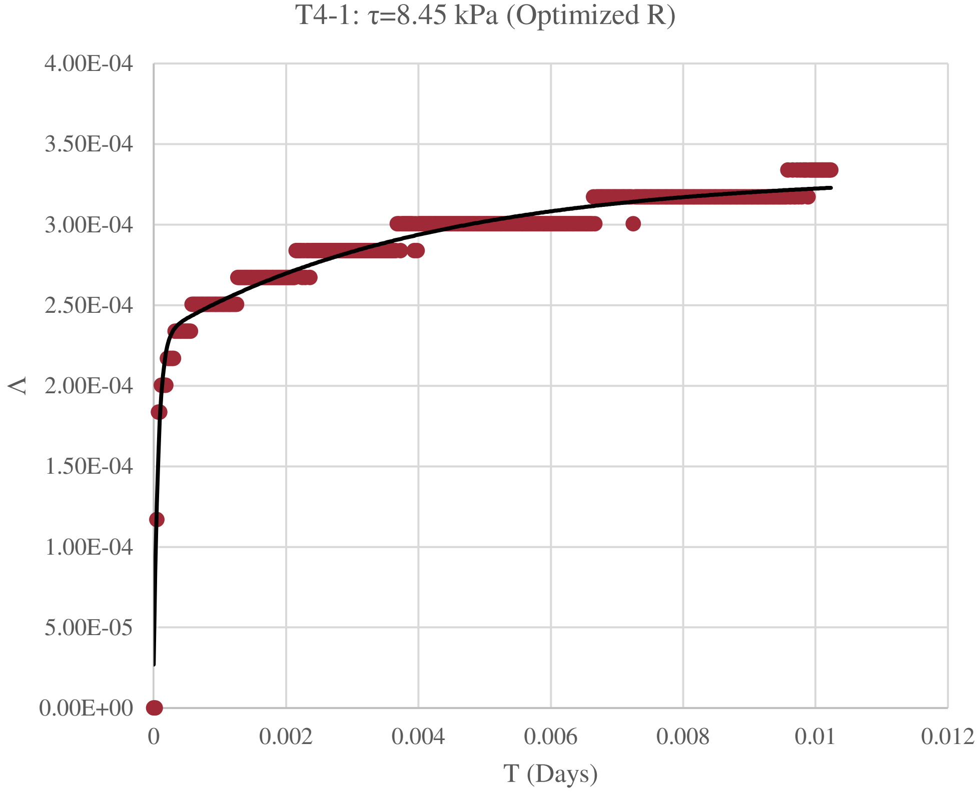
T4-1: τ=8.45 kPa (Optimized R)
4.00E-04
3.50E-04
3.00E-04
2.50E-04
2.00E-04
1.50E-04
1.00E-04
5.00E-05
0.00E+00
Λ
0
0.002
0.004
0.006
0.008
0.01
0.012
T (Days)

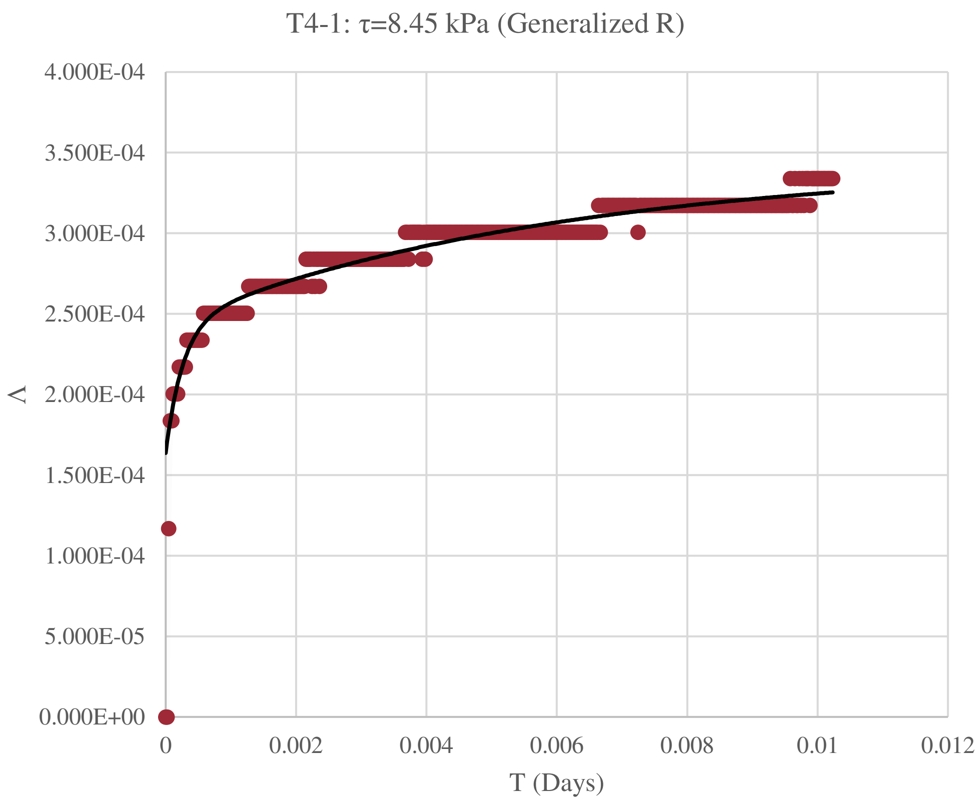
T4-1: τ=8.45 kPa (Generalized R)
4.000E-04
3.500E-04
3.000E-04
2.500E-04
2.000E-04
1.500E-04
1.000E-04
5.000E-05
0.000E+00
Λ
0
0.002
0.004
0.006
0.008
0.01
0.012
T (Days)

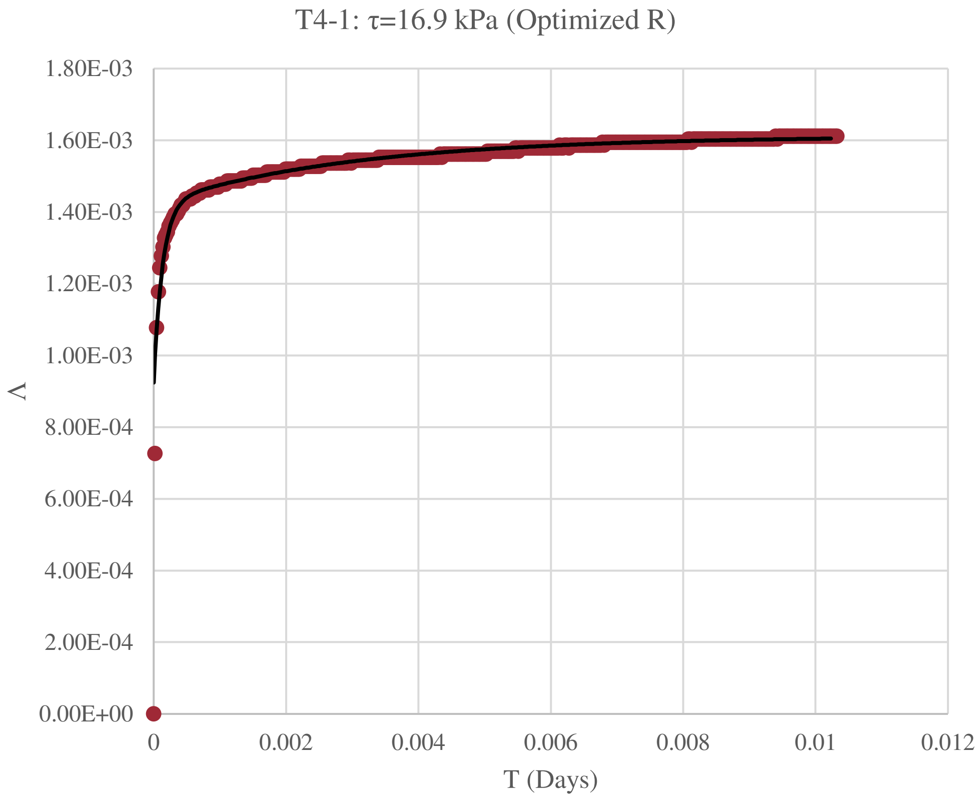
T4-1: τ=16.9 kPa (Optimized R)
1.80E-03
1.60E-03
1.40E-03
1.20E-03
1.00E-03
8.00E-04
6.00E-04
4.00E-04
2.00E-04
0.00E+00
Λ
0
0.002
0.004
0.006
0.008
0.01
0.012
T (Days)

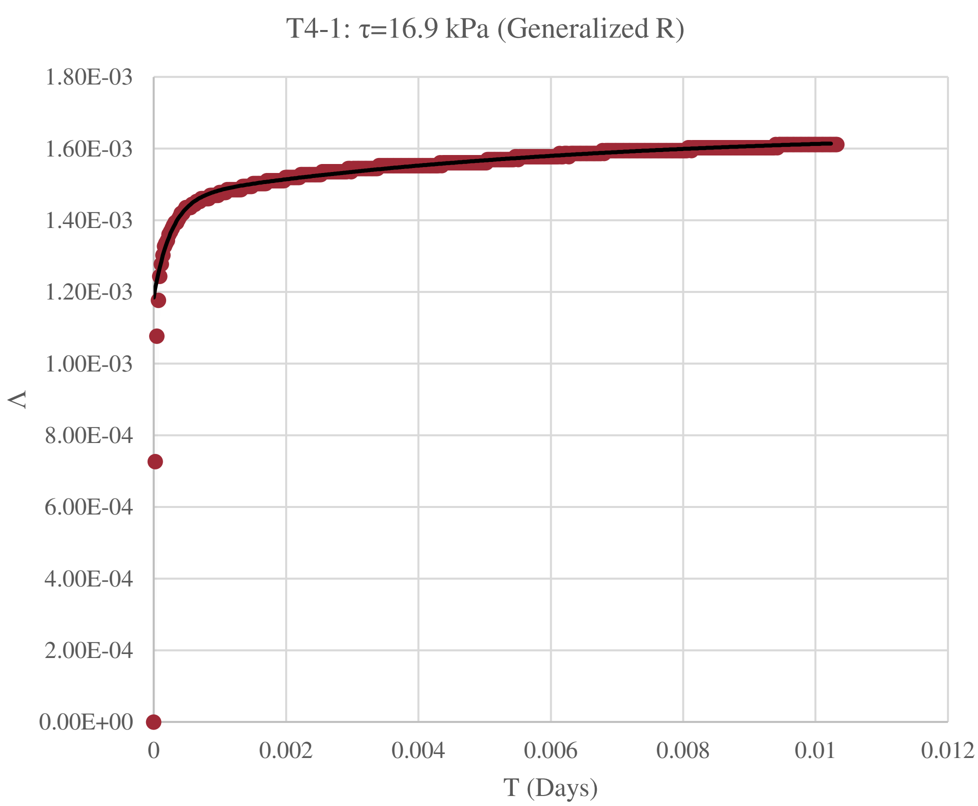
T4-1: τ=16.9 kPa (Generalized R)
1.80E-03
1.60E-03
1.40E-03
1.20E-03
1.00E-03
8.00E-04
6.00E-04
4.00E-04
2.00E-04
0.00E+00
Λ
0
0.002
0.004
0.006
0.008
0.01
0.012
T (Days)

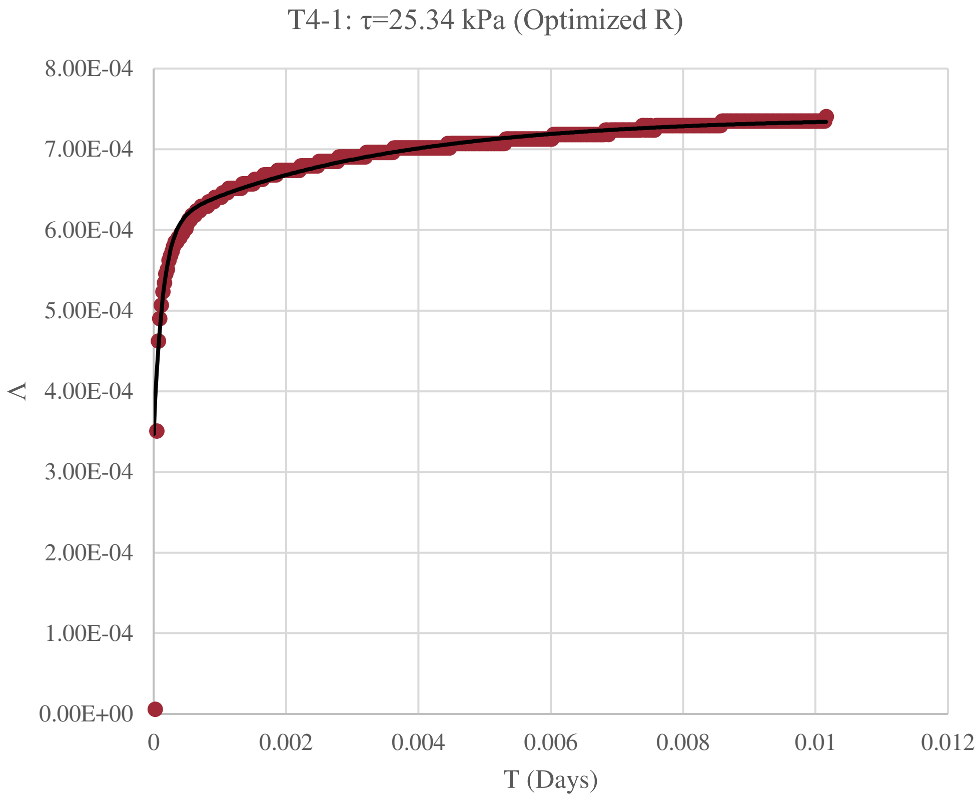
T4-1: τ=25.34 kPa (Optimized R)
8.00E-04
7.00E-04
6.00E-04
5.00E-04
4.00E-04
3.00E-04
2.00E-04
1.00E-04
0.00E+00
Λ
0
0.002
0.004
0.006
0.008
0.01
0.012
T (Days)

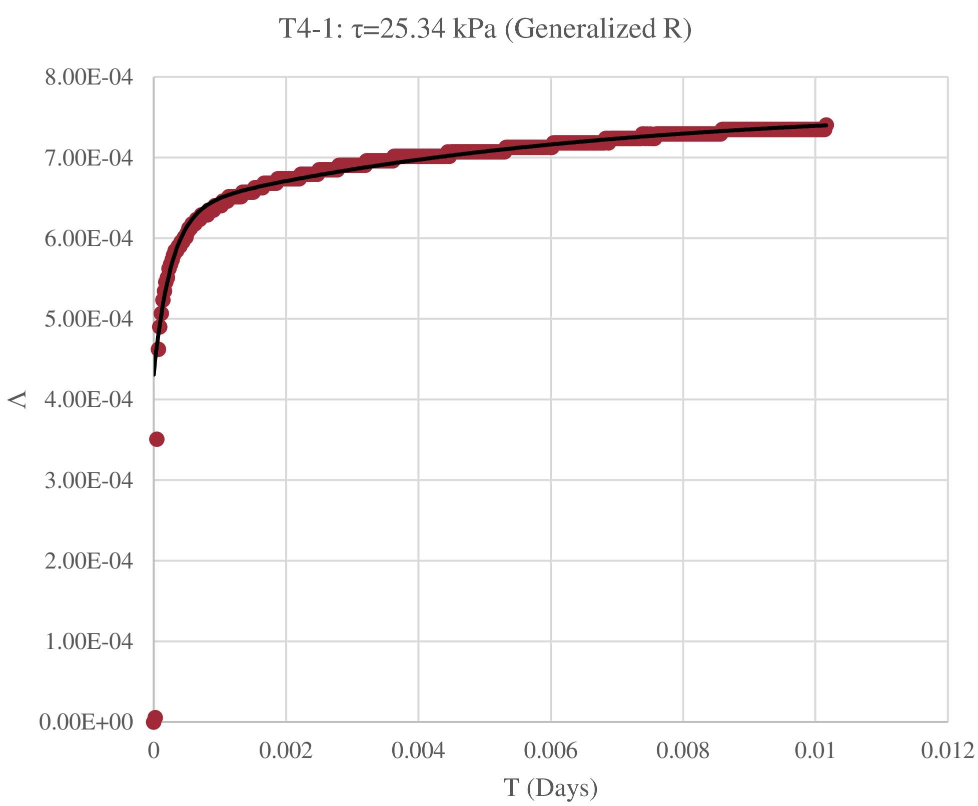
T4-1: τ=25.34 kPa (Generalized R)
8.00E-04
7.00E-04
6.00E-04
5.00E-04
4.00E-04
3.00E-04
2.00E-04
1.00E-04
0.00E+00
Λ
0
0.002
0.004
0.006
0.008
0.01
0.012
T (Days)

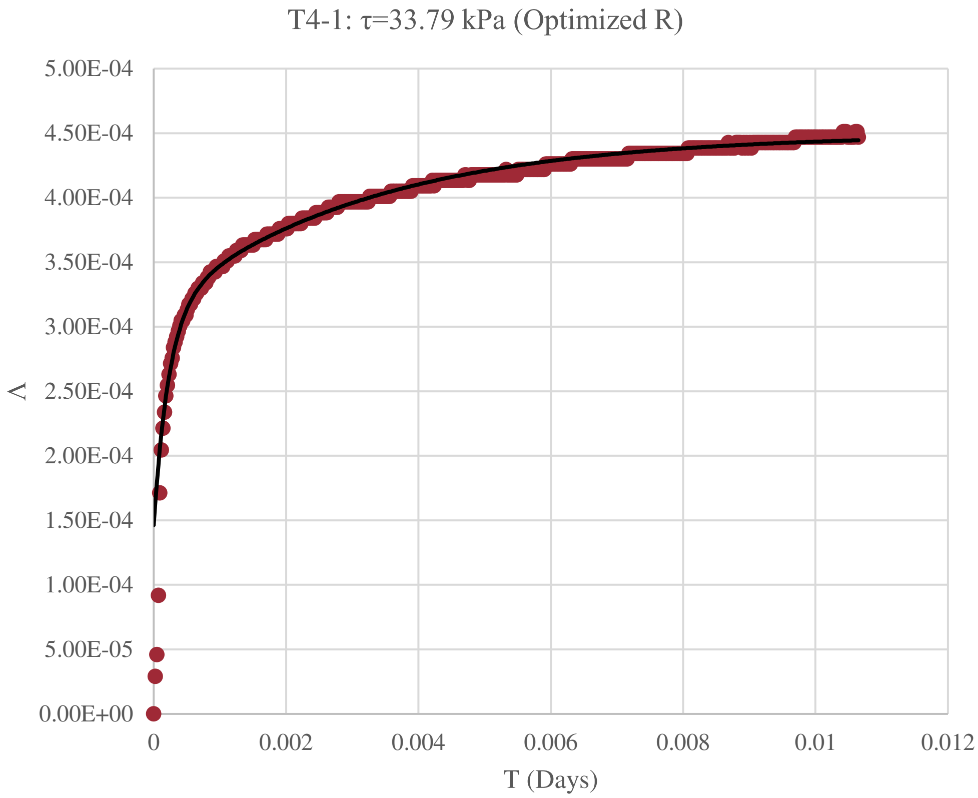
T4-1: τ=33.79 kPa (Optimized R)
5.00E-04
4.50E-04
4.00E-04
3.50E-04
3.00E-04
2.50E-04
2.00E-04
1.50E-04
1.00E-04
5.00E-05
0.00E+00
Λ
0
0.002
0.004
0.006
0.008
0.01
0.012
T (Days)

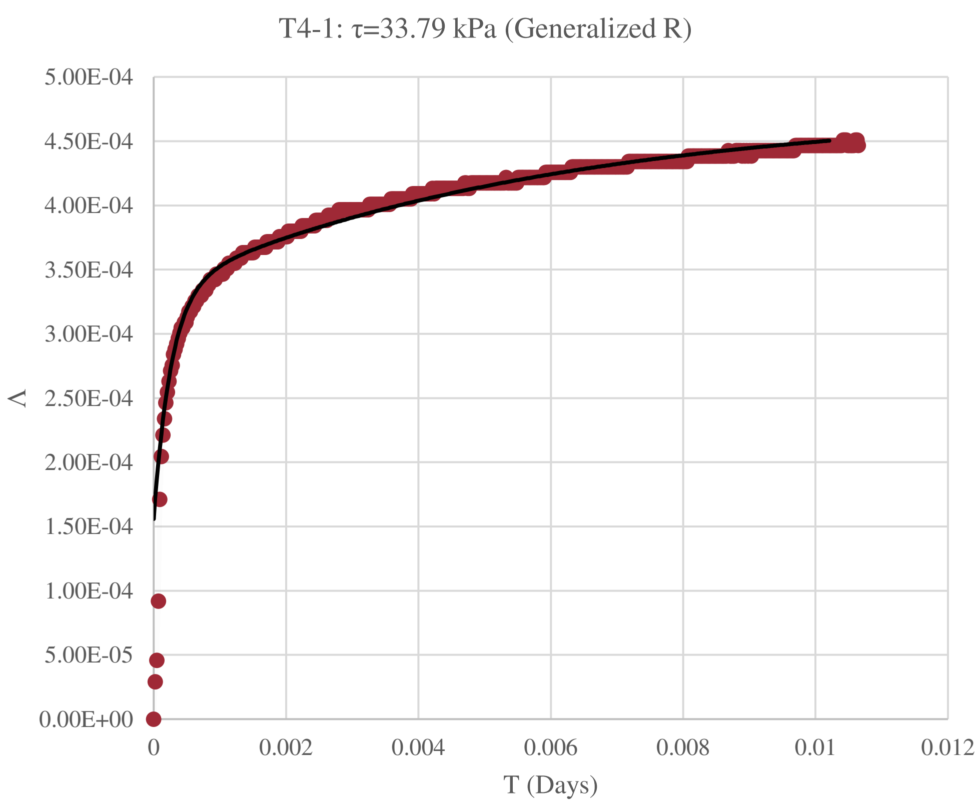
T4-1: τ=33.79 kPa (Generalized R)
5.00E-04
4.50E-04
4.00E-04
3.50E-04
3.00E-04
2.50E-04
2.00E-04
1.50E-04
1.00E-04
5.00E-05
0.00E+00
Λ
0
0.002
0.004
0.006
0.008
0.01
0.012
T (Days)

T4-1: τ=42.24 kPa (Optimized R)

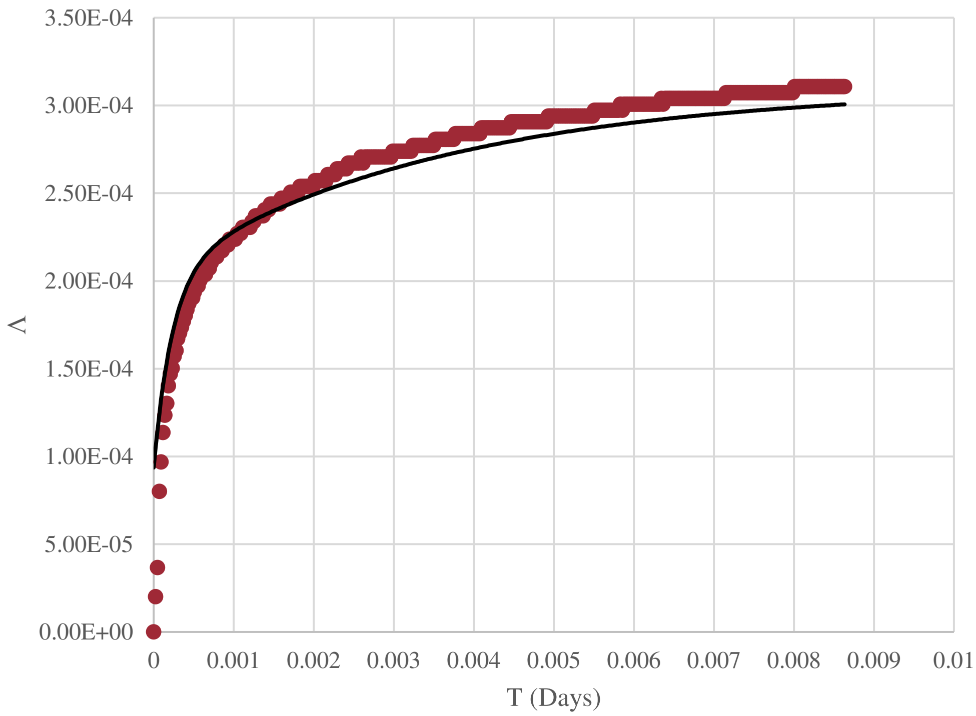

T4-1: τ=42.24 kPa (Generalized R)

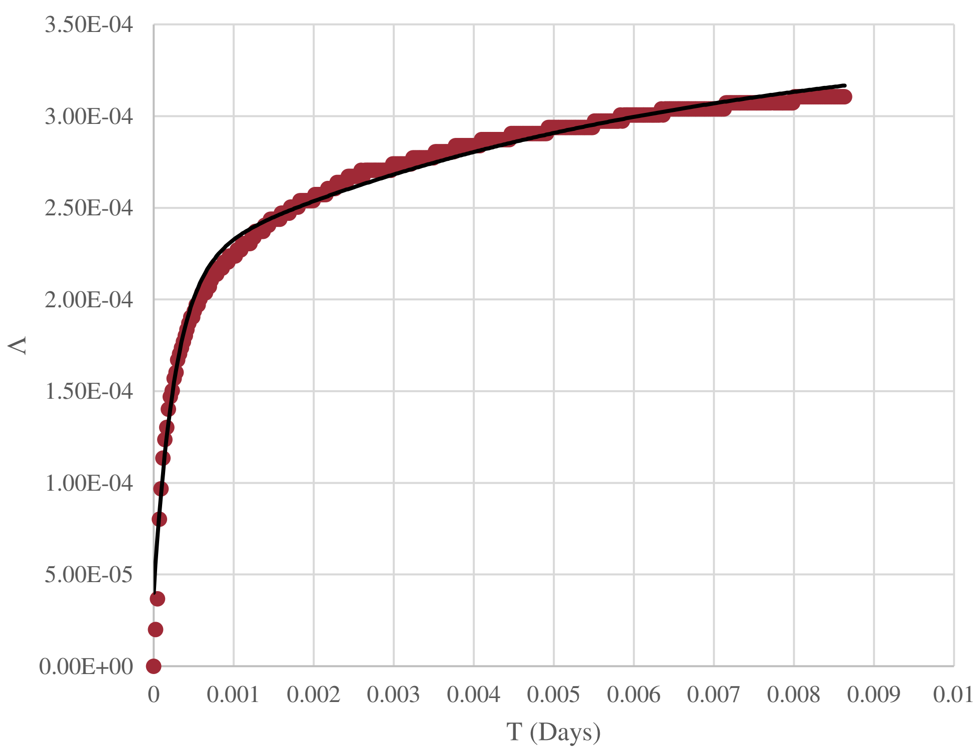

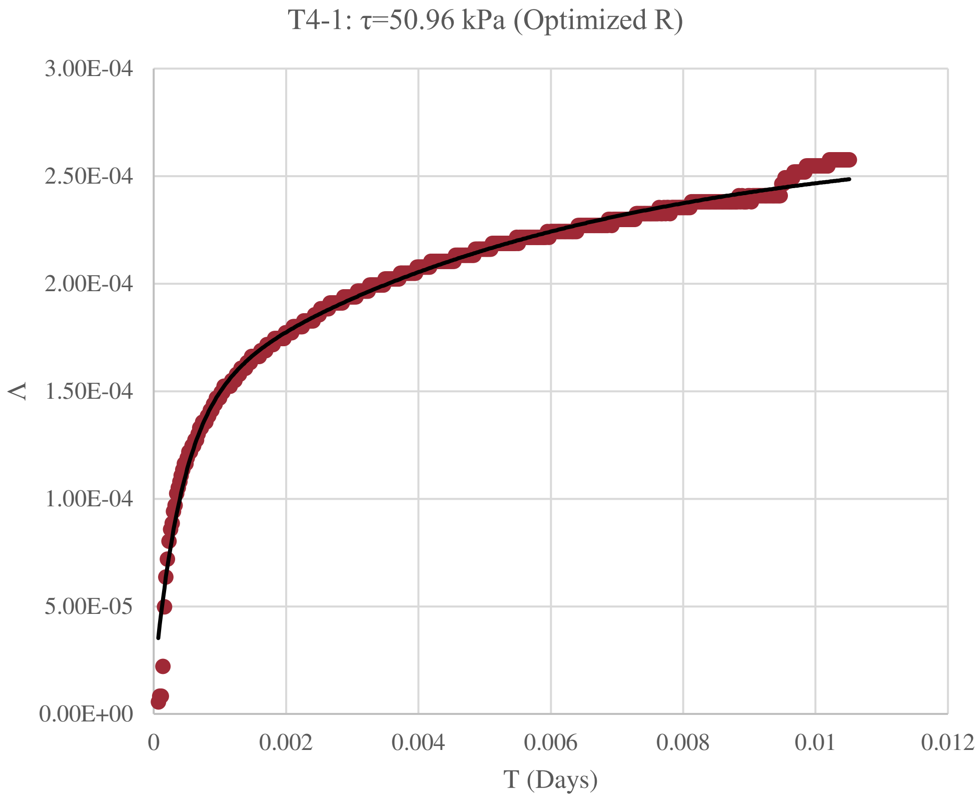
T4-1: τ=50.96 kPa (Optimized R)
3.00E-04
2.50E-04
2.00E-04
1.50E-04
1.00E-04
5.00E-05
0.00E+00
Λ
0
0.002
0.004
0.006
0.008
0.01
0.012
T (Days)

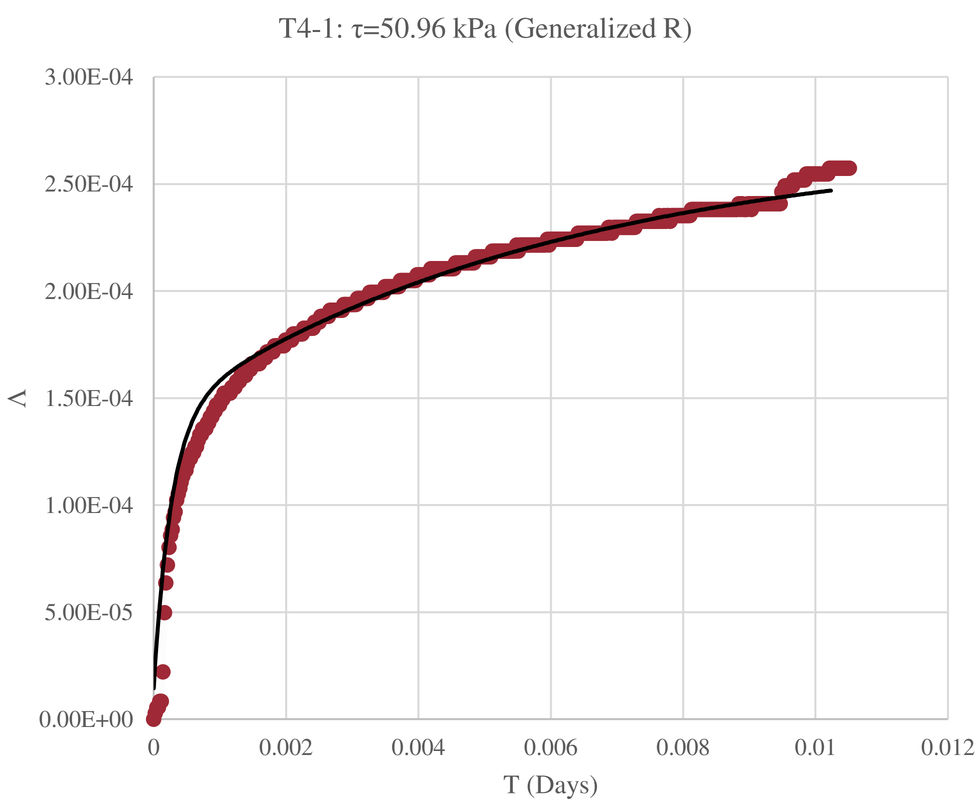
T4-1: τ=50.96 kPa (Generalized R)
3.00E-04
2.50E-04
2.00E-04
1.50E-04
1.00E-04
5.00E-05
0.00E+00
Λ
0
0.002
0.004
0.006
0.008
0.01
0.012
T (Days)

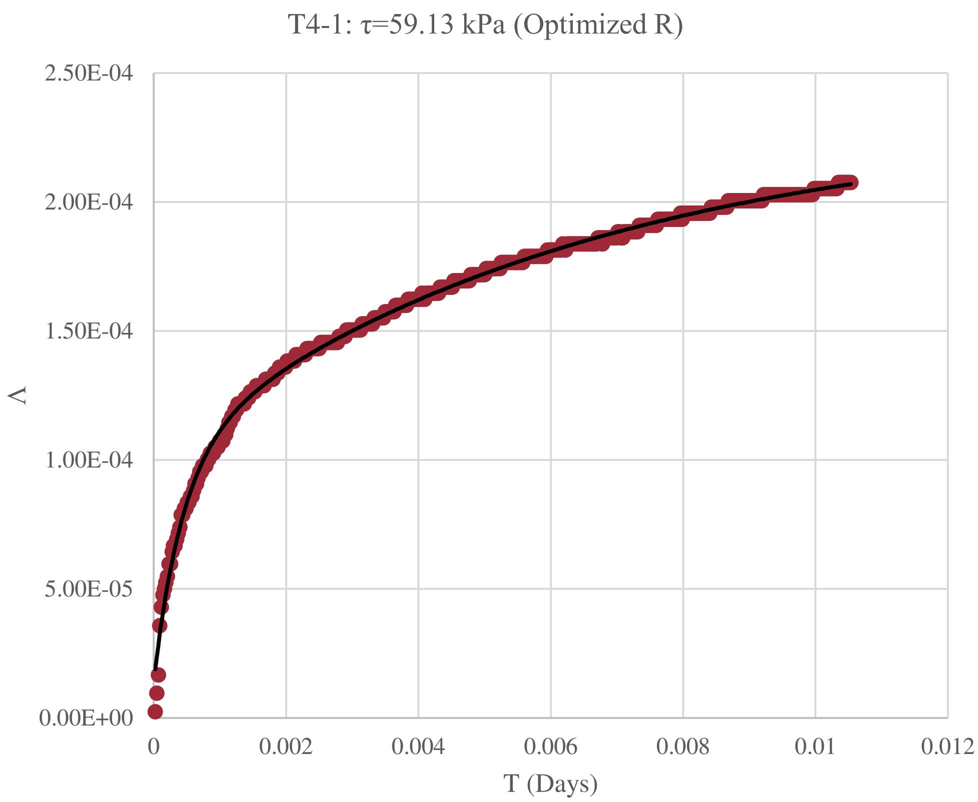
T4-1: τ=59.13 kPa (Optimized R)
2.50E-04
2.00E-04
1.50E-04
1.00E-04
5.00E-05
0.00E+00
Λ
0
0.002
0.004
0.006
0.008
0.01
0.012
T (Days)

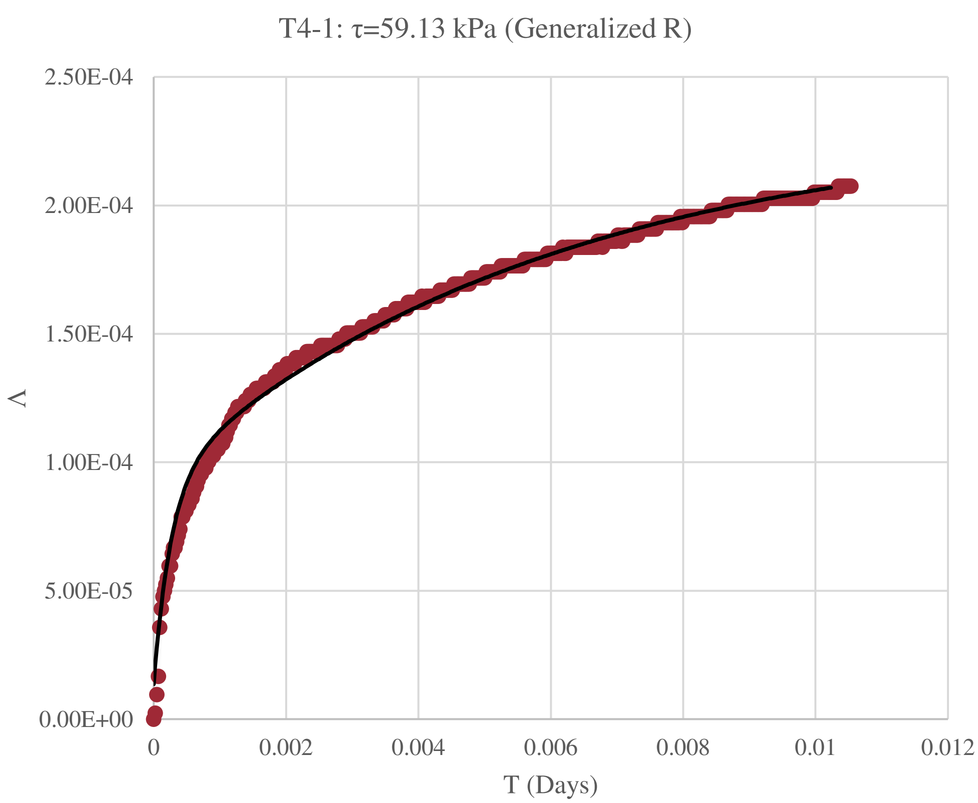
T4-1: τ=59.13 kPa (Generalized R)
2.50E-04
2.00E-04
1.50E-04
1.00E-04
5.00E-05
0.00E+00
Λ
0
0.002
0.004
0.006
0.008
0.01
0.012
T (Days)

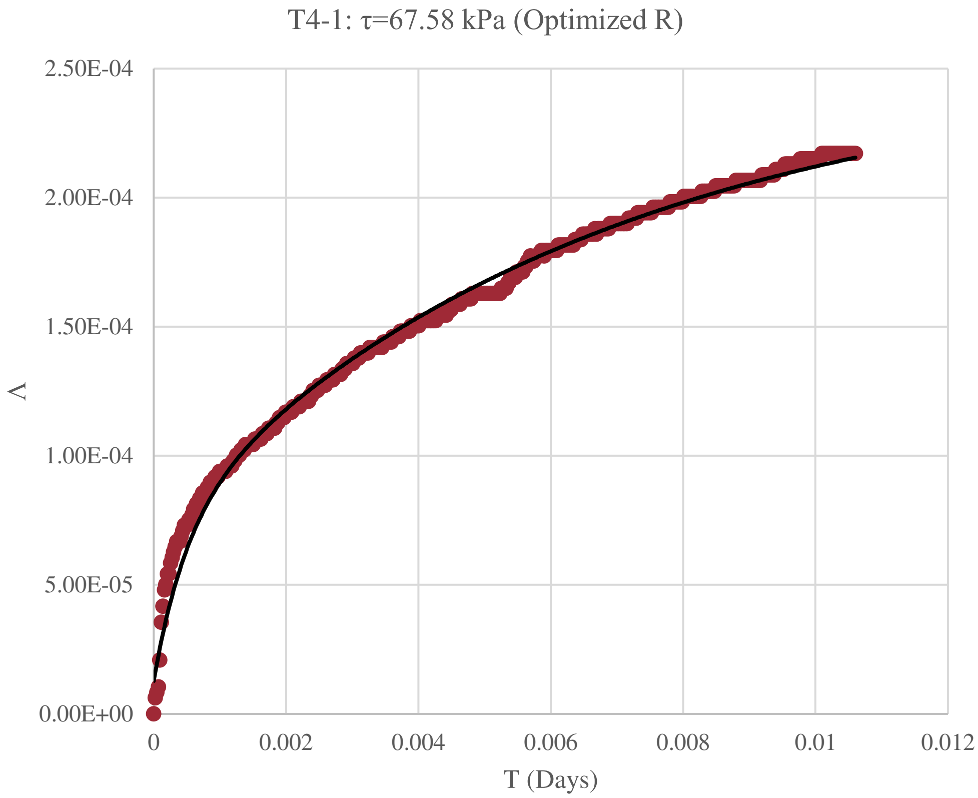
T4-1: τ=67.58 kPa (Optimized R)
2.50E-04
2.00E-04
1.50E-04
1.00E-04
5.00E-05
0.00E+00
Λ
0
0.002
0.004
0.006
0.008
0.01
0.012
T (Days)

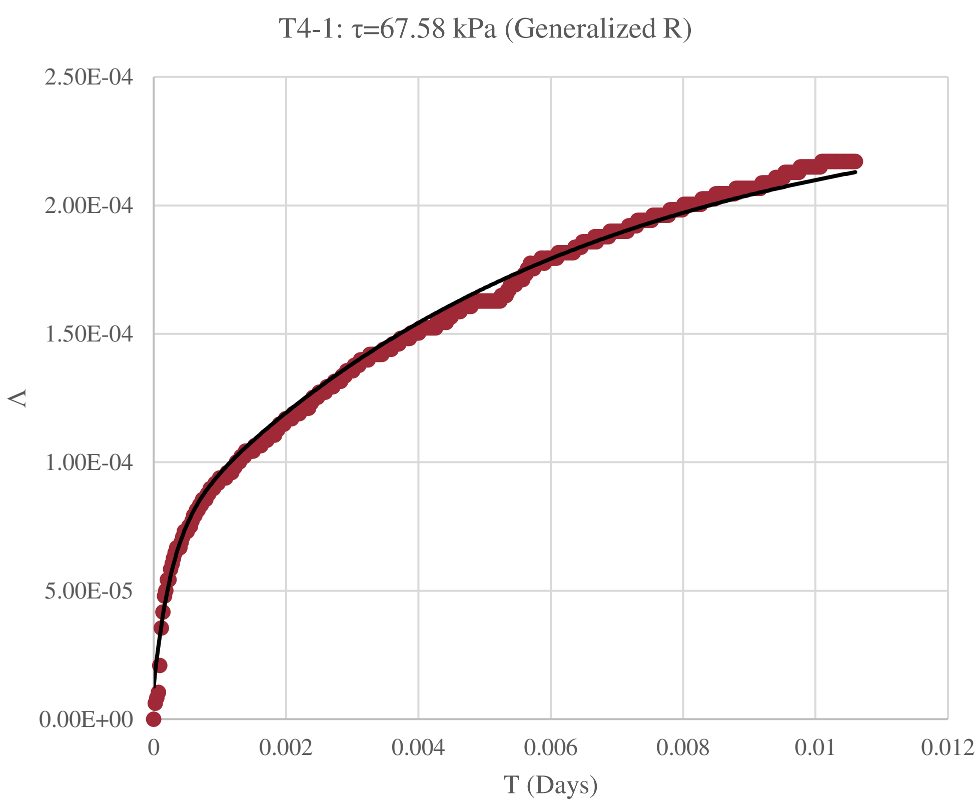
T4-1: τ=67.58 kPa (Generalized R)
2.50E-04
2.00E-04
1.50E-04
1.00E-04
5.00E-05
0.00E+00
Λ
0
0.002
0.004
0.006
0.008
0.01
0.012
T (Days)

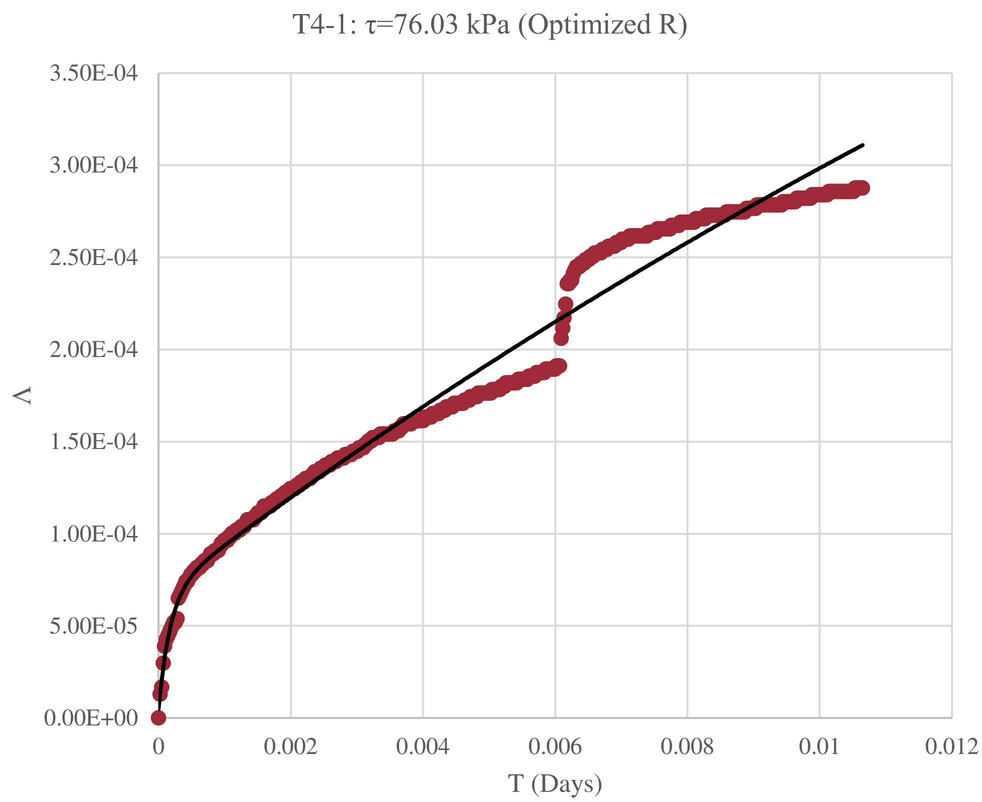
T4-1: τ=76.03 kPa (Optimized R)
3.50E-04
3.00E-04
2.50E-04
2.00E-04
1.50E-04
1.00E-04
5.00E-05
0.00E+00
Λ
0
0.002
0.004
0.006
0.008
0.01
0.012
T (Days)

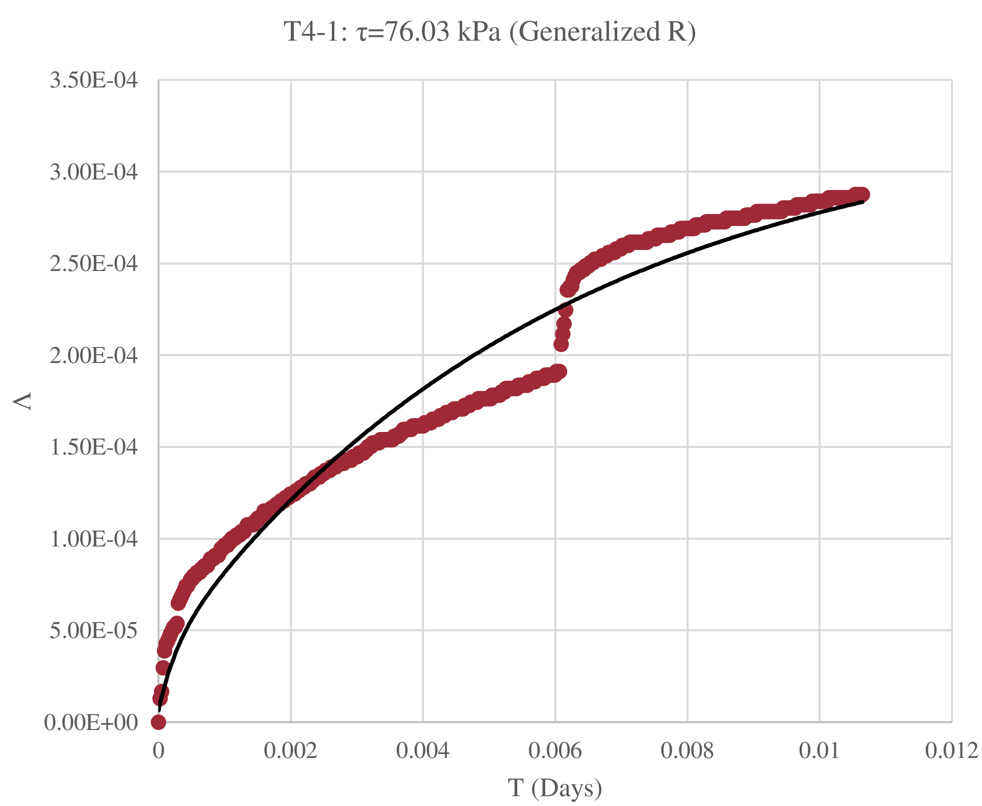
T4-1: τ=76.03 kPa (Generalized R)
3.50E-04
3.00E-04
2.50E-04
2.00E-04
1.50E-04
1.00E-04
5.00E-05
0.00E+00
Λ
0
0.002
0.004
0.006
0.008
0.01
0.012
T (Days)

7.4.2 T4-2

T4-2: τmax = 88 kPa, Optimized Retardation Times						
τ (kPa)	CSR-N	G_{Di} (kPa)	G_{D1} (kPa)	G_{D2} (kPa)	R_1 (d)	R_2 (d)
8.45	0.21	4024	2247	3536	1.00E-04	2.43E-03
16.9	0.42	22065	692	4972	5.04E-05	1.91E-03
25.34	0.58	22928	1953	7138	4.66E-05	1.85E-03
33.79	0.70	24262	4913	7914	5.15E-05	1.88E-03
42.24	0.80	20085	8999	7913	1.86E-04	2.89E-03
50.96	0.89	25432	14064	7964	2.96E-04	5.50E-03
59.13	0.96	25312	14034	8782	2.98E-04	5.51E-03
67.58	0.99	47902	17324	6375	3.33E-04	5.09E-03
76.03	0.99	73120	39768	4042	3.96E-04	8.86E0-3

T4-2: τmax = 88 kPa, Generalized Retardation Times						
τ (kPa)	CSR-N	G_{Di} (kPa)	G_{D1} (kPa)	G_{D2} (kPa)	RG_1 (d)	RG_2 (d)
8.45	0.21	2204	3048	3915	2.63E-04	5.96E-03
16.9	0.42	808	2905	6676	2.63E-04	5.96E-03
25.34	0.58	2458	4648	10114	2.63E-04	5.96E-03
33.79	0.70	6596	6651	10606	2.63E-04	5.96E-03
42.24	0.80	8843	12290	8797	2.63E-04	5.96E-03
50.96	0.89	24510	13204	8308	2.63E-04	5.96E-03
59.13	0.96	30731	17485	6953	2.63E-04	5.96E-03
67.58	0.99	49070	18364	6991	2.63E-04	5.96E-03
76.03	0.99	132324	46849	5063	2.63E-04	5.96E-03

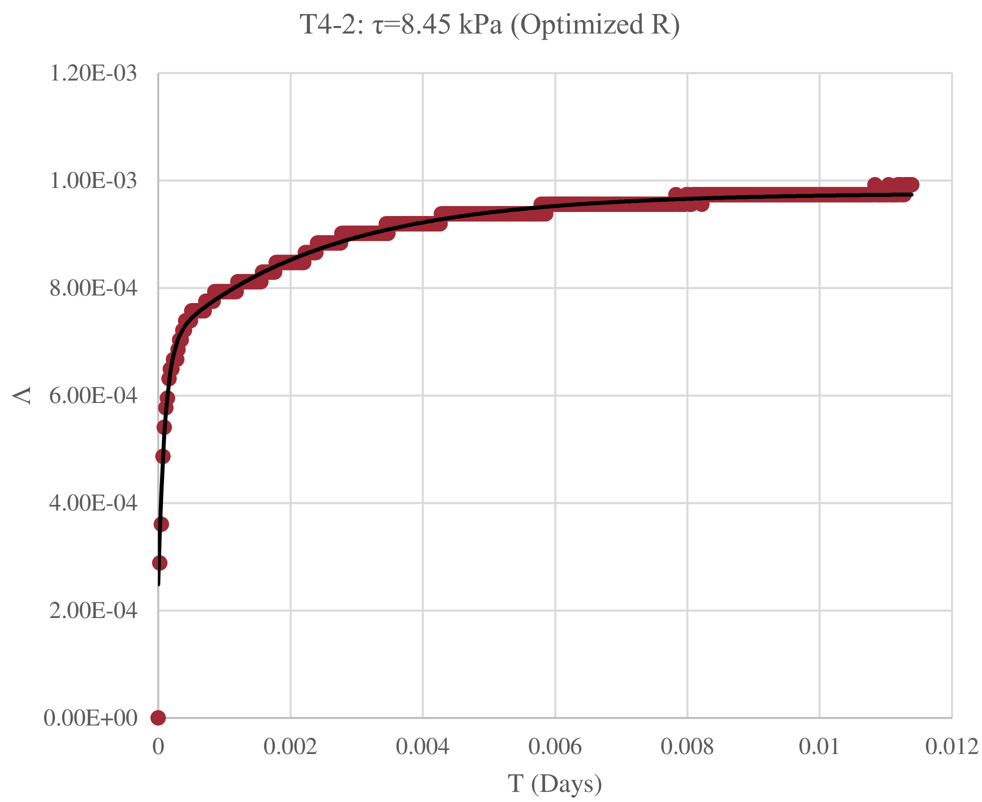
T4-2: τ=8.45 kPa (Optimized R)
1.20E-03
1.00E-03
8.00E-04
6.00E-04
4.00E-04
2.00E-04
0.00E+00
Λ
0
0.002
0.004
0.006
0.008
0.01
0.012
T (Days)

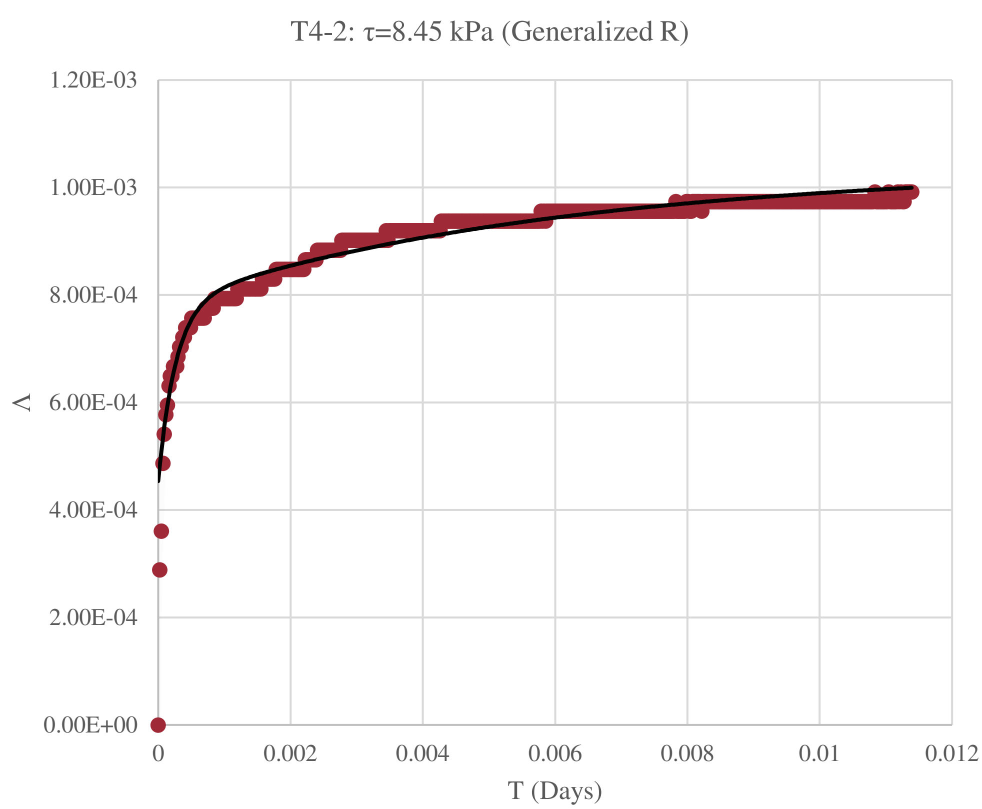
T4-2: τ=8.45 kPa (Generalized R)
1.20E-03
1.00E-03
8.00E-04
6.00E-04
4.00E-04
2.00E-04
0.00E+00
Λ
0
0.002
0.004
0.006
0.008
0.01
0.012
T (Days)

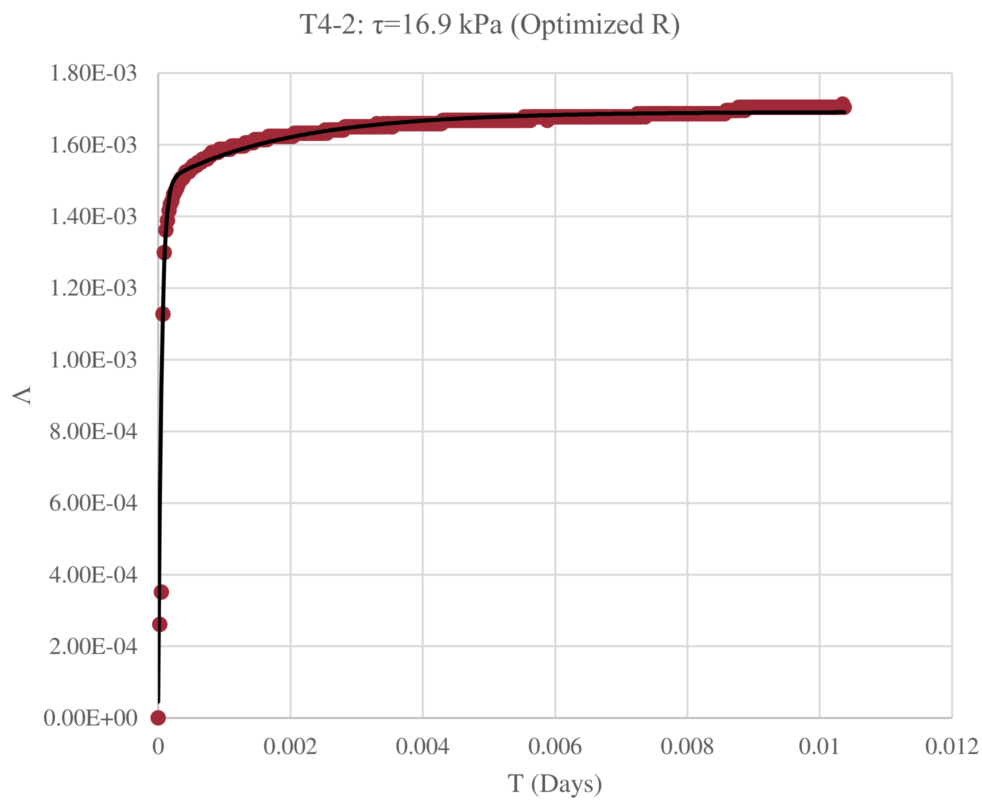
T4-2: τ=16.9 kPa (Optimized R)
1.80E-03
1.60E-03
1.40E-03
1.20E-03
1.00E-03
8.00E-04
6.00E-04
4.00E-04
2.00E-04
0.00E+00
Λ
0
0.002
0.004
0.006
0.008
0.01
0.012
T (Days)

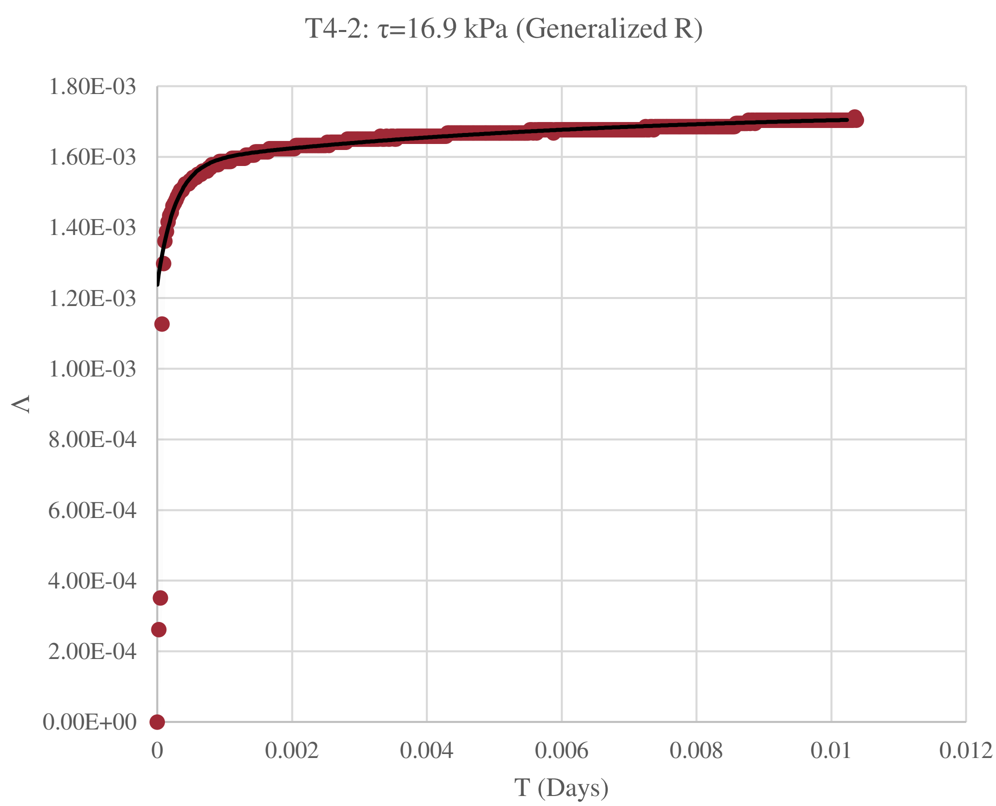
T4-2: τ=16.9 kPa (Generalized R)
1.80E-03
1.60E-03
1.40E-03
1.20E-03
1.00E-03
8.00E-04
6.00E-04
4.00E-04
2.00E-04
0.00E+00
Λ
0
0.002
0.004
0.006
0.008
0.01
0.012
T (Days)

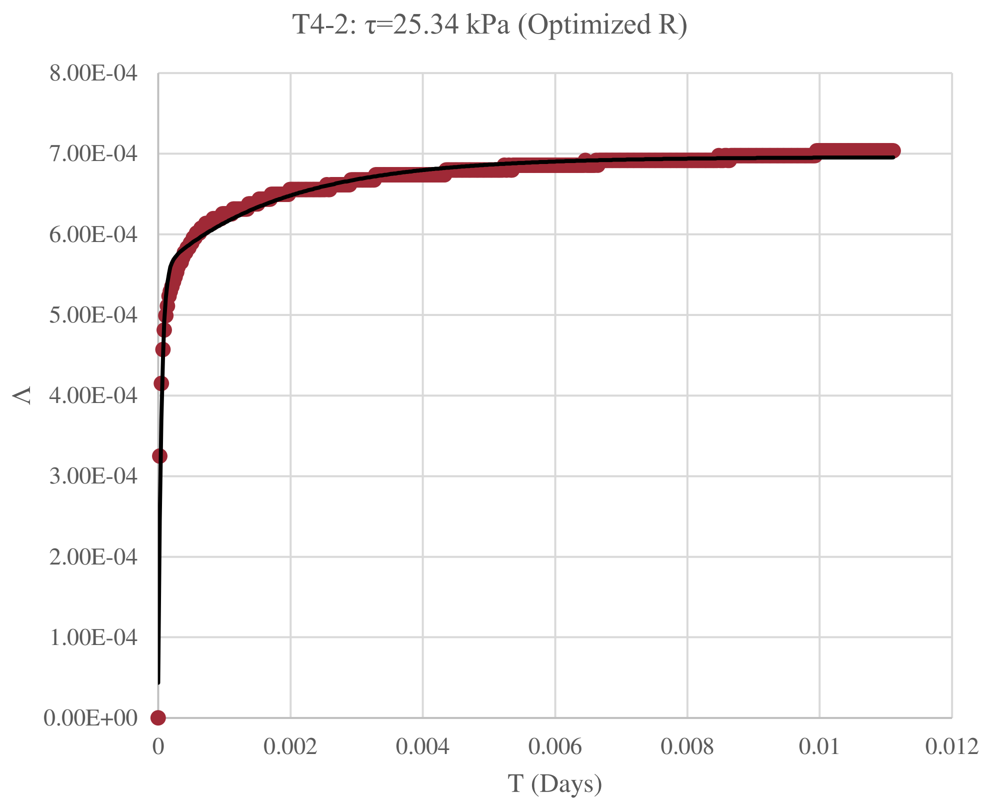
T4-2: τ=25.34 kPa (Optimized R)
8.00E-04
7.00E-04
6.00E-04
5.00E-04
4.00E-04
3.00E-04
2.00E-04
1.00E-04
0.00E+00
Λ
0
0.002
0.004
0.006
0.008
0.01
0.012
T (Days)

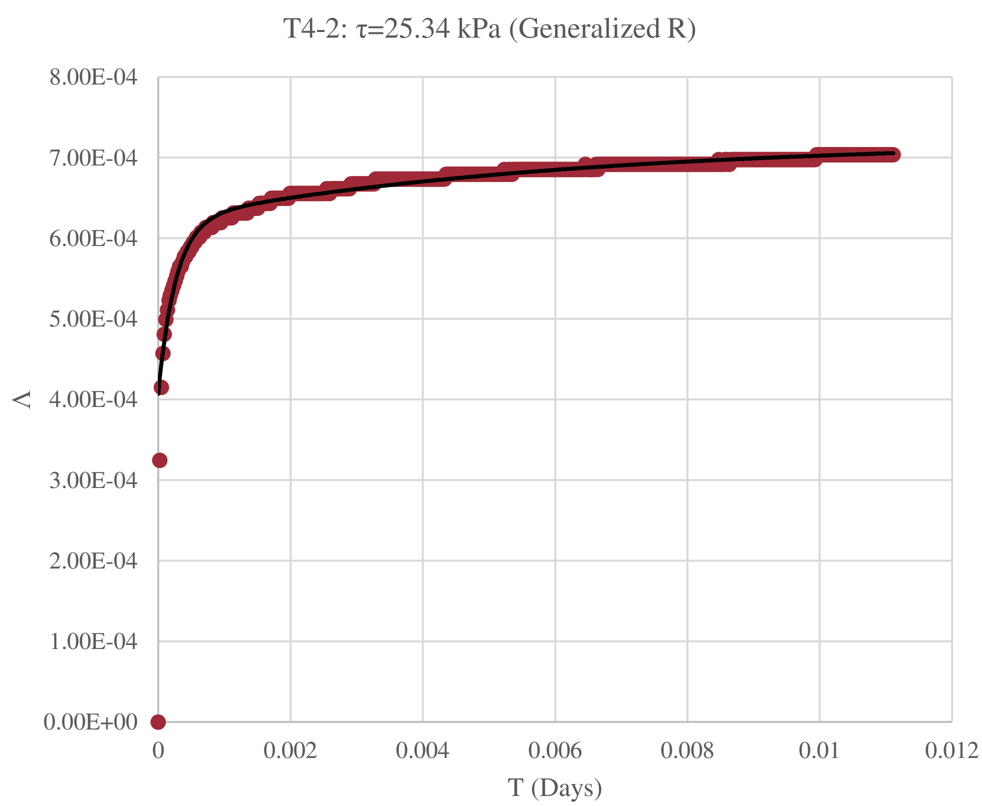
T4-2: τ=25.34 kPa (Generalized R)
8.00E-04
7.00E-04
6.00E-04
5.00E-04
4.00E-04
3.00E-04
2.00E-04
1.00E-04
0.00E+00
Λ
0
0.002
0.004
0.006
0.008
0.01
0.012
T (Days)

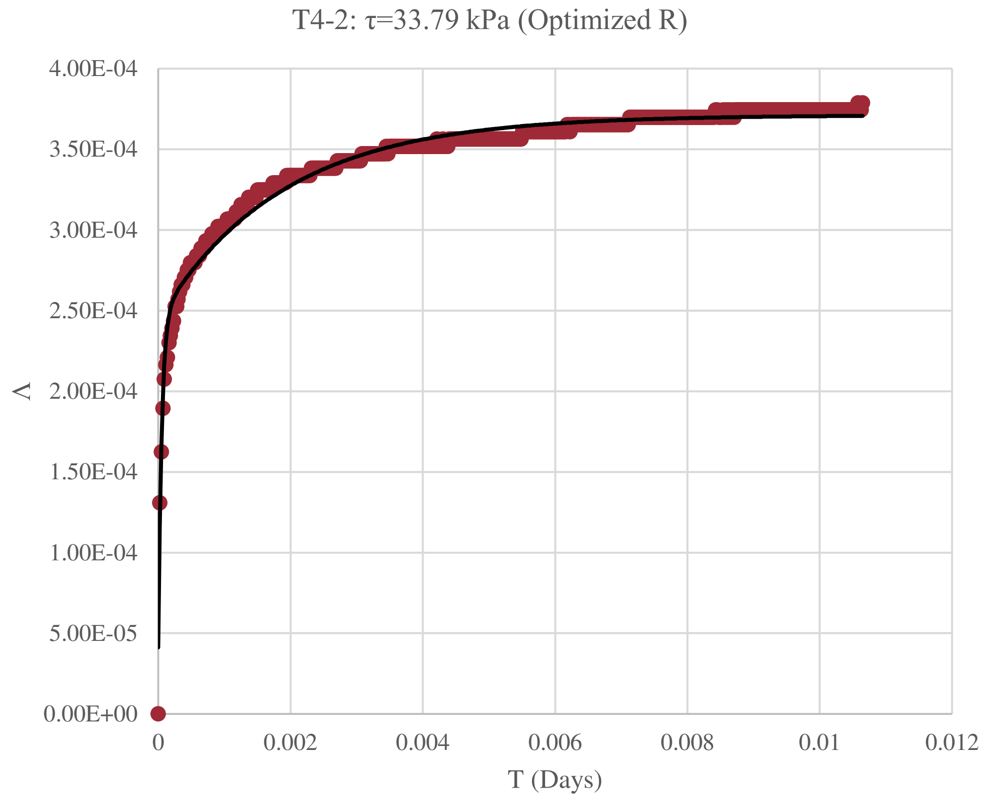
T4-2: τ=33.79 kPa (Optimized R)
4.00E-04
3.50E-04
3.00E-04
2.50E-04
2.00E-04
1.50E-04
1.00E-04
5.00E-05
0.00E+00
Λ
0
0.002
0.004
0.006
0.008
0.01
0.012
T (Days)

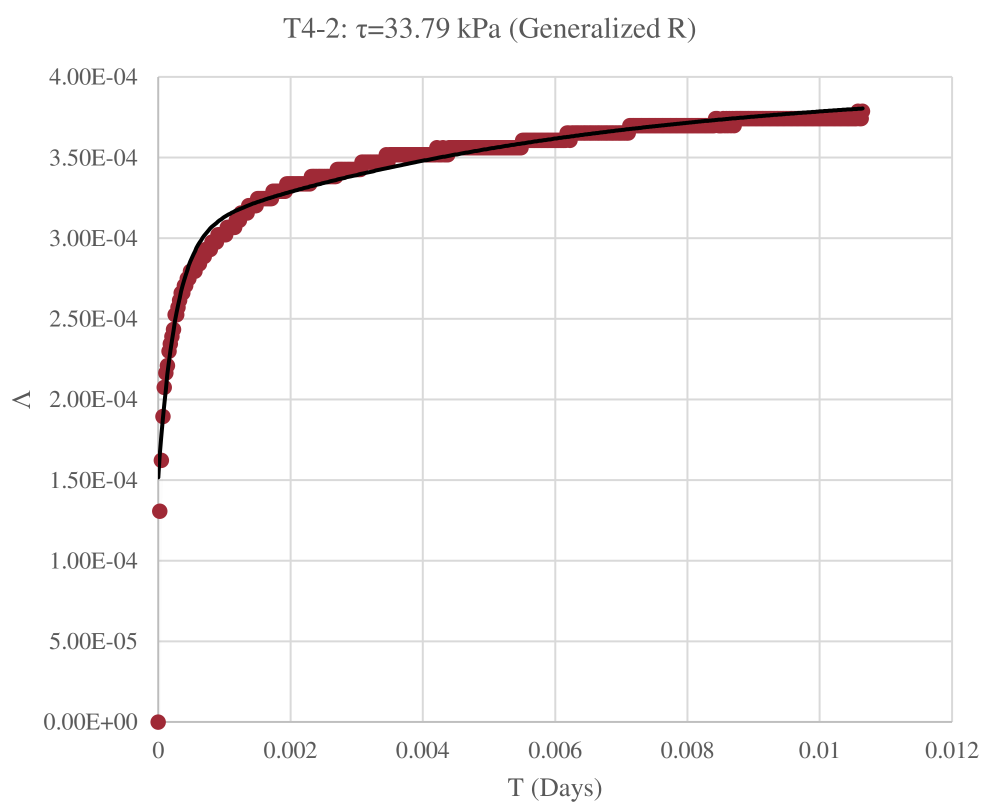
T4-2: τ=33.79 kPa (Generalized R)
4.00E-04
3.50E-04
3.00E-04
2.50E-04
2.00E-04
1.50E-04
1.00E-04
5.00E-05
0.00E+00
Λ
0
0.002
0.004
0.006
0.008
0.01
0.012
T (Days)

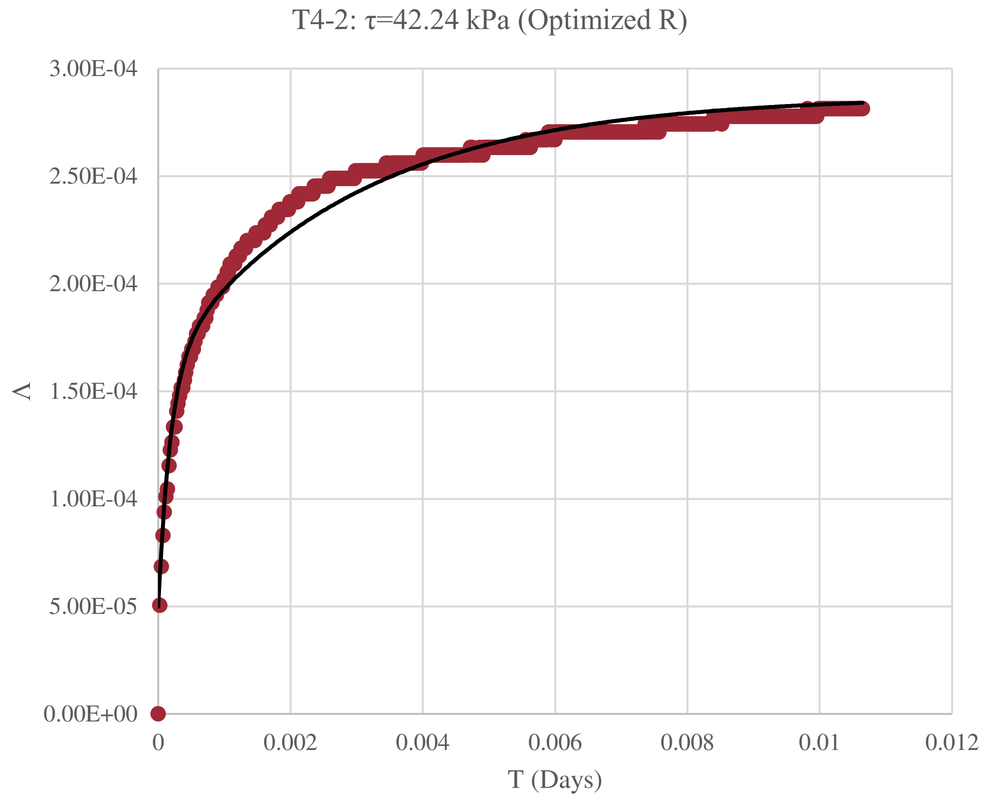
T4-2: τ=42.24 kPa (Optimized R)
3.00E-04
2.50E-04
2.00E-04
1.50E-04
1.00E-04
5.00E-05
0.00E+00
Λ
0
0.002
0.004
0.006
0.008
0.01
0.012
T (Days)

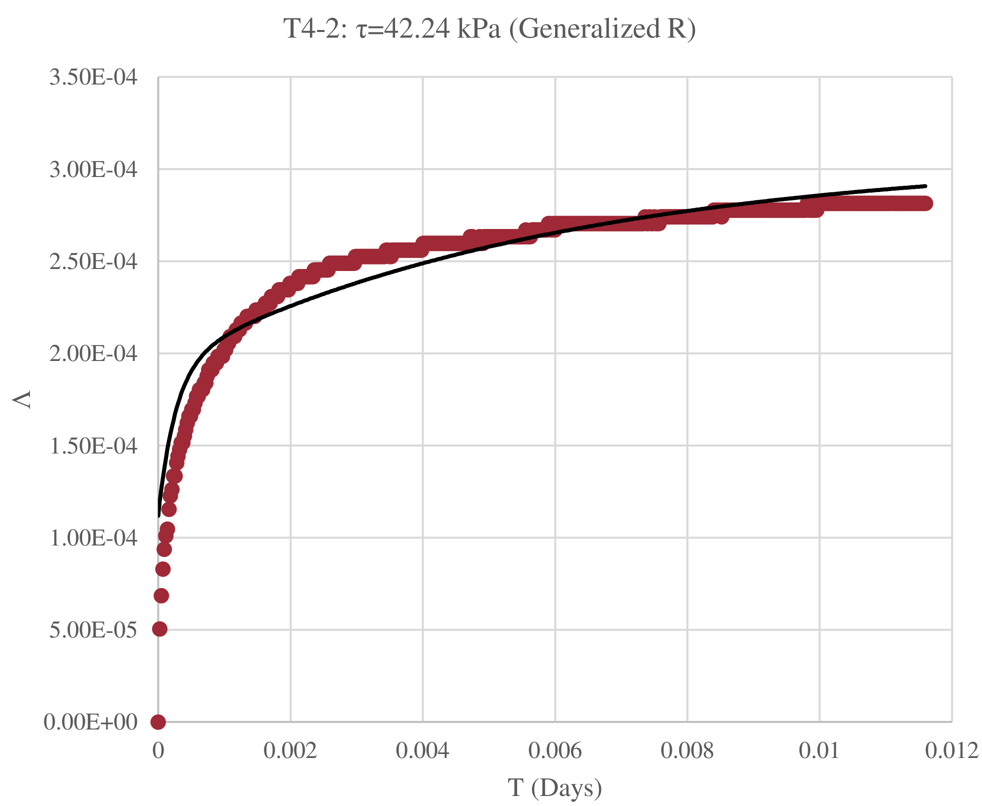
T4-2: τ=42.24 kPa (Generalized R)
3.50E-04
3.00E-04
2.50E-04
2.00E-04
1.50E-04
1.00E-04
5.00E-05
0.00E+00
Λ
0
0.002
0.004
0.006
0.008
0.01
0.012
T (Days)

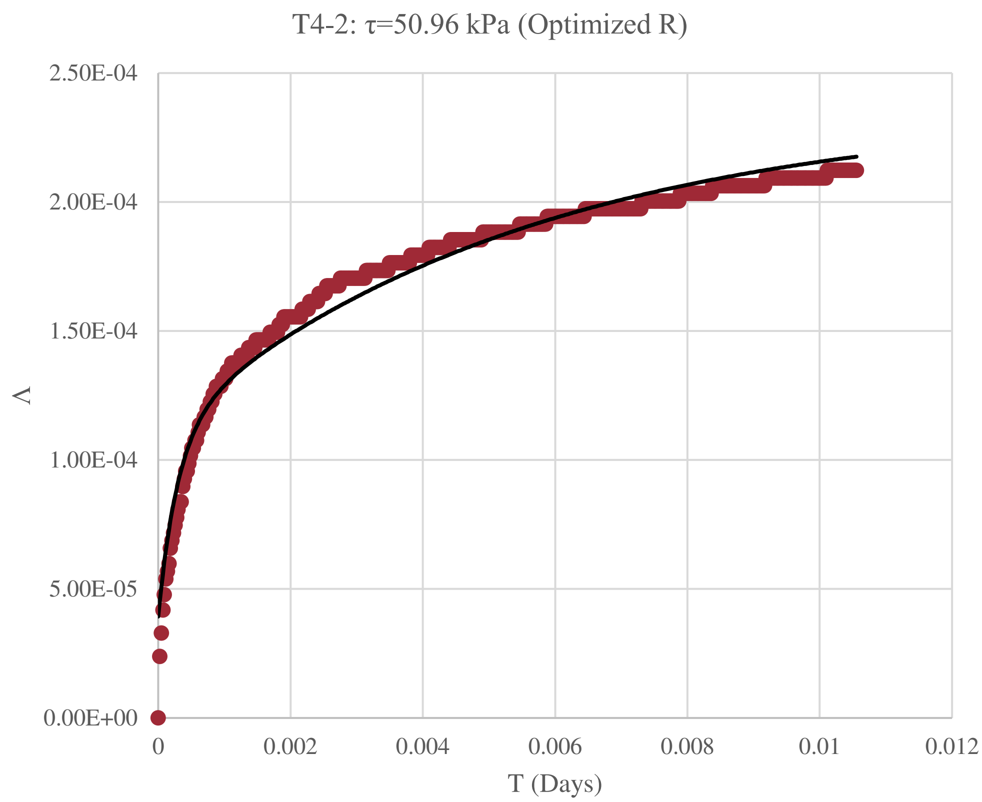
T4-2: τ=50.96 kPa (Optimized R)
2.50E-04
2.00E-04
1.50E-04
1.00E-04
5.00E-05
0.00E+00
Λ
0
0.002
0.004
0.006
0.008
0.01
0.012
T (Days)

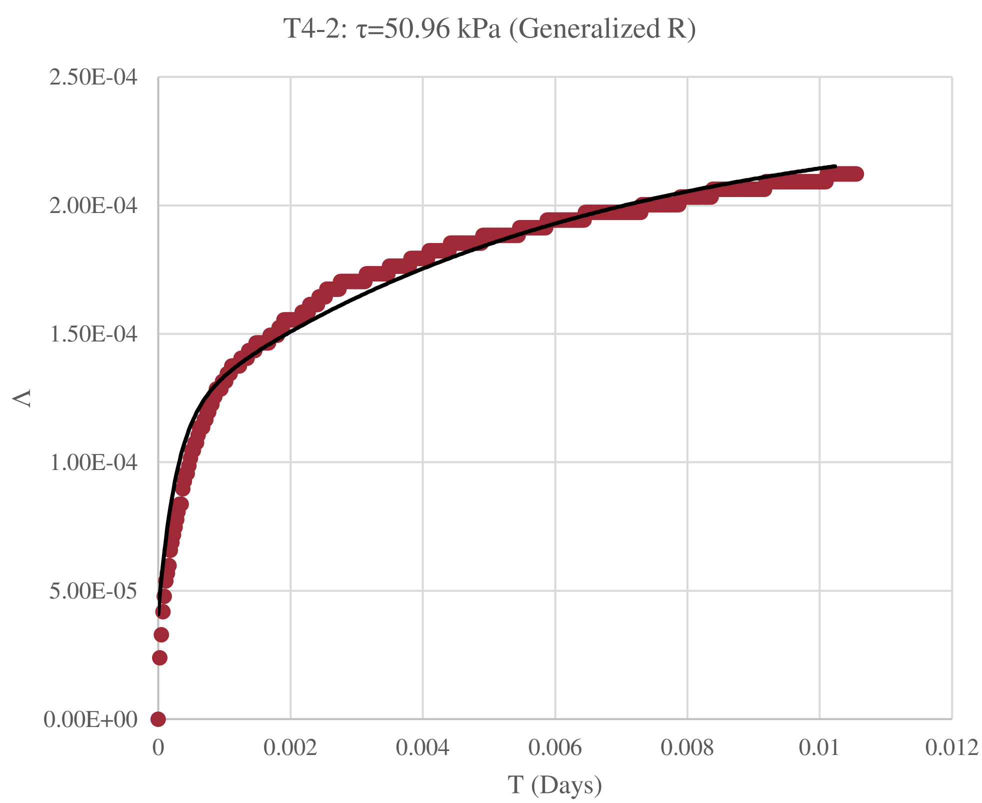
T4-2: τ=50.96 kPa (Generalized R)
2.50E-04
2.00E-04
1.50E-04
1.00E-04
5.00E-05
0.00E+00
Λ
0
0.002
0.004
0.006
0.008
0.01
0.012
T (Days)

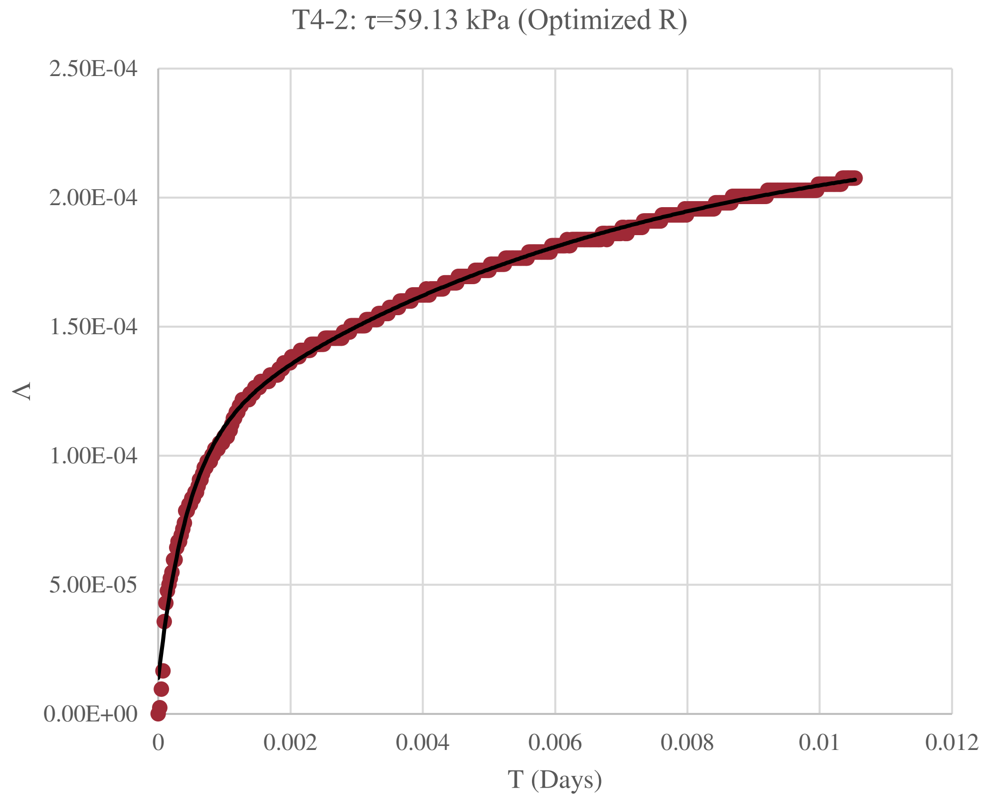
T4-2: τ=59.13 kPa (Optimized R)
2.50E-04
2.00E-04
1.50E-04
1.00E-04
5.00E-05
0.00E+00
Λ
0
0.002
0.004
0.006
0.008
0.01
0.012
T (Days)

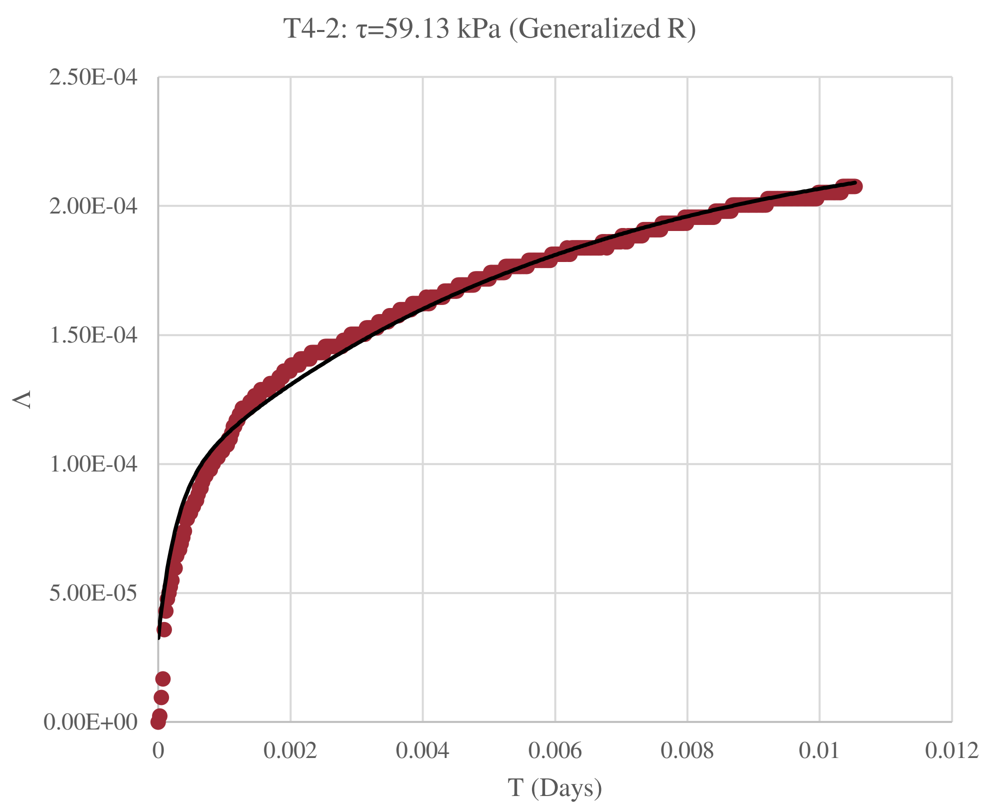
T4-2: τ=59.13 kPa (Generalized R)
2.50E-04
2.00E-04
1.50E-04
1.00E-04
5.00E-05
0.00E+00
Λ
0
0.002
0.004
0.006
0.008
0.01
0.012
T (Days)

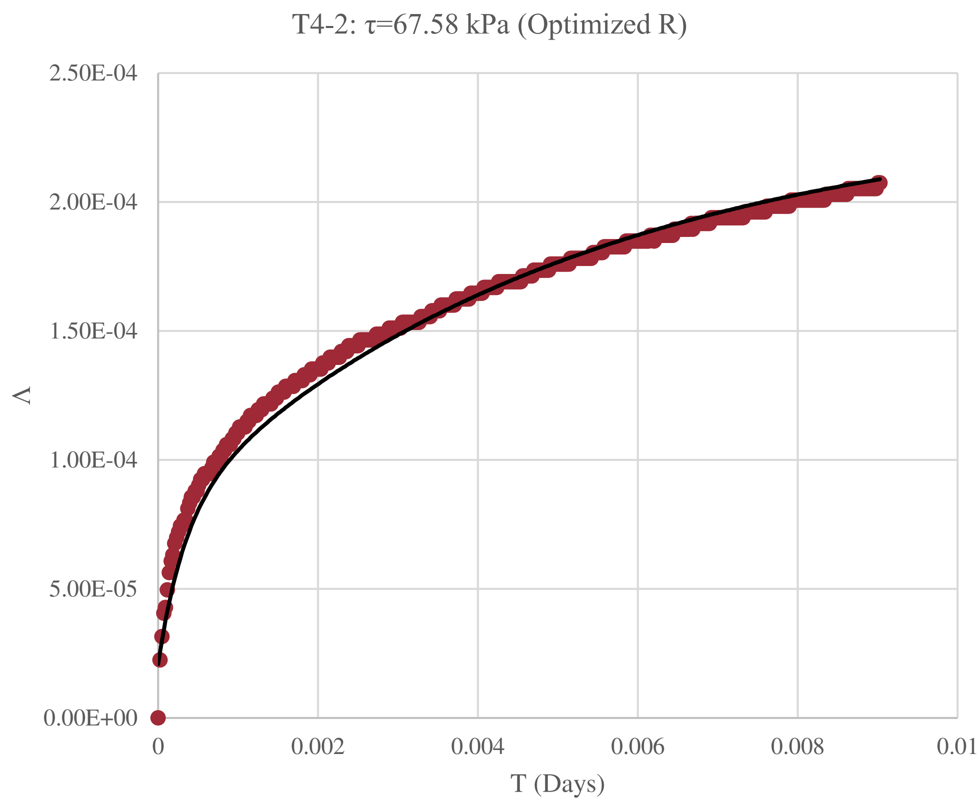
T4-2: τ=67.58 kPa (Optimized R)
2.50E-04
2.00E-04
1.50E-04
1.00E-04
5.00E-05
0.00E+00
Λ
0
0.002
0.004
0.006
0.008
0.01
T (Days)

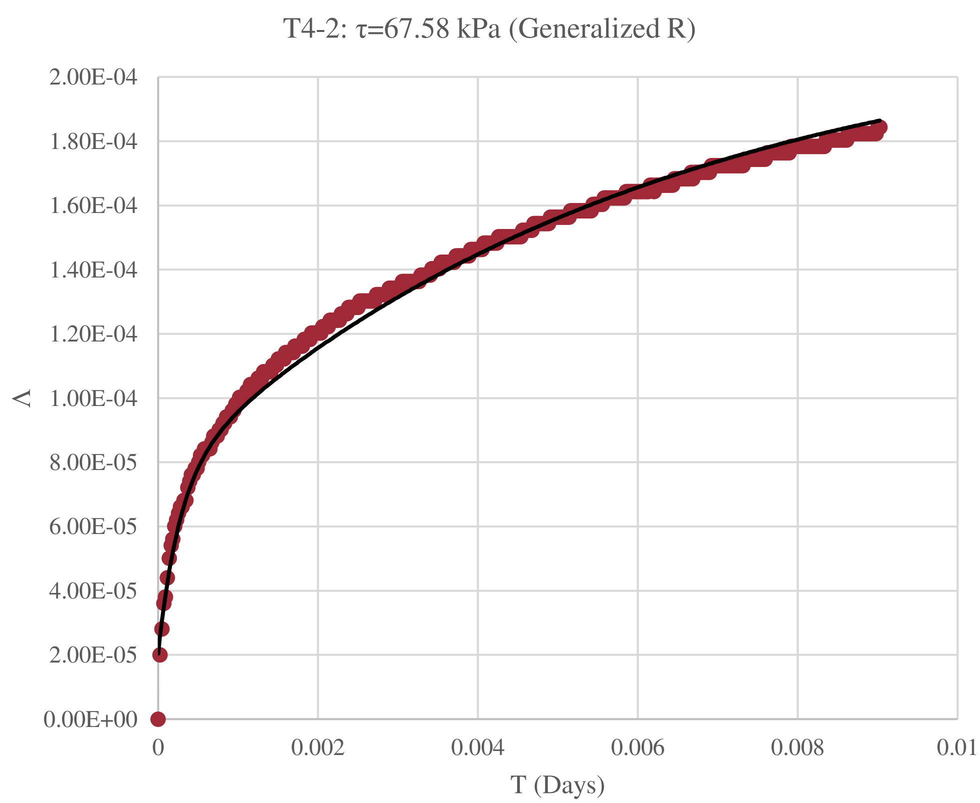
T4-2: τ=67.58 kPa (Generalized R)
2.00E-04
1.80E-04
1.60E-04
1.40E-04
1.20E-04
1.00E-04
8.00E-05
6.00E-05
4.00E-05
2.00E-05
0.00E+00
Λ
0
0.002
0.004
0.006
0.008
0.01
T (Days)

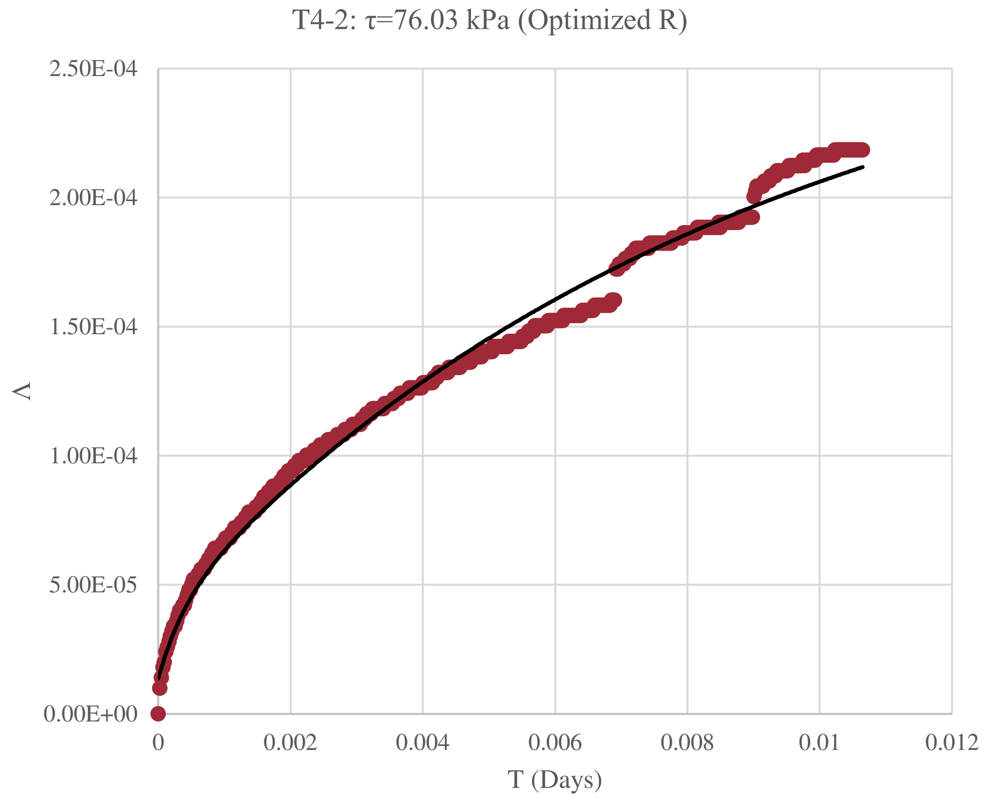
T4-2: τ=76.03 kPa (Optimized R)
2.50E-04
2.00E-04
1.50E-04
1.00E-04
5.00E-05
0.00E+00
Λ
0
0.002
0.004
0.006
0.008
0.01
0.012
T (Days)

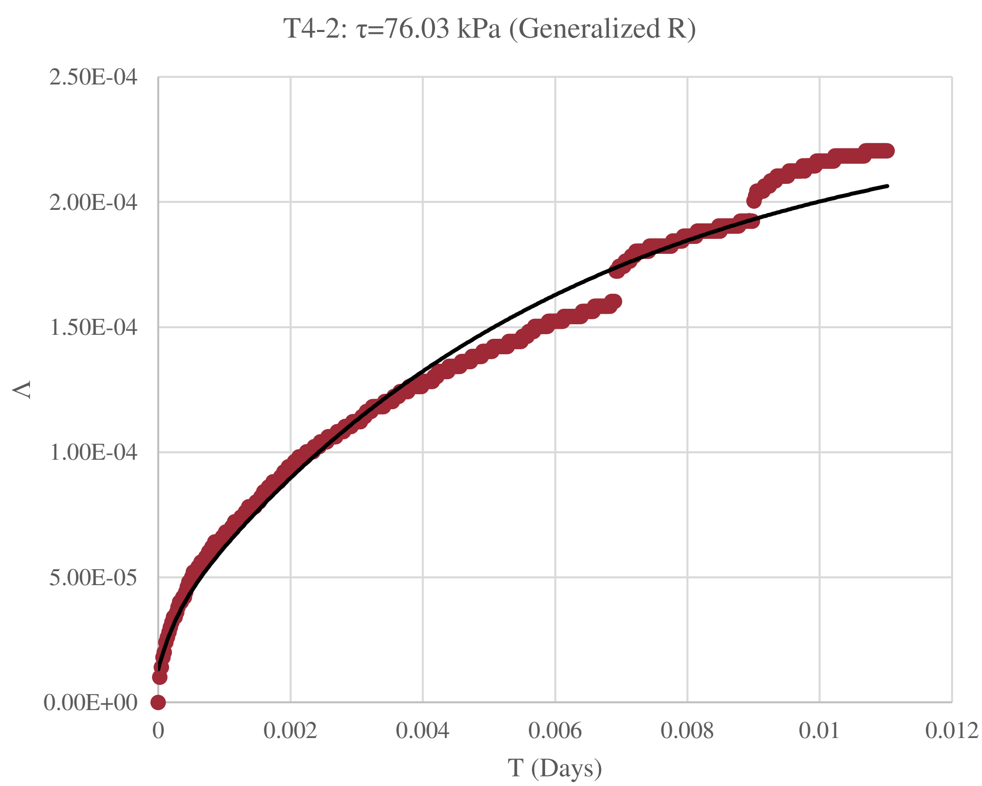
T4-2: τ=76.03 kPa (Generalized R)
2.50E-04
2.00E-04
1.50E-04
1.00E-04
5.00E-05
0.00E+00
Λ
0
0.002
0.004
0.006
0.008
0.01
0.012
T (Days)

7.4.3 T4-3

T4-3: τmax = 84 kPa, Optimized Retardation Times						
τ (kPa)	CSR-N	G_{Di} (kPa)	G_{D1} (kPa)	G_{D2} (kPa)	R_1 (d)	R_2 (d)
8.45	0.21	11981	10532	8998	2.62E-04	2.18E-03
16.9	0.39	11540	4334	3844	4.30E-04	4.07E-03
25.34	0.55	7592	1409	5977	9.61E-05	2.62E-03
33.79	0.66	11323	4803	6829	1.30E-04	2.57E-03
42.24	0.76	18376	7310	6563	1.85E-04	2.73E-03
50.96	0.84	17016	10918	7752	3.10E-04	4.08E-03
59.13	0.90	42895	10171	6763	2.97E-04	4.66E-03
67.58	0.94	100701	11261	6129	3.11E-04	5.05E-03
76.03	0.94	110664	12255	4180	5.14E-04	1.55E-02

T4-3: τmax = 84 kPa, Generalized Retardation Times						
τ (kPa)	CSR-N	G_{Di} (kPa)	G_{D1} (kPa)	G_{D2} (kPa)	RG_1 (d)	RG_2 (d)
8.45	0.21	10679	9208	8328	2.63E-04	5.96E-03
16.9	0.39	17365	3773	3296	2.63E-04	5.96E-03
25.34	0.55	1843	2801	7172	2.63E-04	5.96E-03
33.79	0.66	10734	4229	6523	2.63E-04	5.96E-03
42.24	0.76	17296	6244	5987	2.63E-04	5.96E-03
50.96	0.85	16640	10207	7070	2.63E-04	5.96E-03
59.13	0.89	42277	9554	6401	2.63E-04	5.96E-03
67.58	0.93	100242	10802	5856	2.63E-04	5.96E-03
76.03	0.95	100345	27545	4752	2.63E-04	5.96E-03

T4-3: τ=8.45 kPa (Optimized R)

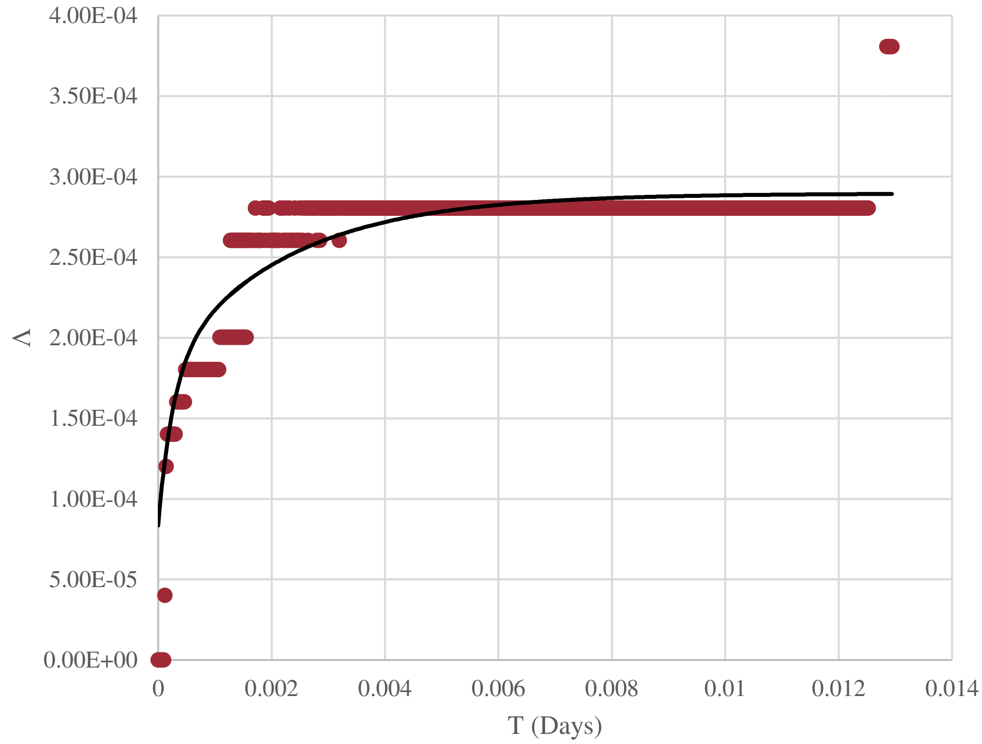

T4-3: τ=8.45 kPa (Generalized R)

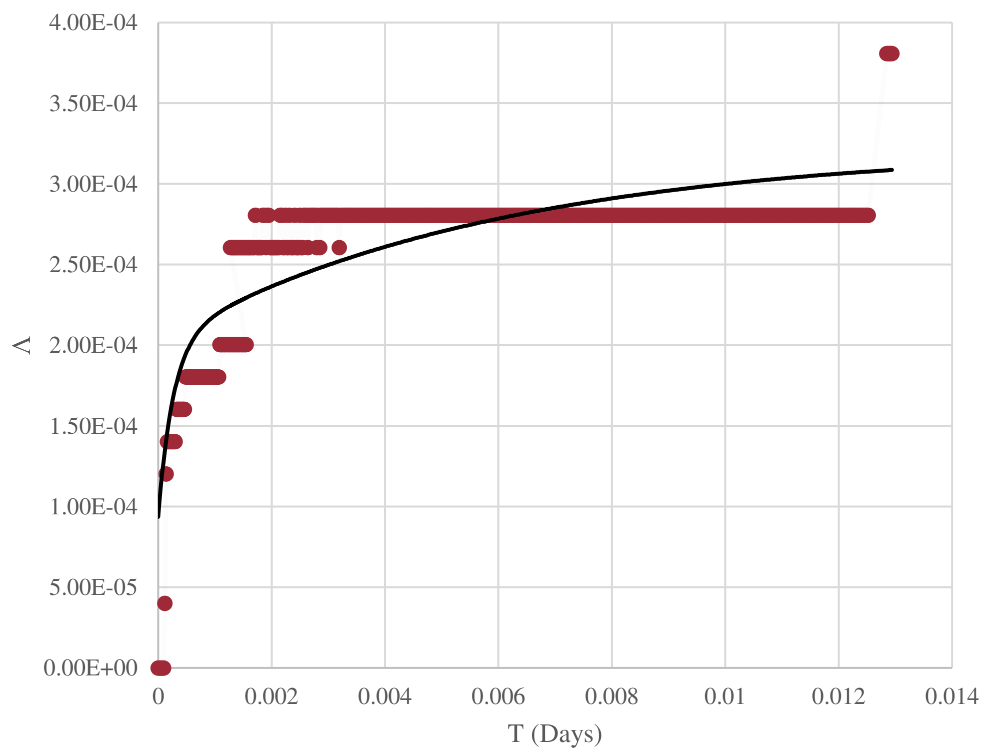

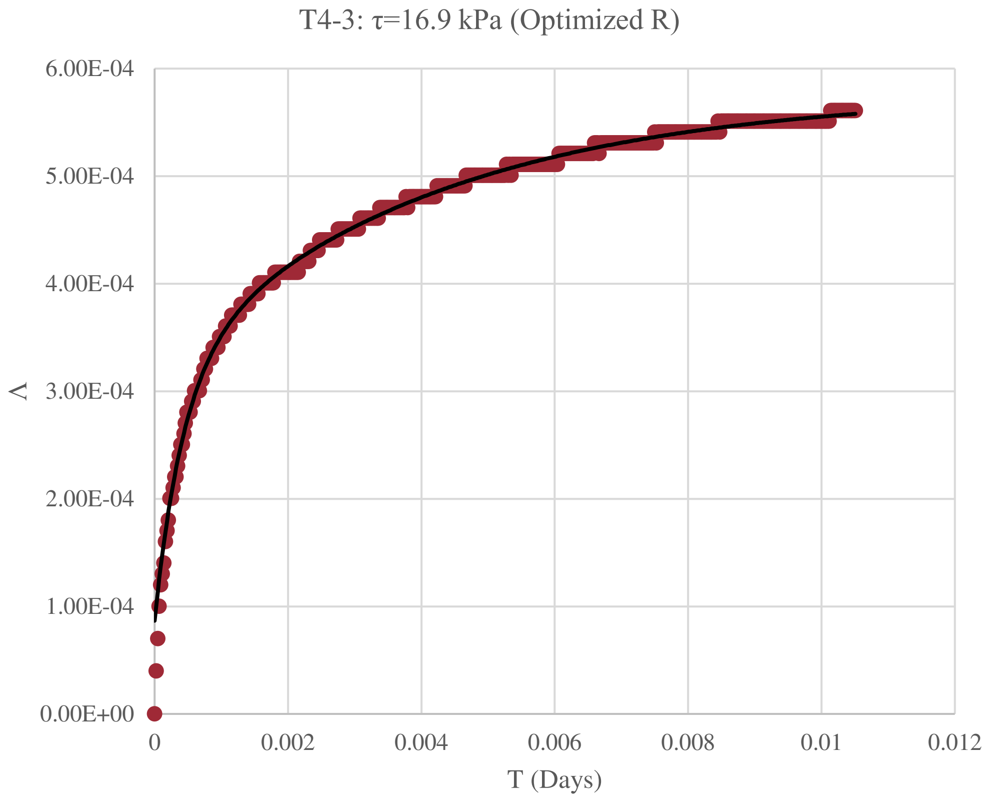
T4-3: τ=16.9 kPa (Optimized R)
6.00E-04
5.00E-04
4.00E-04
3.00E-04
2.00E-04
1.00E-04
0.00E+00
Λ
0
0.002
0.004
0.006
0.008
0.01
0.012
T (Days)

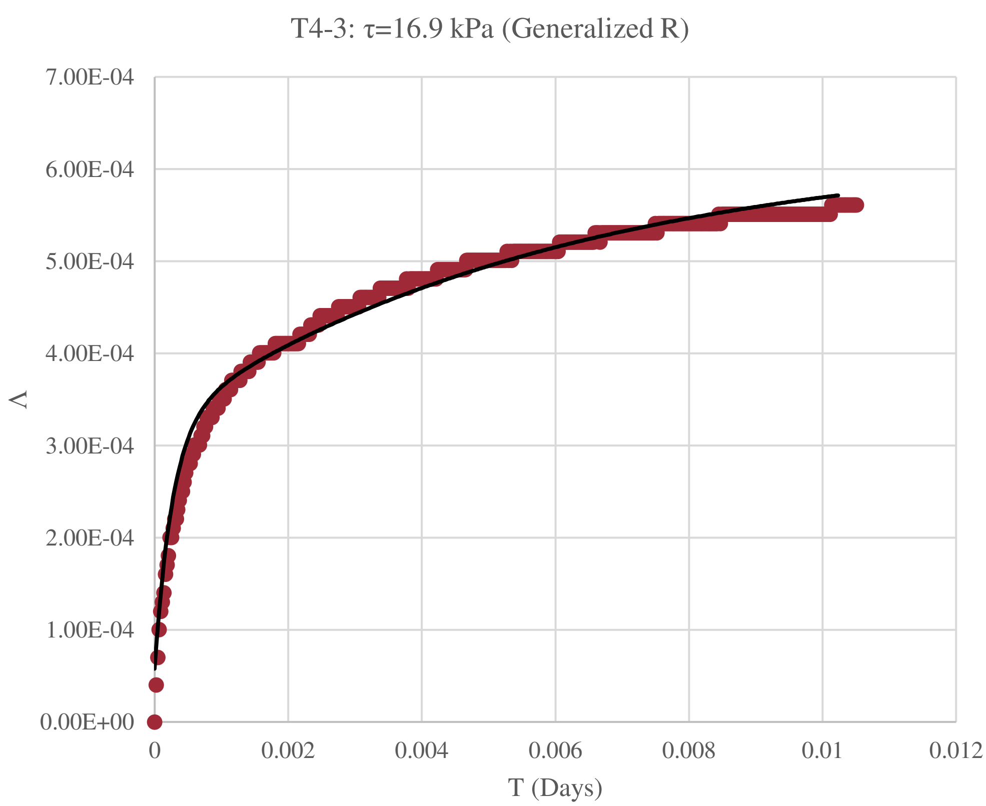
T4-3: τ=16.9 kPa (Generalized R)
7.00E-04
6.00E-04
5.00E-04
4.00E-04
3.00E-04
2.00E-04
1.00E-04
0.00E+00
Λ
0
0.002
0.004
0.006
0.008
0.01
0.012
T (Days)

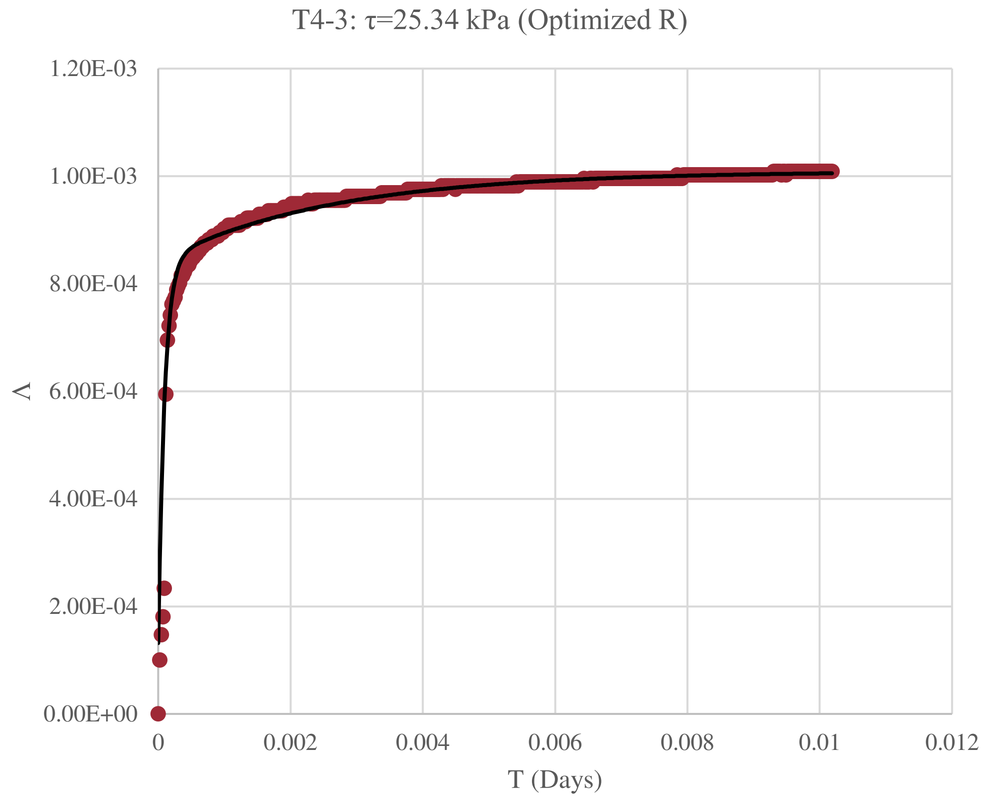
T4-3: τ=25.34 kPa (Optimized R)
1.20E-03
1.00E-03
8.00E-04
6.00E-04
4.00E-04
2.00E-04
0.00E+00
Λ
0
0.002
0.004
0.006
0.008
0.01
0.012
T (Days)

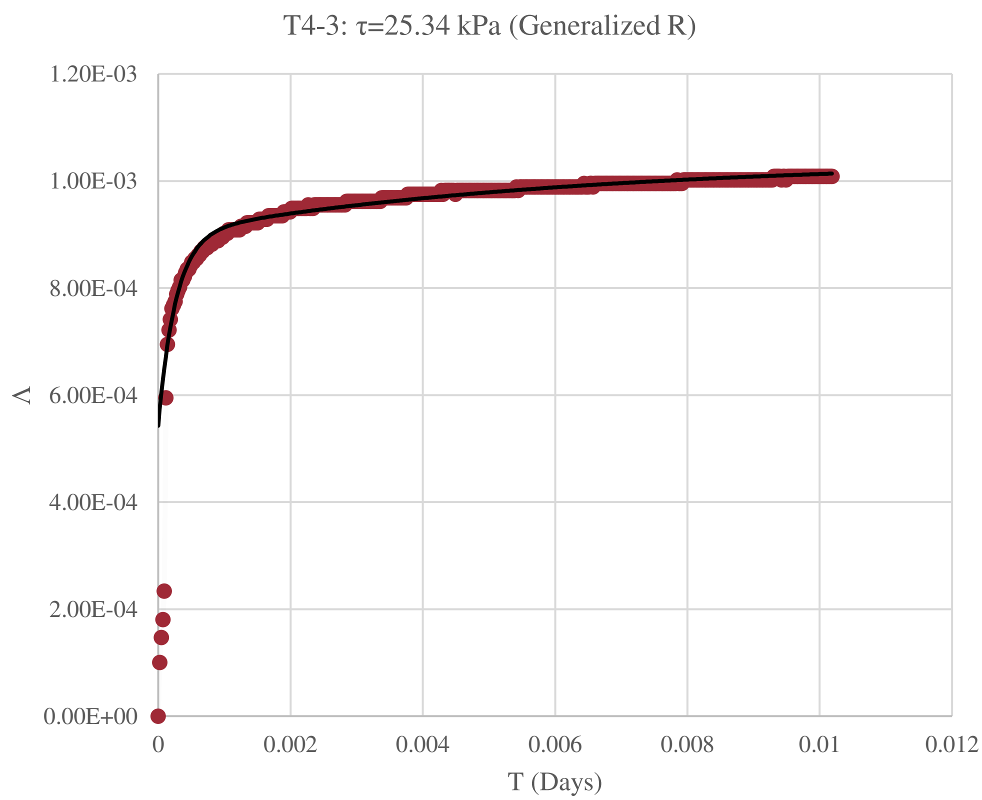
T4-3: τ=25.34 kPa (Generalized R)
1.20E-03
1.00E-03
8.00E-04
6.00E-04
4.00E-04
2.00E-04
0.00E+00
Λ
0
0.002
0.004
0.006
0.008
0.01
0.012
T (Days)

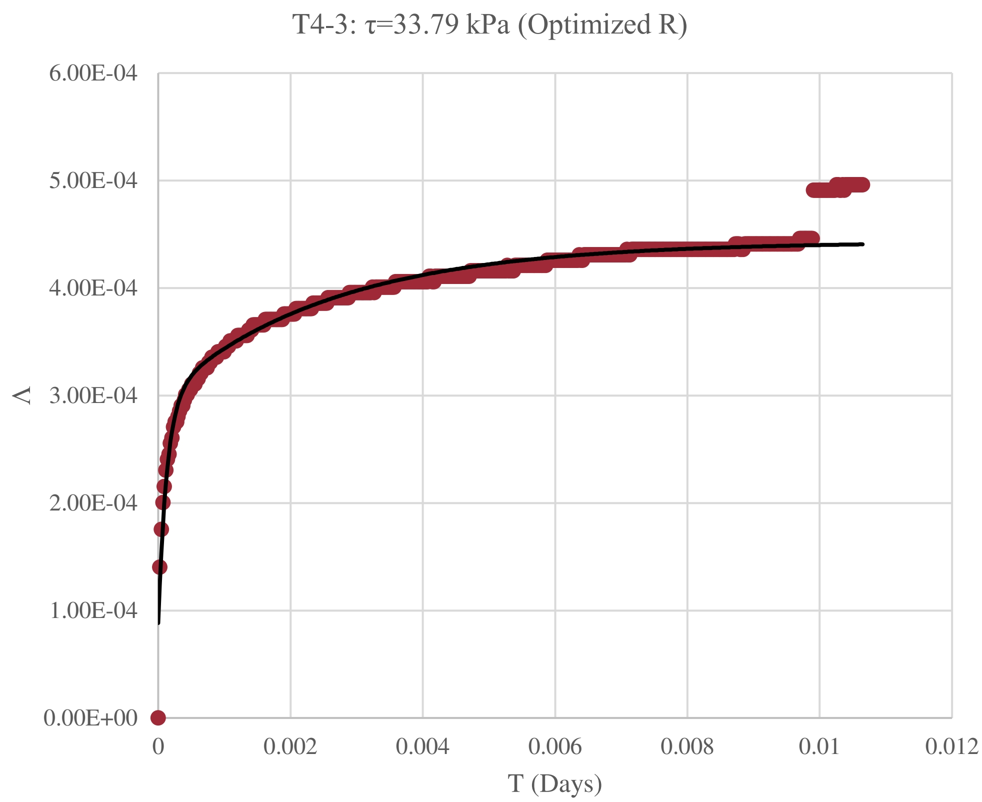
T4-3: τ=33.79 kPa (Optimized R)
6.00E-04
5.00E-04
4.00E-04
3.00E-04
2.00E-04
1.00E-04
0.00E+00
Λ
0
0.002
0.004
0.006
0.008
0.01
0.012
T (Days)

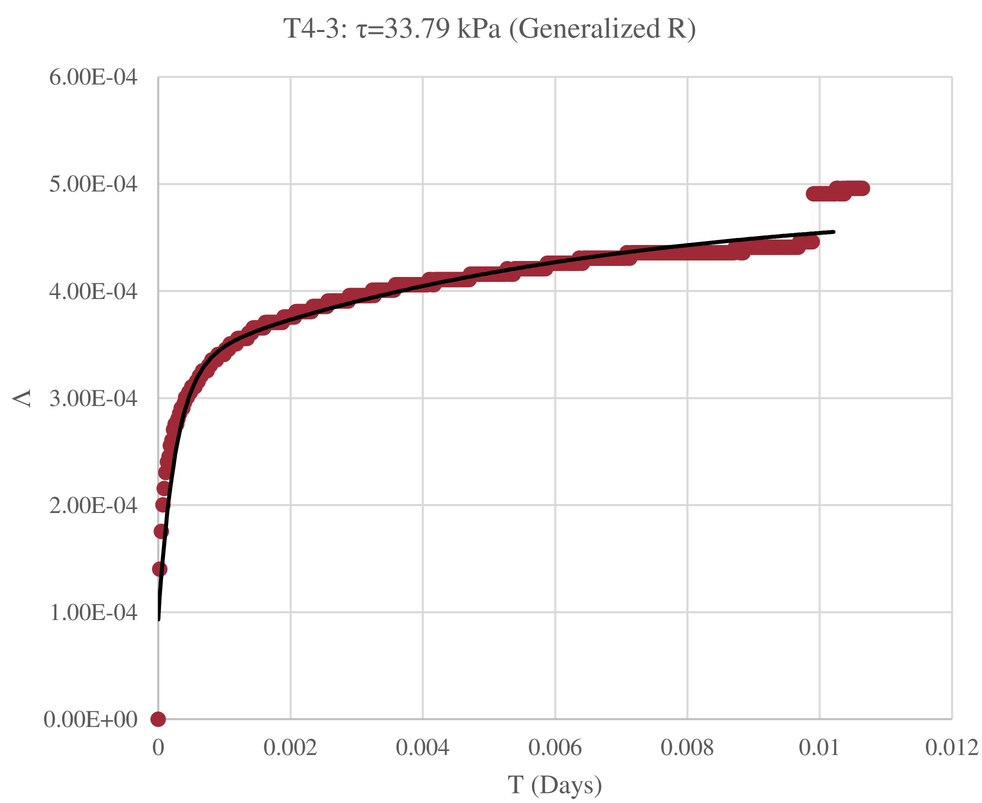
T4-3: τ=33.79 kPa (Generalized R)
6.00E-04
5.00E-04
4.00E-04
3.00E-04
2.00E-04
1.00E-04
0.00E+00
Λ
0
0.002
0.004
0.006
0.008
0.01
0.012
T (Days)

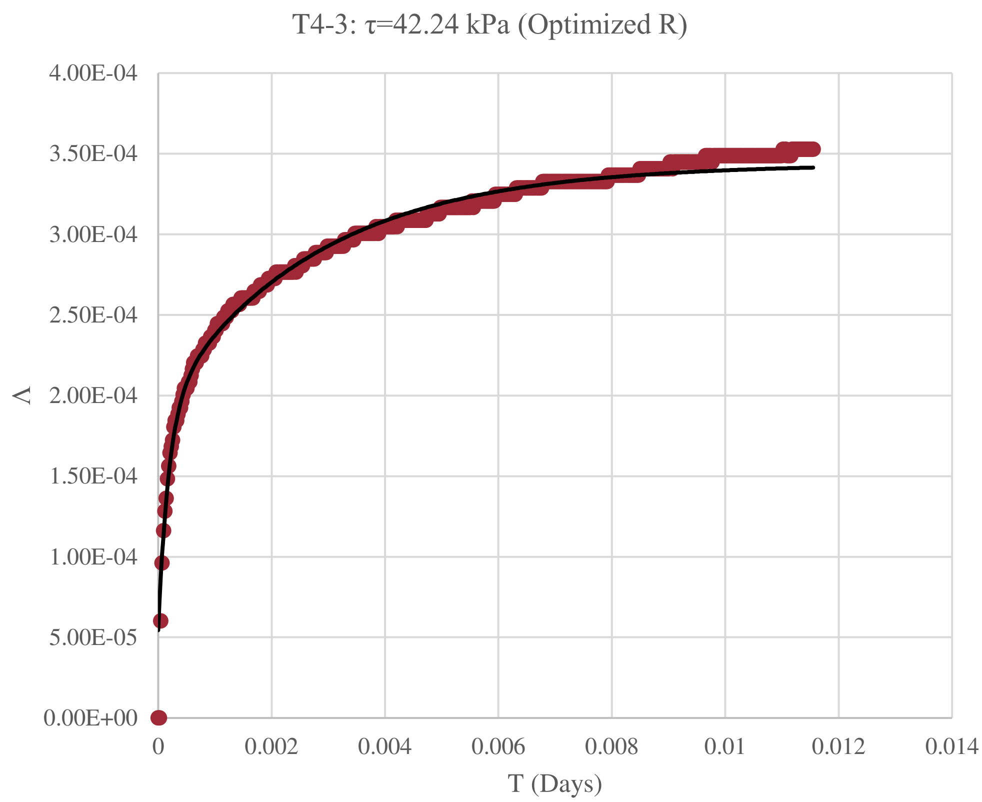
T4-3: τ=42.24 kPa (Optimized R)
4.00E-04
3.50E-04
3.00E-04
2.50E-04
2.00E-04
1.50E-04
1.00E-04
5.00E-05
0.00E+00
Λ
0
0.002
0.004
0.006
0.008
0.01
0.012
0.014
T (Days)

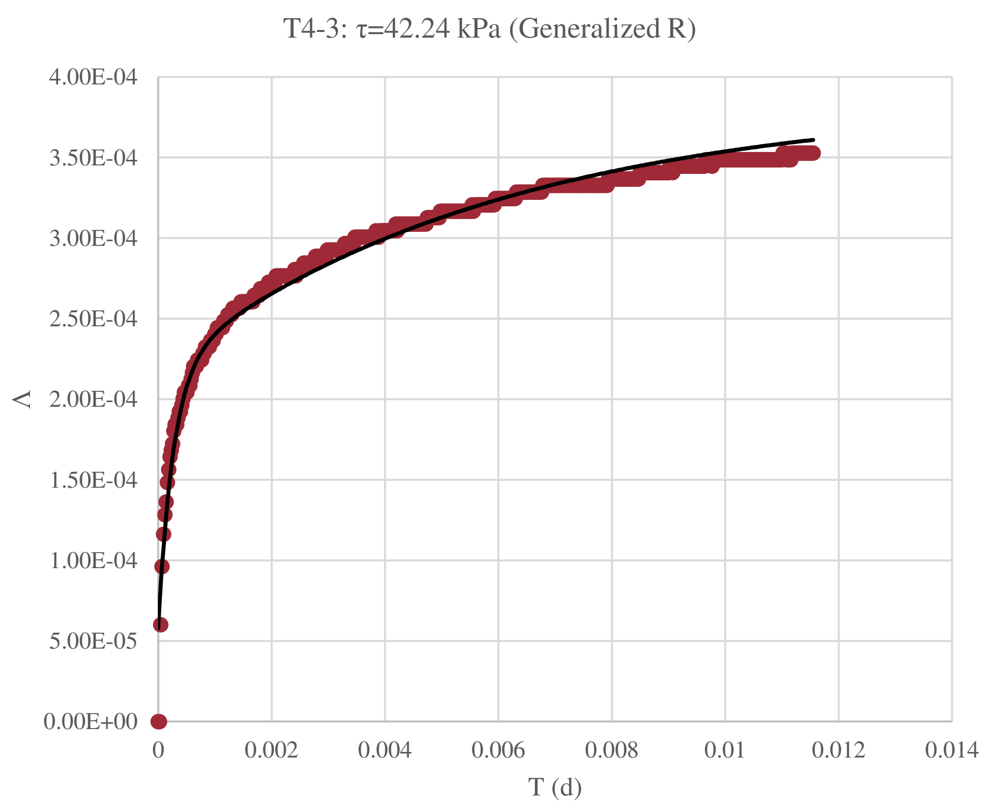
T4-3: τ=42.24 kPa (Generalized R)
4.00E-04
3.50E-04
3.00E-04
2.50E-04
2.00E-04
1.50E-04
1.00E-04
5.00E-05
0.00E+00
Λ
0
0.002
0.004
0.006
0.008
0.01
0.012
0.014
T (d)

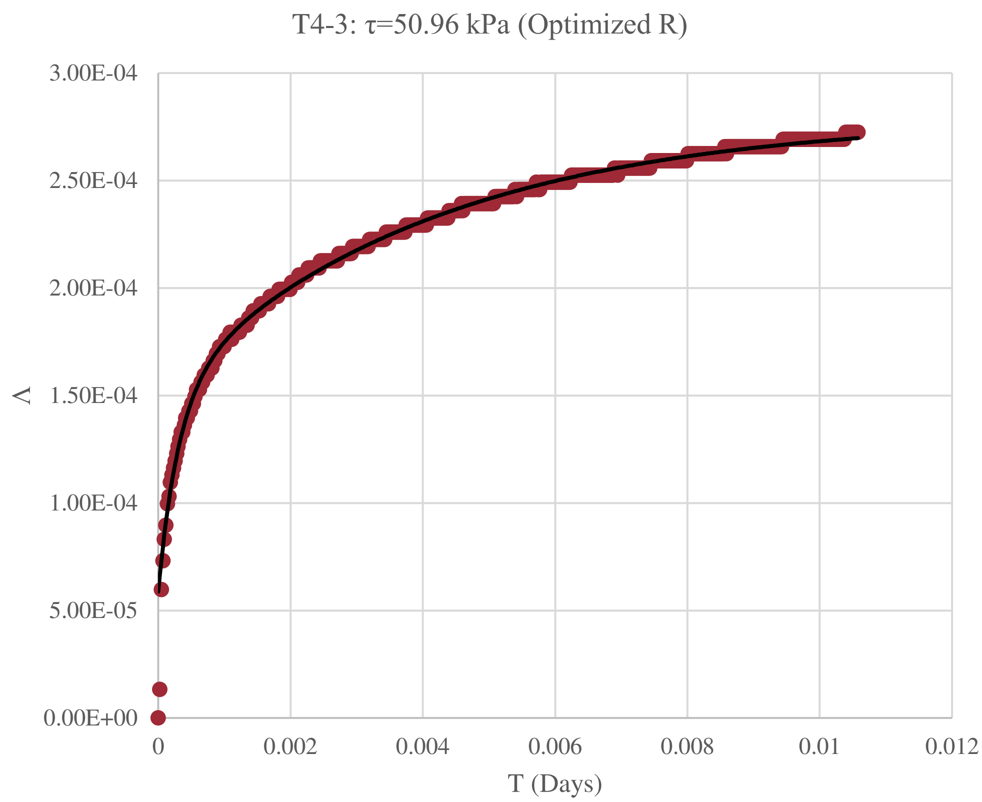
T4-3: τ=50.96 kPa (Optimized R)
3.00E-04
2.50E-04
2.00E-04
1.50E-04
1.00E-04
5.00E-05
0.00E+00
Λ
0
0.002
0.004
0.006
0.008
0.01
0.012
T (Days)

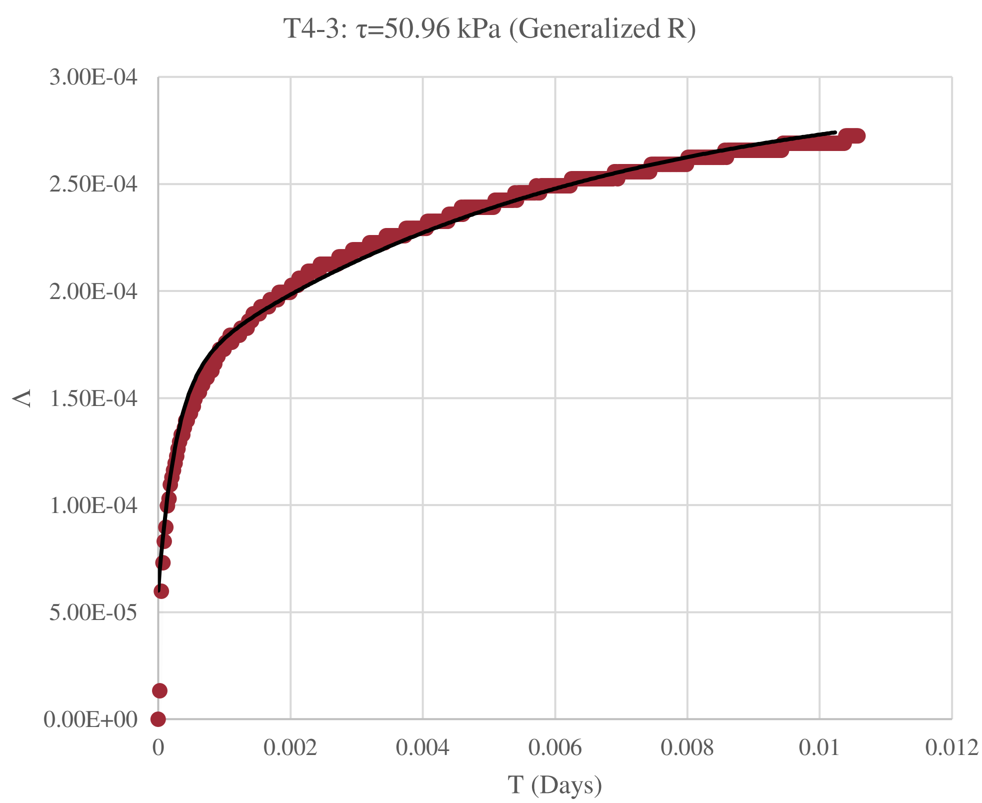
T4-3: τ=50.96 kPa (Generalized R)
3.00E-04
2.50E-04
2.00E-04
1.50E-04
1.00E-04
5.00E-05
0.00E+00
Λ
0
0.002
0.004
0.006
0.008
0.01
0.012
T (Days)

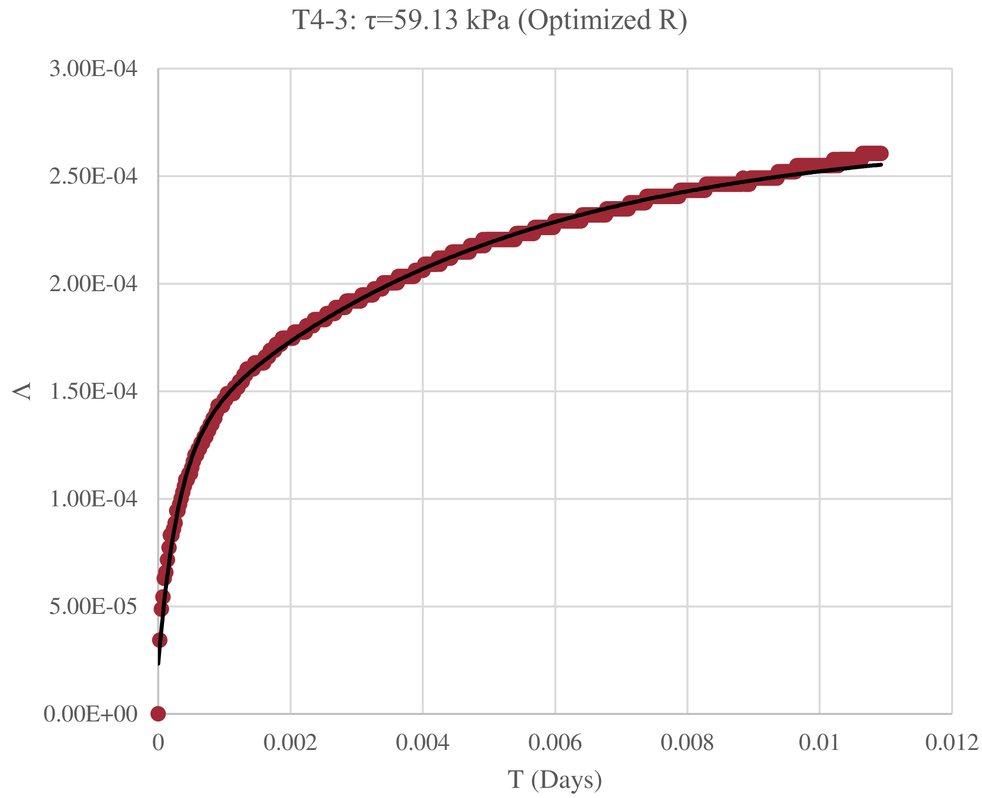
T4-3: τ=59.13 kPa (Optimized R)
3.00E-04
2.50E-04
2.00E-04
1.50E-04
1.00E-04
5.00E-05
0.00E+00
Λ
0
0.002
0.004
0.006
0.008
0.01
0.012
T (Days)

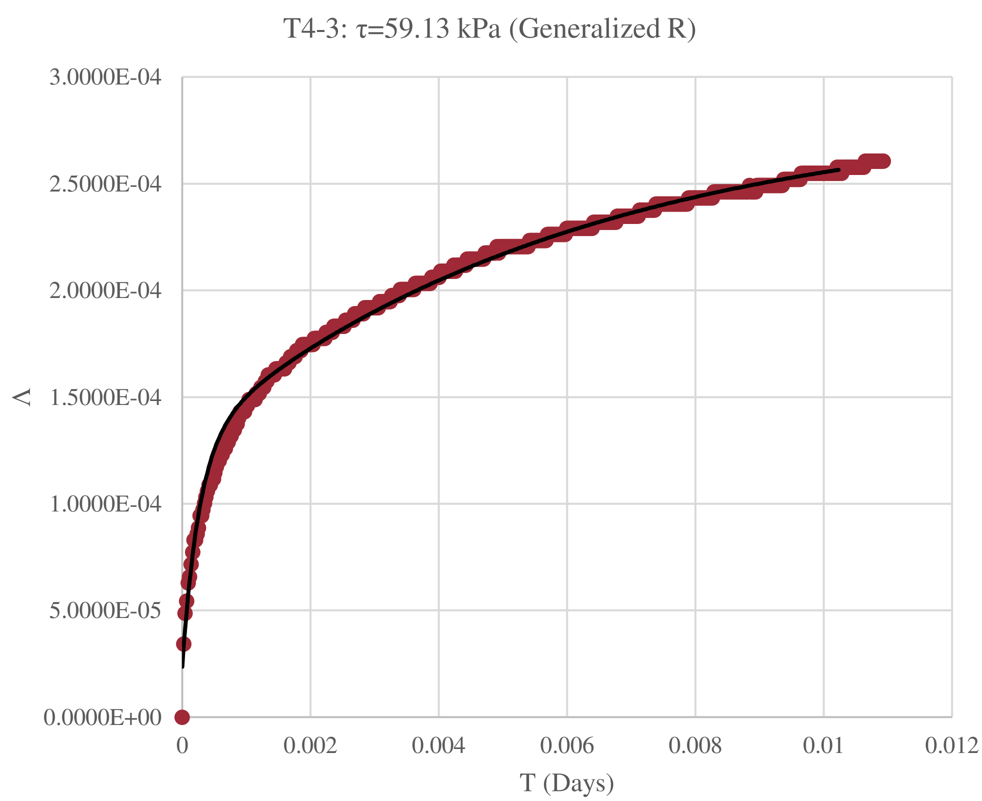
T4-3: τ=59.13 kPa (Generalized R)
3.0000E-04
2.5000E-04
2.0000E-04
1.5000E-04
1.0000E-04
5.0000E-05
0.0000E+00
Λ
0
0.002
0.004
0.006
0.008
0.01
0.012
T (Days)

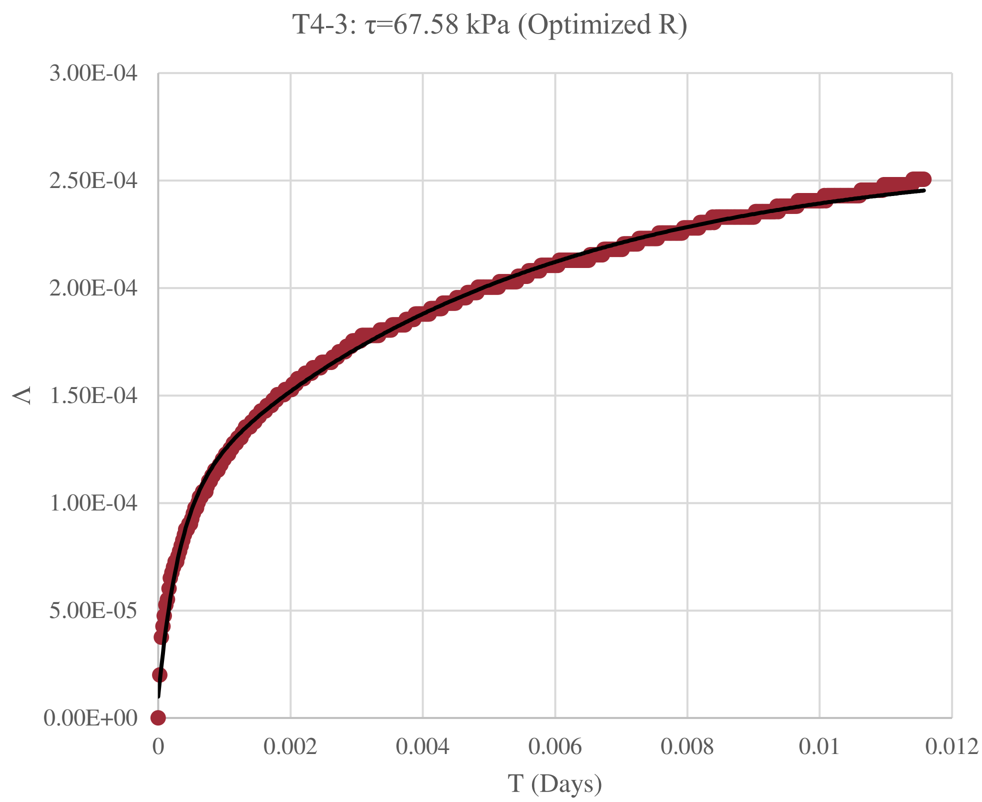
T4-3: τ=67.58 kPa (Optimized R)
3.00E-04
2.50E-04
2.00E-04
1.50E-04
1.00E-04
5.00E-05
0.00E+00
Λ
0
0.002
0.004
0.006
0.008
0.01
0.012
T (Days)

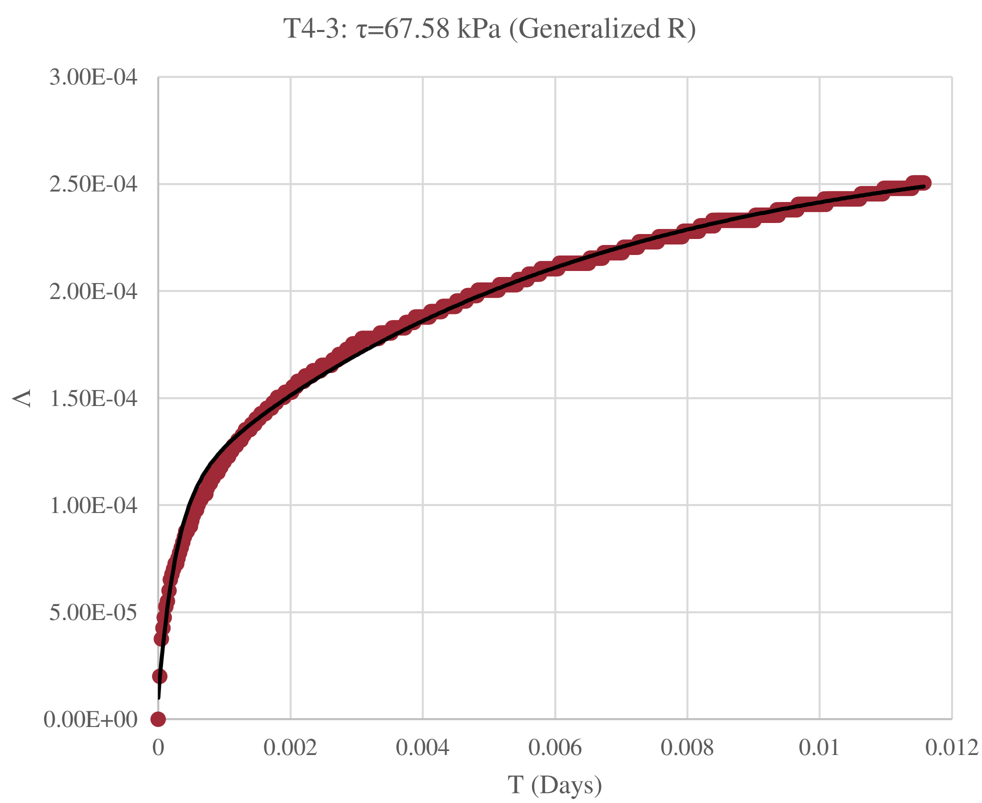
T4-3: τ=67.58 kPa (Generalized R)
3.00E-04
2.50E-04
2.00E-04
1.50E-04
1.00E-04
5.00E-05
0.00E+00
Λ
0
0.002
0.004
0.006
0.008
0.01
0.012
T (Days)

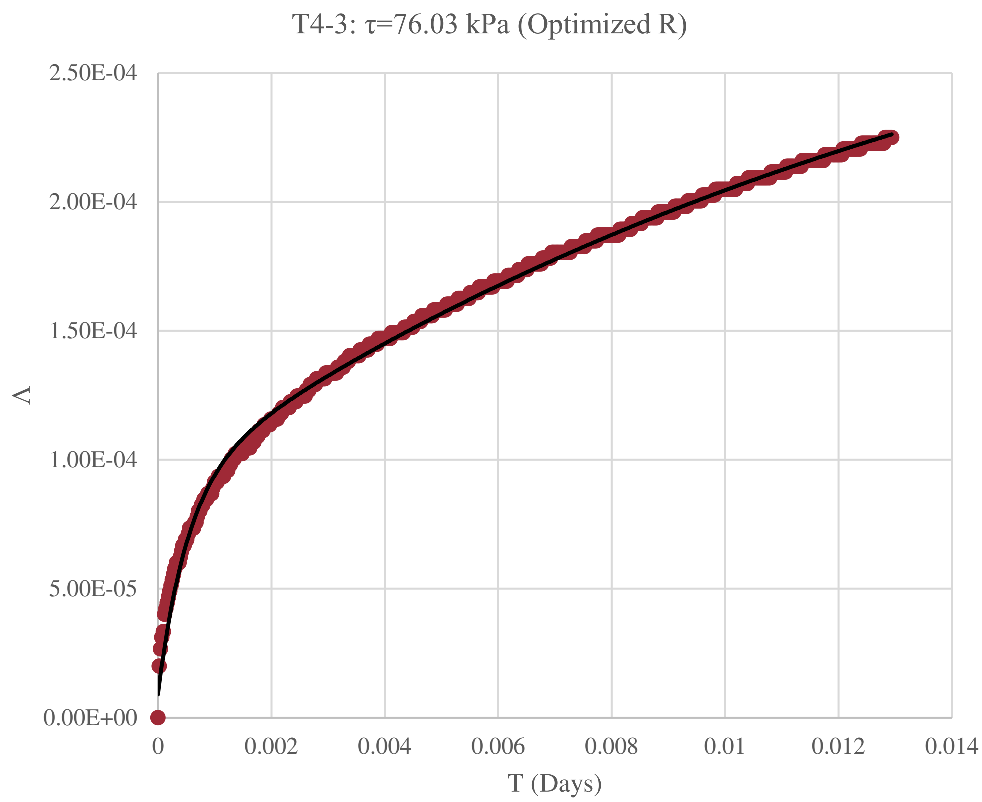
T4-3: τ=76.03 kPa (Optimized R)
2.50E-04
2.00E-04
1.50E-04
1.00E-04
5.00E-05
0.00E+00
Λ
0
0.002
0.004
0.006
0.008
0.01
0.012
0.014
T (Days)

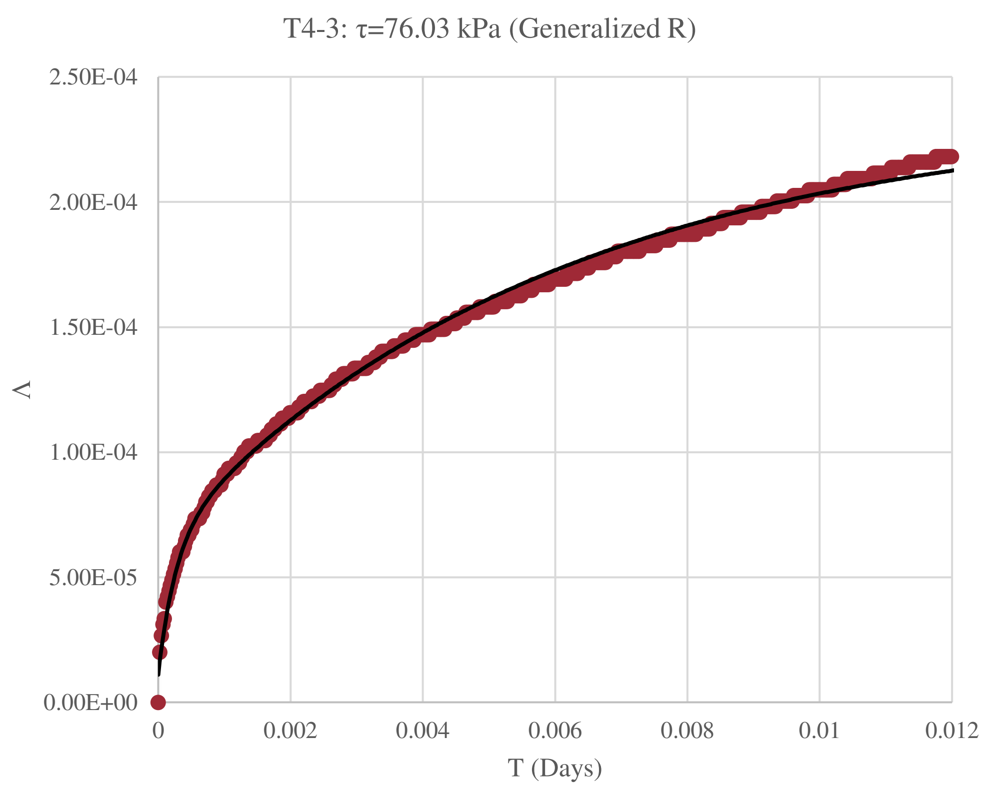
T4-3: τ=76.03 kPa (Generalized R)
2.50E-04
2.00E-04
1.50E-04
1.00E-04
5.00E-05
0.00E+00
Λ
0
0.002
0.004
0.006
0.008
0.01
0.012
T (Days)

7.4.4 T4-4

T4-4: τmax = 80 kPa, Optimized Retardation Times						
τ (kPa)	CSR-N	G_{Di} (kPa)	G_{D1} (kPa)	G_{D2} (kPa)	R_1 (d)	R_2 (d)
8.45	0.19	9302	7906	6827	2.60E-04	2.03E-03
16.9	0.37	5672	3515	2889	2.63E-04	2.56E-03
25.34	0.51	7468	1287	5886	9.59E-05	2.60E-03
33.79	0.62	10706	4188	6352	1.30E-04	2.51E-03
42.24	0.70	20154	9086	7931	1.86E-04	2.89E-03
50.96	0.78	25165	13815	7766	2.96E-04	5.44E-03
59.13	0.84	74199	16737	8108	5.69E-04	7.14E-03
67.52	0.93	142905	35262	7513	7.41E-04	1.02E-02
76.03	0.93	103478	37415	7719	1.54E-04	3.65E-03

T4-4: τmax = 80 kPa, Generalized Retardation Times						
τ (kPa)	CSR-N	G_{Di} (kPa)	G_{D1} (kPa)	G_{D2} (kPa)	RG_1 (d)	RG_2 (d)
8.45	0.19	8148	6796	6302	2.63E-04	5.96E-03
16.9	0.37	5180	3024	2622	2.63E-04	5.96E-03
25.34	0.51	1491	3480	6079	2.63E-04	5.96E-03
33.79	0.62	9555	3564	7170	2.63E-04	5.96E-03
42.24	0.70	18922	7868	7276	2.63E-04	5.96E-03
50.96	0.78	25165	13815	7766	2.63E-04	5.96E-03
59.13	0.84	78577	20045	7550	2.63E-04	5.96E-03
67.58	0.93	108826	81341	8522	2.63E-04	5.96E-03
76.03	0.93	108437	31816	5812	2.63E-04	5.96E-03

T4-4: τ=8.45 kPa (Optimized R)

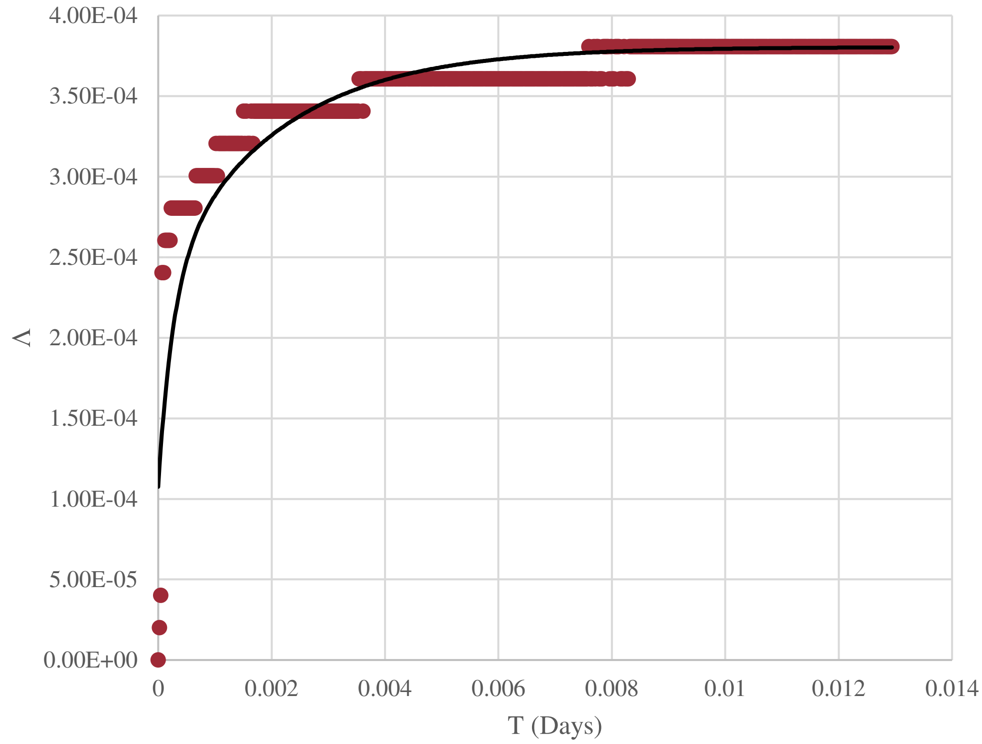

T4-4: τ=8.45 kPa (Generalized R)

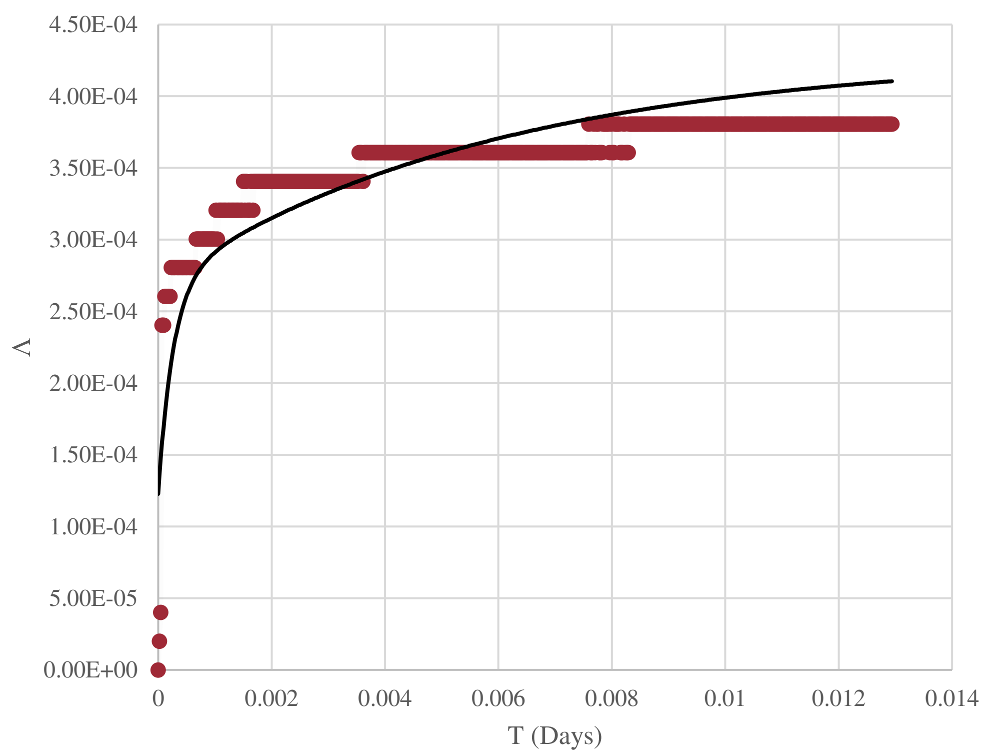

T4-4: τ=16.9 kPa (Optimized R)

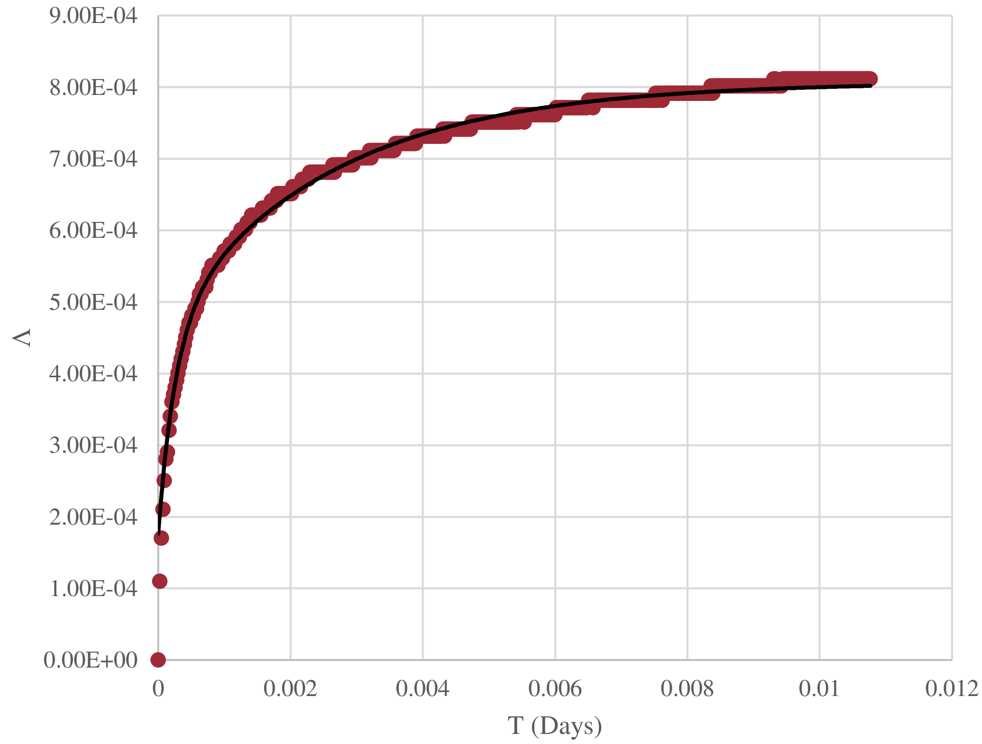

T4-4: τ=16.9 kPa (Generalized R)

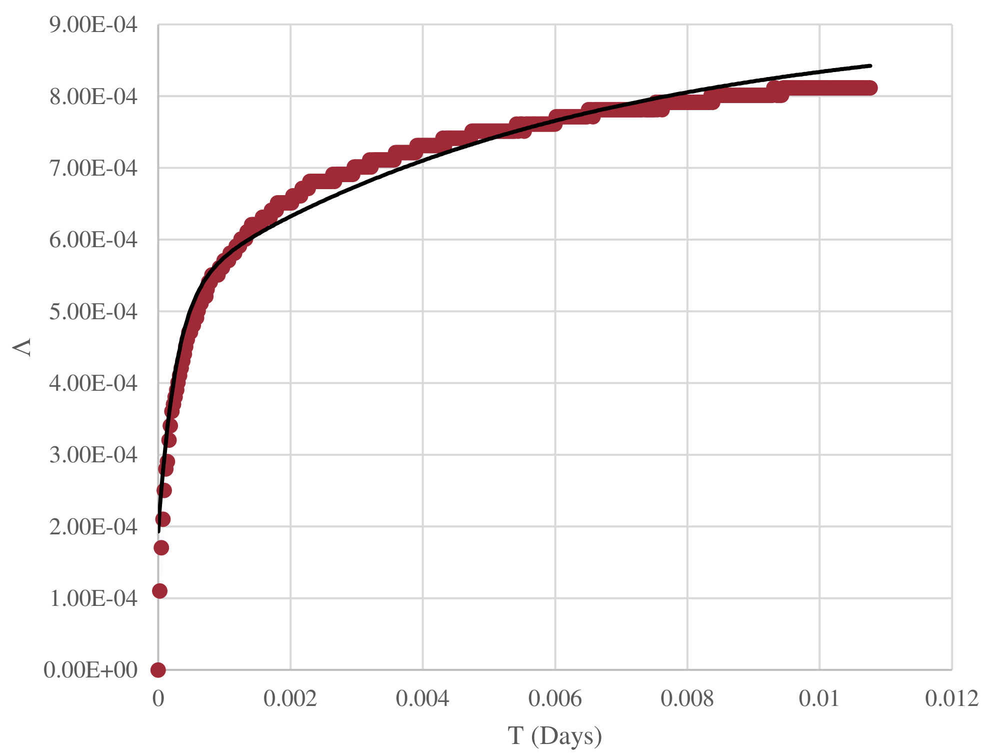

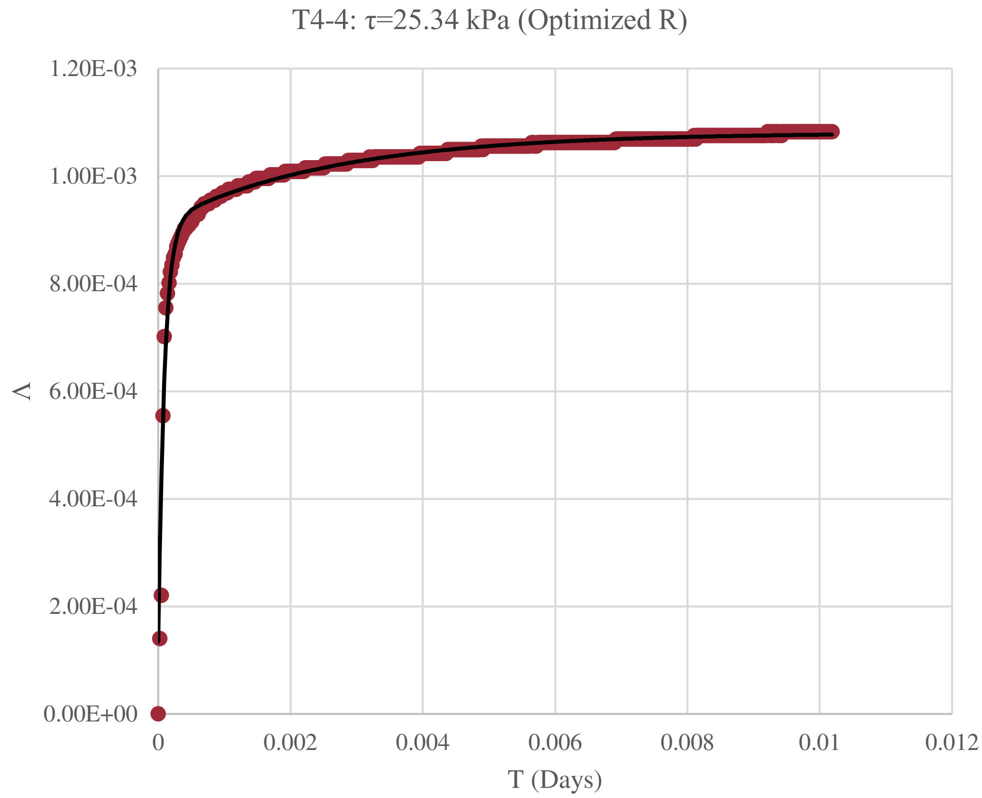

T4-4: τ=25.34 kPa (Optimized R)
1.20E-03
1.00E-03
8.00E-04
6.00E-04
4.00E-04
2.00E-04
0.00E+00
Λ
0
0.002
0.004
0.006
0.008
0.01
0.012
T (Days)

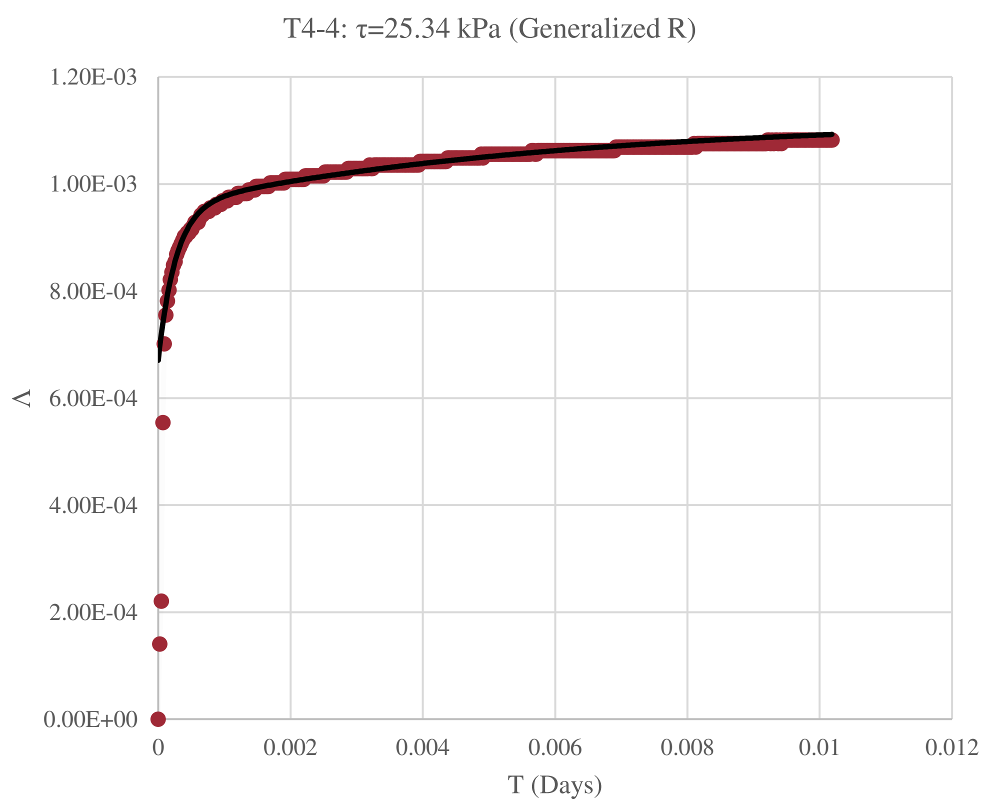

T4-4: τ=25.34 kPa (Generalized R)
1.20E-03
1.00E-03
8.00E-04
6.00E-04
4.00E-04
2.00E-04
0.00E+00
Λ
0
0.002
0.004
0.006
0.008
0.01
0.012
T (Days)

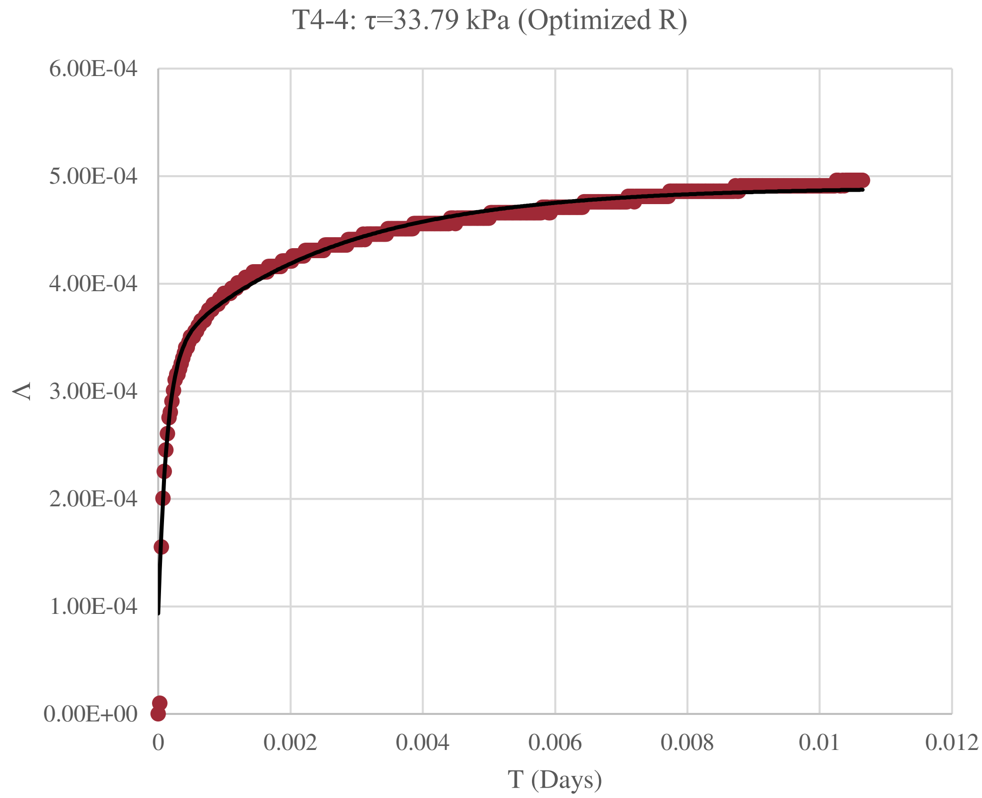
T4-4: τ=33.79 kPa (Optimized R)
6.00E-04
5.00E-04
4.00E-04
3.00E-04
2.00E-04
1.00E-04
0.00E+00
Λ
0
0.002
0.004
0.006
0.008
0.01
0.012
T (Days)

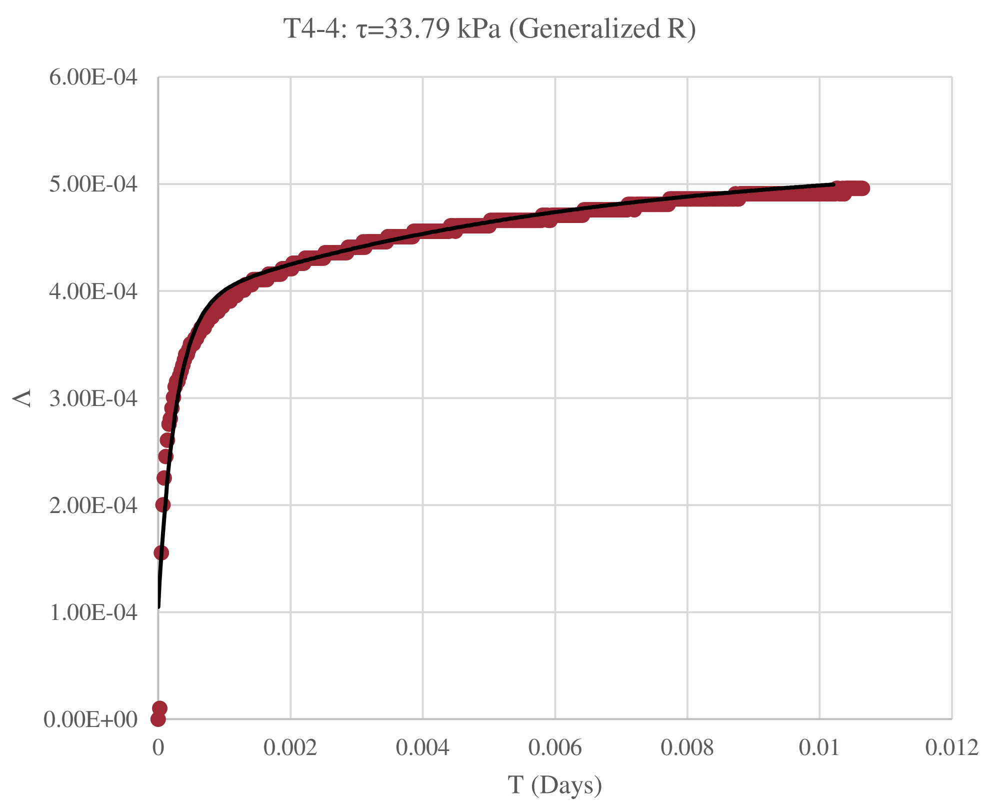
T4-4: τ=33.79 kPa (Generalized R)
6.00E-04
5.00E-04
4.00E-04
3.00E-04
2.00E-04
1.00E-04
0.00E+00
Λ
0
0.002
0.004
0.006
0.008
0.01
0.012
T (Days)

T4-4: τ=42.24 kPa (Optimized R)

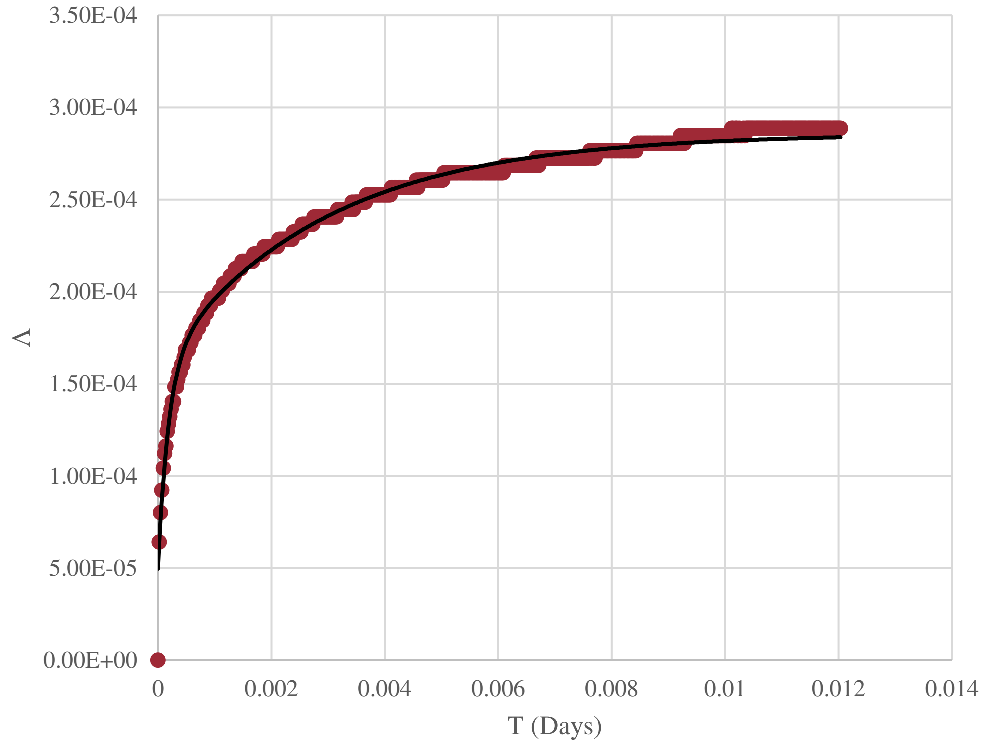

T4-4: τ=42.24 kPa (Generalized R)

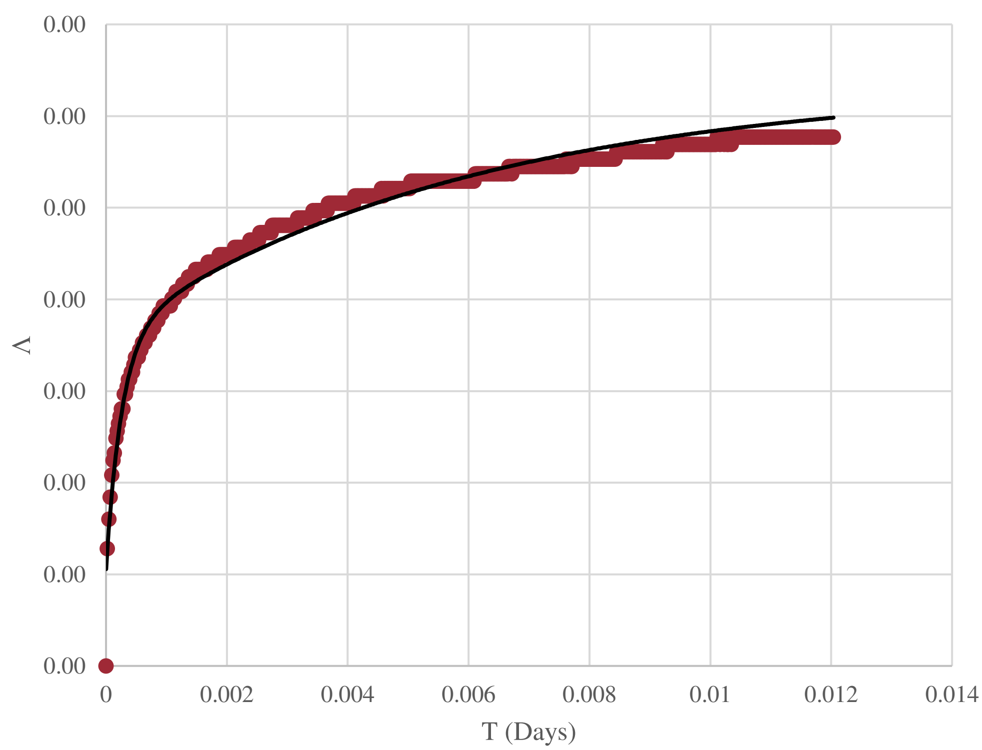

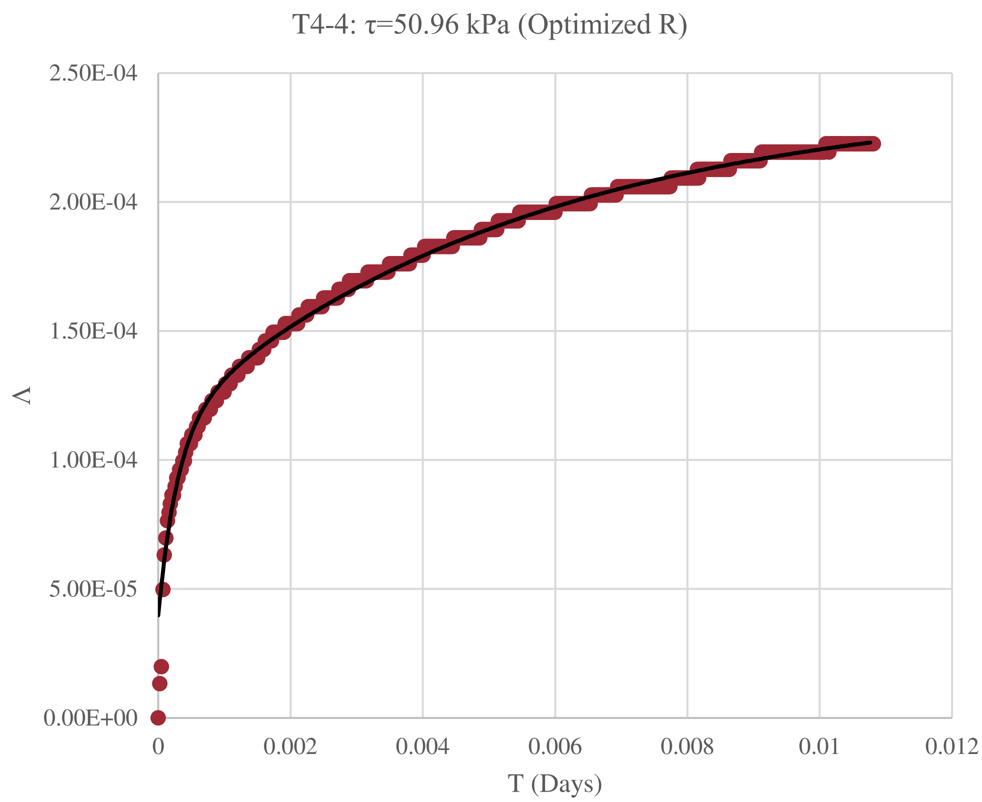
T4-4: τ=50.96 kPa (Optimized R)
2.50E-04
2.00E-04
1.50E-04
1.00E-04
5.00E-05
0.00E+00
Λ
0
0.002
0.004
0.006
0.008
0.01
0.012
T (Days)

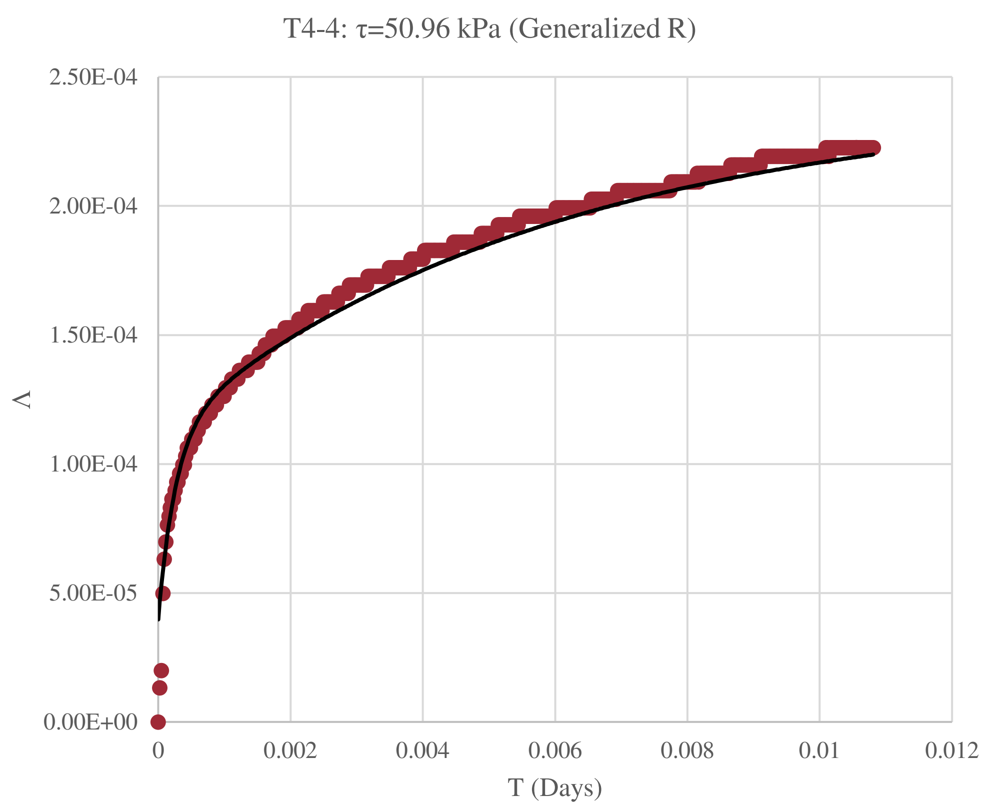
T4-4: τ=50.96 kPa (Generalized R)
2.50E-04
2.00E-04
1.50E-04
1.00E-04
5.00E-05
0.00E+00
Λ
0
0.002
0.004
0.006
0.008
0.01
0.012
T (Days)

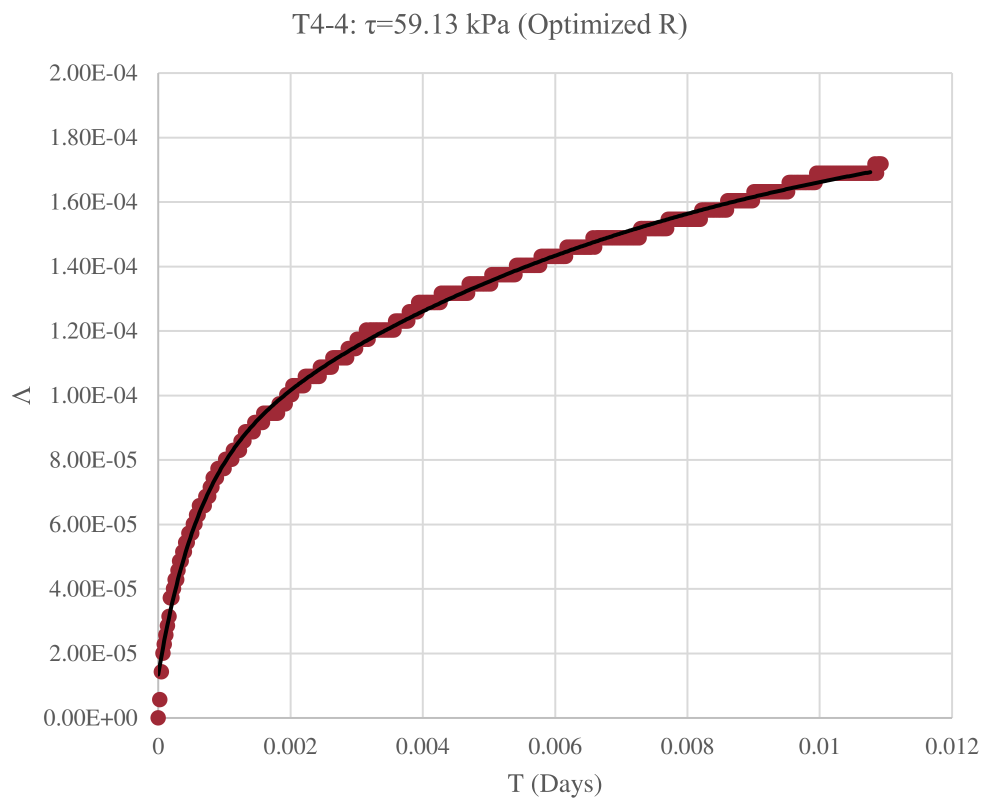
T4-4: τ=59.13 kPa (Optimized R)
Λ
2.00E-04
1.80E-04
1.60E-04
1.40E-04
1.20E-04
1.00E-04
8.00E-05
6.00E-05
4.00E-05
2.00E-05
0.00E+00
0
0.002
0.004
0.006
0.008
0.01
0.012
T (Days)

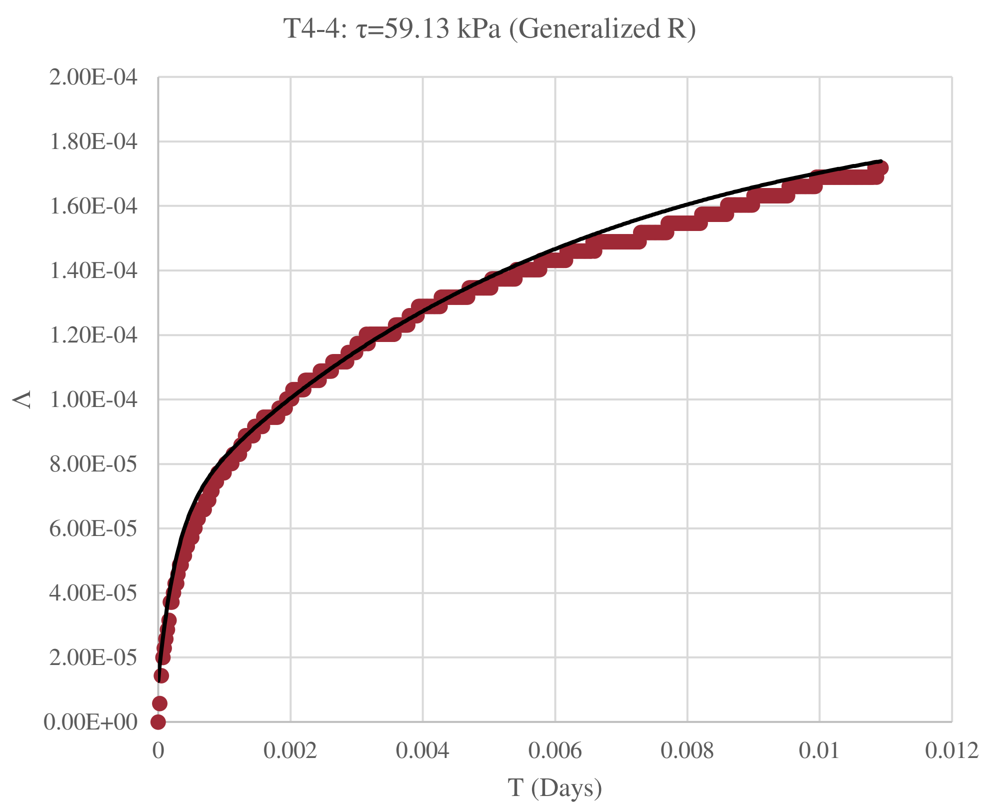
T4-4: τ=59.13 kPa (Generalized R)
Λ
2.00E-04
1.80E-04
1.60E-04
1.40E-04
1.20E-04
1.00E-04
8.00E-05
6.00E-05
4.00E-05
2.00E-05
0.00E+00
0
0.002
0.004
0.006
0.008
0.01
0.012
T (Days)

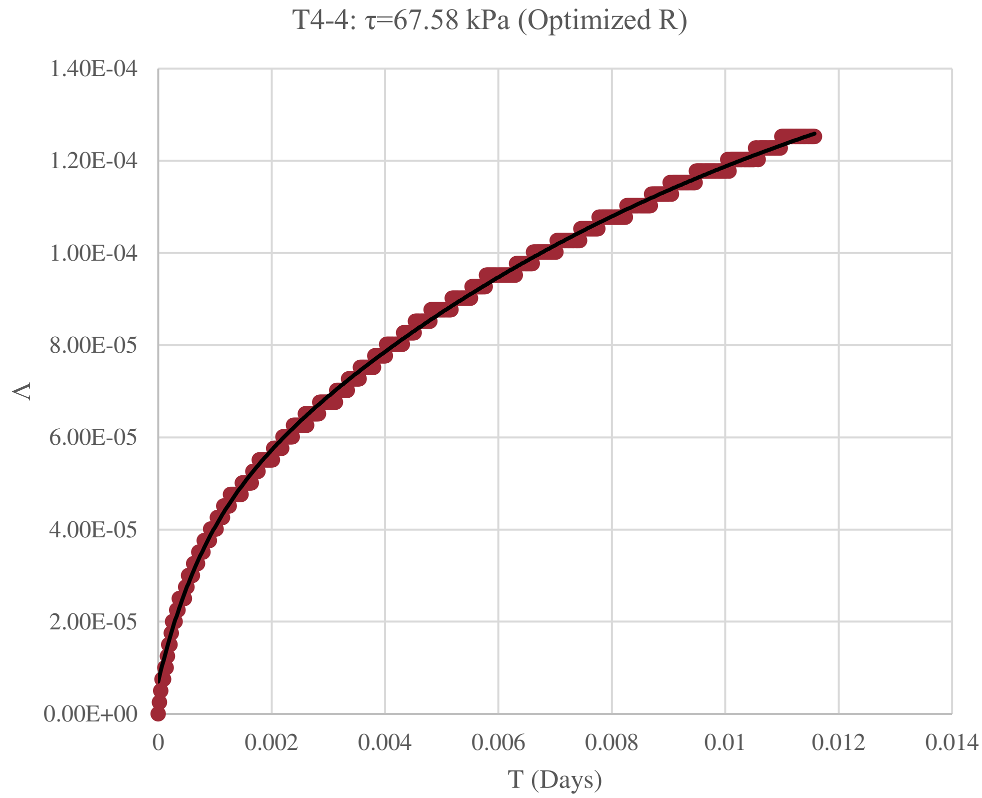
T4-4: τ=67.58 kPa (Optimized R)
1.40E-04
1.20E-04
1.00E-04
8.00E-05
6.00E-05
4.00E-05
2.00E-05
0.00E+00
Λ
0
0.002
0.004
0.006
0.008
0.01
0.012
0.014
T (Days)

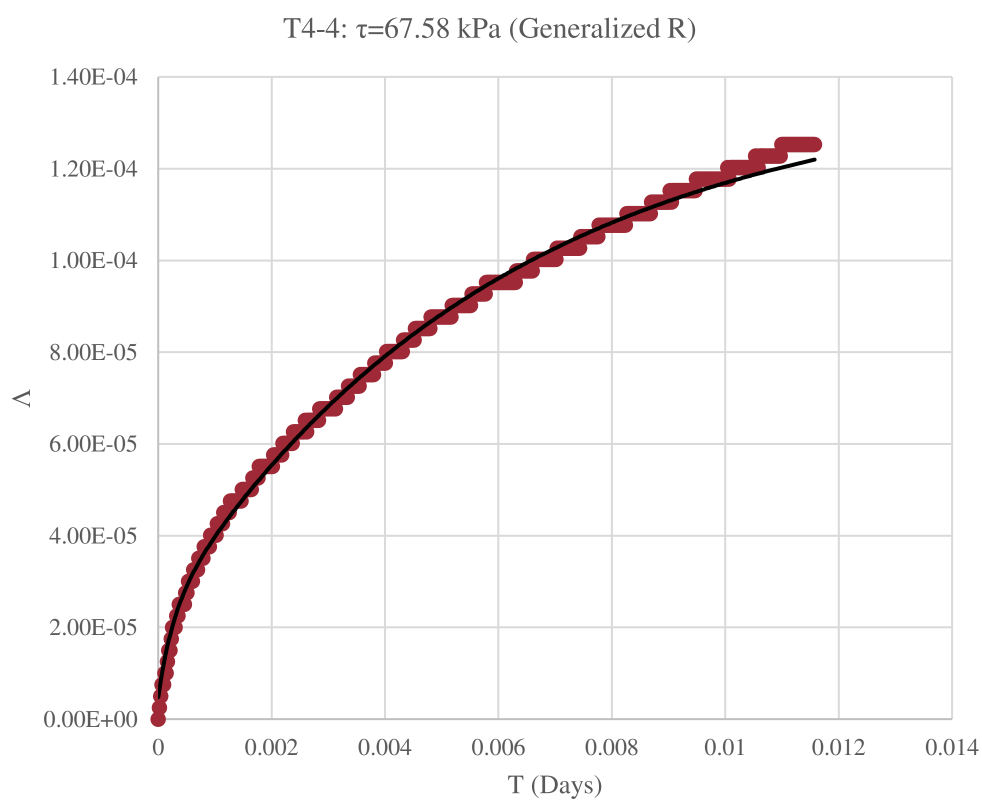
T4-4: τ=67.58 kPa (Generalized R)
1.40E-04
1.20E-04
1.00E-04
8.00E-05
6.00E-05
4.00E-05
2.00E-05
0.00E+00
Λ
0
0.002
0.004
0.006
0.008
0.01
0.012
0.014
T (Days)

T4-4: τ=76.03 kPa (Optimized R)

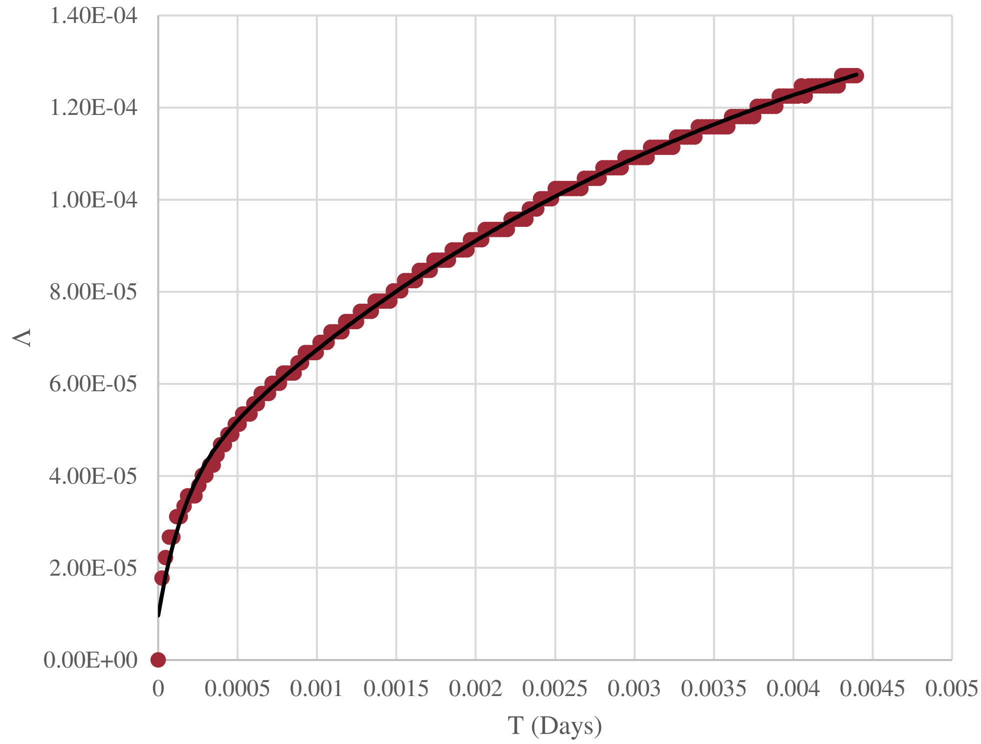

T4-4: τ=76.03 kPa (Generalized R)

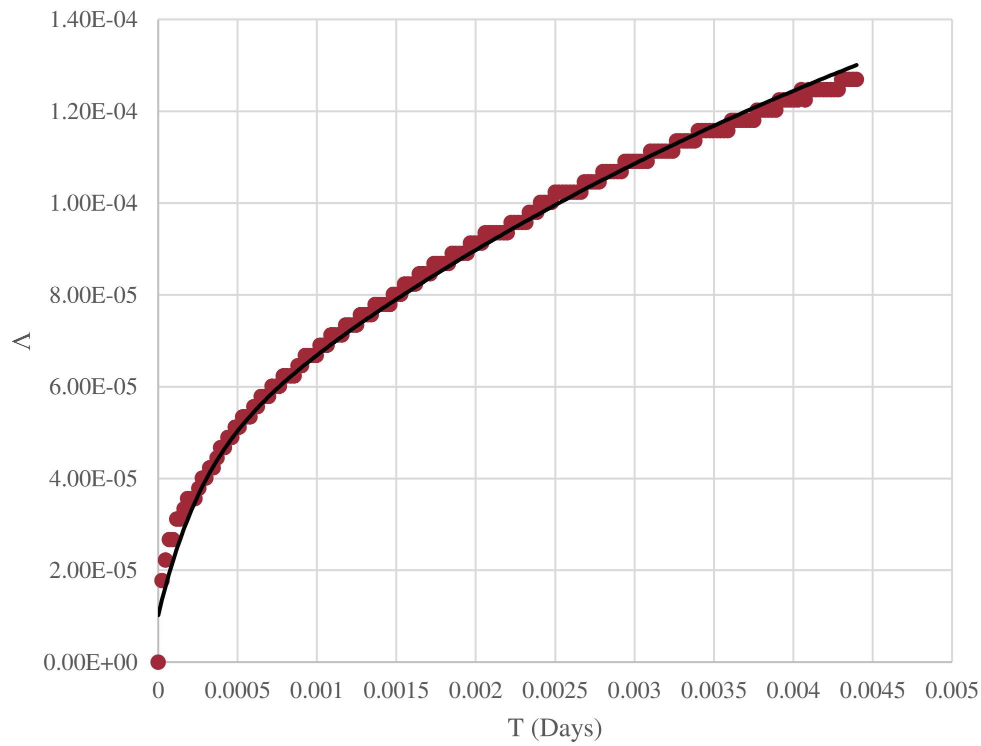

7.4.5 T4-5

T4-5: τmax = 67 kPa, Optimized Retardation Times						
τ (kPa)	CSR-N	G_{Di} (kPa)	GD_1 (kPa)	G_{D2} (kPa)	R_1 (d)	R_2 (d)
8.45	N/A	13743	6672	6927	2.00E-04	2.00E-03
16.9	N/A	5710	2079	3859	6.37E-05	2.69E-03
25.34	N/A	5350	1790	5459	6.08E-05	2.62E-03
33.79	N/A	10903	4613	6113	8.75E-05	3.43E-03
42.24	N/A	23138	8106	6396	1.33E-04	4.76E-03
50.96	N/A	103965	14018	6101	1.96E-04	4.49E-03
59.13	N/A	177232	14911	6199	1.74E-04	4.64E-03

T4-5: τmax = 67 kPa, Generalized Retardation Times						
τ (kPa)	CSR-N	G_{Di} (kPa)	G_{D1} (kPa)	G_{D2} (kPa)	RG_1 (d)	RG_2 (d)
8.45	N/A	12632	5519	6362	2.63E-04	5.96E-03
16.9	N/A	2136	3872	4174	2.63E-04	5.96E-03
25.34	N/A	1730	4567	5930	2.63E-04	5.96E-03
33.79	N/A	4893	7456	6314	2.63E-04	5.96E-03
42.24	N/A	9156	13312	6931	2.63E-04	5.96E-03
50.96	N/A	54371	13618	5855	2.63E-04	5.96E-03
59.13	N/A	56503	15551	5964	2.63E-04	5.96E-03

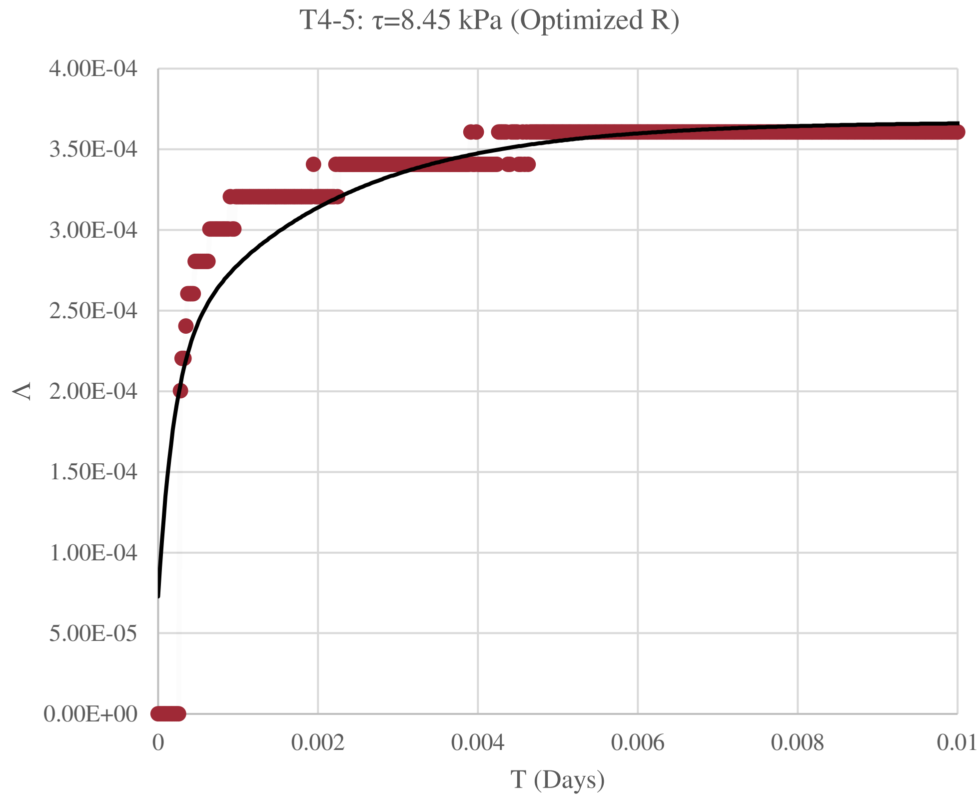
T4-5: τ=8.45 kPa (Optimized R)
4.00E-04
3.50E-04
3.00E-04
2.50E-04
2.00E-04
1.50E-04
1.00E-04
5.00E-05
0.00E+00
Λ
0
0.002
0.004
0.006
0.008
0.01
T (Days)

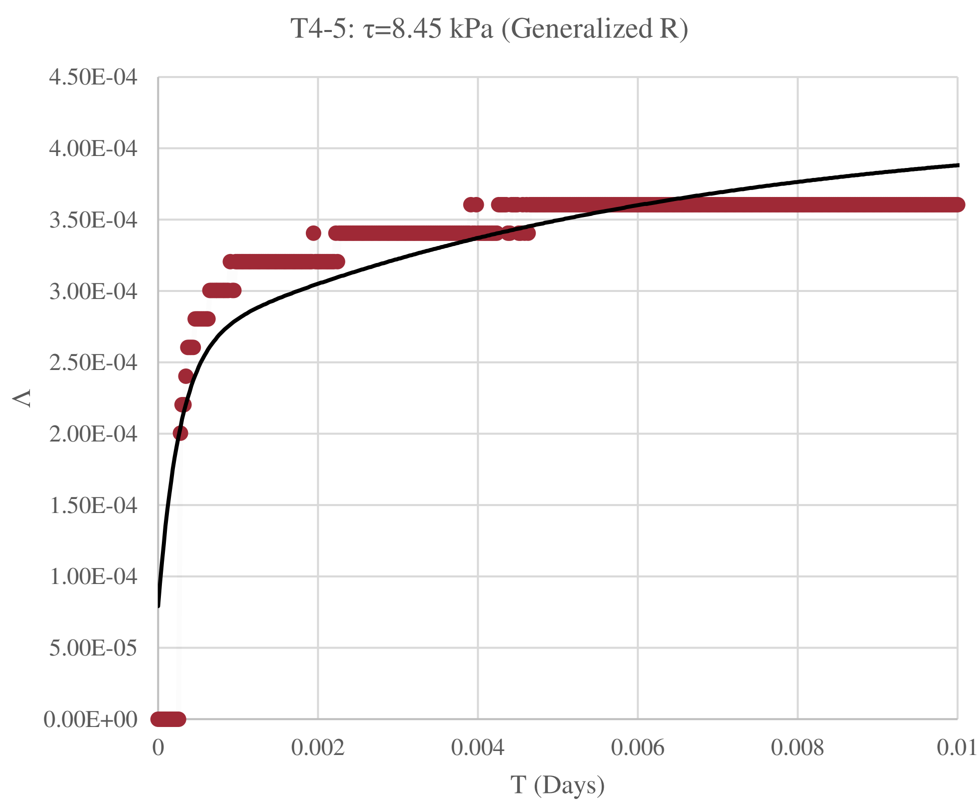
T4-5: τ=8.45 kPa (Generalized R)
4.50E-04
4.00E-04
3.50E-04
3.00E-04
2.50E-04
2.00E-04
1.50E-04
1.00E-04
5.00E-05
0.00E+00
Λ
0
0.002
0.004
0.006
0.008
0.01
T (Days)

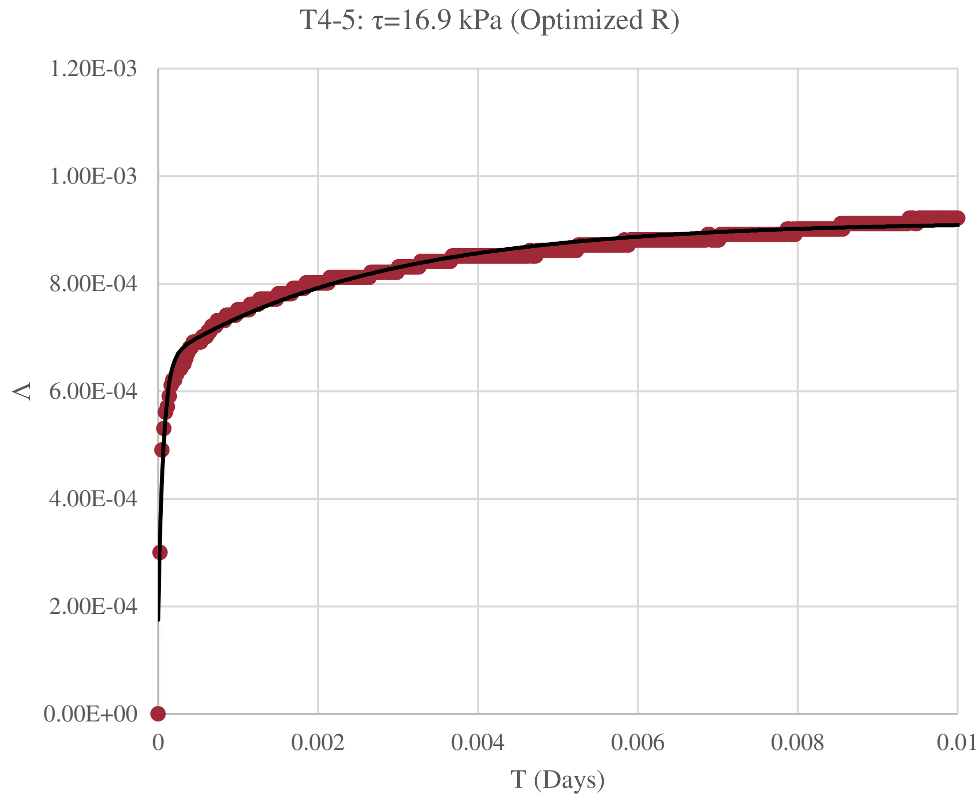
T4-5: τ=16.9 kPa (Optimized R)
1.20E-03
1.00E-03
8.00E-04
6.00E-04
4.00E-04
2.00E-04
0.00E+00
Λ
0
0.002
0.004
0.006
0.008
0.01
T (Days)

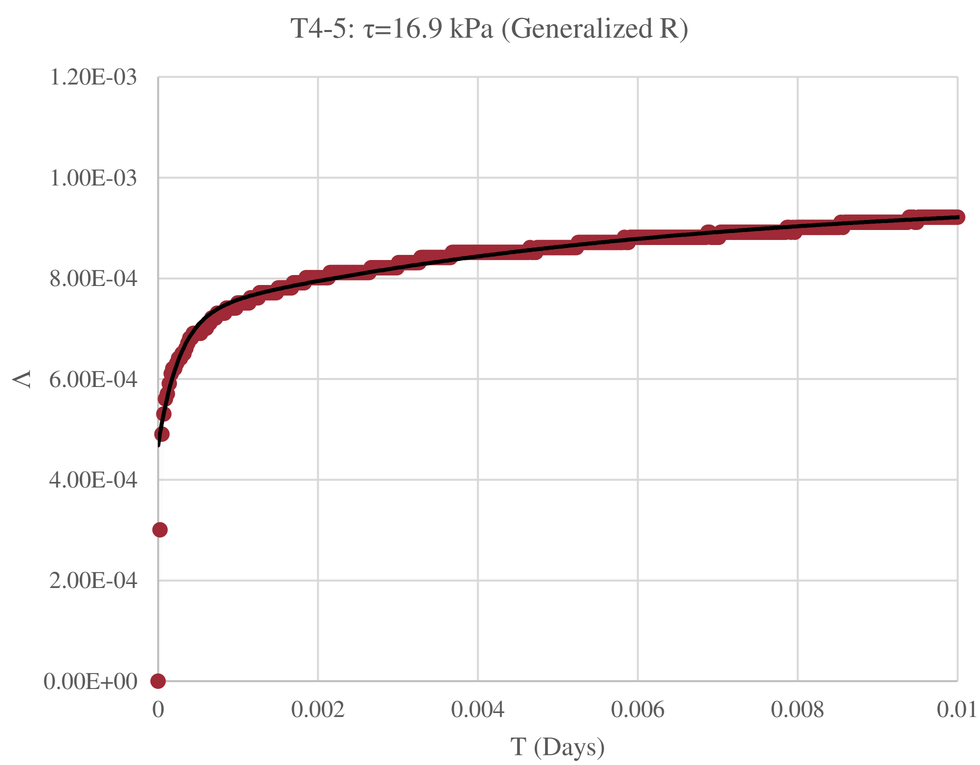
T4-5: τ=16.9 kPa (Generalized R)
1.20E-03
1.00E-03
8.00E-04
6.00E-04
4.00E-04
2.00E-04
0.00E+00
Λ
0
0.002
0.004
0.006
0.008
0.01
T (Days)

T4-5: τ=25.34 kPa (Optimized R)

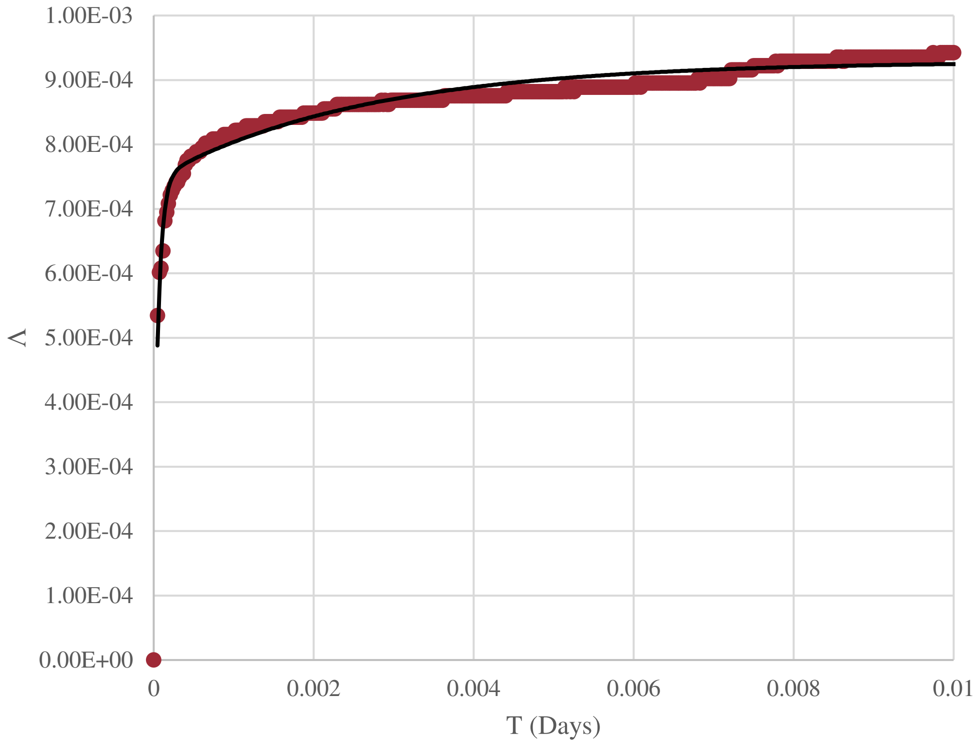

T4-5: τ=25.34 kPa (Generalized R)

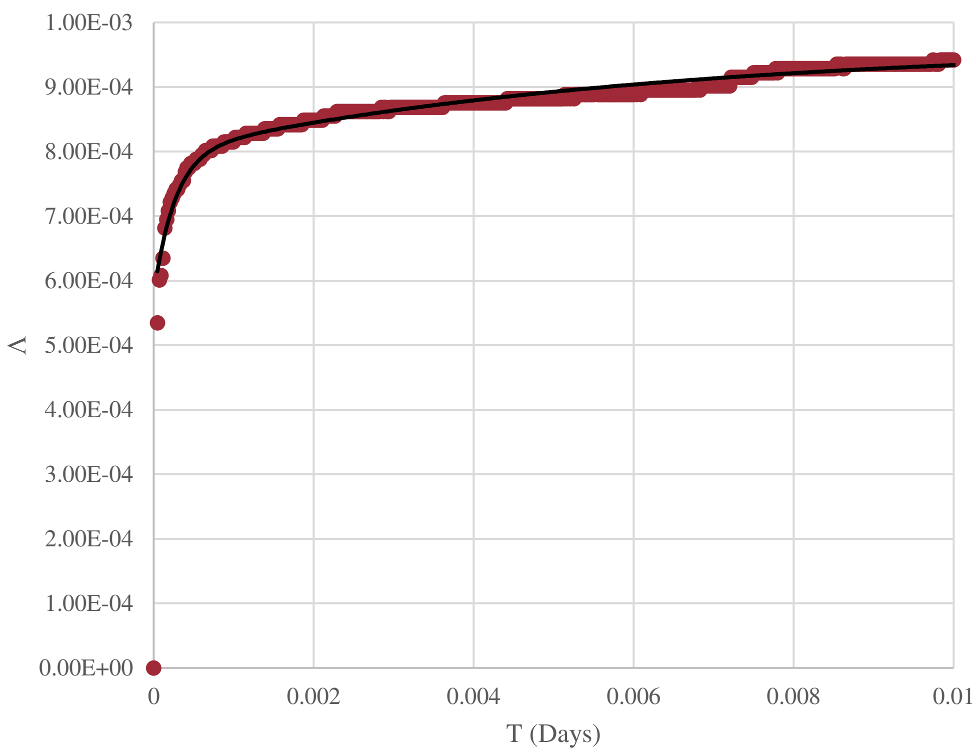

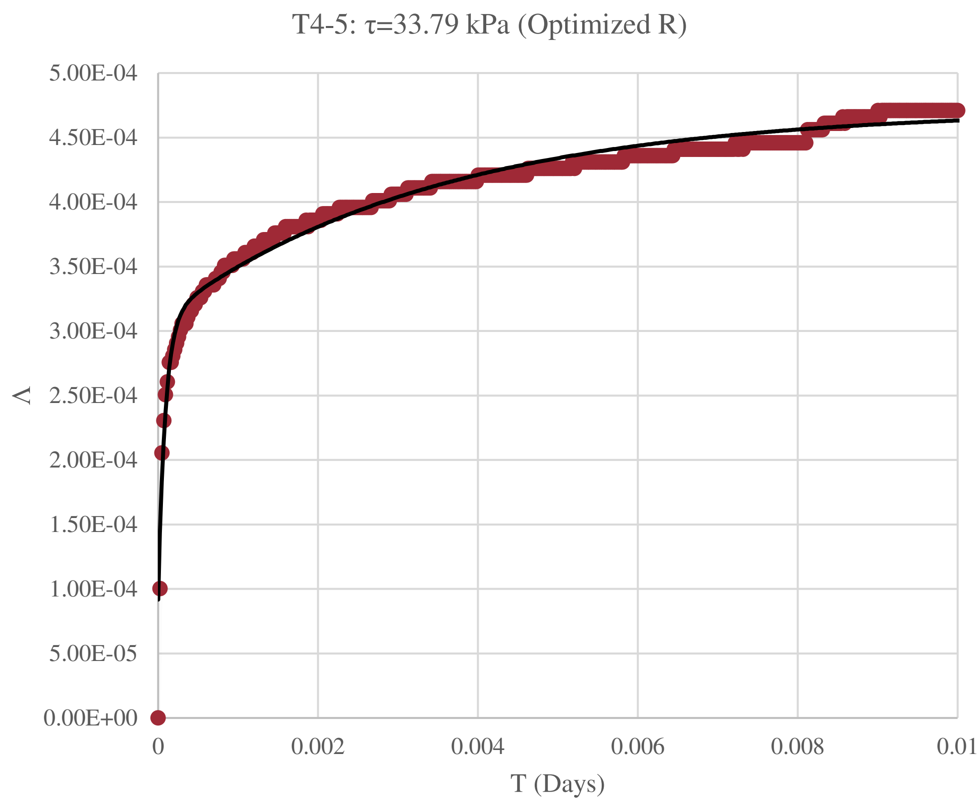
T4-5: τ=33.79 kPa (Optimized R)
5.00E-04
4.50E-04
4.00E-04
3.50E-04
3.00E-04
2.50E-04
2.00E-04
1.50E-04
1.00E-04
5.00E-05
0.00E+00
Λ
0
0.002
0.004
0.006
0.008
0.01
T (Days)

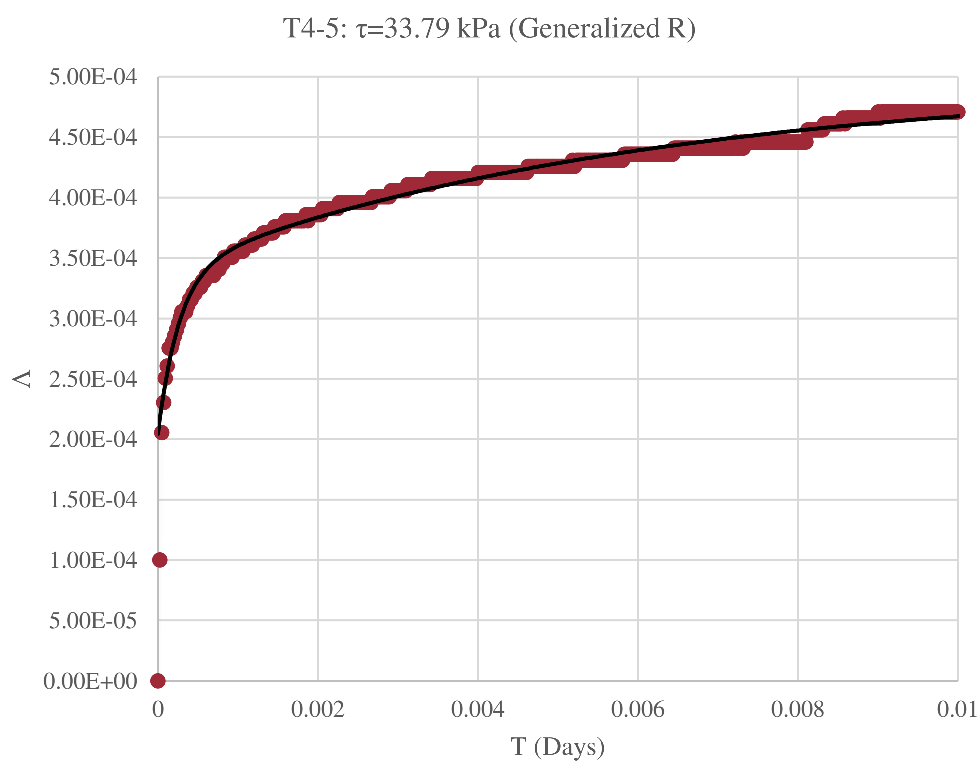
T4-5: τ=33.79 kPa (Generalized R)
5.00E-04
4.50E-04
4.00E-04
3.50E-04
3.00E-04
2.50E-04
2.00E-04
1.50E-04
1.00E-04
5.00E-05
0.00E+00
Λ
0
0.002
0.004
0.006
0.008
0.01
T (Days)

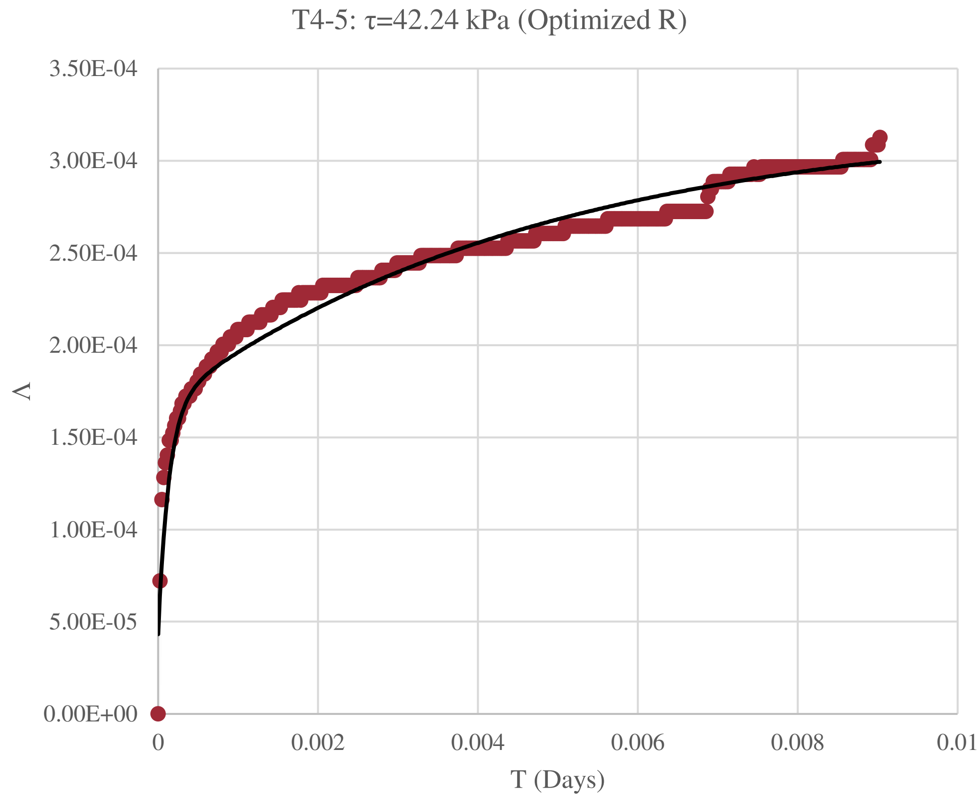
T4-5: τ=42.24 kPa (Optimized R)
3.50E-04
3.00E-04
2.50E-04
2.00E-04
1.50E-04
1.00E-04
5.00E-05
0.00E+00
Λ
0
0.002
0.004
0.006
0.008
0.01
T (Days)

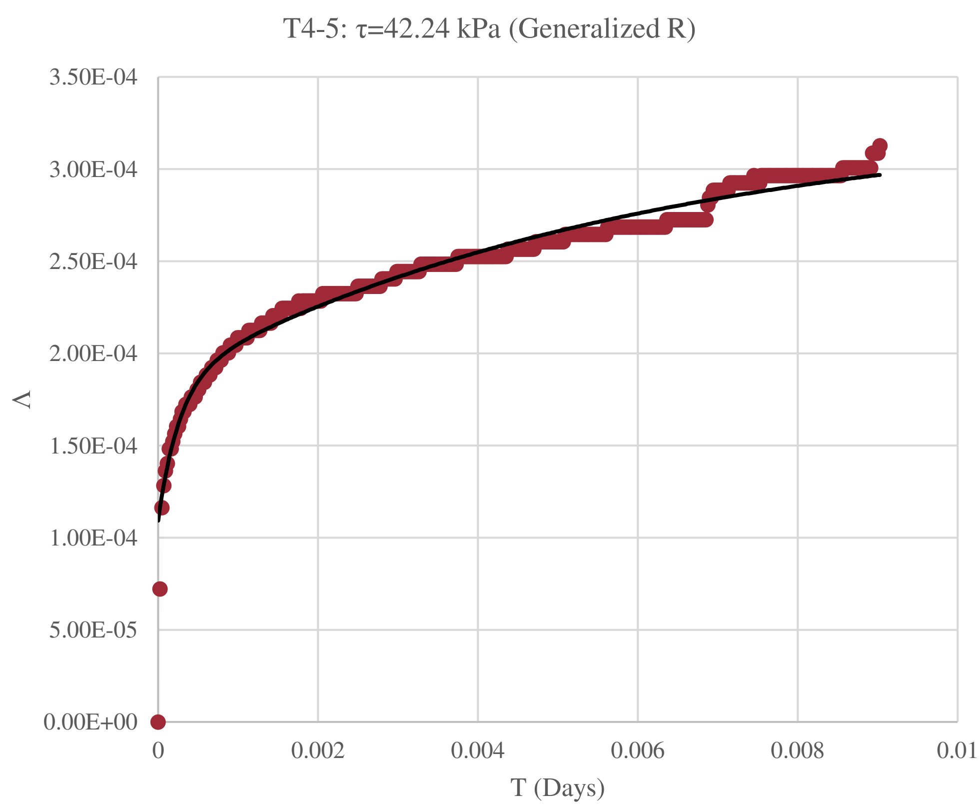
T4-5: τ=42.24 kPa (Generalized R)
3.50E-04
3.00E-04
2.50E-04
2.00E-04
1.50E-04
1.00E-04
5.00E-05
0.00E+00
Λ
0
0.002
0.004
0.006
0.008
0.01
T (Days)

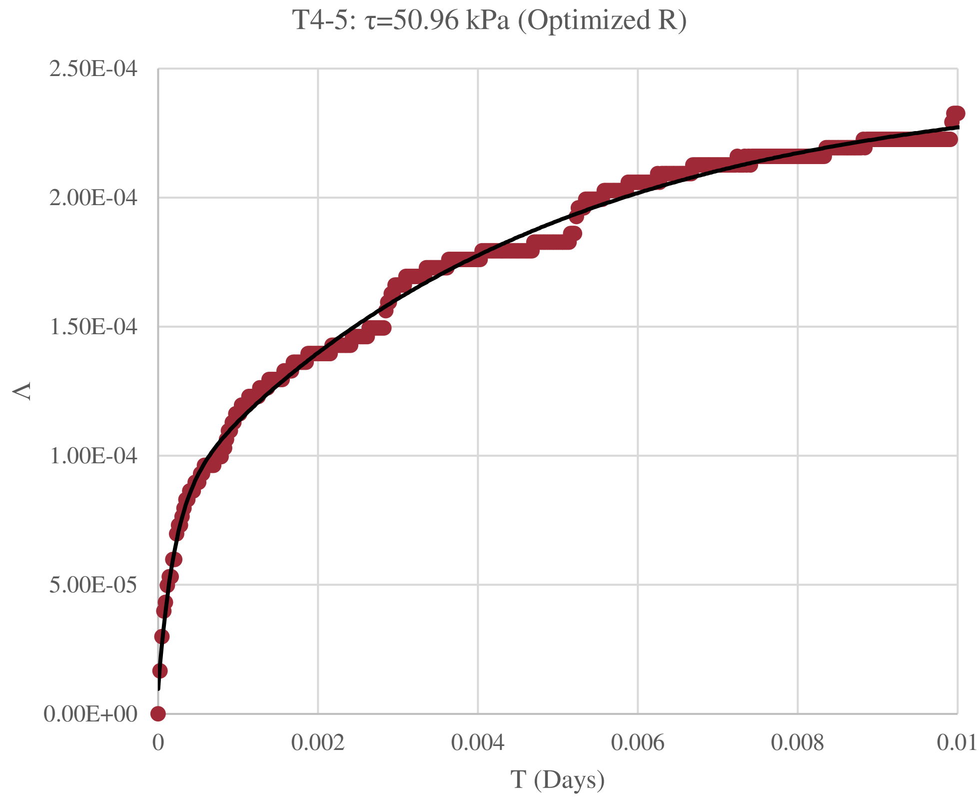
T4-5: τ=50.96 kPa (Optimized R)
2.50E-04
2.00E-04
1.50E-04
1.00E-04
5.00E-05
0.00E+00
Λ
0
0.002
0.004
0.006
0.008
0.01
T (Days)

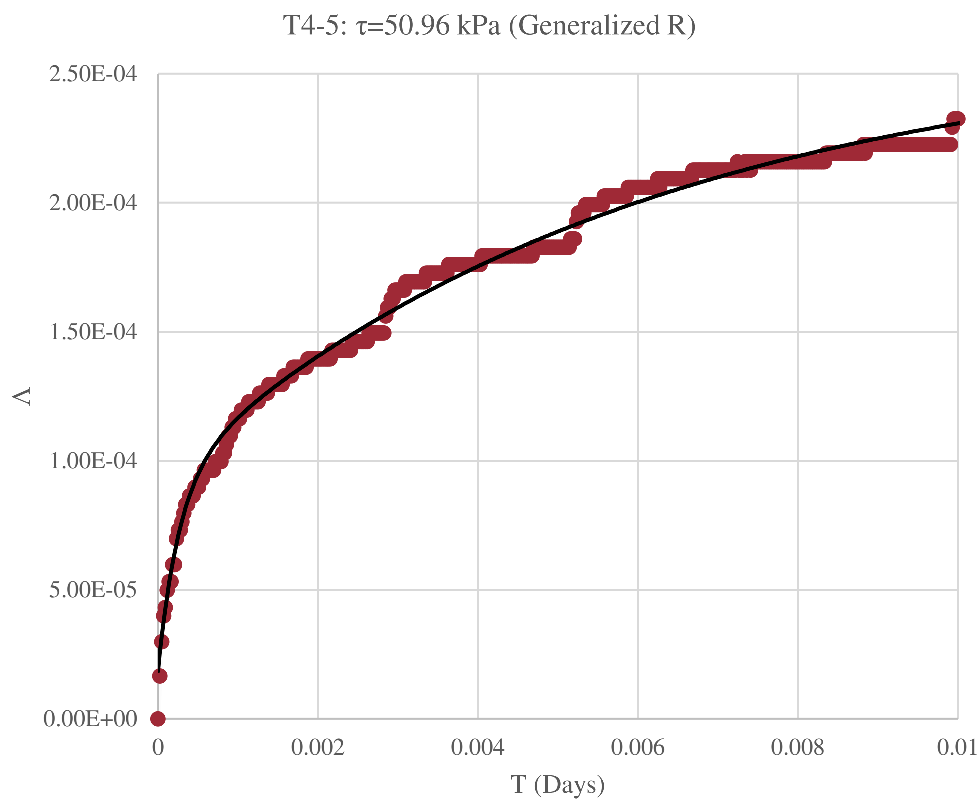
T4-5: τ=50.96 kPa (Generalized R)
2.50E-04
2.00E-04
1.50E-04
1.00E-04
5.00E-05
0.00E+00
Λ
0
0.002
0.004
0.006
0.008
0.01
T (Days)

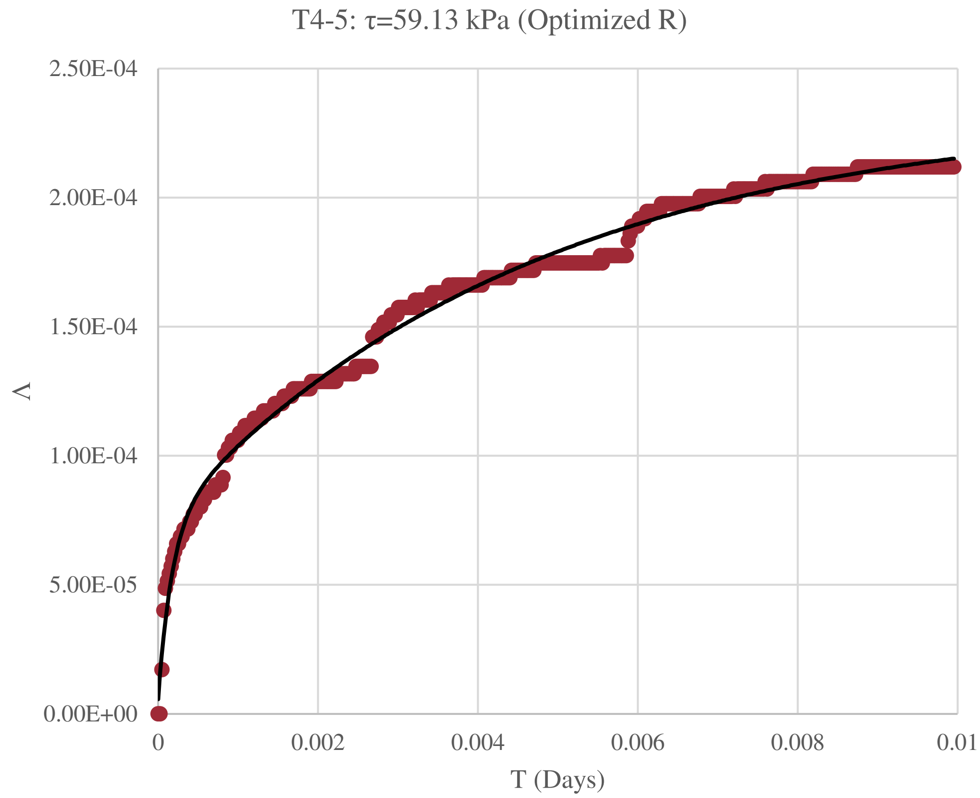
T4-5: τ=59.13 kPa (Optimized R)
2.50E-04
2.00E-04
1.50E-04
1.00E-04
5.00E-05
0.00E+00
Λ
0
0.002
0.004
0.006
0.008
0.01
T (Days)

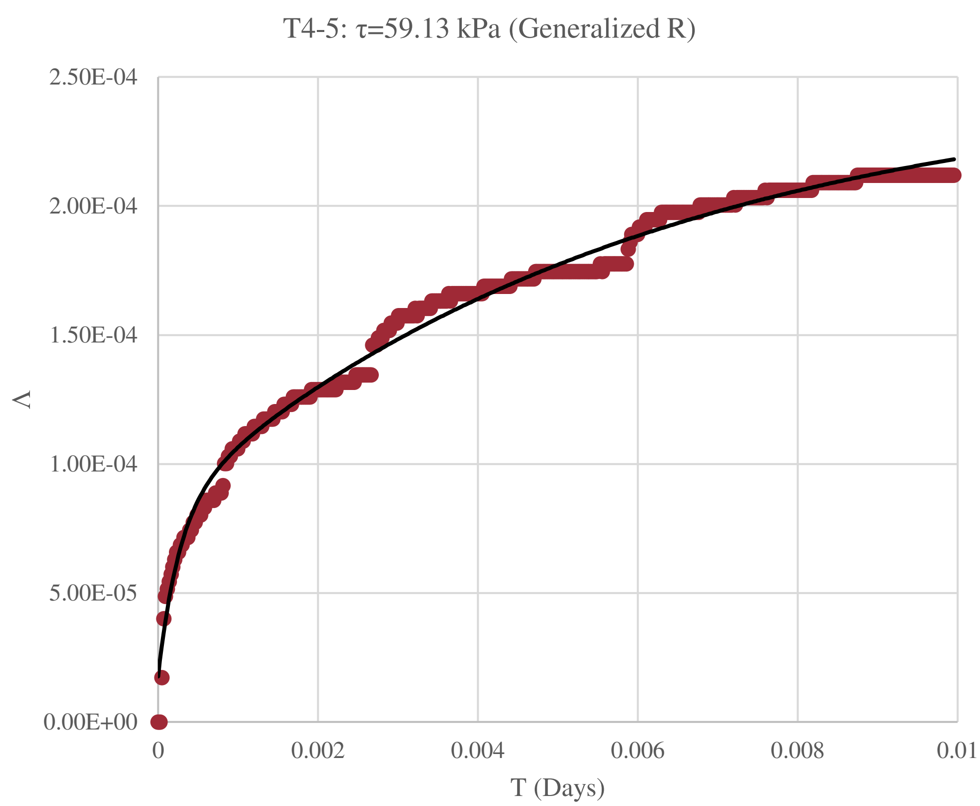
T4-5: τ=59.13 kPa (Generalized R)
2.50E-04
2.00E-04
1.50E-04
1.00E-04
5.00E-05
0.00E+00
Λ
0
0.002
0.004
0.006
0.008
0.01
T (Days)